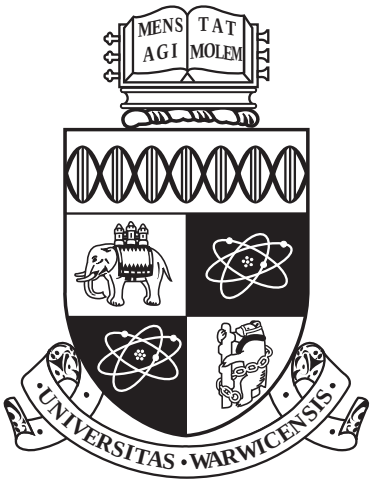

An Investigation of Turbulent Boundary Layers with Streamwise and Spanwise Pressure Gradients

by

Nicholas Farquharson Pearce

Thesis

Submitted to the University of Warwick

in partial fulfilment of the requirements for the degree of

Doctor of Philosophy

Department of Engineering

May 2013

THE UNIVERSITY OF
WARWICK

Contents

List of Tables

List of Figures

Acknowledgments

I would like to begin by thanking my supervisors, Duncan Lockerby and Petr Denissenko for their insight and continuing support throughout this project. Further thanks go to Carlos Duque, Mark Brend, and Karen Kudar for additional help and assistance. Finally, I would like to thank the technical staff at the University of Warwick, in particular Ian Axel, for their hard work and skill.

Declarations

This thesis, and the material in it, is my own work. It has not been submitted for a degree at any other university.

Abstract

An experimental comparison is made between two turbulent boundary layers produced in a low-speed water channel subjected to different pressure gradient distributions. Both flows involve identical favourable streamwise components, generated via a lateral contraction of the flow area; and in the second case, an additional spanwise gradient is imposed by curving the walls.

The measurement system and methods are developed in full, with rigorous testing and validation allowing the uncertainty and accuracy of the results to be estimated. Hot-wire anemometry is employed to take measurements of velocity using miniature single-film probes. A Hydrogen bubble visualisation system enables an inspection of the coherent turbulent structures in the boundary layer near the wall.

The mean-velocity measurements show a continued rise in the Reynolds number downstream accompanied by a fall in the coefficient of friction, in spite of a relatively high streamwise acceleration. This unorthodox behaviour was found to occur for both flows. In response to the acceleration, changes in the statistical moments of streamwise velocity show an increased dominance of high velocity fluctuations near the wall. This corresponds with the results of the structure visualisations which reveal a rise in the mean spanwise spacing of the low-speed fluid elements.

The pressure gradients of the two cases are generated using a novel approach which aims to make the effects from each strain easier to evaluate. The additional spanwise component in the second case induced a crossflow in the boundary layer which reached 11% that of the local external velocity. Despite this, the measurements and low-speed streaks show the turbulence to be relatively insensitive to this level of three-dimensionality.

A simple numerical method is presented to model the development of the low-speed fluid streaks in different mean-velocity distributions. Using this model, greater crossflow magnitudes in the boundary layer are tested for which a positive streak dependence is found.

Abbreviations

A = area (m^2); constant

B = wall-normal axis intercept of the 'universal' law-of-the-wall; constant

C_P, C_f = coefficient of pressure/friction

D, D_{11} = calibration cylinder diameter (m)/spectra structure function

E = one-dimensional power spectral density; anemometer voltage (V)

G = Clauser shape parameter; gain in kinetic energy of the optimum perturbation

H = boundary layer shape parameter

I = current (A)

K = non-dimensional pressure gradient parameter

K_q , K_λ= kurtosis of the streamwise velocity/spanwise streak spacing

L = streamwise distance towards the sink point (m)

P = pressure ($kg{\cdot}m^{-1}{\cdot}s^{-2}$); probability

S_q, S_λ = skewness of the streamwise velocity/spanwise streak spacing

T = temperature (°C)

Q, U, V, W = mean velocities in the local mean-flow/$x/y/z$ directions ($m{\cdot}s^{-1}$)

Q_e, Q_τ = mean velocity at the edge of the boundary layer/friction velocity

R = Resistance (Ω)

Re = Reynolds number

a = constant

a_1 = Townsend's structural parameter

b = perturbation height parameter. Peak in perturbation amplitude occurs at a distance $y = 1/\sqrt{b}$ from the wall

$c_{1,2}$ = curvature of the streamwise/spanwise directions

d = diameter (m)

f = frequency (Hz)

h = flow depth (m); computational domain

k, k_s = turbulent kinetic energy ($\mathrm{m^2 \cdot s^{-2}}$); thermal conductivity ($\mathrm{W \cdot m^{-1} \cdot K^{-1}}$)/ wavenumber

l = length (m)

q, u, v, w; v_k = velocities in the mean-flow/$x/y/z$ directions ($\mathrm{m \cdot s^{-1}}$); kolmogorov velocity

q', u', v', w' = fluctuating velocities in the mean-flow/$x/y/z$ directions ($\mathrm{m \cdot s^{-1}}$)

t, t_i = time/integral time (s)

s = streamwise distance (coordinate) from pressure-gradient generator inlet (m)

n = spanwise coordinate orthogonal to the streamwise direction (m)

y = coordinate normal to the (x,z) and (s,n) coordinate planes and the wall

x = coordinate in cartesian coordinate system; length

z = coordinate orthogonal to the (x,y) plane

z_{α_c} = z-score of normal distribution with α_c significance level

Ω = mean vorticity; angular velocity

Δ = change; length (m)

Δ_c = Clauser boundary-layer thickness

Ξ = diagnostic function for the inner scaled mean-velocity gradient

Π = wake strength

Λ = sweep angle (°)

α = probe yaw angle (°)

α_c = significance level

β = spanwise wavenumber of perturbation

η = Kolmogorov length scale (m); Blasius similarity coordinate

ℓ = eddy length scale (m)

τ = autocorrelation time lag (s)/numerical simulation period

τ_e = eddy turnover time

τ_t = turbulent shear stress

τ_w = shear stress at the wall ($\mathrm{kg{\cdot}m^{-1}{\cdot}s^{-2}}$)

δ = boundary-layer thickness (m)

δ_θ, δ^*, δ_{99} = boundary layer momentum/displacement/where $Q \cdot Q_e^{-1}$=0.99 thicknesses (m)

γ, γ_e, γ_τ = mean-flow direction at the local position/of the freestream/at the wall (°)

σ = standard deviation

ψ = Blasius stream function

θ_τ, θ_g = direction of the shear stress/strain-rate vectors (°)

$\lambda =$ streak spacing (m); Taylor microscale

$\kappa =$ mean-velocity gradient of the 'universal' law-of the wall

$\nu =$ kinematic viscosity ($\mathrm{m^{-2}{\cdot}s^{-1}}$)

$\rho =$ density ($\mathrm{kg{\cdot}m^{-3}}$)

ω, $\omega' =$ vorticity/fluctuating vorticity

Superscripts and Accents

$^{-}$ ensemble average

$^{+}$ non-dimensionalisation with inner (or viscous) length scales using the quantities ν, τ_w, and ρ

Chapter 1

Introduction and Background

This Chapter briefly introduces some of the concepts and nomenclature that will feature throughout this thesis, and gives a background to the research subject. §1.1 discusses the turbulent boundary layer and the different regions and scales used for their analysis. §1.2 introduces three-dimensional turbulent boundary layers which are the main subject of this investigation, and describes their distinguishing features which make them a relevant subject for examination. In §1.3 the aim of the work is given and the structure of the thesis is detailed.

1.1 Turbulent Boundary Layers

The prevalence of turbulent wall flows in engineering and meteorological interests makes them a staple of many research fields. The practical matters of calculating the friction drag on a body in a fluid flow, and the mixing properties of the turbulence in the layer have remained amongst the central themes for industry and engineering. As the turbulence in the boundary layer plays a significant role in both these areas, understanding and predicting the mechanisms at work in complex turbulent wall-flows has become a principle aim of research, largely driven by potential improvements in the efficiency of turbine machinery and fuel consumption.

The additional scale imposed by the wall in a turbulent flow leads to multiple regions or layers being defined for the treatment of boundary layers (Tennekes and Lumley, 1972). The outer layer, which makes up the majority of the boundary layer, comprises mostly non-deterministic turbulent motions made up of large eddies whose lengths scale with the boundary layer thickness δ. The flow in the outer layer is largely inviscid at high Reynolds number, given by $Re = Q_e\delta/\nu$, where Q_e is the velocity of the external flow at the boundary layer edge $Q_e{=}Q(\delta)$. Close to the surface an inner layer develops, which is dominated by viscous effects. The eddies in this region are smaller, scaling in viscous wall units given by ν/Q_τ, where Q_τ is the friction velocity, defined by $Q_\tau = \sqrt{\tau_w/\rho}$, and τ_w is the shear stress at the wall. The two layers overlap in the logarithmic region, though the wall-normal height (y) of the inner layer is commonly referred to be around $y/\delta{\approx}0.1$ (Pope, 2000).

1.2 Three-Dimensional Turbulent Boundary Layers

Two-dimensional turbulent boundary layers are perhaps the rarer amongst those of practical interest. Most will be subject to additional forces such as pressure gradients or the movement of the surface, which have the potential to fundamentally alter their statistical properties. Over almost all aerofoils, for example, both an accelerating and decelerating pressure gradient can be found.

Forces perpendicular to the direction of the mean flow give rise to a three-dimensional boundary layer in which the mean-velocity profile changes direction, creating a crossflow component. Boundary layers with a crossflow occur over swept wings, in curved ducts, oceanic and atmospheric currents, and any moving surface in a turbulent flow that changes its streamwise direction. The prevalence of boundary layer three-dimensionality leads Johnston and Flack (1996) to describe it as the 'rule rather than the exception'; yet it remains among the least well understood features of complex turbulent boundary layers. As Bradshaw (1987) remarks, even a mild

crossflow component can cause dramatic changes in behaviour of the turbulence and this has led to a recent growth in interest to investigate and understand its effects.

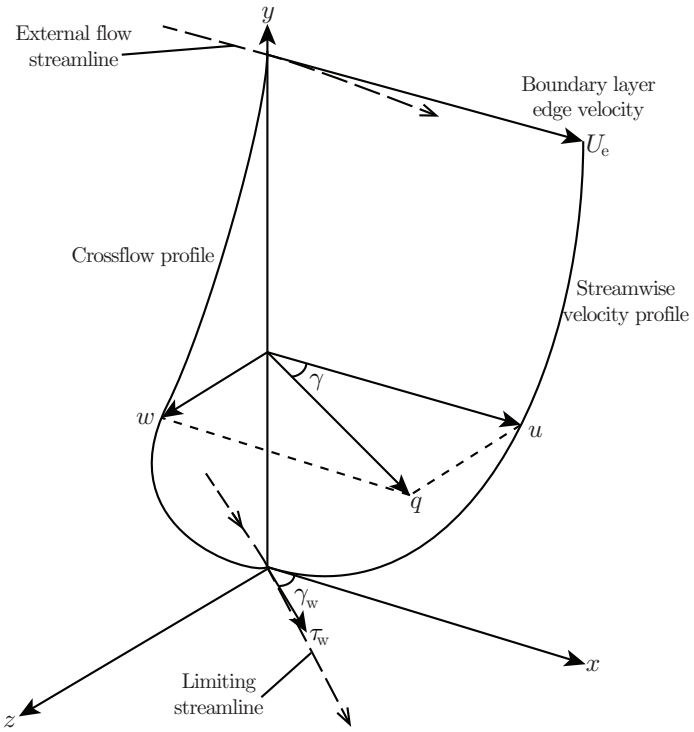

Figure 1.1: A typical velocity profile of a three-dimensional turbulent boundary layer. Modified from Degani et al. (1993).

An example of the velocity profile in a three-dimensional boundary layer is shown in Figure 1.1. The figure shows the external flow to be curved, though this is not a necessity for a crossflow to develop. The change in the mean-flow direction gives rise to many different coordinate systems being used. The figure shows the boundary layer aligned with the local streamwise direction of the external flow, which requires a curvilinear coordinate system to be used, though Cartesian coordinate systems feature more often in the literature. The streamline coordinate system clearly reveals the new cross-stream velocity profile, which distinguishes a three-dimensional boundary layer and gives them an easily recognisable shape. In streamline coordinates: x, y, z define the orthogonal streamwise, wall-normal and spanwise coordinate axes with x aligned with the local direction of external stream-

line; u, v, w denote the fluid velocities along each axis. Velocities are decomposed into their mean (capitals) and fluctuating (primed) components according to:

$$u = U + u' \tag{1.1}$$

$$v = V + v' \tag{1.2}$$

$$w = W + w' \tag{1.3}$$

The velocity in the resultant direction in the boundary layer is defined as: q. The (resulting) mean velocity of the boundary layer (Q) turns away from the streamwise x-direction through an angle γ called the skew angle. The limiting angle at the wall is called the wall skew angle γ_w. At the boundary layer edge, there is no crossflow component and the velocity of the external freestream flow is defined as: Q_e=U_e=$U(\delta)$.

1.3 Thesis Outline

Three-dimensional turbulent boundary layers with streamwise pressure gradients are the central theme of this thesis. The aim is to gain further insight into these particular types of flows and experimental approaches are adopted to pursue this. The remainder of this section outlines the thesis structure.

The main aspects of the current understanding and research into turbulent three-dimensional boundary layers are reviewed in Chapter 2. Though a crossflow is a feature in the majority of the wall flows of interest, more often than not significant streamwise gradients will also be present. Consequently, favourable streamwise pressure gradients will also be a major feature in this investigation and so an examination of the current understanding of accelerated boundary layers is included. Both these reviews follow an initial examination of the research into the coherent turbulent structures found to inhabit the near-wall region of a turbulent boundary layer; structures which are widely thought to play a leading role in shaping and

defining the dynamics of the turbulent flow.

Chapter 3 describes the experimental apparatus and techniques deployed to carry out the work. The experiments were performed in a very large low-speed water channel and conventional hot-wire anemometry used for the bulk of the measurements. The experimental tools and methods are then used to conduct measurements in zero-pressure-gradient turbulent boundary layers. Though these have been thoroughly investigated by others, the measurements provide comparison data with the results obtained in the remainder of the study. Visualisation using Hydrogen bubbles as passive scalars reveals the turbulent structures in the immediate vicinity of the wall.

The three-dimensional flow studied is generated using a spanwise pressure gradient, created by curving the walls of the channel. This approach has been used by others in the past such as Schwarz and Bradshaw (1994) and Flack and Johnston (1998), though as will be seen, complex and deleterious streamwise strains also resulted in their experiments. The method adopted in this thesis attempts to improve on these previous efforts by keeping the ratio of the streamwise to spanwise pressure gradients constant along all streamlines. This has the added benefit that each component can be changed individually, allowing the effects from the favourable pressure gradient to be investigated in relative isolation using a seperate experimental study. The details of this approach and the results are given in Chapters 4 and 5, with the former focusing on the single pressure gradient case study and the latter showing the results using two pressure gradient components.

Chapter 6 details a separate numerical study carried out to model the way in which a mean cross-stream velocity profile influences the initial growth in the kinetic energy of small disturbances to the flow near the wall.

Finally, in Chapter 7 the main findings and conclusions from this research are summarised and suggestions for further work are given.

Chapter 2

Literature Review

Chapter 1 briefly introduced turbulent boundary layers under zero-pressure-gradient conditions though it was shown that these flows rarely exist in isolation to additional forces which modify their behaviour. This chapter looks at some of the ways an additional streamwise acceleration of the flow or a spanwise forcing can change the structure of the turbulence. This begins in §2.1 with an introduction to the coherent turbulent structures currently thought to play a leading role in the boundary layer fluid dynamics. §2.2 then reviews the changes to these structures and the turbulence statistics which occur when an additional spanwise force changes the mean-velocity direction, resulting in a three-dimensional boundary layer. The effects of streamwise pressure gradients on these flows is evaluated and the dearth of studies addressing accelerating three-dimensional boundary layers is highlighted. §2.3 then looks at the current understanding of favourable streamwise pressure gradients on turbulent boundary layers and in §2.4, the scope of this investigation is outlined.

2.1 Coherent Structures in Turbulent Boundary Layers

Investigating and interpreting the complex and predominantly non-linear processes at work in a turbulent boundary layer necessarily accompanies an amount of subjec-

tivity, which is reflected in the many intricate descriptions and explanations given in the literature for the flow patterns observed. Since the early works of Theodorsen (1952) and Kline et al. (1967), the most popular conceptual models involve organisations of spatially coherent structures, the most notable of which are the 'hairpin vortex', 'streamwise vortex' and 'low-speed streaks'. There is now a burgeoning amount of work on the topology of an undisturbed zero-pressure-gradient turbulent boundary layer using these concepts, and their interactions are widely thought to both govern and sustain the turbulence in the boundary layer. A brief outline is therefore pertinent to the current work and further reviews are provided by Robinson (1991), Panton (2001) and Adrian (2007).

2.1.1 Near-Wall Turbulence Events and Low-Speed Streaks

Robinson (1991) describes the cycle of the turbulence near the wall in a boundary layer as comprising a repeating process of 'violent outward ejections of low-speed fluid' and 'inrushes of high-speed fluid toward the wall'. The terms 'sweep' and 'ejection' were first used by Kline et al. (1967), to describe the formation and behaviour of the coherent turbulent eddies they visualised inhabiting the inner-layer of a turbulent channel flow. Their experiments revealed that low-speed (with respect to the mean) fluid close to the wall is 'swept' upward into long streamwise filaments called low-speed streaks. This accompanies an exchange of high velocity fluid towards the wall and hence is a major contributor of near-wall Reynolds stress ($+u'$, $-v'$). As the streaks travel downstream, they rise slowly and begin to oscillate. The oscillations increase in intensity with the distance from the wall and eventually at a height of between $10 \leq y^+ \leq 30$ break-up, releasing low momentum fluid. Here, a + superscript denotes non-dimensionalisation with inner, or viscous, length scales ($y^+ = yQ_\tau/\nu$). The rising or 'lifting' of the low-speed streak is described as an 'ejection' and is also responsible for the production of near-wall Reynolds stress ($-u'$, $+v'$) (Schoppa and Hussain, 2002). Sweeps and ejections have since become used

for the names of these specific stress producing motions in the turbulent boundary layer and have been collectively termed the bursting process (Robinson, 1991).

Spalart (1986) observes that streaks appear to be universal features of turbulent boundary layers. The dimensions of the streaks, in particular their mean spanwise spacing ($\bar{\lambda}$), is readily measurable near the wall using a range of visualisation and statistical techniques. When non-dimensionalised with viscous units, the mean spanwise spacing ($\bar{\lambda}^+$) and streamwise length take on consistent values in all non-perturbed turbulent boundary layers without significant pressure gradients and, consequently, have become 'one of the more reliable measurements in the turbulent boundary layer' (Jeong et al., 1997). At $y^+ \approx 5$, the non-dimensional streak spacing is $\bar{\lambda}^+ \approx 100$ and the streamwise length is $\Delta x^+ \approx 1000$ (Smith and Metzler, 1983). Slight changes to these dimensions occur with the distance from the wall, but available experiments suggest that, generally, these scales remain the same independent of the Reynolds number.

2.1.2 Quasi-Streamwise and Hairpin Vortices

Schoppa and Hussain (2002) comment that the motions of the streaks and the main turbulent events observed in boundary layers simply reflect the passage and behaviour of the quasi-streamwise vortices. Numerous experimental and numerical investigations have revealed the critical and dominant role played by streamwise vortices in the dynamics of the streaks and bursting process. Kim et al. (1987) estimate that the average diameter of the vortices in their direct numerical simulation of turbulent channel flow are approximately 30 viscous wall units, and the centres of the vortices are located around $y^+ \approx 20$. Jeong et al. (1997) show that they are the dominant coherent structures in the region $10 \leq y^+ \leq 40$, are nearly aligned in the streamwise direction (hence termed 'quasi'-streamwise) with a length of $200\Delta x^+$.

Hairpin vortices are another coherent structure model often evoked to describe the essential features of near-wall turbulence (Robinson, 1991). Hairpin (or

horseshoe) vortices consist of streamwise vortex 'legs' in the inner layer that tilt upwards and spanwise to form the 'head' of an Ω-shaped vortex. The passage of the vortices create an elongated region of low-speed fluid not unlike the quasi-streamwise structures above. Hairpins though, are very large, frequently scaling with the width of the boundary layer itself. They are often aligned behind each other in the streamwise direction and grow downstream due to streamwise straining (Adrian et al., 2000). Fluid interactions around the head and legs is responsible for the ejection and bursting 'events' (Adrian, 2007) and Zhou et al. (1999) show that these processes can interact with a single vortex, precipitating the formation of new hairpins.

Though differing in appearance and scale, it is evident that these structures share several important features. Namely, they both involve streamwise orientated regions of vorticity located near the wall and both provide explanations for the formation and dimensions of the low-speed streaks; a necessity for any turbulence model. As observed by Adrian et al. (2000), if isolated to y^+<60, the behaviour of hairpin and quasi-streamwise vortex models are very similar.

2.2 Three-Dimensional Turbulent Boundary Layers

In Chapter 1, three-dimensional boundary layers were introduced and their prevalence in real non-laboratory engineering flows, such as swept wings or turbine blades was shown. This section looks at some of the distinguishing features of three-dimensional turbulent boundary layers which makes their behaviour a topic of interest and necessity for investigation. Further reviews of three-dimensional turbulent boundary layer research are provided by Bradshaw (1987) and Johnston and Flack (1996).

2.2.1 Outline of Three-Dimensional Turbulent Boundary Layers

Simply defined, three-dimensional turbulent boundary layers are those in which there is a significant streamwise mean vorticity component i.e. $\partial W/\partial y$. There are two main methods of driving mean streamwise vorticity into a two-dimensional turbulent boundary layer: pressure and shear. In the pressure-driven variety, the irrotational strain $dW/dx = dU/dz$ induced by an externally imposed spanwise pressure gradient ($\partial P/\partial z$) 'inviscidly skews' or deflects the mean velocity in the boundary layer. The mean spanwise vorticity of the boundary layer is rotated in the opposite direction to that of the mean flow (Bradshaw, 1987; Coleman et al., 2000). When shear drives the streamwise vorticity, the stress from for example, a moving surface such as a rotating disk or traversing channel floor, generates dW/dy directly at the wall. Even in pressure-driven boundary layers however, the near-wall vorticity is generated by the shear imposed from the no-slip condition as it is in the shear-driven variety. The main difference between the two is the presence of the irrotation strain in the outer layer.

There are two principal approaches followed by investigators of introducing forces into laboratory flows and the resulting behaviour may be described accordingly. These include equilibrium (stationary/self-similar) flows in which some time-independent state has been reached, and perturbed (non-equilibrium/transient) flows in which an equilibrium state is disturbed by a sudden force. Given the self-similar nature of equilibrium flows, they tend to lend themselves more readily to simple mathematical or theoretical predictions, though equilibrium conditions are usually harder to implement in the laboratory. Experiments on perturbed boundary layers are generally more complex than equilibrium flows due to the transient period and the practical consequences of applying the perturbation. They are however, more representative of those flows occurring in engineering applications (Coleman et al., 2000)

Examples of pressure-driven perturbed three-dimensional experiments in-

clude those by Schwarz and Bradshaw (1994) and Flack and Johnston (1998), who both use a straight channel with a downstream bend in it; by Anderson and Eaton (1989); Compton and Eaton (1997) and Olcmen and Simpson (1995) who place objects such as wedges into the flow path; and the swept wing experiments of Bradshaw and Pontikos (1985), Baskaran et al. (1990) and Itoh and Kobayashi (2000). A shear-driven non-equilibrium experiment has been conducted by Kiesow and Plesniak (2003). Equilibrium experiments have only been conducted on shear-driven flows such as the rotating disk experiments by Littell and Eaton (1994), Itoh et al. (1992), Chiang and Eaton (1996) and the rotating cylinder experiments by Bissonnette and Mellor (1974) and by Fernholz and Vagt (1981). Currently, there appears to be no equilibrium pressure-driven three-dimensional experiments. Numerical studies are provided by Hanjalic et al. (1994), Coleman et al. (1996), Coleman et al. (2000), Le et al. (2000) and Holstad et al. (2010).

2.2.2 Characteristics of Three-Dimensional Boundary Layers

Degani et al. (1993) observe that despite much effort, models to predict the mean-flow behaviour in three-dimensional turbulent boundary layers remain unsatisfactory. This is especially pertinent to perturbed, pressure-driven flows given their relative complexity. The Squire-Winter-Hawthorn (SWH) relationship however, has been shown repeatedly to provide a reasonable description of the outer layer velocity profile even when subjected to an adverse streamwise pressure gradient (Coleman et al., 2000). The relationship describes the inviscid skewing of the boundary-layer vortex lines away from the (perpendicular) mean-flow direction. The crossflow velocity predicted using the SWH relationship reads:

$$\frac{W}{Q_e} = \left(1 - \frac{U}{Q_e}\right) \tan(2\gamma_e) \tag{2.1}$$

The behaviour of the inner layer is more complicated. Using asymptotic analysis, Degani et al. (1993) investigated the effects of pressure gradients and Reynolds number for equilibrium pressure-driven three-dimensional flows, finding the cross-flow velocity profile dependent on both. Examples of this are the duct-bend flows of Schwarz and Bradshaw (1994) and Flack and Johnston (1998). Despite the similarity in their test section geometries, the skewing at the wall ($\gamma_e - \gamma_w$) is greater in the latter for a given value of γ_e. The only significant difference between the two flows tested appears to be their respective Reynolds numbers.

Turbulent Behaviour

It might be expected that the addition of mean three-dimensionality into a two-dimensional turbulent boundary layer would have a destabilising effect on the flow, supplying additional energy to the turbulence. A distinguishing feature of three-dimensional boundary layers however, is that the opposite is often the case, with many turbulent quantities indicating a more stable flow. This is best illustrated by the structural parameter a_1, calculated as the ratio of the turbulent shear stress to two times the turbulent kinetic energy:

$$a_1 = \frac{\tau_t}{2k} = \frac{\sqrt{\overline{u'v'} + \overline{v'w'}}}{\overline{u'^2} + \overline{v'^2} + \overline{w'^2}} \tag{2.2}$$

This statistic contains much information about the flow and can be thought of as the 'efficiency' with which the turbulent motions can extract energy from the mean shear and turn it into shear stress. For a parallel turbulent boundary layer, a_1 is typically 0.15 between $0.1<y/\delta<0.8$, goes to zero at the wall and drops to low values in the outer regions. Broadly, for three-dimensional turbulent boundary layers, increasing the skew angle $\gamma = \tan^{-1}(W/U)$ leads to a larger reduction in the streamwise shear stress ($-\overline{u'v'}$) and a_1 near the wall; evidence of a flow stabilisation. There is little

agreement though, about the magnitude of the reduction in a_1 and in pressure-driven flows the outer layer of boundary layer seems equally likely to see a rise in the streamwise shear stress.

The typical response is illustrated by the swept-wing flows of Bradshaw and Pontikos (1985), Baskaran et al. (1990) and Itoh and Kobayashi (2000) with all three measuring a reduction in a_1 in excess of 30% as the skew angle increases. A drop in the turbulent kinetic energy and a rapid decline in the streamwise shear stress are also observed. The cross-stream shear stress ($\overline{v'w'}$) rises, which is expected, but at a much slower rate compared to the decline in the streamwise component. Moin et al. (1990), Coleman et al. (1996) and Kannepalli and Piomelli (2000) investigate shear-driven three-dimensional boundary layers in channel flows numerically using DNS or LES. Moin et al. (1990) simulate a spanwise acceleration of the channel wall velocity, and Coleman et al. (1996) and Kannepalli and Piomelli (2000) investigate a sudden, constant motion of the wall. The transient and equilibrium behaviour of Moin et al. (1990) therefore differs, but all three come to similar conclusions with the typical decline in turbulent shear stress, kinetic energy and a_1 near the wall, as well as an increase in the dissipation rate.

A further distinguishing feature of three-dimensional turbulent boundary layers is their anisotropy, as demonstrated by the difference seen in experiments between the shear stress vector direction:

$$\theta_\tau = \tan^{-1}\left(-\frac{\overline{v'w'}}{\overline{u'v'}}\right) \tag{2.3}$$

and that of the strain-rate vector:

$$\theta_g = \tan^{-1}\left(\frac{\partial W}{\partial y}/\frac{\partial U}{\partial y}\right) \tag{2.4}$$

The use of a scalar isotropic eddy viscosity as a turbulence model, is then, clearly inappropriate for such boundary layers. The divergence between these two angles is a consistent trend in almost all three-dimensional turbulent boundary layer studies

and does not appear to be influenced severely by streamwise velocity gradients.

Measurements between studies largely agree with regard to the outer layer, where the shear stress lags behind the velocity gradient direction and the magnitude of the difference depends on the degree through which the flow has turned. Near the wall where available measurements are few, there is greater disagreement. Flack and Johnston (1998) for example, show that θ_g leads θ_τ for most of the outer layer in their 30° bent duct, with a maximum magnitude of 14°. For the inner layer, a region of collateral flow is evident between $20<y^+<50$ and nearer the wall, the shear stress vector is found to lead the velocity gradient vector. Regions where θ_τ leads θ_g are few in the literature and are difficult to explain. A further example is provided by Moin et al. (1990).

Johnston and Flack (1996) imagine that the divergence between the directions of shear-stress and velocity gradient vectors is caused by the 'contamination' of the newer downstream turbulence with the 'history' of the gradually decaying upstream flow. An illustration of this is the difference between perturbed and equilibrium three-dimensional flows. The rotating-disk boundary layer investigated by Littell and Eaton (1994) for example, is close to equilibrium so there is almost no divergence between θ_g and θ_τ and the turbulence appears close to isotropy. In a similar investigation on an enclosed rotating disk, Itoh et al. (1992) show that the stationary side comes closer to equilibrium than the rotating-disk side and demonstrates less deviation between θ_τ and θ_g. A further example is provided by Kannepalli and Piomelli (2000). The section of spanwise moving wall in their channel-flow simulation was long enough to see the formation of an equilibrium collateral region near the wall. This is accompanied by a realigning and recovery of the turbulence as equilibrium is approached, and the divergence between θ_g and θ_τ gradually declines; effects which propagate outwards through the boundary layer with time.

2.2.3 Influence of Streamwise Velocity Gradients

In pressure-driven flows, the disagreement over the stabilisation of the outer layer is often complicated by extraneous practical factors such as additional streamwise pressure gradients imposed on the flow. Adverse streamwise pressure gradients, for example, accompany most pressure-driven three-dimensional flows such as those over swept-wings, and are one of the many influences shown to augment the reduction in a_1 (Johnston and Flack, 1996). Anderson and Eaton (1989) measured a very large decline in a_1 using a downstream 45° split in a rectangular duct, which also produces a strong streamwise deceleration of the flow. They also see a rise in the streamwise shear stress in the outer layer rather than a reduction.

Consequently, there have been attempts to isolate pressure-driven experiments from significant additional streamwise gradients. Schwarz and Bradshaw (1994), Flack and Johnston (1998) and Compton and Eaton (1997) attempt this by keeping the flow area of their experimental ducts constant. Starting with an upstream rectangular duct, the first two generate a spanwise pressure gradient using a downstream 30° bend and the last using a spanwise wedge with an inclined roof. The reduction in a_1 measured in these experiments is more modest, particularly in the outer layer with Schwarz and Bradshaw (1994) even seeing a rise through their bend. The typical behaviour in the shear-stresses are found near the wall but in the outer layer, Schwarz and Bradshaw (1994) see a rise in the streamwise component and Flack and Johnston (1998) and Compton and Eaton (1997) see a fall. Again, the main difference between the two 30° bend flows is the Reynolds number and (Johnston and Flack, 1996) use these cases to highlight the further Reynolds number dependence of three-dimensional results.

A notable investigation into the influence of adverse pressure gradients is carried out by Coleman et al. (2000) using channel flow DNS. Two flows are compared: one representing a swept-wing boundary layer and another which retains only an irrotational strain. Near the wall, the results of the second case show a strong sim-

ilarity to shear-driven flows, which is expected. The strain is shown to impede the energy redistribution between the shear stresses, leading to a stabilisation of the turbulence and a lag in θ_τ. In the outer layer, wall-normal stress is transferred to streamwise shear-stress causing it to rise slightly. When the deceleration is applied however, the flow develops in an entirely different way due in large part, to a rise in the wall-normal stress, which is amplified immediately by the $-\partial U/\partial x = \partial V/\partial y$ strain. The shear stress near the wall now rises and the turbulent energy increases across the layer. The results of Coleman et al. (2000) emphasise the very different behaviour which results when a three-dimensional turbulent boundary layer is subjected to a strong streamwise strain. The deceleration amplifies some three-dimensional behaviour but the immediate effects can overwhelm the slower acting and more subtle influence of the three-dimensionality.

To the writer's knowledge, there are only two investigations into the joint effects of boundary layer three-dimensionality and streamwise acceleration. Launder and Loizou (1992) conduct hot-wire measurements on the flow in a curved duct whose rectangular cross-sectional area decreases with streamwise distance. A complex internal flow structure develops, with strong secondary flows in the streamwise-perpendicular plane. When the acceleration is increased, so is the strength of the secondary flow. Their measurements indicate that for the concave wall, the turbulence level in the boundary layer actually increases for a given non-dimensional distance, despite the higher rate of acceleration. Hanjalic et al. (1994) develop a turbulence model in order to test the combined effects of a shear-driven crossflow perturbation and streamwise acceleration on a turbulent boundary layer. A constant spanwise wall velocity was used and the strength of the acceleration was increased rapidly over a very short streamwise distance. The strong acceleration dampens the growth of the spanwise boundary layer and leads to an almost immediate reversion of the flow back to a 'laminar-like' state in which the turbulence was concentrated in a highly anisotropic field in the buffer layer. Rather than stabilising the near-wall,

the crossflow played a destabilising role sustaining the turbulence in the buffer layer and preventing a complete relaminarisation.

2.2.4 Near-Wall Structures in Three-Dimensional Boundary Layers

Bradshaw and Pontikos (1985) first suggested that the stabilisation of the flow in a three-dimensional turbulent boundary layer is caused by the turning of the structures in the direction of the crossflow, which disrupts the efficiency with which they extract energy from the mean flow. One might also interpret the finding of Coleman et al. (2000), that the irrotational strain reduces the energy transfer between the shear stresses, as the inability of the turning eddies to respond fast enough to produce shear stress effectively in their new direction.

Interpretation of the structural changes usually begins by assuming that the turbulence in a three-dimensional turbulent boundary layer is merely a modified form of that in a conventional two-dimensional boundary layer. This 'base' flow anatomy was discussed above in §2.1. There is little agreement though, between structure investigations in three-dimensional flows which may partly be due to the multitude of methods used to study them. The main areas addressed are the number of streamwise vortices, the number of each vortex 'sign', the strength of the events (ejections and sweeps), the near-wall structure spacing and the effects of crossflow on the behaviour of the events themselves (Johnston and Flack, 1996).

Pressure-Driven Experiments

Anderson and Eaton (1989) reported a more stable wall flow, as the bursting 'events' near the wall were reduced. They suggested that the strength of the streamwise vortices whose sign differed from the mean streamwise vorticity, was being attenuated in some sense. Itoh and Kobayashi (2000) apply a 'quadrant analysis' in which the Reynolds shear stresses are split up to determine the numbers and strengths of the ejections and sweeps. The crossflow produced by their swept wing suppressed

the strength of the ejections, but streamwise gradients are also known to produce large changes in the near-wall structures. Flack (1997) used hydrogen bubble visualisation in the 30° curved duct flow of Flack and Johnston (1998). The crossflow through the bend caused a reduction in the low-speed streak spacing by nearly 10%. The total number of ejections per unit time was also reduced. Ejection strength (or height), vortex sign and the numbers of each were found to be unaffected. Fleming and Simpson (1994, unpublished) saw reduced streak oscillations, measured as a spanwise movement of the streaks. Spanwise streak spacing was also reported to fall by around 10%.

Shear-Driven Flows

In their spanwise moving wall study, Coleman et al. (1996) calculate two-dimensional spectra at y^+=15 which reveal that the larger turbulence scales turn more slowly than the smaller eddies. Contours of wall-normal vorticity reveal the low-speed streaks to be initially 'torn' into smaller structures, but then recovering to become longer and stronger as the flow recovers towards a new state. This tearing up of the wall structures into smaller lengths increases the 'cascade' of energy to the smaller turbulent scales, causing the rise in energy dissipation and the reduction of the turbulent energy. Le et al. (2000), in another simulated spanwise moving wall flow, also see the streaks being 'broken up' into shorter, fewer structures. Using quadrant analysis they recorded stronger ejections but far less of them overall. They hypothesised a 'layering' to the structures, with streaks being dragged by the moving wall under a vortex, impacting each streak depending on the 'sign' of the vortex above it. Kannepalli and Piomelli (2000) see the same wall structure in their LES turbulent boundary layer. They summarise the effects of the shear as not directly impacting the vortices themselves, but changing their interaction with the streaks and it is this reduced, or altered interaction which causes the drop in shear stress and turbulent energy. Finally, Kiesow and Plesniak (2003) provide empirical confirmation

of these observations by using laser-induced fluorescence in their spanwise moving wall experiment. They clearly show the same torn-up streaky structure and large reductions in the mean streak length were measured.

On their rotating disk, Littell and Eaton (1994) conditionally averaged their two-point velocity correlations for strength then apply a quadrant analysis to determine the main turbulent events. Their 'working hypothesis' for the wall layer structure on the disk is one-legged hairpin vortices. They further differentiate the 'sign' of the vortices with respect that of the mean streamwise vorticity. Strong asymmetries between the two-point correlations measured from each type of vortex indicate that for each type, the crossflow weakens one event (either sweep or ejection) whilst strengthening the other. They find equal numbers of both types of vortex and do not postulate as to the cause of the reduced shear stress. Chiang and Eaton (1996) employed hydrogen bubble visualisation on an identical rotating disk to that of Littell and Eaton (1994). They also find an equal number of vortices of each sign and find that equal numbers of a particular event are produced by each. It is found, however, that the strengths of the ejections produced by one vortex type are being significantly weakened by the crossflow. They are unable to address sweep events though, leaving open the possibility of symmetry.

2.3 Turbulent Boundary Layers with Favourable Streamwise Pressure Gradients

There remains some doubt then, that the introduction of mean-flow three-dimensionality into a two-dimensional boundary layer causes a stabilisation of the turbulence. Further, Coleman et al. (2000) show that the introduction of an adverse streamwise velocity deceleration can overwhelm or amplify the influence of the crossflow, resulting in an entirely different flow structure. The limited number studies combining mean-flow three-dimensionality with streamwise acceleration suggest it can play a desta-

bilising role. Favourable pressure gradients themselves remain relatively unexplored compared with their adverse counterparts. In this section, studies of accelerating turbulent boundary layers are reviewed. It will be seen though, that there is far greater agreement between investigations of their behaviour than three-dimensional flows.

2.3.1 Favourable Pressure Gradient Types and Parameters

The modification of a boundary layer by a favourable mean-velocity gradient can vary greatly depending on the way in which it is applied and the Reynolds number or development of the turbulence in the flow itself. Given a mild streamwise acceleration, for example, the friction drag generally continues to increase. Stronger accelerations can lead to the opposite; a reduction in drag. It is well known that a turbulent boundary layer subject to a strong mean-velocity gradient which is sustained for a long streamwise distance will start to undergo reversion back towards a laminar state. This process (often termed relaminarisation, laminarisation, or reversion) is not simple and a typical two-dimensional turbulent boundary layer can pass through many identifiable states on its way back towards a laminar flow. Narasimha and Sreenivasan (1973) review the process of relaminarisation, summarising and simplifying these various states.

A number of parameters have been defined by researchers in order to describe favourable-pressure-gradient turbulent boundary layers. There are four main quantities which appear in almost all studies. The non-dimensional acceleration parameter:

$$K = \frac{\nu}{U_e}\frac{dU_e}{ds} \tag{2.5}$$

was first used by Schraub and Kline (1965). The momentum thickness Reynolds number $Re_\theta = U_e\delta_\theta/\nu$, coefficient of friction, $C_f = 2\tau_w/\rho {U_e}^2$ and boundary layer shape factor:

$$H = \frac{\delta^*}{\delta_\theta} \tag{2.6}$$

are also frequently employed and can disagree between studies not only in magnitude, but also in streamwise development.

Similarly to three-dimensional turbulent boundary layers, favourable pressure gradient flows can also be described as being in equilibrium or perturbed. Here, a perturbed accelerating turbulent boundary layer refers to the situation when the pressure gradient is suddenly imposed on an equilibrium zero-pressure-gradient turbulent boundary layer. Surveys on perturbed boundary layers are provided by, among others, Blackwelder and Kovasznay (1972), the two part survey by Fernholz and Warnack (1998) and Warnack and Fernholz (1998), Piomelli et al. (2000), Talamelli et al. (2002) and Bourassa and Thomas (2009).

The canonical favourable pressure gradient distribution that leads to equilibrium is the sink flow. Sink flows are often favoured by researchers as the pressure distribution is greatly simplified both theoretically and experimentally. It is also the only turbulent boundary layer in which the mean velocity and Reynolds stresses remain invariant when scaled by an appropriate streamwise length (Jones et al., 2001). Under conditions of equilibrium, the four parameters introduced above remain constant with streamwise distance. Further, sink flows have no wake component (the wake strength Π is zero), as found by Coles (1956), because the edge of the boundary layer is also a streamline. The freestream streamlines in a zero-pressure-gradient turbulent boundary layer are directed into the flow itself resulting in entrainment and growth of the boundary layer (Spalart, 1986). Sink flows have been investigated experimentally by Jones and Launder (1972), Jones et al. (2001) and Dixit and Ramesh (2008) among others. A detailed numerical study is provided by Spalart (1986).

Another type of flow which develops a favourable pressure gradient is that in a duct which converges laterally. A straight walled lateral convergence produces the same freestream velocity distribution as the sink flow. Laterally converging ducts have been studied in a four part survey by Murphy et al. (1983), Chambers et al. (1983), McEligot and Eckelmann (2006) and McEligot et al. (2009).

2.3.2 Overview of Investigations and Turbulence Behaviour

The literature addressing the topic of turbulence in an accelerating boundary layer is reasonably large, but a few observations are given in this section which are pertinent to this investigation. The process of relaminarisation is not addressed specifically here as reviews are provided elsewhere (Narasimha and Sreenivasan, 1973). To make comparisons of the results in this project with the literature easier, some of the favourable pressure gradient studies referenced are summarised in Table A.1 in Appendix A.

Favourable Pressure Gradient Perturbations

The experiment by Blackwelder and Kovasznay (1972) provides a good overview of the general response of a turbulent boundary layer to a strong favourable pressure gradient perturbation. In a wind tunnel, they subject a two-dimensional zero-pressure-gradient turbulent boundary layer (Re_θ=2500) with a very strong acceleration rate (K_{max}=4.8×10^{-6}) using a non-linear contraction of the flow area, followed by a downstream straight recovery section. The freestream velocity increases in proportion to the contracted area and the Reynolds number begins a steep decline as the thickness of the boundary layer reduces. For a short initial streamwise distance, the coefficient of friction rises along with the shape factor before they both begin to decline. Shortly after, the shape parameter reaches a minimum then starts to rise as the mean-flow profile tends towards a laminar Falkner-Skan shape. The fluctuating velocity intensities, Reynolds stresses and turbulent energy measured by Blackwelder and Kovasznay (1972) decay through most of the turbulent boundary layer. The majority of this decay however, results from the large rise in free-stream velocity used for non-dimensionalisation. Appropriate scaling units in perturbed turbulent boundary layers are in general not always clear.

This process inevitably entails a gradual departure of the mean-flow profile from the standard 'universal' law-of-the-wall and the nature of this departure can

differ between studies. Some authors (Warnack and Fernholz, 1998) have searched for a parameter or statistic which can be used to signal the 'breakdown' of the law-of-the-wall yet no single satisfactory measure has been found. Generally, the gradient of the mean velocity (κ^{-1}) reduces and the additive constant increases with streamwise distance. The logarithmic mean-flow profile in pressure gradients is investigated by others such as Nagib and Chauhan (2008).

The variability in the possible boundary layer response is evident in the two-part study by (Fernholz and Warnack, 1998; Warnack and Fernholz, 1998). They present the results of detailed hot-wire measurements made in the turbulent boundary layers developed over two different axisymmetric bodies placed in a wind tunnel. The two bodies generate different pressure gradient distributions and the authors perform two experiments for each body using different initial freestream velocities. The resulting four cases allow the parameter space [Re_θ, K, H, C_f] to be explored. Alterations to the turbulence were observed in all cases to varying degrees and two experiments induced the onset of relaminarisation. Their study highlights the importance of the flow history when the perturbation is applied. The acceleration rates in their first and third cases are similar (1.5×10^{-6} and 2.0×10^{-6}), but one Reynolds number is twice as large as the other. The friction in the higher Reynolds number case rises consistently as the flow passes through the region of strongest acceleration. In the other case, the friction reaches a peak before beginning to decline. After passing through the region of maximum acceleration, a sudden sharp increase in friction appears, which the authors interpret as the initial sign of the onset of relaminarisation. A distinction is often made between a 'laminarescent' turbulent boundary layer and a relaminarising one. The authors suggest that this double peak in skin friction distinguishes one state, from the other.

Piomelli et al. (2000) investigate strongly accelerated flows numerically by performing two LES studies of turbulent boundary layers accelerated to two different acceleration rates: a 'mild' rate and a 'strong'. The simulations show that the

turbulence in the boundary layer 'lags' behind the mean flow as the turbulent kinetic energy rises at a slower rate to the mean-flow energy. The structural parameter a_1 reduces near the wall demonstrating that, in a similar way to some three-dimensional boundary layers, the eddies in this region become less efficient at producing shear stress, though this change is not the result of turning the structures.

Bourassa and Thomas (2009) provide detailed hot-wire measurements of a highly accelerated turbulent boundary layer generated in an acute linear contraction (9.5:1). The contraction provides rates of acceleration which eventually leads to relaminarisation of the boundary layer. Despite the severe pressure gradient, logarithmic behaviour of the mean velocity is preserved throughout and a departure from the standard law-of-the-wall is a smooth reduction in the gradient (κ^{-1}). The typical streamwise rise and fall in the friction is seen with a similar streamwise fall then rise for the shape factor. Both parameters change from one type of behaviour to the other around similar streamwise locations near the point where the acceleration reached $K{=}3.0{\times}10^{-6}$. Non-dimensionalised in inner units, the energy and the Reynolds normal and shear stresses decay, but do not scale well with the friction velocity until inside the contraction.

Sink Flows

The behaviour of turbulent boundary layers in sink flow and favourable pressure gradient perturbations share many similarities. Sink flows have been investigated experimentally in detail by Jones and Launder (1972) and Jones et al. (2001). Jones and Launder (1972) investigated three different rates of acceleration: $K{\approx}1.5{\times}10^{-6}$, $2.5{\times}10^{-6}$ and $3{\times}10^{-6}$. For a given K, the inlet boundary layers were varied, but the non-dimensional parameters describing the flow consistently asymptote towards their equilibrium values given by:

$$KRe_\theta(H+1) = C_f/2 \tag{2.7}$$

Profiles of the longitudinal rms velocity, scaled in outer units, appear self-similar (independent of streamwise coordinate) when plotted against a wall-normal similarity variable. It may be noted that the velocity intensity profiles behave differently to those under zero-pressure-gradient conditions. No outer layer 'bulge' is evident and the values decay smoothly from a peak near the wall towards the boundary layer edge. The similarity between sink flow behaviour and that measured in the equilibrium disk boundary layer of Littell and Eaton (1994) is striking. Littell and Eaton (1994) also noted an absence of a wake.

Spalart (1986) explored sink-flow turbulent boundary layers in the same acceleration range to Jones and Launder (1972) using DNS. The energy spectra of the streamwise velocity collapse over the acceleration range when normalised by the total energy. The spectra measured by Spalart also compare favourably with the results of Jones and Launder (1972). An important observation made by Spalart, was that the pressure gradient extended the logarithmic behaviour of the mean flow beyond the region where the shear stress was constant. This has important implications for mixing length and log-law type predictions, a point discussed later in this investigation.

Jones et al. (2001) use smaller acceleration rates and higher Reynolds numbers to explore the development of sink flows from arbitrary initial conditions towards the equilibrium state. Again, three acceleration rates were used, but these result in much larger Reynolds numbers. As the flows come closer to equilibrium, the mean flow evolves towards that of a sink flow; the wake strength decays and the region collapsing with the log-law rises. No change to the standard law-of-the-wall is seen though, as it was for the higher accelerations of Jones and Launder (1972) and Spalart (1986). The fluctuating velocity intensity components and the Reynolds stresses gradually become self-similar downstream. Their profiles each clearly show logarithmic behaviour, which is not predicted by Jones et al..

2.3.3 Modification of the Near-Wall Turbulent Structures

In §2.2.4 the effects of boundary layer three-dimensionality on the coherent turbulent structures was briefly reviewed. In this section, a similar review is made into the effects of favourable pressure gradients. Though still complicated by the flow types and the various investigation methods employed, a more coherent picture is emerging for streamwise acceleration effects. This may be explained in part, by the relatively simpler design of favourable pressure gradient experiments and the fewer complicating practical factors.

Schraub and Kline (1965) used large acceleration rates in a low-speed water channel to investigate the viscous sublayer streaks using hydrogen bubble visualisation. To observe the near-wall bursting activity, dye was injected through the wall and the number of ejections, defined by recognised patterns of violent streak behaviour, were counted for a given time and distance. The streaks were found to be largely unaffected by the pressure gradient within the range: $-2\times10^{-6}<K<1.5\times10^{-6}$, but significant changes occurred for larger accelerations; most notably for the streak spacing and bursting rates. For adverse pressure gradients, the burst rate tended to increase and decreased under favourable gradients. For very large negative pressure gradients ($K> 3.5\times10^{-6}$) the bursting eventually ceased entirely. The non-dimensional mean spanwise spacing of the low-speed streaks ($\overline{\lambda}^{+}$) was also found to increase at strong favourable streamwise gradients, rising to $\overline{\lambda}^{+}=180$ for $K=3\times10^{-6}$ and up to 240 for $K\approx4\times10^{-6}$. Quiescent (laminar-like) regions of bubbles begin to appear at the wall and streaks become more fixed in space, i.e. 'wiggling' less. Eventually, turbulent production in the boundary layer is assumed to cease entirely with the bursting, leading to a laminar state. Further experimental confirmation of the increase in streak spacing is provided by Talamelli et al. (2002) who use time-space correlations of the velocity signals from two spanwise separated hot-wire probes. They measured a rise in $\overline{\lambda}^{+}$ by up to 170% at $K=3.1\times10^{-6}$.

Piomelli et al. (2000) visualised the near-wall turbulence structure using contours of streamwise velocity and vorticity magnitudes for the instantaneous flow field obtained in their LES. Like Schraub and Kline (1965), a slight decrease in the number of low-speed streaks was seen using a mild acceleration suggesting a slight rise in $\overline{\lambda}^+$. With stronger accelerations the streaks became longer and straighter; appearing in general more 'orderly' which suggests less bursting activity. In absolute terms, the magnitude of the streamwise velocity fluctuations rises near the wall, which Piomelli et al. interpret as 'stronger' streaks.

Contours of vorticity magnitude reveal a thinner inner-layer overall, as evidenced by a reduction in the wall-normal extension of vorticity away from the wall. The absolute values of vorticity magnitude also increased, which Piomelli et al. suggest is due to shear between the streaks rather than changes to the quasi-streamwise vortices themselves. Iso-surfaces of the vortices show them to be longer and more aligned in the streamwise direction similarly to the streaks. The vortex strength (the magnitude of streamwise vorticity fluctuations) is not increased however, despite the streamwise stretching caused by the strain. The numbers of vortices are reduced though, which Piomelli et al. explain is caused by the vortex stretching, which reduces their diameter and makes them more susceptible to viscous diffusion. Almost identical behaviour was observed in the sink flow DNS by Spalart (1986). The intense vortical regions which protrude upwards from the wall in a zero-pressure-gradient turbulent boundary layer are more aligned with the wall in the sink flow. The region of intense rotational motion is therefore shallower overall. Streak velocity contours at y^+=11 reveals small regions of quiescent flow, with localised decreases in the number streaks and increased streak spacing and length. Local reductions in the friction velocity and vorticity were also found at these locations.

Bourassa and Thomas (2009) examine the near-wall turbulence behaviour via conditional analysis of their hot-wire measurements. Their strong pressure gradient causes a reduction in the total number of near-wall turbulent events (ejections and

sweeps), but the strength of the upward ejections of fluid increases. The authors reason that the 'mutual induction' between the streamwise vortices is increased by the streamwise straining. This causes a rise in their spanwise separation with an accompanying increase in the spacing of the low-speed streaks. They expect that the reduction in the streak spacing attenuates the local wall-normal vorticity, ω_y, whilst at the same time the streamwise strain increases the local spanwise vorticity, $\omega_z \approx dU/dy$. Reduced local ω_y might also follow from the reduction in streak 'wiggling'. From the observations of Schoppa and Hussain (2002), that the strength of the ejections is determined by the ratio of the 'lifted streak flank' wall-normal vorticity (ω_y) to local ω_z, Bourassa and Thomas (2009) conclude that fewer 'lifted' streaks from ejections will be produced overall, leading to further reductions in streamwise vortex formation and a stabilisation of the near-wall flow. Though the total number of streamwise vortices declines, the streamwise strain increases their angular velocity, resulting in more robust, 'vigorous' wall-normal motions. This disagrees with Piomelli et al. (2000) who suggested that it was the increased susceptibility of the vortices to dissipation, due to their reduced diameter, which lead to a reduction in their numbers.

2.4 Scope and Objectives of the Current Work

Despite considerable research effort, the current understanding of the basic features of three-dimensional boundary layers is far from complete. The evidence that a mean crossflow velocity necessarily accompanies a stabilisation of the turbulence remains inconclusive. Further, the studies by Coleman et al. (2000) and Hanjalic et al. (1994) suggest that three-dimensionality combined with a strong streamwise pressure gradient leads to an entirely different behaviour in the boundary layer. Despite the prevalence of such flows in, for example, high-lift wings and turbine geometry, there are few investigations combining streamwise acceleration and three-

dimensionality. It is the aim of this project therefore, to explore such flows and attempt to address a number of issues as outlined below.

- *Mean-flow distortion*: The mean-flow behaviour in an accelerating three-dimensional boundary layer has not been explored experimentally in any detail. It remains to be seen how the irrotational strain affects the pattern of mean-velocity profile distortion induced by a strong streamwise acceleration, and whether the damping effect of acceleration modifies the development of the spanwise boundary layer. The adequacy of the SWH relationship has also not been tested in accelerating three-dimensional flows.

- *Stabilisation*: It is known that a strong favourable streamwise gradient has a stabilising effect on the turbulent boundary layer. Mean streamwise vorticity can also produce this response, however the results of Hanjalic et al. (1994) suggest that when combined with a streamwise acceleration, the opposite can occur. Experimental surveys of turbulent activity in such flows have yet to be performed and the outer layer remains to be addressed.

- *Streak distortion*: There is more consensus about the pattern of behaviour exhibited by the low-speed streaks in response to a strong streamwise acceleration, than to a mean streamwise vorticity. The effects of a crossflow on this pattern have yet to be explored.

- *Wall structure modification*: There is little agreement between studies of the near-wall structure in three-dimensional turbulent boundary layers. Though there is greater consensus for accelerating boundary layers, the reasons behind the modified wall structures in both flows remain elusive.

To carry out this investigation, a variation of the strategy employed by Coleman et al. (2000), that is, comparing two flows one with and one without streamwise vorticity, is adopted since it facilitates a clearer interpretation of the results. The

design of the experiment must be such that three-dimensionality can be added to the streamwise component without a significant alteration of its strength. The method used to achieve this is detailed in Chapters 5 and 4. It should be kept in mind that, given the highly non-linear interaction between external strains, it cannot be assumed that the resulting behaviour from both will simply be the superposition of their individual effects, i.e., there are limitations to what the current strategy can tell us. The last objective is addressed using a computational study.

The acceleration is required to be strong enough such that the familiar modification of the boundary layer mean-flow and low-speed streaks takes place. Immediate relaminarisation is also undesirable. Following §2.3 above, an acceleration of the order of $K \approx 3 \times 10^{-6}$ will satisfy these conditions. The requirements for the three-dimensionality are more difficult to specify given the variety of observations and behaviour. Johnston and Flack (1996) suggests that the crossflow velocity (W/Q_e) can be used when categorising three-dimensional flows, and consider with Littell and Eaton (1994) that W/Q_e of the order of 10% is significant. From the pressure-driven experiments reviewed, a freestream deflection (γ_e) of 10° would be expected to generate $W/Q_e > 10\%$. All the experiments cited in §2.2 measured large wall skew angles ($\gamma_w - \gamma_e$) for this magnitude of crossflow, and substantial changes to the boundary layer turbulence statistics.

Chapter 3

Experimental Setup and Measurement Techniques

3.1 Introduction

The previous chapters outlined the need for further investigation into the effects of pressure gradients on turbulent boundary layers, and detailed the particular flows being studied and the aims of this investigation. This chapter discusses the measurement system developed for experimentation and the operational methods followed for its use. The main measurement tool is hot-wire anemometry, which has a long and proven history in the study of turbulent boundary layers. As water is the measurement medium, the resulting turbulent length scales are large, providing excellent spatial resolution, especially when used in combination with hot-wire anemometry.

In this chapter, the facility in which the experiments are conducted is discussed first in §3.2, followed in §3.3 by the background and details of the hot-wire measurement system. §3.4 presents the various errors in the measurement system and an estimate is made as to the overall experimental uncertainty. The method employed to measure the wall shear stress is detailed in §3.5, which was used in the turbulent boundary layer measurements reported in §3.6. These experiments

were performed in a two-dimensional flow with no pressure gradient. This provides an effective test of the experimental setup whilst also producing useful data for comparison with later experiments. Finally, §3.7 documents the hydrogen bubble visualisation method used to investigate the coherent structures in the boundary layer near the wall.

3.2 Experimental Facility

The experiments were conducted in a 1 m wide low-speed open water channel which forms part of a recirculating water system (Figure 3.1) that includes two large storage tanks with a total water capacity of approximately 8000 ltrs. The channel is raised from the floor on stilts with the storage tanks beneath, and a frequency controlled pump lifts the water from the storage tanks to the channel via a suspended pipe. The pump outlet delivers the water into a settling region, distributing it through four outlet nozzles. The settling region is filled with porous foam which dampens turbulence exiting the nozzles. The water exits the settling region through a fine mesh screen, before passing through two 50 mm long honeycomb screens with cell diameters 7 mm and 5 mm. These are followed by a set of three further flow screens with large open-area ratios spaced 100 mm apart.

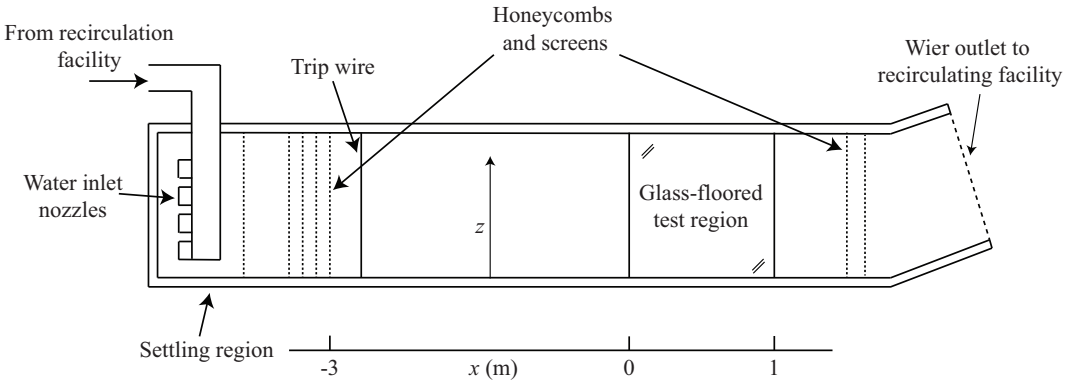

Figure 3.1: A schematic of the experimental water-channel facility.

The channel itself is straight, 3 m in length and constructed from long smooth acrylic sections. This is followed by a 1 m long glass-bottomed test region. Care was taken during construction to ensure that the channel floor and walls were kept flush, both with each other and with the glass-bottomed section. This was done with the aim of eliminating the need for an extra flat plate on which to generate the boundary layer, as this may have hindered optical access through the test region floor needed for streak visualisation. Changes in the channel floor height were measured at the interface between sections using a Mitutoyo micrometer height gauge. The largest step change was found at a far corner of the test section glass floor, which was less than 0.5 mm. As this is downstream of the testing region and shorter than the height of the boundary layer sublayer, it does not pose a problem for experiments.

Following the test section is a further 0.5 m of straight channel, in which a removable honeycomb screen could be placed to act as a flow straightener. The channel then turns, allowing the water to exit over an adjustable weir, and back into the storage tanks below through delivery pipes. To reduce channel vibration, no direct connection between the channel and pumping-recirculation system is made, and the pumps themselves are fixed to rubber shoes to prevent transmission through the floor.

Water was introduced into the rig from the municipal supply and filtered through 20 then 5 micron water filters. A continuous recirculating water filter was operated to clean stored water, which was replaced with fresh water at regular intervals. Temperature stability is critical for using thermal anemometry, so the water temperature was monitored using a platinum-resistance thermometer (PRT) with a resolution of ±0.002℃, which was located in the settling region. Fluctuations in water temperature were kept small, thanks largely to the very large water storage tanks; however should pumping and mixing cause the temperature to rise over a longer run, cool filtered water could be seeped into the tanks to compensate. Changes in water temperature could be kept within ±0.03℃, over a 6 h running period and the temperature record of a typical run is shown in Figure 3.2.

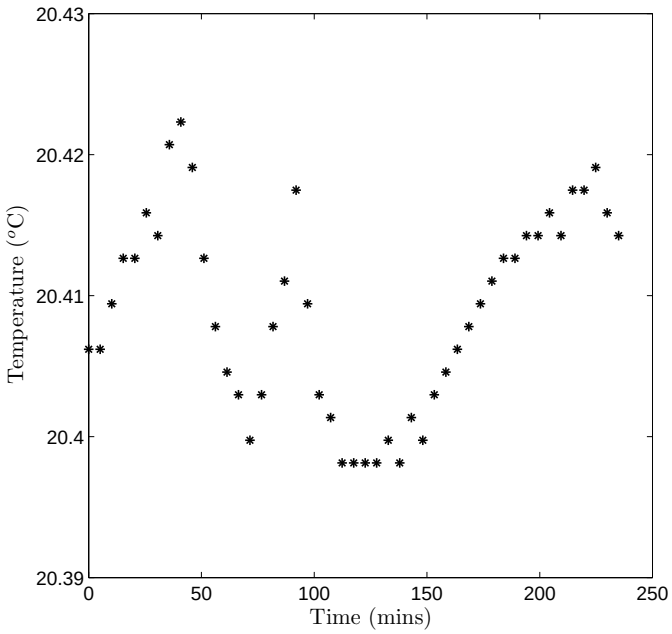

Figure 3.2: Temperature record for a typical test run.

The flow conditions in the testing region were measured using the thermal anemometry system outlined in the next section. For most experiments, the freestream flow at the test section was Q_e=0.125 m·s^{-1} at a flow depth of h=0.15 m. Free-surface effects and wall boundary layers prevented flow uniformity across the entire width of the channel, but a region spanning 0.4 m either side of the centerline was found to have a reasonable uniformity with most of the flow velocity magnitude falling within ±5% of the mean (Figure 3.3). A slight acceleration of the flow in the channel should be expected however, as flow depth is lost to friction with the walls.

The turbulence intensity was <1%, again measured using the thermal anemometry system. Intermittent disturbances were noticed however, below 40 mm from the channel floor. These could be traced upstream by laying dye along the floor using a syringe. A disturbance is identified by a slight movement or lifting of the dye from channel floor. Although some disturbances may have been expected given the Reynolds number at the start of the test area ($Re(x{=}0){\approx}3.8{\times}10^5$), some were found to originate at the interface between the channel and the flow conditioning screens.

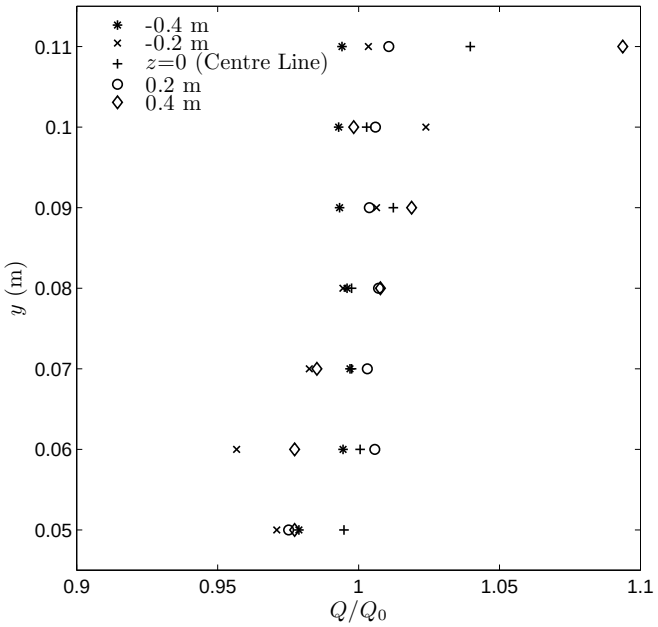

Figure 3.3: Flow uniformity in the testing region.

Isolation of such disturbances from experiments could have been achieved with the addition of a flat plate suspended above the channel floor, but since the floor boundary layers were tripped using a 3 mm diameter rod, this step was felt unnecessary and would have reduced the overall flow depth. The trip wire triggers early transition of the floor boundary layers to turbulence, which helps to maximise the available channel length in which the boundary layer turbulence can develop. This subject is discussed further in §3.6, where low Reynolds number effects in the test section boundary layers are evaluated.

3.3 Hot-Wire Anemometry

Despite its age, hot-wire anemometry remains one of the most popular experimental tools for the investigation of simple and complex turbulent flows (Johnston and Flack, 1996). The excellent spatial resolution provided by most hot-wire probes, makes them highly suited for resolving the intricate details of turbulent flows, the

dimensions of which can be diminutive in laboratory conditions. This is particularly pertinent for the investigation of boundary layers, as the thinness of most artificially produced layers, combined with the restrictions on access imposed by the presence of a solid wall, place considerable demands on available techniques.

This investigation is limited to the use of a one-dimensional, single normal probe for the majority of measurements for two main reasons; the first being that the mean-flow direction in the boundary layer must be found. The low speed of the fluid prevents the use of pressure devices such as pitot-static tubes (ΔP<10 Pa) so the flow direction in a three-dimensional system must be obtained from mean-flow measurements using the hot-wire system. Multicomponent probes cannot be used as these require that the flow direction be known beforehand (Bruun, 1995). The second requirement is that, as explained by Johnston and Flack (1996), the wall shear stress cannot be obtained indirectly, for example, by assuming that the law of the wall holds in the boundary layer, as this and other mean-velocity laws have been shown to fail for three-dimensional and strongly accelerated boundary layers. The large dimensions of multicomponent and 'yawed' probes prevent their operation in the viscous sublayer which is a requirement for direct measurement.

3.3.1 Hot-Wire Operation

As its name suggests, hot-wire anemometry measures the velocity of a flow via the use of a heated wire element placed in the fluid stream. The heat transfer by fluid convection cools the wire, thereby changing its electrical resistivity. By consideration of the heat transfer from a long cylinder by convection, King (1914) was the first to derive a relationship between the fluid and cylinder properties. This takes the non-dimensional form known as King's Law:

$$Nu = A + BRe_{d_w}^{1/2} \tag{3.1}$$

where Nu is the Nusselt number, A and B are empirically determined constants and the Reynolds number is based on the wire diameter d_w and fluid velocity. Equation (3.1) is still used as a model for heat transfer due to its simplicity, though different relationship forms are commonly used to improve accuracy.

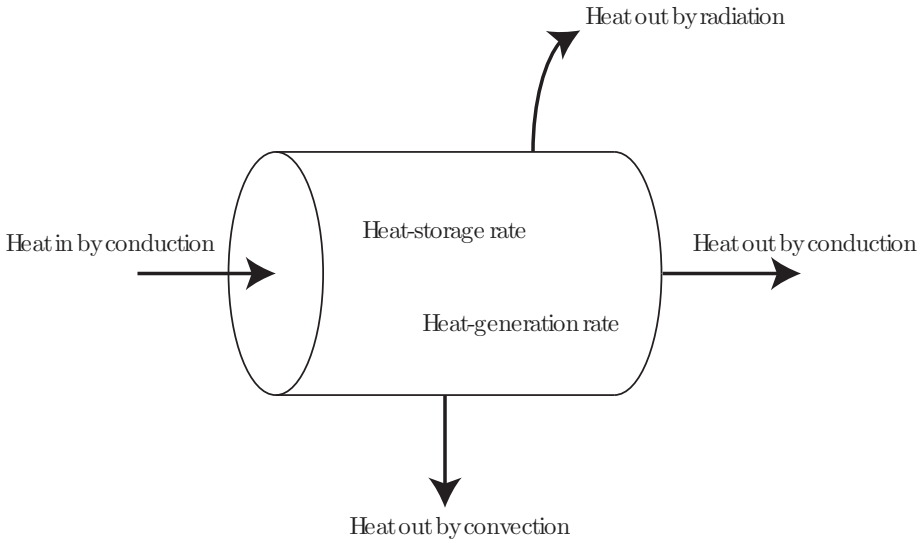

Figure 3.4: Heat transfer terms for an incremental wire element

A more familiar form of King's law can be derived by carrying out a heat-balance analysis for a finite length of wire, taking into account relevant heat sources and sinks of the wire element such as those shown in Figure 3.4. This exercise is carried out by Lomas (1986) and Bruun (1995) and leads to the following expression for King's law:

$$\frac{I^2 R_w}{T_w - T_a} = \pi l_w k_w Nu \tag{3.2}$$

where I, R_w, l_w and k_w are the wire's current, resistance, length and thermal conductivity coefficient and T_w and T_a are the wire and fluid temperatures. In terms of the wire voltage E_w, this is expressed as:

$$\frac{E_w^2}{R_w(T_w - T_a)} = A + BRe_{d_w}^{1/2} \tag{3.3}$$

where the empirical constants A and B are assumed to be modified by the remaining

constants in equation (3.2) and are determined during the calibration procedure.

The left-hand side of equation (3.3) may by simplified to a single value: that of the anemometer output voltage E. This requires the use of a constant-temperature anemometer, as explained in §3.3.2. As noted above, King's law, which was used to express the Nusselt number dependence of the wire, has been found to be an inaccurate representation of the system response. Many ad-hoc modifications to this relationship have been made (Wu and Bose, 1994), the most popular of which is the variation of the Reynolds number exponent, whose value is determined during calibration. Further forms of the heat-transfer equation are discussed in §3.3.3 with the calibration procedure.

3.3.2 Anemometer and Measurement System

The variations in the wire's resistance with the fluid velocity can either be measured whilst keeping the current in the wire constant, or compensated for by increasing the current, hence, resistance and temperature. This gives rise to the two principle modes of hot-wire operation: constant-current (CC) and the simpler, more widely applied, constant-temperature anemometry (CTA). The latter is employed for this experiment. In both operating modes, the wire is placed in a Wheatstone bridge and in CTA, the output of the bridge is amplified and the output fed back to the top of the bridge (Figure 3.5). The bridge is 'rebalanced' as a consequence of the change in bridge current, which restores the probe resistance (R_w) and temperature (T_w). The change in the amplifier output can then be translated to velocity with the particular heat-transfer relationship determined during calibration.

The anemometer used is a DISA 55M10 system, which includes the 55M01 amplifier and 55M10 CTA bridge and signal conditioning circuits. The wire resistance fed into the bridge will clearly be modified by the resistances elsewhere in the system, such as those of the probe cabling and holder, which are compensated for during the system setup procedure (DISA, 1977). The probe is a TSI model

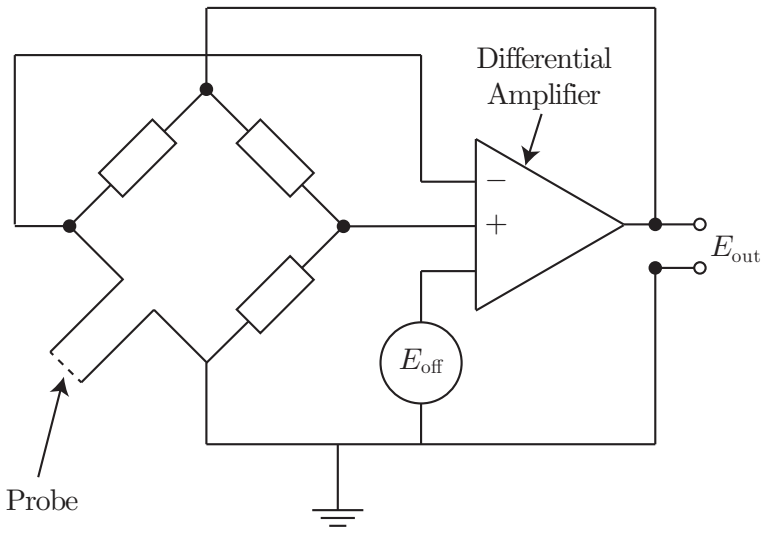

Figure 3.5: Circuit diagram of a constant temperature anemometer. E_{off} and E_{out} are the amplifier offset and anemometer output voltages respectively

1261A miniature single-normal hot-film type (Figure 3.6). The 'boundary-layer-type' prongs on these probes reduce the interference from the stem, and allow the wire to be placed close to a surface without the need to pitch the probe. The film is made of quartz coated platinum, has an active length (l_w) of 0.5 mm and a diameter (d_w) of 25 μm.

The variation of the hot-wire resistance with temperature is given by:

$$R_w = R_{ref}[1 + \alpha_w(T_w - T_{ref})] \tag{3.4}$$

where α_w is the temperature coefficient of resistance and T_{ref} and R_{ref} are reference temperature and resistance. This relationship is provided with most commercial hot-wire probes and for those used, α_w=0.0024°C^{-1}. An overheat ratio of R_w/R_a=1.05 was selected, corresponding to a 20°C excess temperature ($T_w - T_a$). At this overheat ratio, bubble formation on the probe was rare (despite the omission of a de-aeration system) and the maximum frequency response of the probes is 200 kHz (Ricco and Wu, 2004). The probes are held on 150 mm long supports (TSI model 1150) and introduced into the water through the free surface.

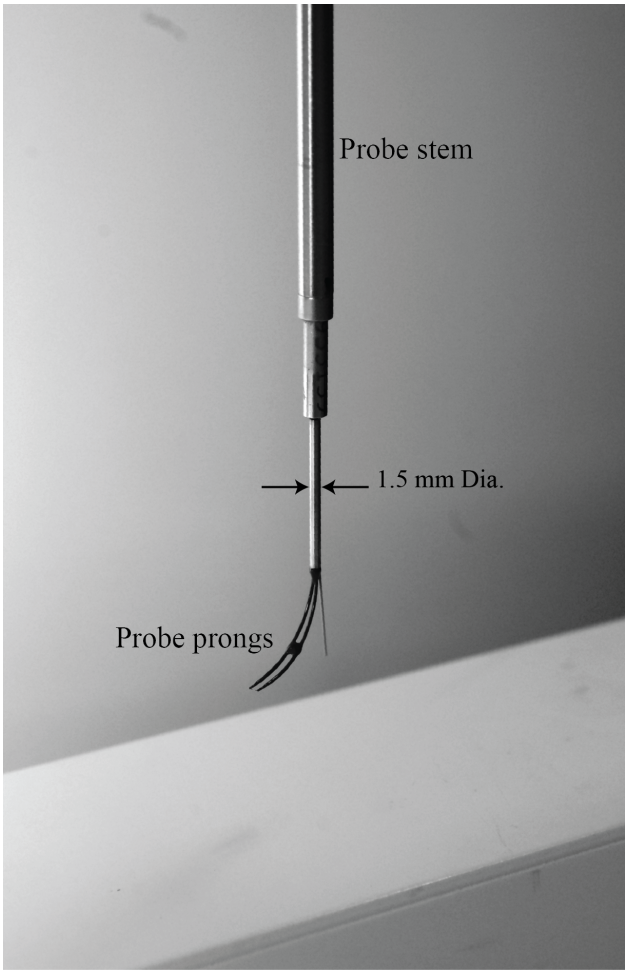

Figure 3.6: A photograph showing a TSI 1261A hot-film probe.

No great demands are placed on the measurement system's frequency response, because the low velocities and relatively large spatial resolutions in this experiment result in low sampling frequencies (see §3.4). The larger diameter of film probes relative to wires causes significant frequency attenuation in the probe response when operated in air, due to the heat transfer and storage in the quartz substrate; however this effect is negligible when film probes are operated in water due to water's higher thermal conductivity (Bruun, 1996). The anemometer and signal conditioning system are calibrated (DISA, 1977) using the built-in square-wave generator for a frequency of 300Hz. All measurements were recorded with a 14-bit 6009 National Instruments DAC.

The probes were positioned around the test section using a custom designed and automated 4-axis traverse (Figure 3.7). A rigid frame above the test section supports two longitudinal linear rails, 1 m in length. The rails convey a horizontal 'trolley' in the channel x-wise direction, which is constructed from a rigid beam and on which, a further two 1 m long linear rails are supported. These rails transport a flat plate, held perpendicular to the test section floor, in the z-wise direction. Mounted to the vertical plate was a linear traverse stage, with a stroke length of 120 mm, and fixed to this was a final rotation stage. These provide translation in the vertical direction, i.e. perpendicular to the channel floor, and allow the probe to be rotated or 'yawed' about the perpendicular stem. The rotational stage was designed such that the probe revolved concentrically about the film element. This extra design step accounted for the added spatial error that would result from the probe's boundary-layer-type prongs, were it rotated solely about the stem.

The traverse was fixed to the channel itself and levelled using an inclinometer. All axes were optically encoded to give ± 4 μm resolutions along the x and z channel axes, ± 2 μm in y and $\pm 0.03^\circ$ in rotation about the y axis. Automation was provided for the horizontal axes by two commercial proportional-integral-derivative (PID) motor controllers ('Motion Mind' controllers manufactured by Solutions Cubed LLC).

Two PIC controllers were programmed to control stepper motors on the remaining two axes. This was necessary as PID motor control took a very long time to reach a destination to a precision achievable using the encoders and would have increased the experiment time considerably.

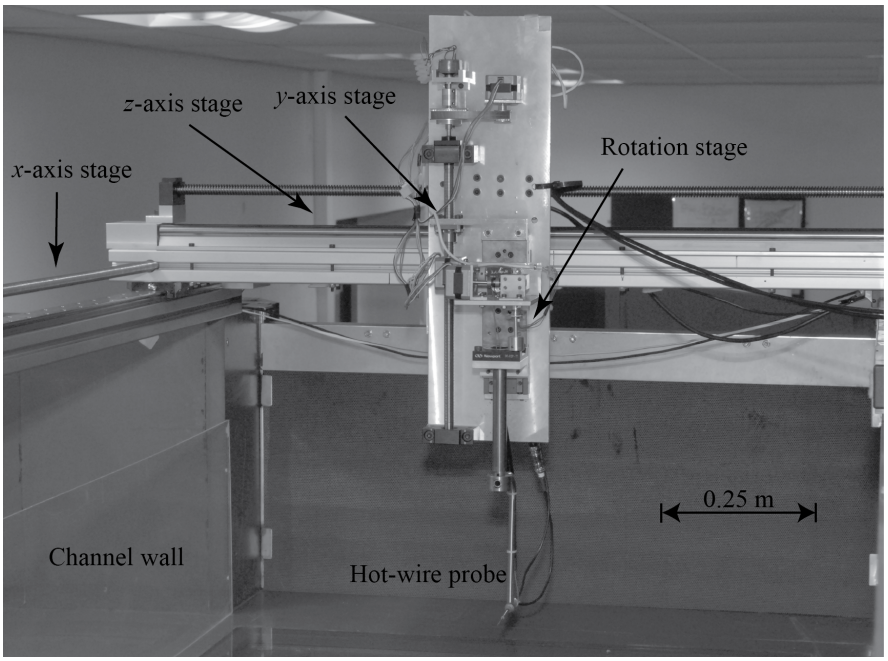

Figure 3.7: A photograph of the hot-wire traverse.

3.3.3 Calibration

To calibrate the measurement system, the velocity of the fluid in which the process is carried out must be known to a reasonable accuracy. When the calibration is carried out in a wind tunnel or high-speed water flow, the velocity is usually obtained with a pressure-difference device. As mentioned previously however, the changes in pressure in this investigation are too small to be measured practicably, so other means must be found instead.

'Moving-probe' calibration (Tewari and Jaluria, 1990; Wu and Bose, 1993) involves traversing the probe at a constant velocity in a stationary fluid and measuring the speed of the traverse mechanism. This is often performed in a separate

towing tank, which requires moving the probe and measurement system to and from the experimental application. McEligot and Eckelmann (2006) use this technique *in situ* in their oil channel. Samways et al. (1994) calibrate their hot-wire probes in a pipe by measuring the pipe flow profile with the probe, then relating the anemometer voltage result to the pipe centerline velocity, measured separately. This technique is also described by Bruun et al. (1990) to calibrate a two-film 'X-probe'. Commercial calibration equipment often makes use of a similar principle; requiring the measurement of the flow profile produced by an object, such as a submerged jet (Alfredsson and Johansson, 1984a).

For this experiment, the 'shedding-frequency' calibration method is used, in which the frequency of the vortex modes shed by a cylinder placed in a fluid stream are measured. The Strouhal-Reynolds (SR) relationship then relates the shedding frequency to the flow speed. Lee and Budwig (1991) investigate three calibration approaches, the shedding-frequency method amongst them. They note the variability of published SR data for low Reynolds numbers, with discrepancies as high as 20% between authors. This is due to the tendency for unconditioned finite-length cylinders to shed oblique modes, resulting in a discontinuity in the otherwise smooth curve-fit to the SR data.

Williamson (1989) investigates cylinder shedding modes and eliminates experimental conditions as a cause of oblique shedding. Using smoke to visualise the vortex street, oblique modes were seen to 'disconnect' from the cylinder and travel along its length with a different oblique mode forming behind it. For calibration purposes, it is therefore important that parallel shedding be used because, for given flow conditions, the shedding frequency may change otherwise. 'End plates' angled greater than 12° were found to induce parallel shedding for the cylinder spanning between them, resulting in a smooth SR curve. Lee and Budwig (1991) obtain parallel modes using 'end cylinders', or sleeves, with a larger diameter than that of the main cylinder. Hammache and Gharib (1989) used two large cylinders spanning

a certain distance, placed upstream and perpendicular to the horizontal shedding cylinder.

For modelling, it is useful to express the Strouhal-Reynolds relationship in terms of the cylinder Reynolds number (Williamson, 1989):

$$Str = A_D Re_D^1 + B_D Re_D^0 + C_D Re_D^{-1}, \tag{3.5}$$

where the Strouhal number (Str=$f_D D/Q$) and cylinder Reynolds number (Re_D=QD/ν) are based on the cylinder diameter D and shedding frequency f_D. The coefficients A_D, B_D and C_D are determined empirically. This form is only valid for the low Reynolds number region (Williamson, 1989), in which the wake remains laminar (approximately between 50<Re_D<160) . Above this, the wake becomes turbulent and calibration cannot be achieved using the shedding-frequency method. Two stainless steel cylinders with diameters 0.95 mm and 3 mm are therefore needed for the calibration velocity range. The 'end cylinders', or sleeves, designed by Lee and Budwig (1991) are used to generate parallel modes for the two calibration cylinders, since they are simple and convenient to manufacture. For the larger diameter cylinder, the end sleeves are machined in brass, whereas in the smaller case plastic is used. The distance between the sleeves is kept greater than 40 cylinder diameters so that the central cylinder span is not influenced by any local effects around them (Williamson, 1989).

Each cylinder is fixed into its own frame (Figure 3.8) to hold it and provide a slight tension to keep it straight. This allows them to be removed from the facility after calibration and for the process to be performed *in situ*, which is simpler and generally more reliable than having to move the probes (Bruun, 1995). For the smaller cylinder, the tension is supplied by the frame during cylinder clamping. For the larger, tension is provided from a screw in the frame side which is attached to the cylinder end via a metal cable. Vinyl was fixed between the cylinder and each

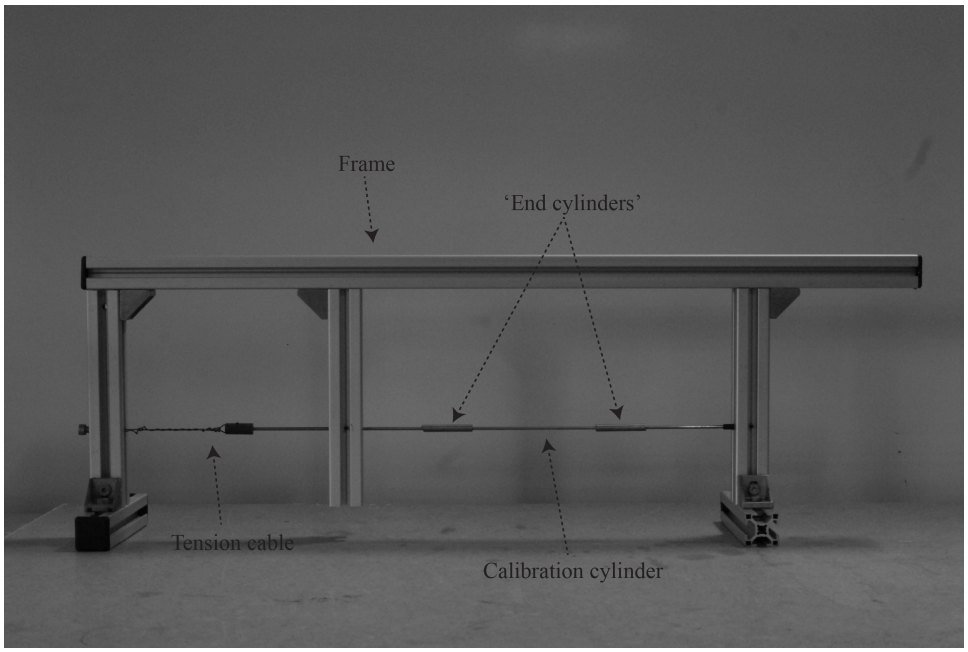

(a)

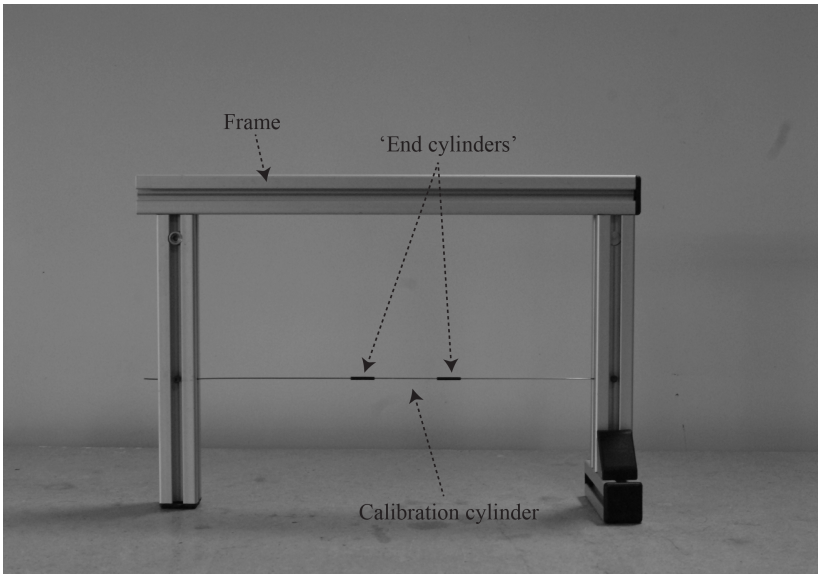

(b)

Figure 3.8: The calibration shedding cylinders. (a) 3 mm cylinder; (b) 0.95 mm cylinder.

frame to provide a slight damping. The shedding modes are checked for parallelism visually by stringing a platinum wire, 25 μm in diameter, downstream and parallel to the cylinder and using it to generate hydrogen bubbles. Figure 3.9 shows an image of the parallel shedding by the smaller cylinder. The bubbles in the figure are illuminated with a lamp.

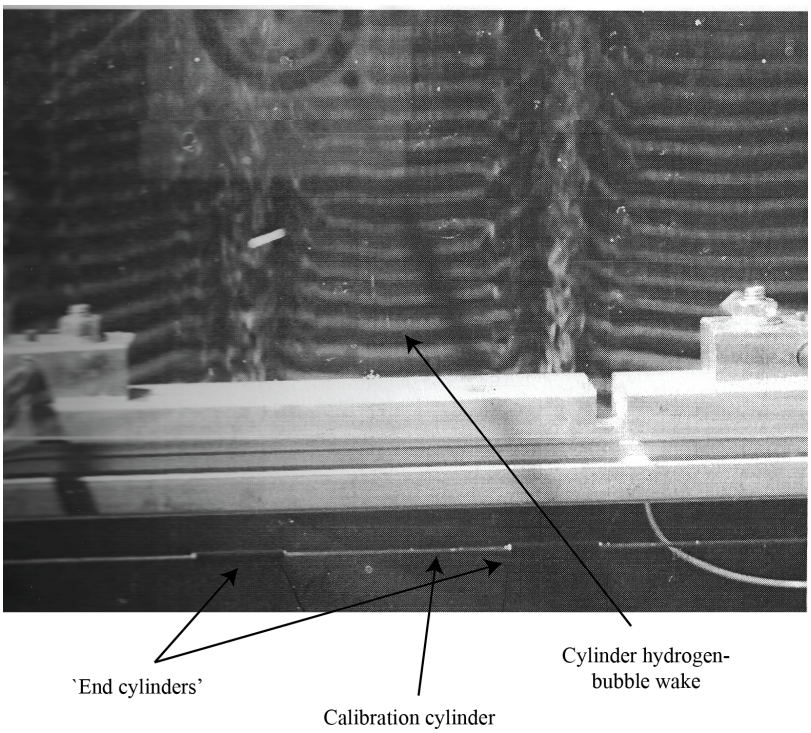

Figure 3.9: The shedding modes from the 0.95 mm calibration cylinder. The central portion of the cylinder wake, revealed by the hydrogen bubbles (illuminated with a lamp), shows the parallel shedding modes. The distance between the 'end-cylinders' is >40 cylinder diameters

The frequency of the cylinder wake was measured with the hot-film probe, positioned at least 10 cylinder diameters downstream and slightly off-plane of the cylinder itself. The calibration procedure involved sampling the shedding frequency of a cylinder, then traversing the probe out of the wake and sampling the freestream. A minimum of 10 different calibration velocities are needed (Bruun, 1995), spanning the velocity range required. The cylinders are exchanged when their particular Reynolds numbers are exceeded. The SR relationship obtained by Lee and Bud-

wig (1991) using both their empirical data and the parallel-mode data from other authors, is also applied here. The coefficients in the power-law equation (3.5) read: A_D=1.247e^{-4}, B_D=0.1906, C_D=-3.671. As no prior knowledge of the freestream velocity was available, the passage of dye markers down the channel were timed and found to differ from the velocity obtained using the shedding frequency method by 2%. 30-minute samples of the shedding frequency show the freestream velocity error to be σ/Q_e = 0.5%, which also provides a measurement for estimating the anemometer drift (§3.4).

A wide number of hot-wire heat-transfer equations have been used by investigators to calibrate the anemometer's output response, and these often vary according to application. King's law with a variable velocity exponent has replaced the original in terms of popularity, to improve accuracy. Other equation forms such as polynomials are reviewed by Bruun et al. (1988). Wu and Bose (1994) criticise the often ad-hoc nature of most tailored heat-transfer functions, because obtaining an accurate physical representation comes second in priority to the accuracy of the fit to the calibration data. They propose an extended power-law model of the form

$$Nu = \sum_{k=0}^{m} A_k Re^{kn} \tag{3.6}$$

which is based on physical considerations more than fit accuracy. Nevertheless, a better fit to their calibration data is found over a wider range of Reynolds numbers compared to other equations. Low Reynolds number effects such as buoyancy are accounted for, making it especially appropriate for low-speed flows.

Inserting equation (3.6) into equation (3.2), and setting m=2, the output voltage of the CTA can be modelled as:

$$E^2 = A_0 + A_1 Q^n + A_2 Q^{2n} \tag{3.7}$$

A least-squares curve fit of this model to the calibration data obtained via the

shedding frequency method is shown in Figure 3.10 and Table 3.1 shows the accuracy of the fit. King's law is included in the table for comparison, and the accuracy is seen to improve using Wu and Bose's model, particularly for the lower velocity data.

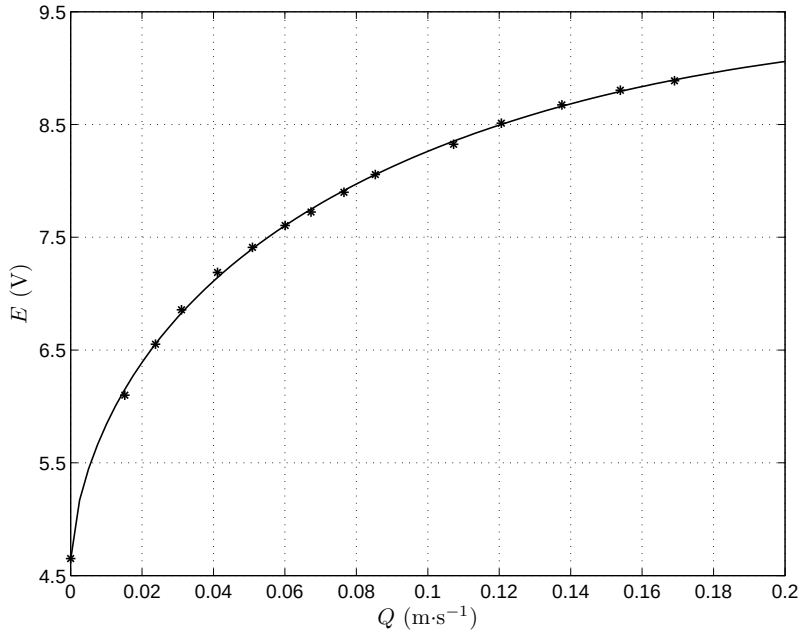

Figure 3.10: A least-squares fit of the heat transfer model from Wu and Bose (1994) (–) to the calibration measurement data (∗).

Appendix B shows the results of two calibrations, performed before and after a boundary layer experiment. To calculate the error between the two calibration curves, a set of 'test' voltages is converted to velocities using their respective heat transfer models. For 20 test voltage values, the total rms error in the velocity is 0.15%. From equation (3.7) it is clear that the error rises as the velocity increases. Experiments were performed starting in the freestream and working towards the wall which should help to reduce the error in the larger velocities. Extrapolation to higher voltage values outside of the calibration range may also be subject to larger error. The error between the two calibrations can also be used as measure of calibration drift along with the value given above determined from long-time samples of the shedding frequency.

Data		**Wu and Bose (1994)**		**King's Law**	
Q_e **(m·s^{-1})**	E **(V)**	e_Q (%)	e_E (%)	e_Q (%)	e_E (%)
0.1691	8.8880	0.7301	0.0865	6.4413	1.1116
0.1539	8.8033	0.9060	0.1165	2.2625	0.3961
0.1376	8.6735	0.9391	0.1300	0.5646	0.0992
0.1206	8.5122	0.9036	0.1334	2.8927	0.5068
0.0853	8.0560	0.0169	0.0027	4.7396	0.7984
0.0765	7.8984	1.2379	0.2016	3.5356	0.5804
0.0673	7.7241	1.9335	0.3166	2.4107	0.3844
0.0601	7.6044	0.0539	0.0090	3.7509	0.5917
0.1072	8.3250	2.1337	0.3245	1.6496	0.2818
0.0509	7.4103	1.0079	0.1679	3.3510	0.5116
0.0411	7.1875	3.7119	0.6197	3.9010	0.5738
0.0310	6.8573	2.6811	0.4285	1.5736	0.2104
0.0238	6.5519	0.1954	0.0291	10.4925	1.2478
0.0152	6.1001	6.7179	0.8523	31.3122	2.9568

Table 3.1: The percentage curve fitting errors of the data points in Figure 3.10 to different calibration models; e_Q and e_E are the respective velocity and voltage errors, calculated as the the absolute difference between the measurement value and the curve value, divided by the calibration value.

3.4 Measurement System Error and Uncertainty

The previous sections detailed the experimental facility, measurement equipment and its operation. Mention was also made of the errors resulting from their respective properties or the behaviour. These will all contribute to the overall inaccuracy of the measurement system and in this section, the various error sources are collected and used to make an estimate of the overall uncertainty in the results (§3.4.5). Preceding this though, the remaining sources of error will be identified as these too may contribute to the final uncertainty result.

3.4.1 Sampling Parameters

Turbulent boundary layers consist of a wide range of scales extending from the size of the layer itself down to Kolmogorov microscales, at which turbulence dissipates. The sampling parameters selected for the measurement of fluctuating turbulent statistics are therefore determined by the particular features of the boundary layer being investigated. This becomes particularly relevant near the wall where viscous effects dominate and the scales of the flow become small.

An estimate of the near-wall scales in a boundary layer can be made using the Prandtl-Schlichting formula for skin friction:

$$C_f = \frac{2\tau_w}{\rho U_e^2} = \frac{0.455}{(logRe_L)^{2.58}} \tag{3.8}$$

where Re_L is based on the length of the wall to the measurement point. The wall shear stress τ_w is then used to determine the friction velocity $U_\tau = \sqrt{\tau_w/\rho}$ and viscous length scale (ν/U_τ) from which the turbulent time scales $(t^+ = \nu/U_\tau^2)$ can be determined. At the test region of the channel the Reynolds number is of the order Re_L=3.8×10^5. The wall shear stress calculated using equation (3.8) is τ_w=0.039, giving an inner time-scale of around 0.025 s. The sampling frequency required to resolve the smallest scales then becomes $f_s = 40\ Hz$.

Alfredsson and Johansson (1984b) however, find that the governing frequency of the boundary layer inner-region is dependent on outer-layer effects as well. Consequently, they suggest that the inner-region sampling frequency should be a combination of both the largest and smallest scales of the flow. According to Khoo et al. (2001), a sampling frequency greater than $1/15t^+$ is required as this corresponds to the typical near-wall turbulent times scales obtained from the DNS by Spalart 1988. The sampling rate used for the current experiments is 200 Hz, which is the same as that selected by Ricco and Wu (2004) whose boundary layer is dimensionally similar to those in this experiment, though at a slightly higher Reynolds number. Their stated uncertainty is ±3% for the velocity variance, although their sample time and corresponding number of samples is smaller.

The sampling time for a particular measurement is limited by the need to reasonably resolve the boundary layer profile as well as determine the wall shear stress, which was obtained directly using hot-wire measurements in the viscous sublayer. A sufficient resolution of this region is therefore required to accurately calculate the velocity gradient. To satisfy these requirements the sampling time for most of the measurements was limited to five minutes. The number of samples, N_s, at a sample rate of 200 Hz is therefore 60,000.

From the number of samples collected, the uncertainty in the measurement of the velocity stress can be calculated. For a given flow with a real fluctuating velocity of q', the true mean squared value will be $\overline{q'^2}$. Given two sets of q' measurements with N_s samples in each; $a'_1 \ldots a'_{N_s}$ and $b'_1 \ldots b'_{N_s}$, the square of the sample difference can be calculated:

$$\left(\overline{a'^2} - \overline{b'^2}\right)^2 = \left(\frac{1}{N_s}\sum_{i=1}^{N_s} a_i'^2 - \frac{1}{N_s}\sum_{i=1}^{N_s} b_i'^2\right)^2 = \frac{1}{N_s^2}\left(\sum_{i=1}^{N_s}\left(a_i'^2 - b_i'^2\right)\right)^2$$

If the brackets are expanded and ensemble averaged using the following:

$$\begin{aligned}
\overline{a_i'^2 a_j'^2} &= \overline{q'^2}^2 \quad \text{if } i \neq j, \\
\overline{a_i'^2 a_j'^2} &= \overline{q'^4} \quad \text{if } i = j, \\
\overline{a_i'^2 b_j'^2} &= \overline{q'^2}^2
\end{aligned}$$

it can be shown that:

$$\overline{\left(\overline{a'^2} - \overline{b'^2}\right)^2} = 2\frac{\overline{q'^4} + \overline{q'^2}^2}{N_s} \tag{3.9}$$

Using this, the relative uncertainty in the measurement of stress becomes:

$$\frac{\sqrt{\overline{\left(\overline{a'^2} - \overline{b'^2}\right)^2}}}{\overline{q'^2}} = \sqrt{\frac{2}{N_s}} \cdot \sqrt{\frac{\overline{q'^4} + \overline{q'^2}^2}{\overline{q'^2}^2}} = \sqrt{\frac{2}{N_s}} \cdot \sqrt{K_q + 1} \tag{3.10}$$

where K_q is the kurtosis, defined as $K_q = \overline{q'^4}/\overline{q'^2}^2$. As can be seen later, K_q in a turbulent boundary layer near the peak turbulence intensity is K_q=2.4, resulting in a relative uncertainty in stress measurements of approximately 1%.

3.4.2 Spatial Resolution Errors

The finite length of the hot-film probe element introduces error from the effects of spatially 'averaging' the very small turbulent fluctuations along the length of the film. As mentioned previously, turbulent flows contain eddies whose dimensions vary in size, with the smallest proportional to the Kolmogorov scale ($\eta \approx 1.5\nu/Q_\tau$). If the probe active element length (l_w) is much greater than η, the 'eddy averaging' of the fine scale structures over the wire acts as a low-pass filter; resulting in poor resolution of the velocity moments, gradients and spectra. The error from the spatial filtering effect will consequently be larger for non-isotropic flows, such as the near-wall region of a turbulent boundary layer.

The hot-film probes used in this experiment have inner lengths of $l_w^+ = l_w\nu/Q_\tau \approx 3$

to 5, which is of a similar order to the Kolmogorov scale and far smaller than the l_w^+=20 – 25 maximum recommended by Ligrani and Bradshaw (1987). They propose that the limit on probe spatial dimensions results from the smallest non-dimensional spanwise spacing of the near-wall coherent structures ($\lambda_{min}^+ \approx 20$). The diminutive length of the probes used in this study mean spatial resolution error will have a negligible effect on the measurements made, illustrating one of the strengths of hot-wire anemometry for turbulent boundary layer measurements.

The short lengths required for high spatial resolution must be balanced by the need to minimise the conductive heat losses to the probe prongs, which are large in size compared to the element. For wire probes used in air, this error is generally mitigated by ensuring that the length to diameter ratio l_w/d_w is greater than 200 (Ligrani and Bradshaw, 1987). The TSI film probes used here have $l_w/d_w \approx 20$; however film probes have been shown to exhibit comparable prong conduction losses as wire probes (Bruun, 1995), due to the thinness of the film on the substrate. This characteristic should be emphasised when used in water flows as the convective heat transfer from the film is much larger. The same property allows the heat storage by substrate conduction to be neglected as well (Bruun, 1995).

3.4.3 Temperature Errors

Changes in the ambient fluid temperature can be a particular problem for thermal anemometers, because the heat-transfer equation assumes a constant wire excess temperature ($T_w - T_a$) when used to model the output of a CTA. Evident from equation (3.3) is that temperature errors are more pronounced when the probe excess temperature is small, which is true in this experiment. Since a CTA holds the film resistance R_w constant, equation (3.3) can be used to predict the magnitude of temperature errors. For a general heat transfer function $f(Q)$, equation (3.3) reads:

$$E_w/R_w = \sqrt{f(Q)(T_w - T_a)} \tag{3.11}$$

At a constant velocity, variations in the ambient fluid temperature ΔT_a correspond to a change in wire voltage of:

$$\Delta E_{err} = \sqrt{\frac{(T_w - T_a)}{(T_w - T_a) \pm \Delta T_a}} \tag{3.12}$$

For a 'worst-case' velocity error, the maximum change in fluid temperature will be used, which was measured using the PRT probe to be ΔT_a=±0.03℃. At an excess probe temperature of $(T_w - T_a) \approx 20$℃, the change in wire voltage will be ΔE_{err}<0.1%. From the calibration curve shown in Figure (3.10), the largest error results when the velocity is highest. In this range, the voltage-velocity gradient is typically $\Delta Q/\Delta E_w \approx 0.18$. If a correct or initial wire voltage is taken to be E_w=9 V, the voltage error resulting from the largest change in temperature would be:

$$E_{err} = E_w - E_w \Delta E_{err} = 0.0067V \tag{3.13}$$

corresponding to an error in velocity of $Q_{err} = E_{err}(\Delta Q/\Delta E)$=0.0012 m/s, or approximately 0.6% at a velocity of 0.19 m/s.

3.4.4 Mean-Velocity Direction

The mean velocity vector in a three-dimensional boundary layer rotates away from the direction of the external streamline as the distance to the wall is reduced. Satisfactory models for this behaviour do not currently exist (Degani et al., 1993), so the mean-flow direction in three-dimensional experiments must be found. Determining this direction is one of the largest sources of uncertainty in this experiment. As was the case with calibration, pressure probes cannot practicably be used in low-speed water flows, so the flow direction must be found by other means. Whilst visual methods such as marker tracing may be applicable when the turbulence intensity is low, the situation changes in the turbulent boundary layer. In wind tunnel three-dimensional boundary layers, the limiting flow angle at the wall can be found by

allowing an ink-oil mixture to be dragged along the surface on to which glass or paper is positioned (Schwarz and Bradshaw, 1994; Olcmen and Simpson, 1995).

By rotating or 'yawing' their hot-wire probe away from the mean-velocity vector, Bissonnette and Mellor (1974) were able to trace its direction by finding the point of symmetry in the anemometer's mean output response. A similar technique is also applied by Littell and Eaton (1994). The same principle is adopted here, made simpler by the fact that the probe is single-normal type, and that the probe stem is downstream of the wire element. Bissonnette and Mellor (1974) used an inclined probe where the wire is angled at 45° between the prongs. This necessitates prior knowledge of the probe's yawing behaviour, requiring an extra calibration and transformation. Their probe prongs and stem are orientated perpendicular to the mean-flow direction, directly above the wire, which may interfere with the oncoming flow close to the wire itself.

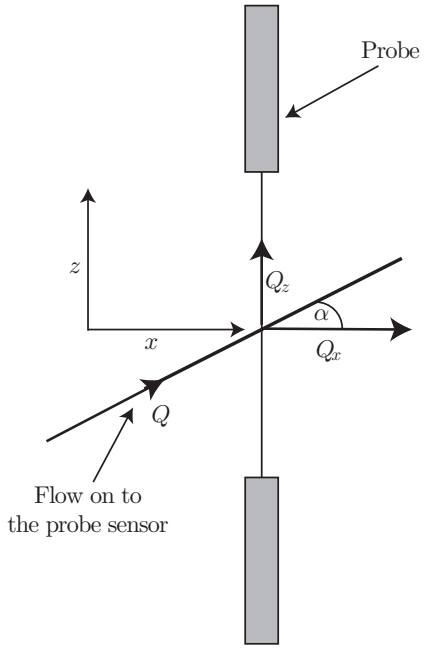

Figure 3.11: The velocity components of a hot-wire probe not aligned with the mean-flow direction. The x-z axis shown is aligned with x normal to the wire and z tangential to it.

The velocity sensitivity of a hot-wire element to a non-alignment with the

mean direction of the local flow (α) can be expressed in the form:

$$Q_m = Qf(\alpha) \tag{3.14}$$

where Q_m is the velocity reported by the probe, Q is the mean-flow velocity, and $f(\alpha)$ is a 'yaw function'. Typically, a cosine-law is assumed for this function, and the velocity-yaw dependence becomes:

$$Q_m = Q\sqrt{(\cos^2\alpha + k^2 \sin^2\alpha)} \tag{3.15}$$

where the parameter k is found by performing an extra calibration procedure. The second extra term in the parenthesis results from the tangential cooling effect of the flow component along the length of the wire; as illustrated by the term Q_z in Figure 3.11. The process to obtain the mean-flow direction involves recording the velocity Q_m whilst yawing the probe over a sufficient angle range such that the symmetry position in the velocity-yaw response is obtained. The velocity and yaw angle at approximately the symmetry point correspond to the mean velocity and direction of the local mean-flow. Figure 3.12 shows an example of the voltage response obtained from yawing the probes used here in the channel.

A three-dimensional boundary layer has two significant mean-velocity components (U and W). With a single-normal type probe orientated in the local mean-flow direction Q at a particular height in the boundary layer, it is shown by Bruun (1995) and Bissonnette and Mellor (1974) that, to second order, the fluctuating velocity measured is also that in the local mean-flow direction, defined here as q'. Littell and Eaton (1994) used a single-normal probe in an identical manner to that here in a three-dimensional turbulent boundary layer. The turbulent fluctuations measured in the local mean-flow direction agreed with that measured using a crosswire probe to within 5%. To separate the single-wire data into the fluctuating components aligned with a space fixed coordinate system (u', w', etc) requires the use of multicomponent methods which are unavailable.

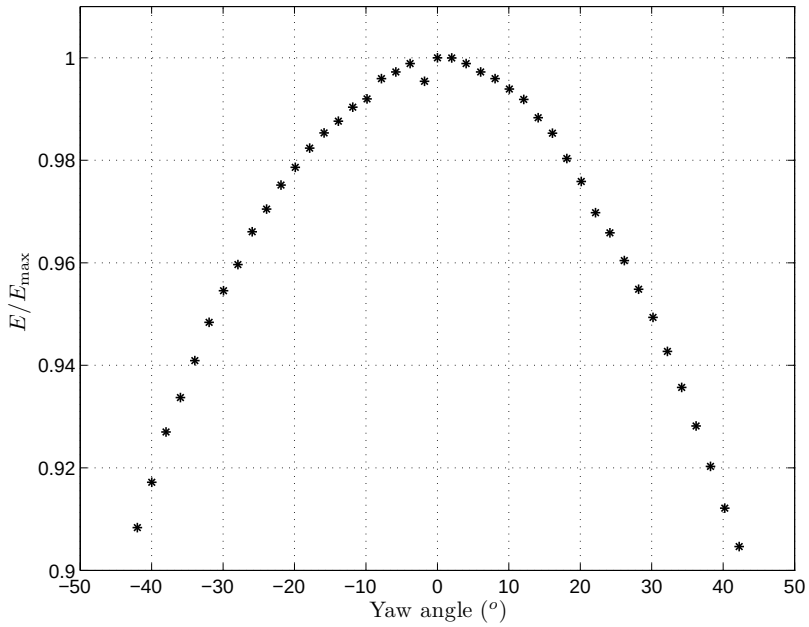

Figure 3.12: The voltage-yaw response of the hot-film probe obtained in the channel freestream flow. E is the anemometer voltage.

A number of factors add to the difficulty and inaccuracy of using this approach in this experiment. Since the boundary layer is turbulent, the velocity must be sampled at discrete angles in order to sufficiently resolve the mean. Also, the increased viscosity and low Reynolds number in the channel both work to increase the characteristic length and time scales of the turbulence, resulting in long sampling times. In order to resolve the yaw-velocity dependence sufficiently, the mean-flow direction had to be obtained separately before the velocity profile was measured. A smooth curve was then fitted through the mean-flow direction measurements, which was used to orientate the hot-wire probe for subsequent velocity measurement. This approach has two advantages: since only the symmetry point in the yaw response is required to obtain the mean-flow direction, the anemometer voltage can be used in place of the velocity, negating the requirement for an additional velocity calibration and reducing the subsequent experiment time. It also allows more boundary layer heights to be sampled during a subsequent velocity measurement, improving the resolution of the turbulent flow profile.

A number of techniques, such as the angle bisection were attempted to minimise the time needed to obtain each flow angle. The most reliable method found used a sampling time based on the local integral time scale. The probe was then yawed over the angle range ±20° from the mean-flow direction found at the previous measurement. At discrete angles, the mean anemometer voltage is obtained and the mean-flow direction determined by fitting a cosine-law function to the voltage samples using a least-squares method.

The yaw response shown in Figure 3.12 was obtained in the freestream of a zero-pressure-gradient turbulent boundary layer. Figures 3.13a and 3.13b show yaw samples measured in the inner region at $y^+ \approx 40$ and $y^+ \approx 10$ applying a yaw angle resolution of 2°. The curves indicate cosine-law fits to the data with least squared errors of 4.7×10^{-5} and 1.1×10^{-3} respectively. Repeating the process for the $y^+ \approx 10$ position three times results in a precision of σ=3.6°; much larger than that cited by Littell and Eaton (1994) or pressure probes, which can obtain uncertainties of σ=±1°(Anderson and Eaton, 1989); though generally not for the inner region. Though the uncertainty in flow angle is large near the wall, from the figures it is clear that velocity measurements and the calculation of the wall shear stress should not be severely affected since the variation in the magnitude of the yaw response is small.

3.4.5 Uncertainty

The uncertainty in an experimental result will be a product of the errors in the tools and methods used to obtain it. The various error sources in the measurement system considered in previous sections are summarised in Table 3.2. The total is calculated from the root mean square of the errors. The values represent the impact of each error source on the measured statistic, made under the most demanding experimental conditions in this study. This corresponds to the near-wall region of the turbulent boundary layer for maximum fluctuations in temperature.

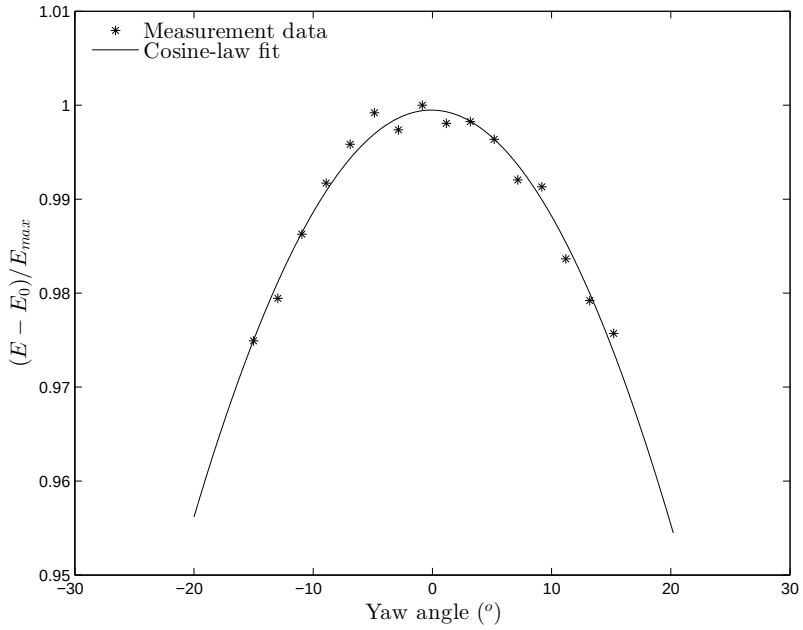

(a)

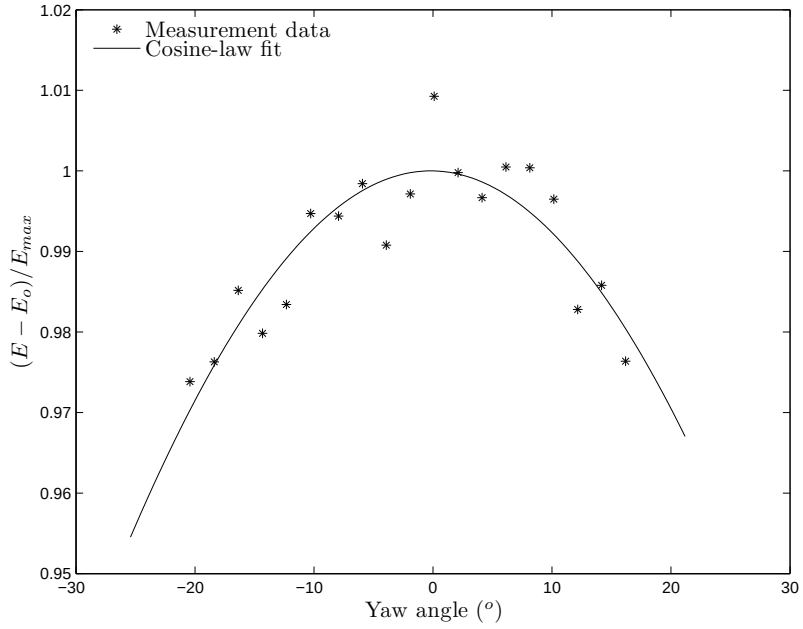

(b)

Figure 3.13: Yawing responses from the hot-film probe obtained in ZPG turbulent boundary layer. (a) at y^+≈40; (b) at y^+≈10. E_0 is the anemometer offset and E_{max} is the maximum value of the curve fit.

Source	Q	$\overline{q'^2}$	γ
Calibration velocity	±2%		
Calibration equation	<0.01%		
Calibration drift	±0.5%	±0.1%	
Spatial resolution error	<0.5%	<0.5%	<0.5%
Temperature	±0.6%	<0.01%	<0.01%
Sampling parameters	±1%	±1%	
Total	±2.4%	±1%	±3.6°

Table 3.2: Experimental errors

The largest error in the mean-velocity results from the uncertainty in the actual calibrating velocity, which should not result in errors for velocity variance or flow angle as it simply produces a change in the absolute 'location' of their calculation. These are also therefore invariant to the error in the calibration equation. Calibration, or anemometer drift represents the deviation in velocity over time. For the calculation of the uncertainty, two values reported in §3.3.3 can be used. The larger value is preferred here as it represents a more direct measurement of the drift deviation. Re-calibrating at each measurement station, combined with the filtration and temperature monitoring measures, should minimise this error along with that resulting from probe contamination (Bruun, 1996). Further, hot-wire measurements in a boundary layer were performed by starting in the freestream, where drift was seen to have largest impact, and working towards the wall.

The error in the rotation stage of the traverse is small (§3.2) and would have a correspondingly negligible impact on the flow angle uncertainty. The remaining three traversing errors reported in §3.2 are not included in the table either, because the viscous length scales are far longer ($4\mu m \approx 0.04 l_w^+$) and, from the discussion in §3.4.2, will be negligible. The uncertainty in flow angle does not include calibration drift either as the precision of this method was measured directly (§3.4.4).

The total uncertainty for the mean velocity is comparable with other studies applying thermal anemometry techniques such as the ±2% reported by Anderson and Eaton (1989) or the ±2% of Kline et al. (1967) and ±4.5% of Ricco and Wu (2004), who both used film probes in water flows. As reported above, Ricco and Wu (2004) cite an uncertainty in the normal stress of ±3.6% and Anderson and Eaton (1989) give a value of ±4%.

3.5 Wall Shear Stress

Knowledge of the wall shear stress, τ_w, is a necessity for most studies on turbulent boundary layers and consequently, a variety of techniques have been developed by researchers to measure this quantity experimentally. These may be divided into two categories (Fernholz et al., 1996): indirect methods where τ_w is inferred or deduced, usually by assuming typical logarithmic-layer behaviour exists in the boundary layer; and direct methods. Direct measurement must be used for the experiments in this thesis as indirect methods become invalid for turbulent boundary layers in the presence of pressure gradients and mean-flow skewing (Johnston and Flack, 1996).

Direct methods range from oil-film interferometry (e.g., Olcmen and Simpson, 1995; Pailhas et al., 2009) to the use of force balances (e.g., Pompeo et al., 1993). As with other experimental techniques in this investigation however, the use of water means that just one direct method can be applied: the wall-slope method. This technique relies on the observation that very near the wall in a turbulent boundary layer, the turbulent shear stress becomes a small proportion of the total shear stress such that, below approximately $y^+ \approx 5$ to 8, the velocity profile becomes linear, i.e., $Q^+ = y^+$. The shear at the wall can therefore be determined by measuring the velocity gradient in this viscous sublayer: $\tau_w = \nu(dQ/dy)_{y=0}$. This argument is actually relied upon for most direct methods, reviewed by Hutchins and Choi (2002), who comment that using the linear velocity-profile in the viscous sublayer appears to

be the only reliable way to determine the wall shear stress in complex turbulent boundary layers.

3.5.1 Wall Positioning

Bruun (1995) review the complications of carrying out near-wall measurements using hot-wire anemometry. The main difficulties include the effects induced by a probe's proximity with the wall, the spatial resolution, and accurate probe positioning with respect to the wall. Spatial resolution was addressed in a previous section, where the probe's dimensions were found to be similar in size to the Kolmogorov scale. The problems of probe proximity arise from the aerodynamic interference caused by the hot-wire probe's holding stem, and the heat conduction between the probe and the wall or the 'wall effect'. The use of boundary-layer type probe prongs should help minimise the aerodynamic interference from the probe stem and heat conduction to the wall has not been encountered when hot-films have been used in water, owing to the larger thermal conductivity of water and low film operating temperatures. Over the test section, the ratio between the thermal conductivity of the water (k_{water}) and the glass floor (k_{glass}) is $k_{water}/k_{glass} \approx 0.55$. In air flow studies, ratios typically range from 10 (Perspex or Plexiglas) up to 1400 (steel). The problem of obtaining an accurate wall position is not critical to wall shear stress measurements, as the linear fit to the velocity profile can be used to correct for the boundary-layer height, y, afterwards. This is the more common approach (Hutchins and Choi, 2002), however the accuracy of a linear fit will be improved if the wall position is known.

Achieving an accurate probe-wall positioning commonly involves locating the probe at some reference point first, where the height above the wall is known to a high accuracy, then traversing the probe using a fine-scale zero-backlash mechanism (Bruun, 1995). This is the first method tried in this investigation. Before measurements took place, the probe was positioned onto a small aluminium block whose surfaces were machined, polished flat, and whose thickness was measured with a

micrometre screw gauge. A digital video camera with a microscopic lens was used both to position the probe on the block and to measure the distance from the block surface to the wire's aerodynamic centre. An image of the probe on the block is shown in Figure 3.14. A precision measurement shim was photographed by the same process in a reference image so that the length in the images could be determined. The height to the aerodynamic centre of the wire from the block is measured here as 0.152 mm ($y^+ \approx 0.7$ to 1.5) with an uncertainty ± 30 μm.

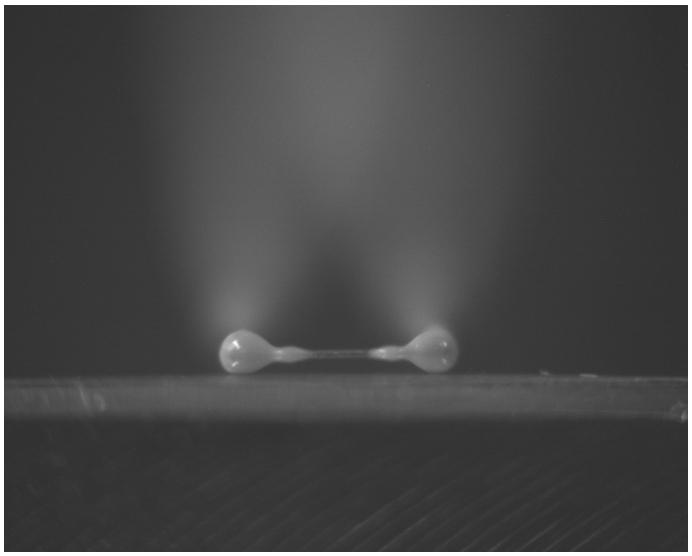

Figure 3.14: The miniature hot-film probe on the calibration block. The length of the sensing region is 0.5 mm.

3.5.2 Measurement Spatial Error and Shear Stress Uncertainty

During testing, large spatial errors were found at the wall as demonstrated in the 32 point near-wall velocity sample shown in Figure 3.15. The data in Figure 3.15 were obtained at a very low freestream velocity in order to maximise the viscous length scales. The 'presumed' wall position line (and hence the figure ordinate) was determined using the microscope and block method described above, and it is on this line that Q=0 is expected. It is clear from the data however, that extrapolation to Q=0 locates the probe far below the wall's assumed location, indicating a spatial error.

The measurement points at the lowest heights eventually start to curve downward becoming constant.

The traverse mechanism was deliberately constructed using zero-backlash components and absolute positional encoders. Nevertheless, errors in the mechanism were rechecked by repeatedly traversing the probe over the entire y-axis stroke length and checking the position with the microscope camera and wall block. The large spatial error also appeared with the same magnitude regardless of variations in the freestream velocity; whether the anemometer voltage was used in place of velocity; and whether the boundary layer was turbulent or laminar; thereby eliminating hot-film calibration and measurement techniques as the source of this error. Finally, Vernier depth-gauge measurements revealed that the glass floor in the test region was actually deflected slightly (<0.5 mm) when the channel was filled with water. The downward curve at the bottom of the velocity profile indicates where the probe has made contact with the wall itself. Further movements downwards will either cause the probe to deform or slide forwards along the glass due to the prong shape.

This spatial error meant that two probe-positioning methods were available. The first applies a post-processing correction using the linear fit to the velocity profile. Figure 3.16 shows the result of correcting and non-dimensionalising the data given in Figure 3.15 using the data between the 5th and 16th lowest points. This procedure simply involves locating the wall at the height where Q=0, thereby shifting the wall-normal axis upwards by the difference to this new wall location. The height of the viscous sublayer ($y^+ \approx 5$) extends above the 16th point, so a second linear fit could be performed using more data points or eliminating others should the need arise. The second method available involves a process similar to Bhatia et al. (1982) and Hutchins and Choi (2002), where the start of the discontinuity in the velocity profile determines the wall's position. The data in Figure 3.15 suggests that the probe makes contact with the wall around the fourth lowest measurement point. From Figure 3.14, however, the wire and the wall will clearly not be touching at this point. The height of the wire's aerodynamic center was determined earlier

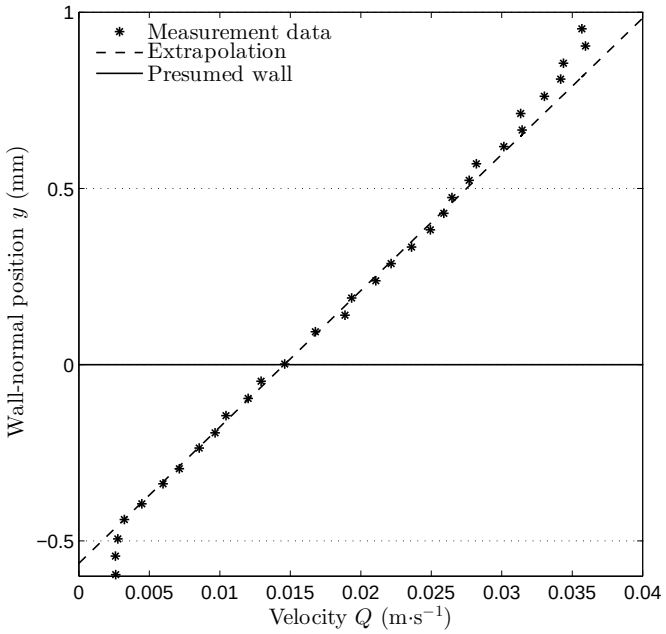

Figure 3.15: A near-wall velocity profile showing the spatial error in the wall-normal position. The axis ordinate and 'presumed' wall position (–) were determined using the microscope and block method. The extrapolation (– –) is a straight-line fit to the linear data. The freestream velocity for this test was Q_e=0.097 m·s^{-1}.

from the microscope images and would therefore be used to correct the height of the fourth measurement point.

Comparing the two probe-positioning methods, the second procedure has immediate improvements as the number of data points in the linear fit is increased by two: the contact point and zero. To illustrate these improvements, both methods are applied to the data in Figure 3.15. Using the first procedure, the uncertainty in the linear fit to the velocity gradient is 1.9% and in the second it is 1.6%, the shear stress magnitude itself differs by 2%, and the probe height difference is 9.3 μm. Using the second approach the wall shear stress is τ_w=0.0259 kg·m^{-1}s^{-2}, which compares reasonably well with that calculated using equation (3.8) at the measurement location (τ_w≈0.0263 kg·m^{-1}s^{-2}).

Despite the slight improvement in uncertainty, the second procedure is far more involved than the standard correction and is fraught with potential errors.

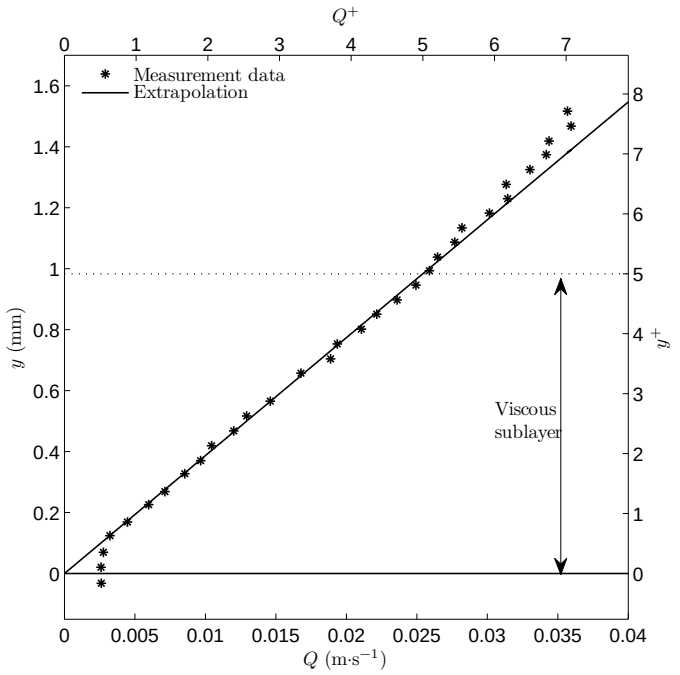

Figure 3.16: The data in Figure 3.15, corrected and non-dimensionalised using the linear correction.

There is also the added danger of causing damage to the probe and hence, the standard correction procedure using the least squares fit to the linear velocity gradient is preferred. In the interest of accuracy however, and because blockage effects caused by the probe film and prongs are unknown, the wall-contact point in the velocity profile is obtained first and used as a preliminary measurement of the wall position from which the extent of the viscous region can be estimated. Obtaining the wall contact point also ensures that the wall is reached. The data between $y^+ \approx 2$ to 4.5 are then selected for a second linear fit, from which the wall shear stress magnitude is determined.

3.6 Turbulent Boundary Layer Measurements

Turbulent boundary layers were sampled a number of times in this investigation and measurements performed in a laminar boundary layer can be found in Ap-

pendix C. In this section, two turbulent examples are shown for comparison: a higher speed flow with freestream velocity Q_e=0.122 m·s^{-1} and a lower speed flow at Q_e=0.105 m·s^{-1}.

The results in this section serve two purposes: the measurements from the higher speed case complement the low-speed streak investigation presented in the next section, and they provide a test for the experimental accuracy. For the latter, several properties are investigated including: satisfactory development of the turbulent boundary layers in the channel, indicated by an absence of low-Reynolds number effects and other channel-dependent artefacts; that an acceptable wall-shear stress measurement is obtained; and to examine the accuracy of the velocity statistics measured with the hot-film system under practical conditions.

3.6.1 Mean Flow

Table 3.3 shows some of the mean-flow quantities of interest in this section from both cases. The boundary layer thickness, δ, is calculated by interpolating the velocity profiles and locating the position for which $Q = 0.995Q_e$. The boundary-layer displacement δ^*, and momentum δ_θ, thickness were calculated by integrating the profiles. The coefficient of friction C_f is calculated from the wall shear stress using the first equality in equation (3.8). The shape factors ($H = \delta^*/\delta_\theta$) are 1.41 and 1.4 respectively; acceptable values for flat-plate boundary layers without pressure gradients (Schlichting, 1979).

The shape parameter G, given by $G = \int_0^\infty F'^2 d\frac{y}{\Delta_c}$, can be used as a test for flow equilibrium. The function F' is the defect velocity defined as $F' = (Q_\infty - Q)/Q_\tau$, and Δ_c is a boundary-layer thickness parameter, calculated by $\Delta_c = \int_0^\infty F' dy$. A $G \approx 6.6$ describes an equilibrium flat-plate turbulent boundary layer. For the lower Reynolds number flow G=5.7 whereas for the the higher G=6.2 suggesting that the second case is approaching mean-flow equilibrium, but the lower Reynolds number flow is 'further away'. Profiles of the mean velocity non-dimensionalised in outer

Quantity	**Low-speed**	**High-speed**
Q_e (m·s^{-1})	0.105	0.122
δ (m)	0.0898	0.0935
δ^* (m)	0.0102	0.0125
δ_θ (m)	0.0072	0.0089
H	1.41	1.4
Re_θ	821	1080
Re_τ	486	530
τ_w (kg·m^{-1}s^{-2})	0.0293	0.0324
C_f	0.0052	0.0043
κ	0.41	0.39
B	4.82	4.82

Table 3.3: The mean-flow statistics for two zero-pressure-gradient turbulent boundary layers.

units and as 'defect profiles' can be found in Appendix D.

The wall shear stress τ_w for the lower speed case agrees favourably with that predicted by equation (3.8), though the higher speed flow differs more. Another method commonly used to calculate τ_w, is called the cross-plot technique (Schraub and Kline, 1965), which assumes that the 'universal' law-of-the-wall given by:

$$\frac{Q}{Q^+} = \frac{1}{\kappa} \ln y^+ + B \tag{3.16}$$

is valid for the velocity magnitude. The gradient of the logarithmic region of the velocity profile is then used to calculate the friction velocity Q_τ. With κ=0.4 and B=5, τ_w computed using this approach differs from that given in the table by 5%. The table value is preferred however, as it is calculated directly rather than by assuming that the equation (3.16) is accurate.

The friction Reynolds numbers ($Re_\tau = Q_\tau \delta/\nu$) of the two flows are 486 and

530 respectively. The mean-velocity profiles non-dimensionalised by inner units are shown in Figure 3.17. The law-of-the-wall and Re_θ=680 DNS result from Spalart (1988) are also provided. Regions displaying logarithmic behaviour are present in both cases and the boundary layers are sufficiently developed (Re_τ>180) such that low-Reynolds number effects are absent in the mean velocity (Moser et al., 1999).

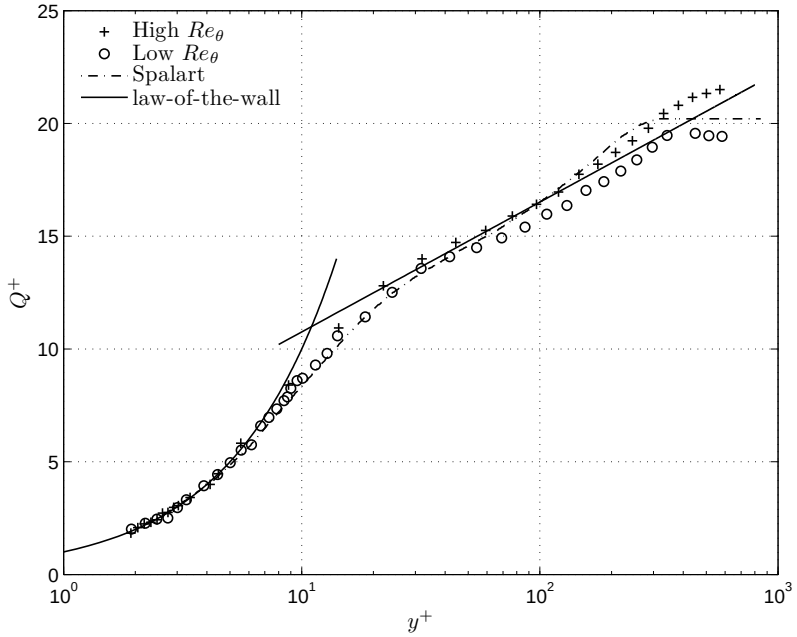

Figure 3.17: Mean-velocity profiles non-dimensionalised in inner units ($Q^+ = Q/Q_\tau$, y^+=yQ_τ/ν. The law of the wall given by equation (3.16) is shown (–) for the constants: κ=0.4, B=5 and the Re_θ=680 DNS results from Spalart (1988) are also presented (- -).

The gradient of the logarithmic layer κ^{-1} and the intercept B are calculated directly for all flows in this study using a similar technique to Spalart (1988) and Moser et al. (1999), by finding where the function $\Xi = y^+(dQ^+/dy^+)$ is approximately constant. This is analogous to the crossplot method described above, but where the gradient of the logarithmic region is found rather than assumed. A 'window' of 8 Q^+ points is run over the profile and Ξ is obtained for each window. The gradient is found by least squares for the window with the smallest variation in Ξ.

Figure 3.18 shows the wall-normal variation of Ξ, which should be constant

with a value κ^{-1} where logarithmic-law behaviour is being followed. For both flows, the logarithmic layer appears to start at around $y^+ \approx 50$ to 80 and extend to $y^+ \approx 200$ to 240, before a peak signals the onset of decline. The resulting parameters κ and B are given in each figure for reference as well as in Table 3.3. κ is larger in the flow with a lower Reynolds number, though this is probably due to experimental noise and poor spatial resolution. Both values are acceptable for zero-pressure-gradient boundary layers. Finally, Figure 3.19 compares the mean-flow data from the high speed case with the velocity profile described by Spalding's law of the wall and Coles' law of the wake, which reads:

$$y^+ = Q^+ + e^{-\kappa B}\left[e^{-\kappa Q^+} - 1 - \frac{(\kappa Q^+)^2}{2} - \frac{(\kappa Q^+)^3}{6}\right] + \frac{2\Pi}{\kappa}\left[3\left(\frac{t}{\delta}\right)^2 - 2\left(\frac{t}{\delta}\right)^3\right] \qquad (3.17)$$

where Π is the wake parameter which takes the value 0.45 for flat-plate boundary layers.

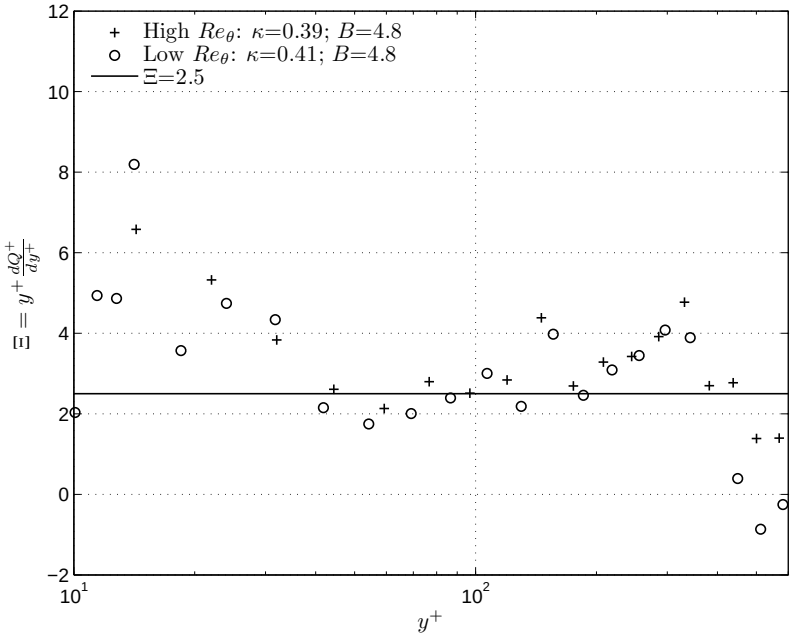

Figure 3.18: The wall-normal behaviour of the diagnostic function Ξ, which is constant in the logarithmic region. $1/\kappa$=2.5 is also shown (–) illustrating the gradient of the law of the wall.

In summary, these mean-velocity results appear to show that the flows in the channel are not being adversely affected by an insufficient channel length, absence of an extra test plate or by the relatively low velocities used in this investigation. Low Reynolds number characteristics such as a high log-law intercept, B, or absence of logarithmic region are not seen and the Reynolds numbers of both flows are sufficiently high to avoid such problems.

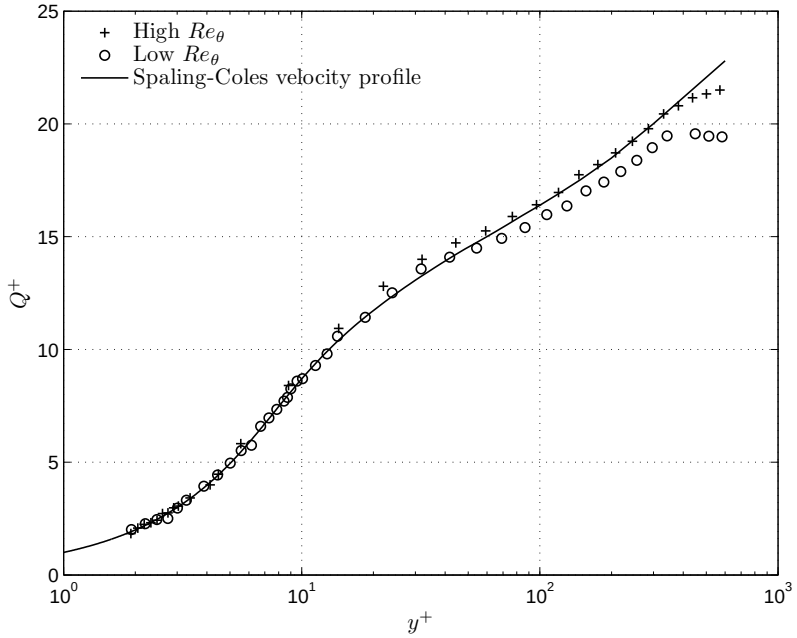

Figure 3.19: Streamwise mean-velocity profiles non-dimensionalised in inner scales compared to a Spalding-Coles profile (–) defined by equation (3.17). For the Spalding-Coles profile: Re_τ = 400, Π=0.5.

3.6.2 Fluctuating Velocity

The streamwise rms velocity is particularly sensitive to Reynolds number effects as seen in the DNS results of Spalart (1988) and Moser et al. (1999). Profiles of the rms velocity non-dimensionalised with inner units ($\sqrt{\overline{q'^2}}/Q_\tau$) are shown in Figure 3.20 and compared with the DNS result obtained by Spalart (1988) at Re_θ=670. The peak rms in the higher Reynolds number flow occurs with a magnitude 2.5 at $y^+\approx$14.5. This wall-normal height is in good agreement with the commonly accepted

locus of y^+=14 (Fernholz et al., 1996; Spalart, 1988), though the spatial resolution is clearly quite course. The magnitude is slightly lower than the more commonly reported value of 2.7. In the lower Reynolds number flow, the spatial resolution is improved and the measured peak occurs at $y^+ \approx 12.5$ with a magnitude of 2.4.

Profiles of the higher moments of skewness S_q and kurtosis K_q for the streamwise velocity are given in Appendix E. The skewness illustrates the contribution to the turbulence from the high and low speed velocity fluctuations (with respect to the mean) and the contribution from the large and small scale fluctuations is described by the kurtosis. Profiles of these statistics agree reasonably well between the two flows and their respective behaviours correspond with that observed by Fernholz et al. (1996), who present S_q and K_q statistics measured in some high Reynolds number turbulent boundary layers. In particular, the near-wall peaks in skewness and kurtosis occur within $2<y^+<3$, and at magnitudes within the range given by Fernholz et al. (1996) ($0.9<S_q<1.65$; $4.1<K_q<7$).

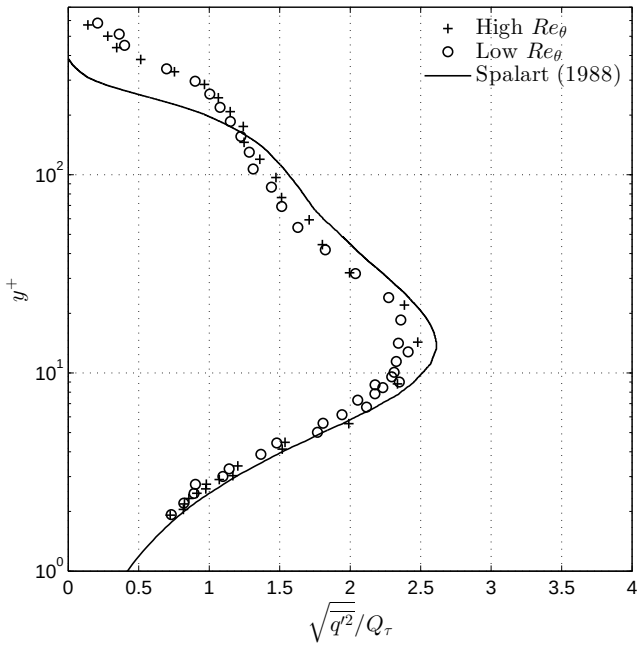

Figure 3.20: Streamwise rms velocity profiles non-dimensionalised with inner units; (–) the result obtained by Spalart (1988) at Re_θ=670.

3.6.3 Spectra

The distribution of turbulent energy among the structures in the boundary layer is revealed by the energy spectrum of the turbulent boundary layer. Velocity information can be used to obtain spectral measurements if a conversion to the frequency domain be made. It is common therefore, that Taylor's hypothesis be applied which asserts that the turbulence field is 'frozen' and carried along by the flow at the local mean velocity Q. Spatial correlations are then approximated with temporal ones. Application of Taylor's hypothesis is only appropriate for regions of the boundary layer where the turbulence intensity is low ($\sqrt{\overline{q'^2}}/Q \leq 0.1$), which limits spectral measurements above the buffer region. The stress density of the turbulence in the local mean-flow direction can then be expressed by the one-dimensional power spectral density E as (Saddoughi and Veeravalli, 1994):

$$\overline{q'^2} = \int_0^\infty E(k_s) dk_s$$

where a conversion to wavenumber space was made using $k_s = 2\pi f$, for the frequency f. E is computed using windowed Fourier transforms of the fluctuating velocity measurements.

To investigate the spectra in the boundary layer, authors have tested a variety of wavenumber scalings; usually with the aim of achieving similarity. Spalart (1988) lists four possible normalisation forms with some, such as the viscous lengthscale ν/Q_τ, remaining constant with wall-normal height. The normalisation used in this section is carried out in terms of the Kolmogorov velocity $v_k = (\varepsilon\nu)^{1/4}$ and microscale $\eta = (\nu^3\varepsilon)^{1/4}$, where ε is the dissipation. The density E, is non-dimensionalised by $v_k^2\eta$ and the wavenumber k_s, by η. The technique employed by Warnack and Fernholz (1998) is also applied, which determines dissipation from the one-dimensional power

spectrum using the structure function D_{11}:

$$D_{11} = 2\nu \int_0^\infty k_s^2 E(k_s) dk_s$$

where, for isotropic turbulence, $\varepsilon \approx 15D_{11}/2$.

When normalised by Kolmogorov units as above, the spectra should collapse for flows with the same Taylor-scale Reynolds number Re_λ. Re_λ is defined as:

$$Re_\lambda = \overline{q'^2}\lambda/\nu$$

where λ is the Taylor microscale, calculated using the autocorrelation function $\rho(\tau)$ (Pope, 2000):

$$\lambda = -Q\left(\frac{1}{2}\frac{d^2\rho}{d\tau^2}\bigg|_{\tau=0}\right)^{-1/2}$$

The Taylor Reynolds number measured in the high speed turbulent boundary layer is shown in Figure 3.21. A region where Re_λ is approximately constant can be seen starting at around y^+=70. The spectra measured at various wall-normal locations in the boundary layer are shown in Figure 3.22 with lines illustrating the $k_s^{-5/3}$ and k_s^{-7} power laws.

Low energy electronic noise created by the hot-wire bridge circuit was found to contaminate the spectra for the highest wavenumbers, causing a 'levelling off' of the PSD. This limits the available bandwidth and so is not included in the presentation of the PSD. Despite a high frequency spike, the profiles appear to collapse for high wavenumbers even down to y^+=45, and evidence of the Kolmogorov power law behaviour may also visible. For the spectra shown in Figure 3.22, the difference between the Kolmogorov and viscous lengthscale alternative normalisation varies from -12% through to 24%.

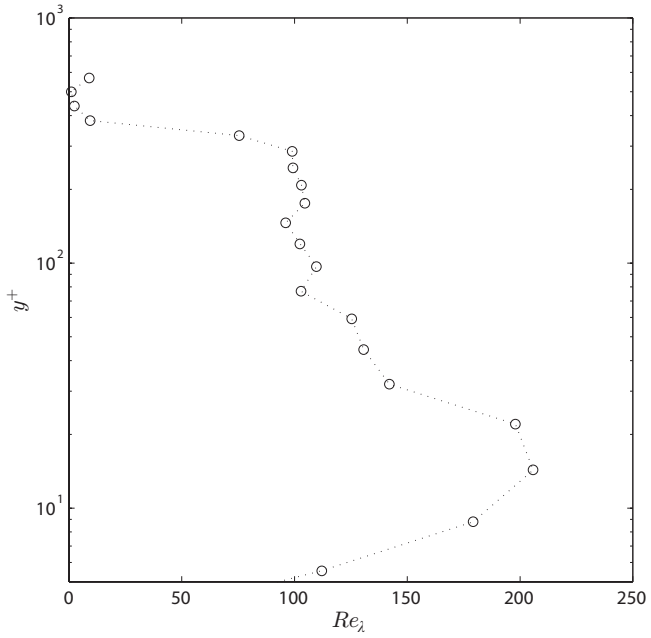

Figure 3.21: The variation of the Taylor Reynolds number with wall-normal height in the turbulent boundary layer

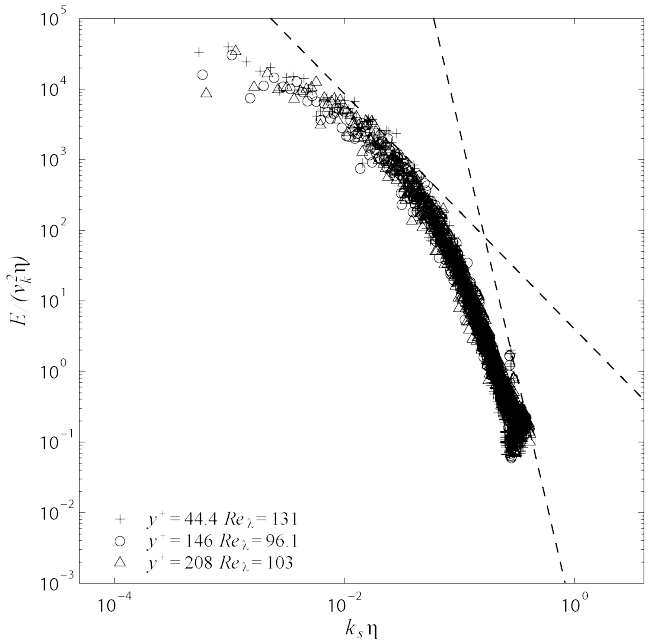

Figure 3.22: The one-dimensional power spectra measured at various wall-normal distances in the zero-pressure-gradient turbulent boundary, normalised in Kolmogorov units.

3.7 Low-Speed Streak Visualisation

In this thesis, the effects of pressure gradient perturbations on the near-wall turbulent structures is investigated through the mean spanwise spacing between the viscous sublayer low-speed streaks: $\bar{\lambda}$. This structural property has a well-defined value in unperturbed turbulent boundary layers over a wide range of Reynolds numbers and provides one of the few reliable quantitative descriptors for the configuration of the turbulent eddies. Compared to similar structural analyses it is relatively less subjective, being less dependent on the investigator's particular interpretation of the boundary layer turbulence organisation. The reading of streak spacing, for example, does not require the existence of an intricate flow model such as the 'hairpin vortex' or 'packet' structures described in §2.1, and their significance to the turbulence was shown by Kim et al. (1971) who identified streaks as sites of appreciable turbulent energy production.

The structures inhabiting the viscous regions (y^+<30) are identifiable, or 'coherent', within some region of space. Consequently, aspects of their appearance and behaviour are not easily identified experimentally using the single-point measurements provided by individual hot-wires or LDA instruments. Multiple probes are better suited and can identify important structural information such as size and inclination angles (Dixit and Ramesh, 2010). Since the structures occupy a region of space, they lend themselves favourably to visualisation methods such as dye markers, hydrogen bubble visualisation, and PIV (though categorising PIV as a visualisation technique is probably now inappropriate). The most common way to investigate streak behaviour is hydrogen bubble visualisation, first employed for this purpose by Runstadler et al. (1963) and has since proved successful in turbulent boundary layers that are three-dimensional (Chiang and Eaton, 1996; Flack, 1997; Kiesow and Plesniak, 2003) or subjected to streamwise pressure gradients (Schraub and Kline, 1965).

3.7.1 Visualisation Technique and Procedure

The hydrogen bubble visualisation method applied here is similar to that of other studies and involves placing a thin platinum wire in the flow. This serves as the cathode in a DC circuit and generates hydrogen bubbles by the process of electrolysis. The wires used here are 200 mm in length ($\Delta z^+ \approx 2000$) and 25 μm in diameter (0.25 viscous units). The bubbles are generated with a similar size to the diameter of the wire, giving them a small buoyancy allowing them to be used as passive scalars.

The bubble patterns are illuminated with a laser light sheet located under the glass plate and reflected onto the wires using a mirror. The mirror has a height of 5 mm and is angled at 45°, giving it an effective height of $y^+ \approx 35$. The mirror is located far downstream of the wires ($x^+ > 3000$) so that flow disturbances are kept small. The rise rate of the bubbles was checked in still water and estimated to be around 0.15 mm·s^{-1}. With Q_e=0.122 m·s^{-1}, the local velocity at y^+=2 is 12 mm·s^{-1}. Out of plane motion by the streaks does not therefore pose a problem, aided by the small variation in streak spacing for $y^+ < 5$ (Smith and Metzler, 1983), which is effectively the same height as the lightsheet itself. The bubble patterns were photographed using a Nikon D80 digital SLR camera located beneath the glass plate. A reference grid printed on a transparent plastic sheet was positioned on the plate, photographed, and then removed before starting the experiment in order to provide reference lengths for the remaining images.

To hold and position the wires, a traversable wire holder similar in design to those used by Smith and Metzler (1983) and Chiang and Eaton (1996) was intended so that different heights in the boundary layer could be visualised easily. The shift of the glass plate, however, meant that a different approach was required so that the wall-normal height of the wire could be known accurately. Here, the wires were supported on shims fixed to the glass plate. The wire was strung across the shims and tensioned before fixing to the glass using a combination of water proof tapes and sealants. This somewhat clumsy arrangement was necessary as wall inserts were not

possible and keeping the wire reliably taught and straight over the entire width of the channel proved futile. The shim and wire heights were checked and measured using a Mitutoyo precision height gauge with a reported accuracy of ±30 μm (±0.3y^+). Figure 3.23 shows the configuration of the visualisation experiment.

Streaks are visualised at x=0.4 (0.4 m from the start of the glass section) at two heights corresponding to y^+=4 and y^+=8. Up to 950 images were obtained for each height and a delay of t^+>100 between image captures ensured that each was statistically independent. A window in each image with dimensions Δx^+=300, Δz^+=800 was used for the spacing calculation. The uncertainty in mean non-dimensionalised streak spacing, $\bar{\lambda}^+$, is $\bar{\lambda}^+$±5%. The spacing is usually determined using the 'streak-counting' method, where streaks are identified visually in an image according to a set of rules, such as minimum streak length, and the mean spacing determined from the number of streaks counted. Here, the spanwise Fourier transforms of the image intensity in combination with a hamming window function were used to determine the spacing at all streamwise distances in an image window. The mean of all spanwise transforms in an image was interpreted as the spacing for that particular image. Had all the transforms in a single image been used independently instead of averaging in the streamwise direction, then each spacing would not be statistically independent.

3.7.2 Visualisation Results

Figure 3.24a shows a typical example of a visualisation image showing the interrogation window. Figure 3.24b shows the spectral transform of the window data. Histograms of the streak spacing distributions, obtained at a freestream velocity Q_e=0.122 m·s^{-1} are shown in Figure 3.25 for the wire heights y^+=4 and y^+=8. The statistical measures of standard deviation, σ_λ^+, skewness, S_λ, and kurtosis, K_λ describing each distribution are included. Also shown is a log-normal probability density function fitted to the data, demonstrating the typical shape of the spacing distri-

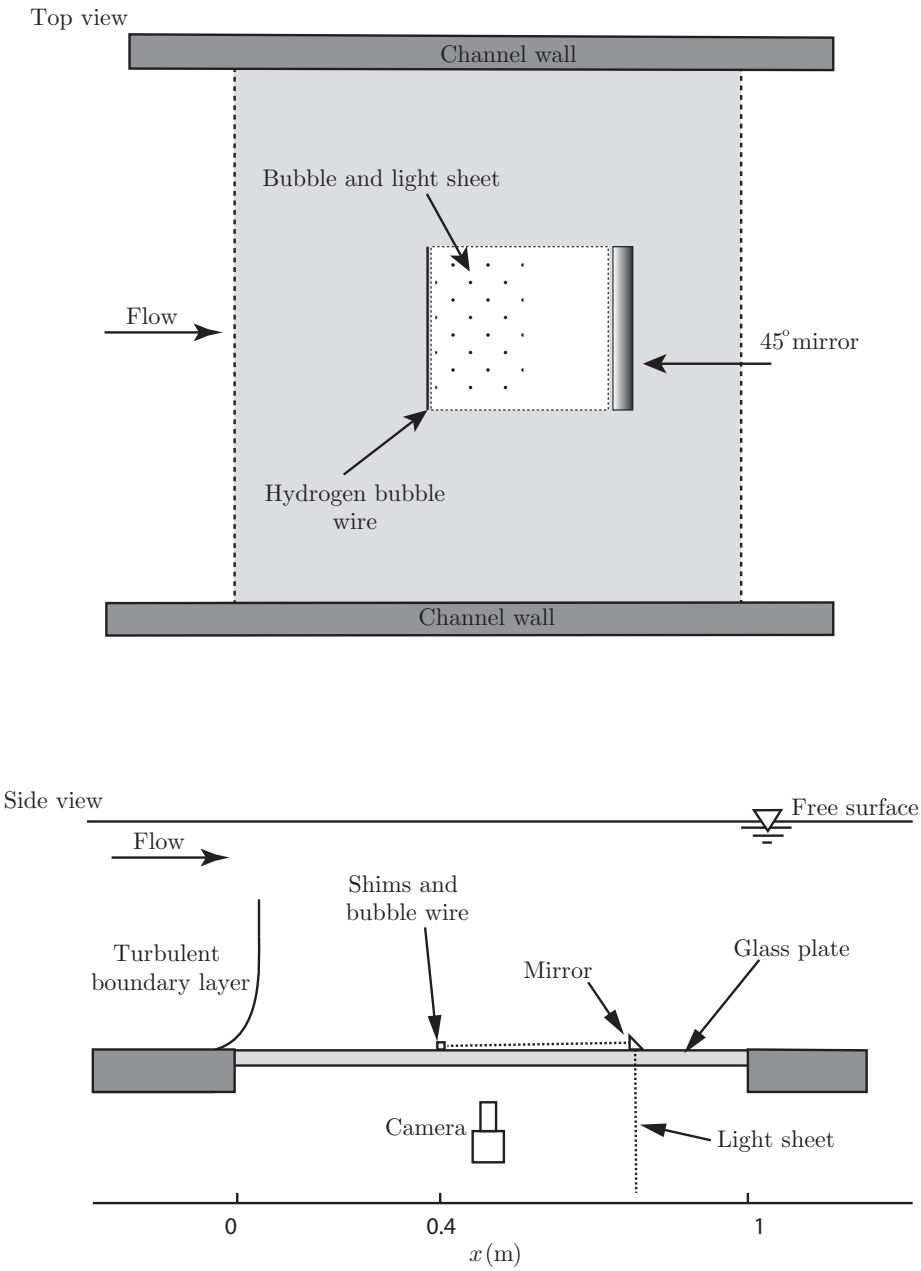

Figure 3.23: A schematic of the experimental visualisation configuration (not to scale).

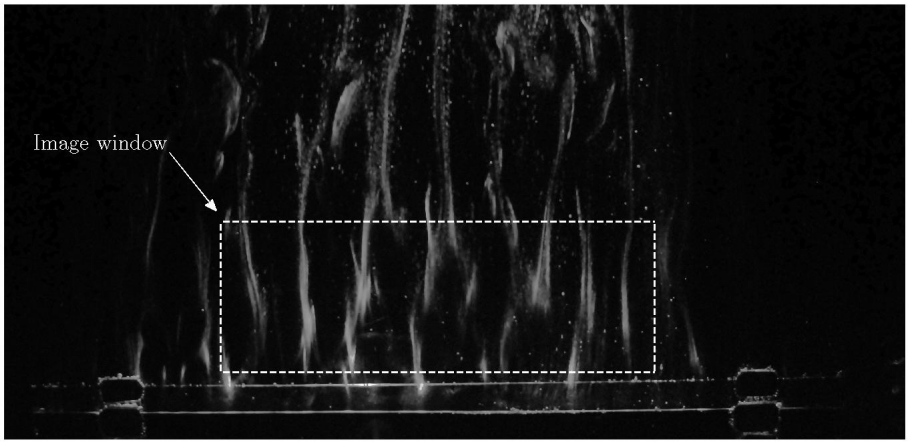

(a)

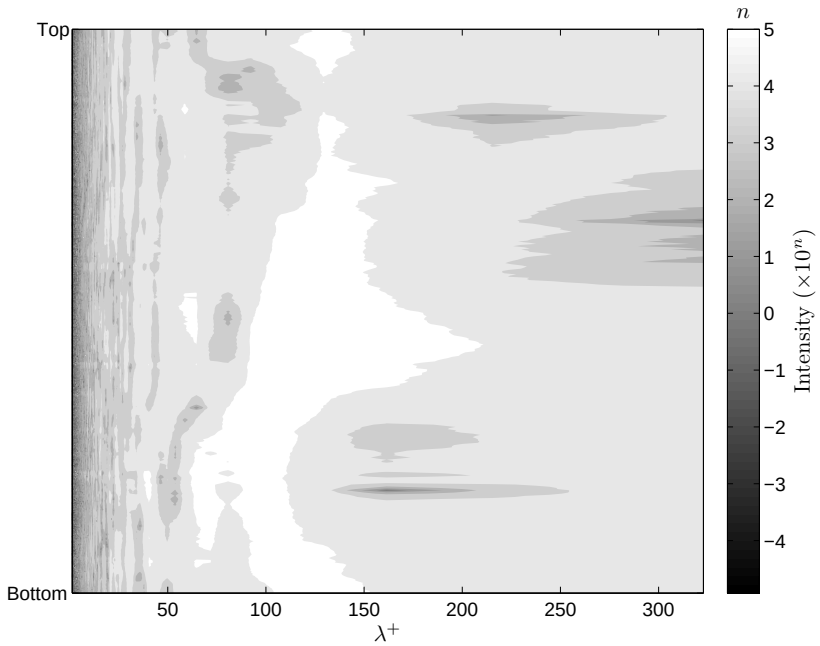

(b)

Figure 3.24: The streak visualisation process. (a) An example image of the low-speed streaks showing the image interrogation window (−−). The flow direction is up the page. (b) The spectral transform from the windowed image. 'Top' and 'Bottom' labels refer to the top (downstream) and bottom (upstream) of the image window.

bution. Each function fit was tested against the data using the Kolmogorov-Smirnoff goodness-of-fit test, confirming that the log-normal density function provides an appropriate model for the streak spacing distribution. At y^+=4 the mean streak spacing is $\bar{\lambda}^+$=109 and at y^+=8, $\bar{\lambda}^+$=111, both of which are within the accepted range of values for zero-pressure-gradient boundary layers: $\bar{\lambda}^+$=100±20 (Smith and Metzler, 1983). S_λ and K_λ are also comparable to accepted ranges, but the standard deviation appears slightly lower.

Smith and Metzler (1983) comment that the log-normal distribution of streak spacing suggests the independent influences causing variations in λ (about $\bar{\lambda}$), have an effect which is proportional to the magnitude of λ itself. In addition to this is the fact that λ will always be positive and has a 'potentially unconstrained upper limit'. Here, it is merely observed the the velocity fluctuations in this region (Figure 3.26) are also distributed log-normally, as confirmed by the Kolmogorov-Smirnoff test. The statistics of the distribution are also similar to those in the streak spacing distribution. This is to be expected though, as each streak in an image represents a low-speed velocity fluctuation surrounded by fluid moving at or above the mean velocity. Changes in streak spacing statistics should therefore correspond, in some respects, to changes in the streamwise velocity statistics.

3.8 Chapter Summary

This chapter documents the main experimental setup and the techniques applied and uses them to examine some simple boundary layer flows. The channel flow facility has been described in §3.2, along with the water conditioning and temperature monitoring equipment. The flow properties in the measurement region are summarised and information needed to evaluate the facility's suitability for experimentation given.

Since thermal anemometry provides the main measurement tool, a brief back-

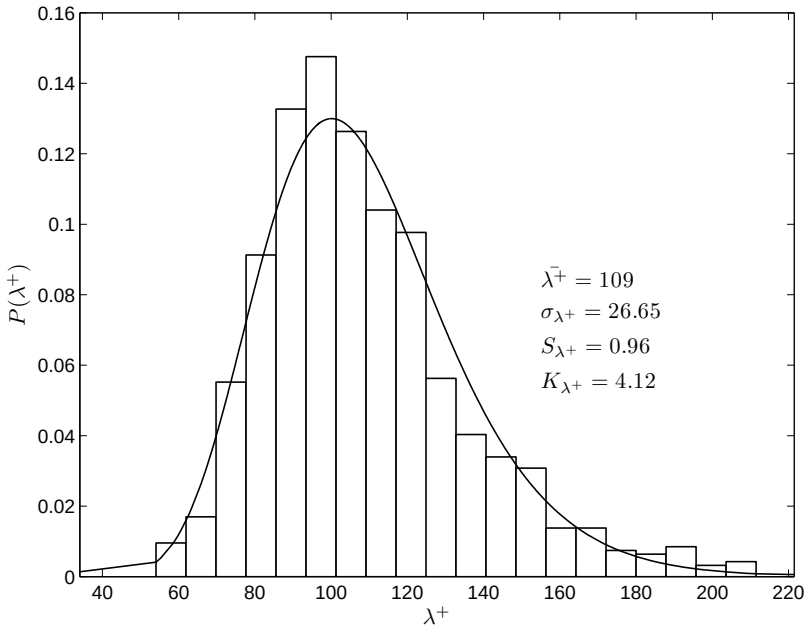

(a)

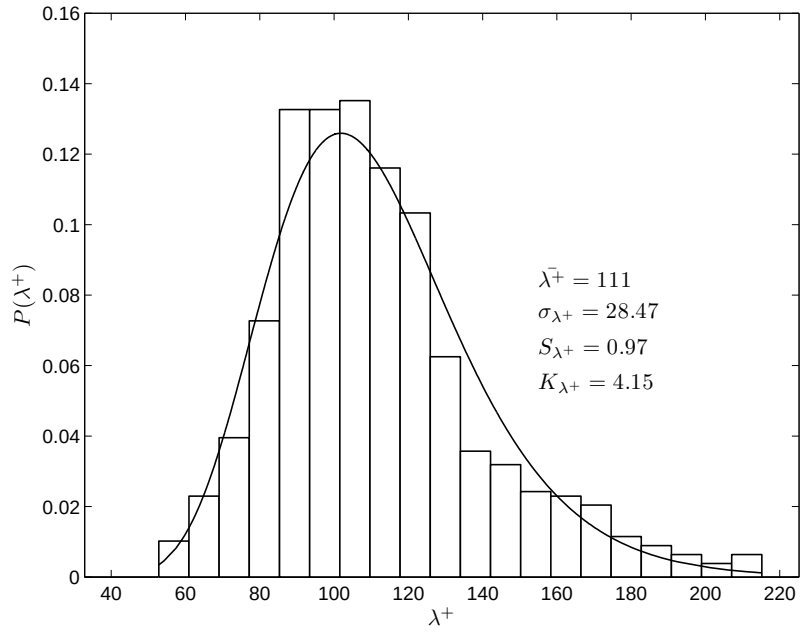

(b)

Figure 3.25: Streak visualisation results. The curve (–) is the log-normal distribution fit to the data. (a) Platinum wire located at y^+=4; (b) wire located at y^+=8.

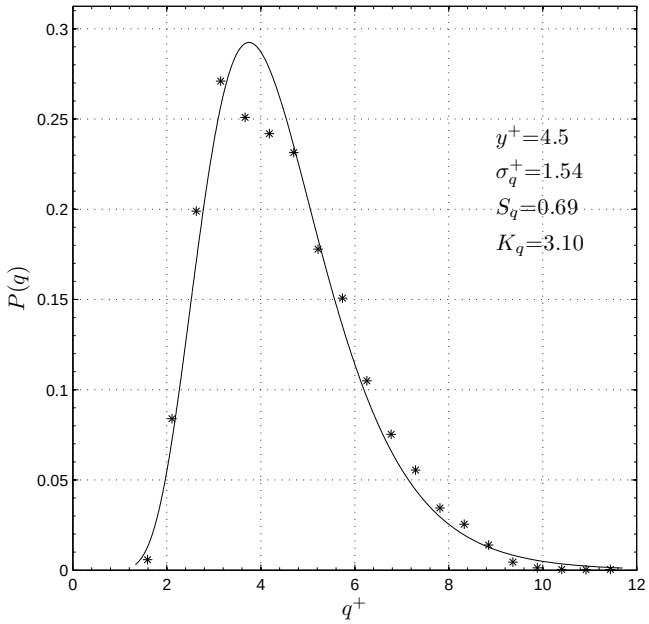

Figure 3.26: Probability density distribution of streamwise velocity at $y^+ \approx 4.5$. $(*)$ binned data; $(-)$ the log-normal distribution fit to the data.

ground to its operation was provided in §3.3 along with the various assumptions made for its use. Details are also provided for the particular equipment used, its setup and its operational characteristics. A discussion of the calibration procedure follows and the uncertainty in the calibration method is determined.

An overall evaluation of the experimental uncertainty is given in §3.4, calculated using the various error sources present throughout the experiment. These sources are described and estimates are provided for their respective magnitudes. This uncertainty must be used when evaluating the experimental results and will influence any conclusions drawn from them.

Since the wall shear stress is important for this investigation, §3.5 outlines the methods used and the difficulties encountered during its measurement. An unforeseen spatial error, described in §3.5.2, resulted in different approaches being tried for probe positioning. The final method relied on standard techniques in combination with a more novel, initial process and tests show that levels of uncertainty could be kept below 2%.

Following the measurement system documentation, the results of experiments carried out on two-dimensional boundary layers is reported. These were performed in the testing region of the facility under zero-pressure-gradient conditions and the information obtained has several uses: the flows investigated provide the data against which later experiments in different conditions can be compared, and it allows the performance of the experimental setup described previously to be evaluated in practice. The results from both laminar and turbulent boundary layers are presented and comparisons made with the literature on similar flows. These results show that typical zero-pressure-gradient turbulent boundary layers can be generated and measured accurately in the test region.

In §3.7 an experimental method is described to measure the spanwise spacing of the viscous sublayer low-speed streaks. The practical approach is based on standard hydrogen bubble visualisation, but analysis of the streak images obtained is made using Fourier transforms instead of the counting procedures more common in the literature. This method proved successful when used in a turbulent boundary layer and will be employed in later chapters to investigate the effects of the pressure gradients on the organisation of near-wall streaks.

Chapter 4

Case 1: Favourable Pressure Gradient Experiments

The strategy in this thesis, as outlined in §2.4 is to compare the effects from different pressure gradients on a turbulent boundary layer. By using pressure gradients that allow individual forces to be subtly introduced, it is hoped their particular effects on the boundary layer behaviour can be distinguished in a clearer manner to previous studies. This particular chapter presents the results from the experiments performed on a turbulent boundary layer in a favourable pressure gradient. This favourable pressure gradient case, hereafter termed Case 1, can be compared with the zero-pressure-gradient experiments in the previous chapter and to those given in the following chapter where an identical favourable pressure gradient is combined with a spanwise pressure gradient (Case 2).

In §4.1, details about the design and implementation of the Case 1 pressure gradient generator are given. The freestream potential flow that results from the generator was measured and is described in §4.2, and §4.3 presents the streamwise development of the turbulent boundary layer. Finally, §4.4 shows the effects of the generator on the viscous layer low-speed streaks.

4.1 Case 1 Generator Design and Implementation

When designing the geometries of the two pressure gradient generators, the requirements for the second Case, which included the spanwise pressure gradient component, proved far more demanding than those of the case with just a single streamwise component. The main difficulty is the need to introduce the spanwise component whilst keeping other influences the same. This becomes very problematic to achieve when pressure drives the three-dimensionality of the boundary layer; a subject discussed in more detail in the following Chapter. As such, the design of the single-component generator Case 1, which is described in this section, was dictated largely by that of Case 2, so some details have been left for the following chapter.

4.1.1 Design

The favourable pressure gradient is generated by converging the flow channel in the lateral direction. Compared to the alternative approach, convergence in the vertical direction, there are far fewer investigations into laterally converging ducts. A four part experimental study is provided, however, by Murphy et al. (1983), Chambers et al. (1983), McEligot and Eckelmann (2006), and McEligot et al. (2009) that considers the idealised laterally-converging duct flow.

A schematic of the pressure gradient generator in the water channel is shown in Figure 4.1, where the Cartesian coordinates are referenced to the channel rig walls and flow direction, so are termed throughout as 'channel coordinates'. Also shown in the figure are three streamlines, evenly spaced in the generator's geometry, which are used for reference later. As the walls are kept straight, the resulting flow behaviour within the generator itself is a laterally converging sink-flow. In the idealised case, described by McEligot and Eckelmann (2006), the freestream flow is two-dimensional in circular coordinates and radially inward towards the sink point. Neglecting the boundary layer displacement, the freestream velocity towards the

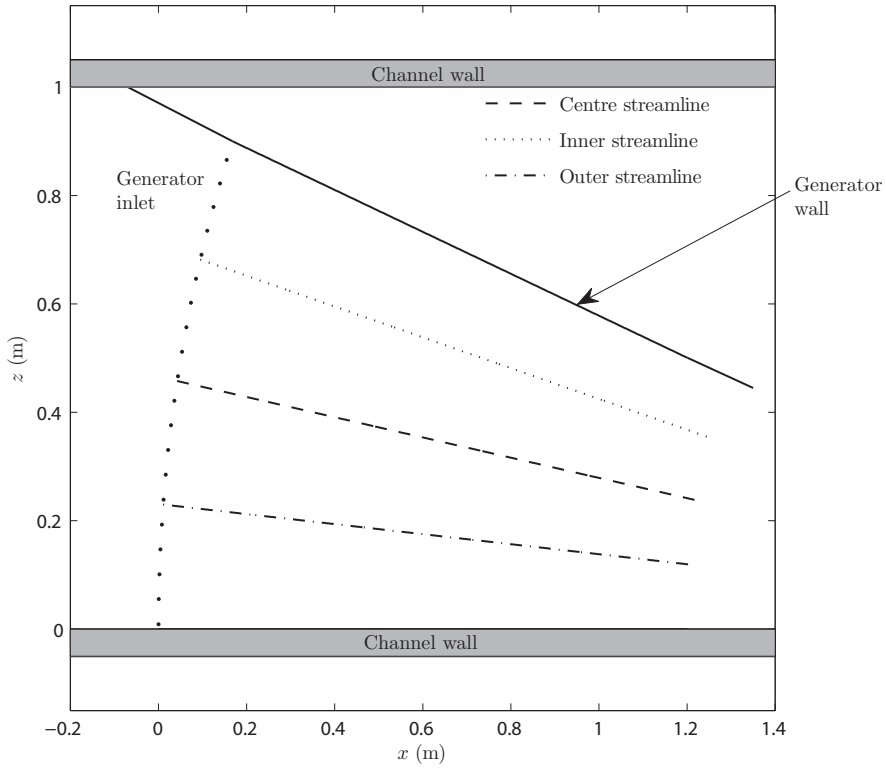

Figure 4.1: A plan-view schematic of the Case 1 pressure gradient generator in the flow rig. The Cartesian coordinates (x and z) refer to the 'channel coordinates' employed in Figure 3.1, which shows a wider view of the flow rig.

sink point is described by:

$$Q_e(s) = Q_e(0)L(L-s)^{-1} \tag{4.1}$$

where s is the streamwise distance from the contraction inlet which is ideally at a large distance upstream, $Q_e(0)$ is the initial velocity at the inlet, and L is the total distance towards the sink point. The continuity equation is given by:

$$\frac{Q_e}{L-s} + \frac{dQ_e}{d(L-s)} = 0 \tag{4.2}$$

and the streamwise pressure gradient is described by:

$$\frac{1}{\rho}\frac{dP}{ds} = -Q_e\frac{dQ_e}{ds} = -Q_e(0)^2L^2(L-s)^{-3}, \tag{4.3}$$

where P is the pressure. The parameter K, first introduced by Schraub and Kline (1965) is used to characterise the pressure gradient. K in sink flow or laterally converging ducts becomes:

$$K = \frac{\nu}{Q_e(s)^2}\frac{dQ_e(s)}{ds} = \frac{\nu}{Q_e(0)L} \tag{4.4}$$

The quantity L defining the physical size of the generator's geometry is set to the value used in the curved channel to keep the accelerations identical. From §2.4 an acceleration magnitude of the order $K{\sim}3{\times}10^{-6}$ is required. In both cases L=2.5 m was chosen for reasons discussed further in the next chapter. With $Q_e(0)$=0.125 m·s^{-1}, the acceleration parameter becomes K=3.2×10^{-5}.

In Cartesian or channel coordinates, s is a function of both x and y:

$$s = \int_{x_{inlet}}^{x}\left[1+\left(\frac{dz}{dx}\right)^2\right]^{1/2}dx$$

where x_{inlet} refers to the x coordinate at the inlet to the contraction. The streamwise

velocity towards the sink point has two components: $Q=(U^2+W^2)^{1/2}$, where U and W are the velocities in the x and z directions respectively.

The angle between the channel's straight wall and the generator wall is 21°, which is clearly not negligible and will produce curvature effects in the flow in its vicinity. The obvious way to generate a laterally converging duct flow experimentally is to angle both walls symmetrically, thereby keeping curvature effects negligible along the centre streamline and reducing the magnitude of the wall angle. A different approach is to have two disks with a separation between the disk surfaces and a suction pipe at the disk centre providing the sink force. Murphy et al. (1983) and Chambers et al. (1983) use this system for their experiments but it becomes very demanding if large spatial dimensions are desired. The decision to angle only one wall was made here so that a fairer comparison could be made with the Case 2 study. The data obtained from this case can therefore also be used to assess the impact from the undesired inlet curvature effects, which are present in Case 2, as well as any other practical factors which might otherwise be confused with those created by the Case 2 channel geometry.

4.1.2 Construction

The angled wall is constructed using smooth 3 mm thick Perspex. The wall was supported and held rigid on an adjustable frame that allows the angle with the channel to be set then locked in position. Screws fix the wall to the frame above the water surface, and waterproof glue was preferred below the surface to minimise flow disturbances. Small adjustable wedges on the frame side of the wall could be set to locate and fix the geometry at the correct position. The length of the wall extends beyond the testing region to keep the exit, and any disturbances created by it, located far downstream. Figure 4.2 shows a photograph of the generator in the rig.

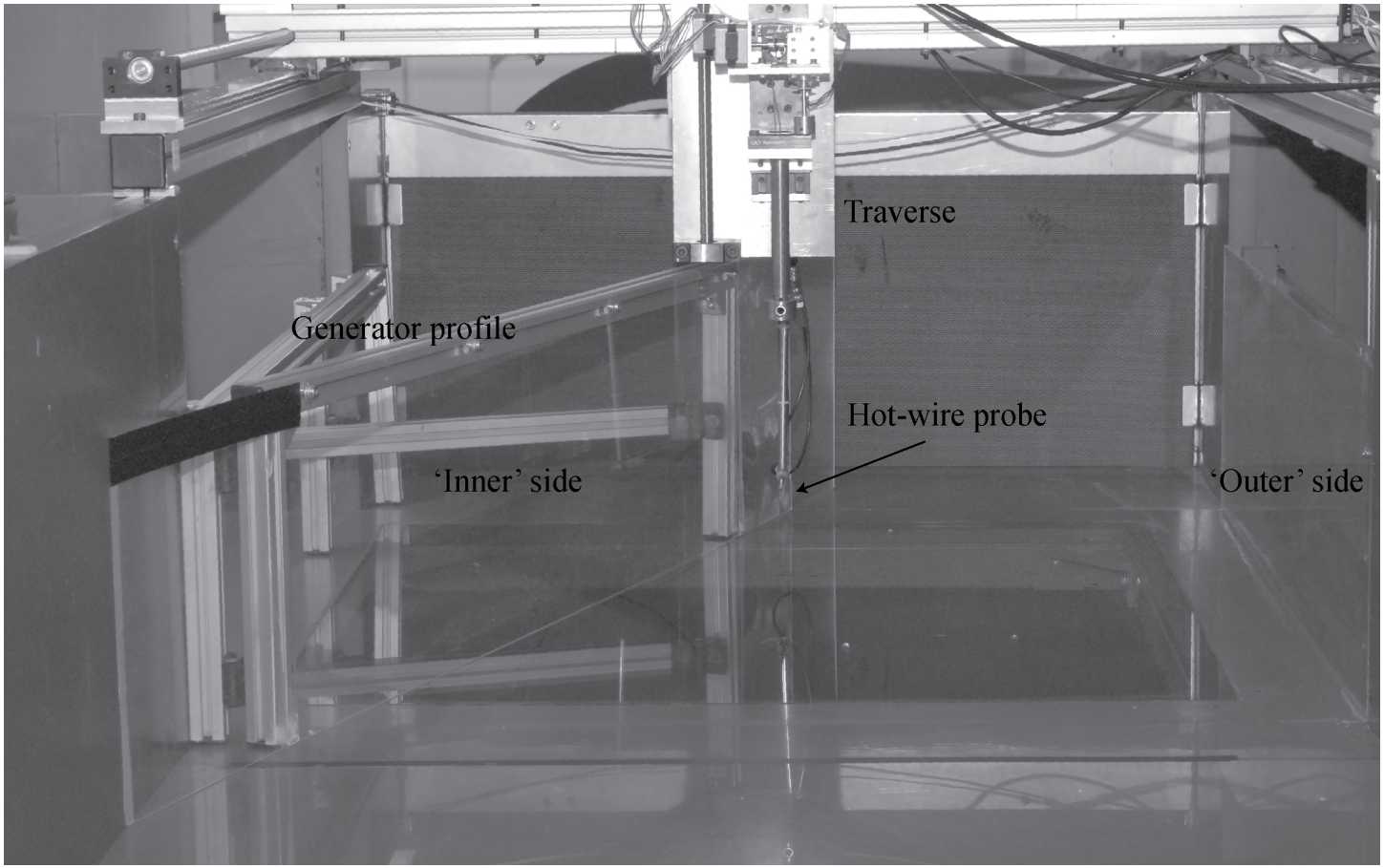

Figure 4.2: A photograph showing the Case 1 generator in the experimental rig. The left and right hand sides of the photograph correspond to the 'inner' and 'outer' regions of flow referenced in the text respectively

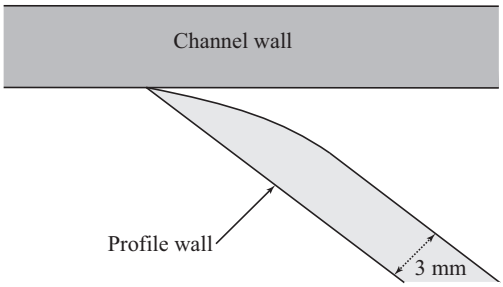

Figure 4.3: An illustration of the interface between the generator wall and the channel wall.

The generator inlet curve shown in Figure 4.1 only spans 90% of the channel rig, which is evident from the figure because the point where the contraction wall meets the channel wall does not correspond with the dotted line indicating the referenced inlet of the generator geometry. A short straight extension fills the gap between the two, which was included owing to the practical concern regarding the flow near this interface. Should significant flow disturbances develop, this section would be modified. It could not be removed entirely because this would cause circulation around the generator and a very large disturbance at the wall's leading edge.

No significant alterations were needed however, as it was found that by filing the outside corner into a sharp point, as illustrated in Figure 4.3, a small force could be applied on the wall to generate a slight curvature at this point and therefore a smoother interface. An examination of the flow using dyes revealed only small disturbances to the flow resulted by using this approach. The stabilising effect from the relatively large streamwise acceleration also helped to keep these disturbances small with streamwise distance.

The extension of the contraction length also means that the onset of flow acceleration starts upstream of the inlet curve ($\cdot\cdot\cdot$). The flow velocity at the

referenced inlet will consequently be higher. If the freestream velocity in the channel is kept the same, it means the total contraction length is increased to L=2.74 m, which reduces the acceleration parameter. To compensate for this, the channel flow rate was adjusted slightly such that by the inlet curve indicated in Figure 4.1, the freestream velocity was $Q_e \approx 0.125$ m·s^{-1}. This means that the boundary layer will enter the contraction at a lower Reynolds number, but as this procedure was repeated in the Case 2 experiment, they will remain comparable.

4.1.3 Channel Position and Adjustments

Two further practical problems stemmed from allowing the design of Case 1 to be dictated by Case 2. Firstly, the resulting streamwise measurement positions towards the end of the Case 1 contraction lie outside the reach of the traverse, which had a finite stroke length of only 1 m. Secondly, the location where the streak spacing is determined was closer to the end of the glass floored region, and would therefore require modifications to be made to the hydrogen-bubble visualisation method.

These two problems arise, however, only because the same channel coordinates were used for Case 1 as were used in Case 2. A simple compensation could therefore be made by shifting the entire Case 1 geometry upstream in the channel by x=-0.21 m such that the centre streamlines shown in Figure 4.1 of each sit at the same x coordinate in the water channel. An added benefit is that the turbulent boundary layers entering each generator at the centre streamline will have had the same streamwise distance in the channel to develop. The maturity of the turbulence in each will therefore be closer and the comparison between the Cases fairer. To prevent confusion when using the channel coordinate system, the x-axis for Case 1 is also shifted upstream such that the layout in Figure 4.1 and accompanying coordinate system can still be used.

4.2 Potential Flow

Measurement of the potential flow through the geometry would ideally be carried out by measuring the pressure, but as has been mentioned previously, the low operating velocities in the channel result in very small differences in pressure. Instead, the freestream velocities and flow angles were measured with the hot-wire probe, allowing an evaluation of the potential flow behaviour through the geometry.

Measurements of the freestream velocity (Q_e) and direction (γ_e) were made at five locations along each of the streamlines shown in Figure 4.1. Unfortunately, the finite stoke length of the traverse limited all measurement locations using the hot-film probe to within the generator geometry area. This meant that samples from further upstream could not be measured and it is therefore not possible to check whether the flow entering that the generator is in an 'unperturbed' state. It will be seen later however, that the effects of a slight streamwise acceleration can be seen in the 'inlet' flow profiles. The measurement of potential flow is made using an automated procedure which was carried out before the more detail measurements in the boundary layer took place.

An initial idea of the potential behaviour through the geometry can already be made by using the idealised case from §4.1.1, where the velocity and pressure gradient in an axisymmetric laterally converging duct were given. The streamlines in Figure 4.1 indicate the radial streamlines towards the sink point that would result from such a flow and so these can be used to estimate the flow freestream direction. Their directions compared to the channel x-axis are -16° for the inner streamline, -10.6° for the centre and -5.8° for the outer streamline. The negative value indicates turning in the -z direction.

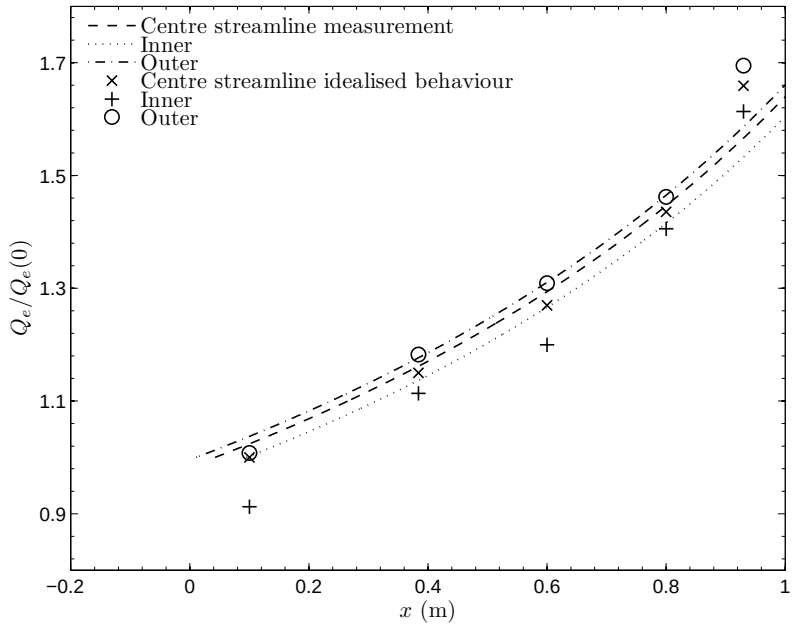

Figure 4.4: The change of the freestream velocity through the Case 1 geometry along the three streamlines in Figure 4.1 versus channel coordinates. The markers indicate measurements and the lines indicate the idealised data described in the text. $Q_e(0)$ refers to the initial velocity measured on the 'Centre' streamline.

4.2.1 Freestream Velocity Measurements

The freestream velocity was measured by first orientating the probe into the mean-flow direction found beforehand. A faster approach could have found both the magnitude and the direction simultaneously using the maximum point in the cosine-law fit obtained from one angle sweep of the probe (see §3.4.4). The method used instead is preferred because a longer sampling time can be used for each velocity.

The freestream velocity measurements are plotted as markers in Figure 4.4 versus channel coordinates. The measurements are normalised by the initial velocity of the centre streamline and the lines indicate the idealised or 'equilibrium' velocity behaviour which follows from the discussion above. The hot-film measurements at the furthest downstream stations may contain some error, as the velocity exceeded the range of the calibration cylinders so an extrapolation along the response relationship was necessary.

The flow here is not an equilibrium flow but is instead perturbed from the horizontal channel x-axis into the generator geometry. The effects of this perturbation are clearly evident in Figure 4.4 at the inlet of the geometry, where the measured velocity of the inner streamline lies below that of the others. This initial velocity 'deficit' is continued throughout. The flow has started to turn upstream of the contraction and hence the velocity towards the region where that turning is largest slows down. Despite these initial perturbation effects, the overall freestream velocity behaves surprisingly close to the behaviour in §4.1.1. It may be remembered though, that it is not critical for the streamwise pressure gradient to represent any particular model specifically, or that the boundary layer achieve equilibrium conditions. It is merely desired that the streamwise components from the Case 1 and Case 2 generators be comparable.

4.2.2 Mean-Flow Direction

The mean-flow angle was measured by following the probe sweeping procedure outlined in §3.4.4. Using this procedure in the freestream is more reliable than near the wall as can be seen from Figure 3.12. The difference between the freestream direction, and the channel x-wise direction (γ=0) is shown in Figure 4.5 versus channel coordinates. The lines indicate the radial direction towards the sink point. The magnitude of the flow turning upstream of the inlet is now evident in the furthest upstream measurements. That the flow has started to turn upstream of the inlet means that the remainder of the turning in the generator itself is smaller, resulting in a large downstream test area for which the conditions are close to those desired. It can also be anticipated that the boundary layer will be more two-dimensional than otherwise.

After 0.4 m, the freestream flow appears to have stopped turning significantly and like the velocity, is quite close to the idealised behaviour. To illustrate the resulting potential flow in the geometry, the measurements are shown as vectors in

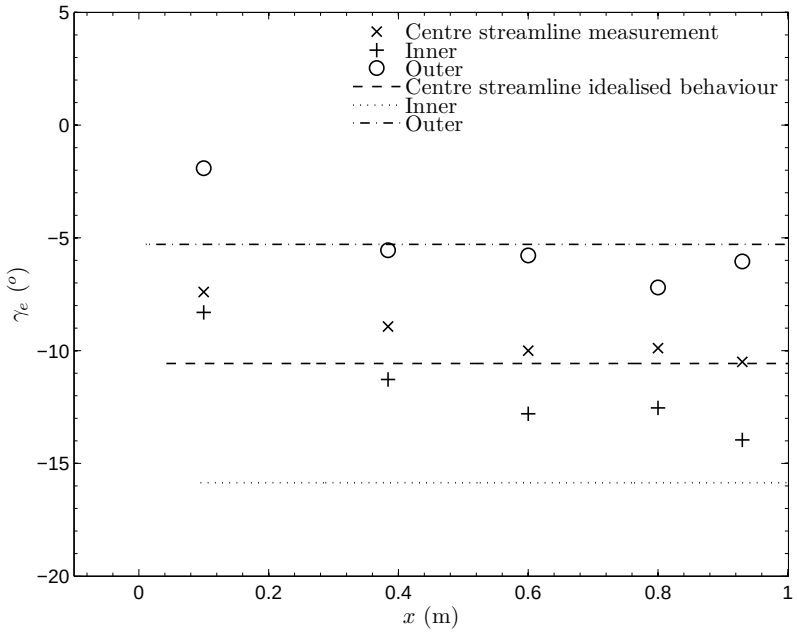

Figure 4.5: The deflection of the freestream flow (γ_e) by the generator from the direction of the flow upstream (γ_e=0). The x coordinate refers to the channel coordinate system. Markers indicate the measurements and the lines indicate the direction of the the three streamlines in Figure 4.1.

Figure 4.6, where the vector length indicates the velocity magnitude. Streamlines, computed from the measurements, are also shown. The results in this section and the one above indicate that the freestream flow is behaving reasonably close to that desired over quite a large region of the testing area.

4.2.3 Pressure and Acceleration

By using an inlet centreline flow depth of 0.15 m, the flow energy and pressure can be calculated from the energy equation using the results in the previous sections. The change in the coefficient of pressure, is calculated in this investigation by:

$$C_P = \frac{P - P(0)}{\frac{1}{2}\rho Q_e(0)^2},$$

where the reference pressure $P(0)$ and velocity $Q_e(0)$ are those of the centreline measurement furthest upstream. The overall changes in pressure coefficient are

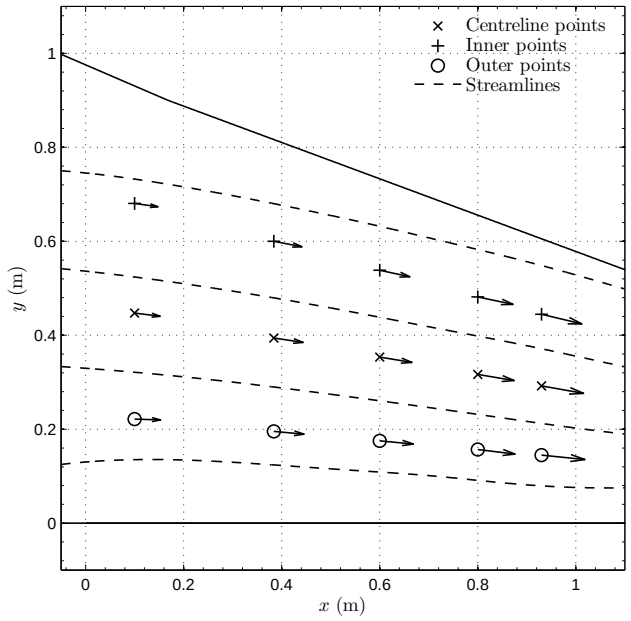

Figure 4.6: The freestream flow through the Case 1 pressure gradient generator. Velocity vectors are shown at the measurement locations (markers) and streamlines (−−) are included to demonstrate the broader behaviour. The streamlines are computed by interpolating the measurements onto a larger mesh.

shown in Figure 4.7 and are similar in size to the Case 1 acceleration study by Fernholz and Warnack (1998), but over a much longer streamwise distance.

The gradient of the coefficient of pressure is computed for two coordinate systems: the streamline coordinate system, which is defined with respect to the streamwise distance s; and the channel coordinate system. The behaviour of each is shown in Figure 4.8 versus channel coordinates and non-dimensionalised using the initial boundary-layer displacement thickness. The magnitude of the spanwise component ($\partial P/\partial n$) is much smaller than the streamwise component and reduces in the generator as expected. It should be mentioned that the markers in Figure 4.8 highlight the locations of the measurement stations and do not represent independent calculations.

The acceleration parameter defined in equation (4.4) is computed for the centreline measurements using a streamline coordinate system only and shown in

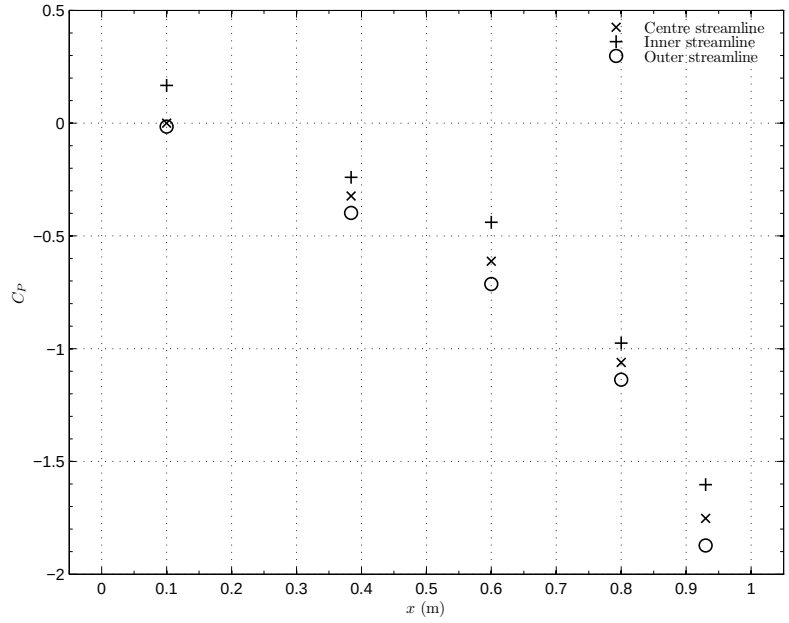

Figure 4.7: The change in the coefficient of pressure through the Case 1 pressure gradient generator versus channel coordinates.

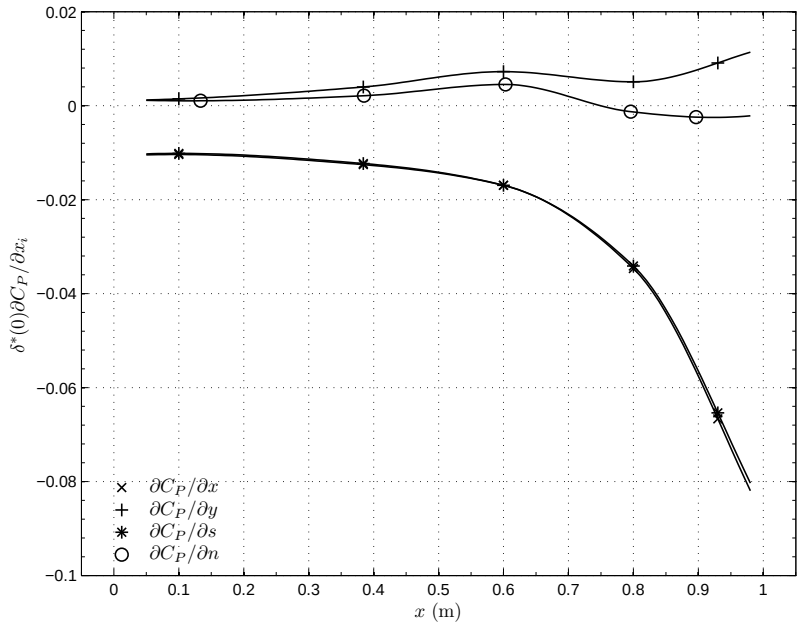

Figure 4.8: The pressure gradient generated by the Case 1 generator in a streamline (curvilinear) and channel coordinate systems. Markers indicate the locations of the measurement stations and do not represent independent calculations.

Figure 4.9. Error bars are also shown for a 2.3% error in the mean-velocity magnitude, which was found in §3.4.5. The acceleration rate is in between the $2.75\times10^{-6}\leq K\leq 3.7\times10^{-6}$ range, so the recognisable changes in the boundary layer associated with large acceleration rates should be evident, as desired in this investigation.

The relaminarisation process can be complex and take long streamwise distances (Narasimha and Sreenivasan, 1973). The turbulent boundary layer in the testing region was measured in the previous chapter. The Reynolds number (Re_θ) of this flow was relatively high compared to the minimum of $Re_\theta\approx330$ seen during relaminarisation (Spalart, 1986). If a similar boundary layer is present at the generator inlet, it may be expected that turbulent flow persists throughout. This is confirmed with dye marker measurements. When dye is laid on the channel floor in fully turbulent boundary layers using a long syringe inserted from the above, the dye can be seen to be dragged along the floor by the shear stress. Intermittently, the dye is lifted from the floor in filaments, 'wiggling' and becoming turbulent in a manner very similar to the streak patterns obtained using hydrogen bubble visualisation. The dye injected on the channel floor in the Case 1 geometry behaves in a similar way, indicating that the flow in the boundary layer is still turbulent and bursting is still active. This observation, though qualitative, is confirmed by the hydrogen bubble visualisations and velocity measurements that follow later in this chapter.

4.3 Boundary Layer Measurements

Velocity measurements in the turbulent boundary layer were made using the single-normal hot-film probe in separate experiments to the investigation of the potential flow. The measurements were carried out at five streamwise stations along the centre streamline referenced in Figure 4.1 and their locations over the testing region are shown in Figure 4.10. The coordinate locations are referenced to the streamwise distance, s, from the geometry inlet line. In perturbed three-dimensional bound-

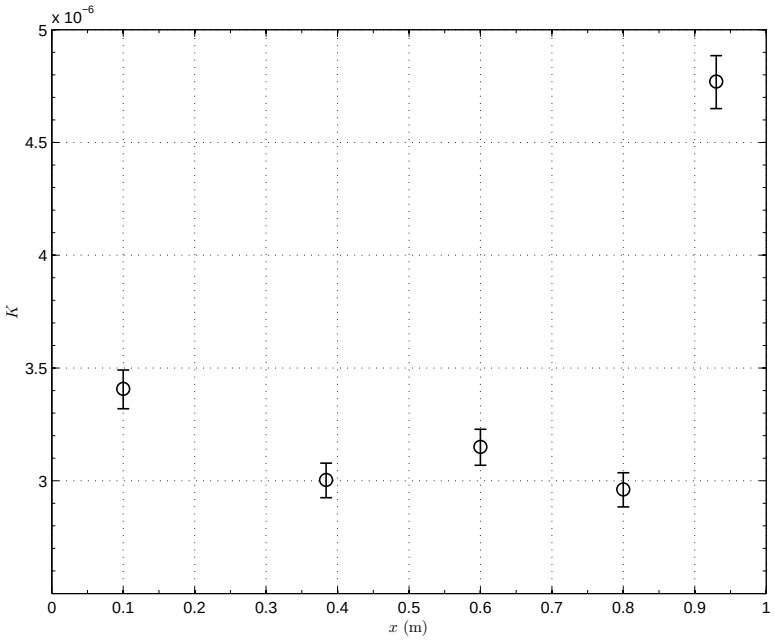

Figure 4.9: The behaviour of the pressure gradient parameter along the centre streamline. The error bars are calculated assuming negligible uncertainty in s and 2.3% error in Q_e. The real error for the last measurement station will therefore be much greater as the calibration error at this station has not been taken into account.

ary layer studies, a Cartesian coordinate system is often used, as it highlights the changes in behaviour resulting from the perturbation (Coleman et al., 2000). As the perturbation in Case 1 is largely confined to the streamwise direction, the streamline coordinate system is preferred to channel coordinates in this section. Also included in the results, are the zero-pressure-gradient case measurements in §3.6 of the previous chapter.

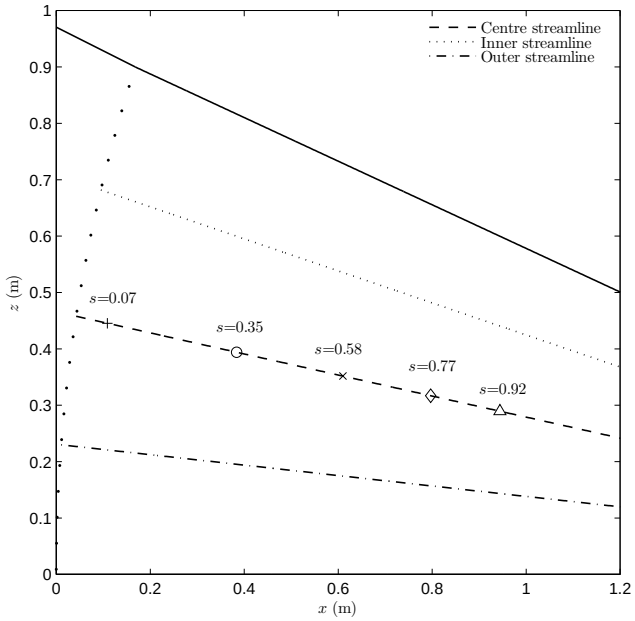

Figure 4.10: The locations of the five boundary-layer measurement stations in the generator.

4.3.1 Mean-Flow Direction in the Boundary Layer

Before the velocity of the boundary layer could be sampled, it was necessary to determine the mean-flow direction, γ, so that the hot-wire probe could be orientated properly. The extent of the three-dimensionality in the boundary layer induced by the slight turning at the inlet can also be evaluated using the results. Similarly to the previous section, the process of obtaining the mean-flow direction could have been performed simultaneously to the velocity profile by using the sweep method at each height in the boundary layer. In the boundary layer, however, the turbulence

intensity is high. This, combined with the large number of samples required to estimate the mean-flow direction to a reasonable uncertainty, make it necessary to carry out the two processes separately. Performing two experimental runs has the advantage that the velocity calibration of the hot-film anemometer is not required for the mean-flow direction measurement. The cosine-law could simply be applied to the anemometer output voltage, freeing up experimental time for more samples.

The mean-flow direction was only found for seven to eight wall-normal heights through the boundary layer; again a result of the length of time required obtaining each. The locations of the sampling point heights were focused towards the inner region of the boundary layer, where the magnitude of the turning is largest. Once the samples were collected, a smooth curve was fitted through the data points and this determined the orientation of the probe for the subsequent velocity measurements. No satisfactory models have yet been established for the mean-flow behaviour in a three-dimensional boundary layer, especially for the inner region (Degani et al., 1993) so for the case here, a monotonic second-order polynomial was used.

The flow direction results are shown in Figure 4.11 with the fitted curves showing the direction used for the probe orientation during subsequent velocity measurements. No measurements below $y^+ \approx 10$ were employed to fit the curves so the orientation of the probe in the viscous sublayer is dictated only by the fitted polynomials. As mentioned previously, the insensitivity of the probe to modest changes in angle near the wall, combined with the small levels of skewing measured here, should help minimise probe misalignment error when measuring the velocity and determining the wall shear stress (τ_w). Few three-dimensional boundary layer experiments attempt to measure below $y^+ = 100$, preferring instead to assume models for the behaviour of the mean-flow such as the log-law. Of the few studies obtaining measurements in the viscous regions ($y^+ \leq 30$), Flack and Johnston (1998) and Compton and Eaton (1997) for example, very different patterns of skewing emerge with the results of the latter agreeing more with those here; lending weight to the use of second-order polynomials.

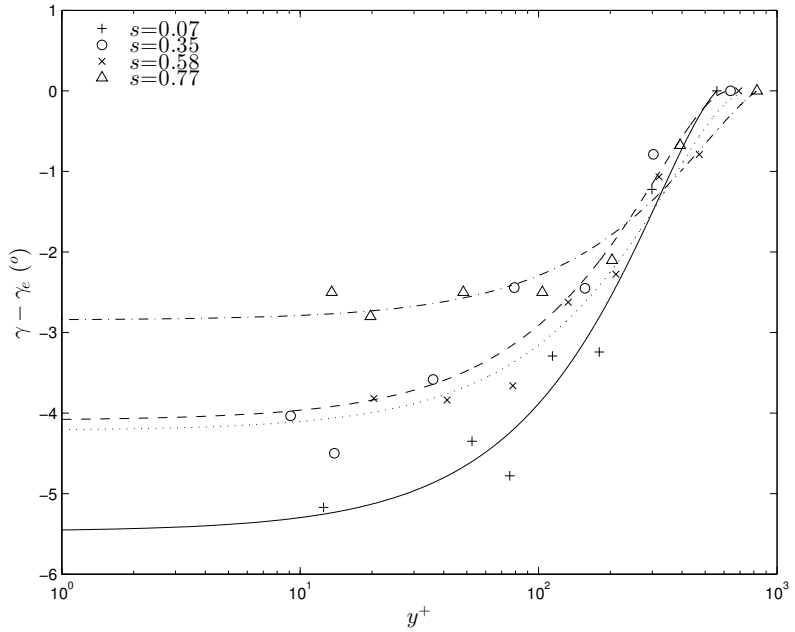

Figure 4.11: Profiles of the mean-flow direction in the turbulent boundary layer (γ) relative to the freestream direction (γ_e) through the Case 1 generator. Curves indicate the direction in which the probe is orientated.

The fluid nearest the wall leads the freestream as expected and it is clear that turning has started upstream of the inlet. After entry, the freestream direction 'catches up' with that near the wall as the levels of skewing reduce slightly through the geometry after the inlet. The error in the measurement method is clearly evident in the figure, but the three-dimensionality in the boundary layer is small and below the 11° of mean-flow skewing which Littell and Eaton (1994) consider to be a significant level of three-dimensionality. The magnitude of the largest surface crossflow measured here is also comparable to the initial measurement stations in other three-dimensional experiments, for example, the upstream 'reference' station of Flack and Johnston (1998), the second station of Schwarz and Bradshaw (1994) and station D in Compton and Eaton (1997). Comparing these experiments, it may be expected that the crossflow component has a negligible impact on the turbulence in the inner layer of Case 1 and minimal effect in the outer layer.

4.3.2 Boundary-Layer Integral Parameters and Quantities

The four non-dimensional boundary-layer parameters most commonly employed to describe favourable pressure gradients are the acceleration parameter (K), the boundary-layer shape factor (H), the momentum thickness Reynolds number (Re_θ), and the coefficient of friction (C_f). In an equilibrium sink-flow turbulent boundary layer, these four parameters are constants with streamwise distance. The acceleration parameter is also constant in the idealised laterally converging duct flow geometry described in §4.1.1 and recreated experimentally by Murphy et al. (1983) and Chambers et al. (1983); though it is unknown whether this type of flow has an equilibrium solution similar to the sink flow. It may be noted that the acceleration parameter is also a type of Reynolds number and is independent of the boundary layer behaviour itself. That this study involves a pressure gradient perturbation on a developed boundary layer, combined with the short contraction length relative to boundary-layer thickness, make it highly unlikely that any equilibrium behaviour will result.

The behaviour of the acceleration parameter was shown above in Figure 4.9 and the streamwise evolution of the remaining parameters is shown in Figure 4.12. For reference, the wall shear stress (τ_w) has been included. The values of these and other pertinent quantities are tabulated for the first measurement station in Table 4.1, along with the results from the zero-pressure-gradient experiments in the previous chapter. The techniques applied to calculate the integral parameters and the wall shear stress in these measurements are the same as those in the previous chapter. Here again, the measurements at the last station were conducted outside the calibration range and so will likely contain errors.

A striking feature of the results is that their streamwise variation remains so small throughout the test region despite the relatively large acceleration. The total contraction length is greater than $100\delta^*(0)$, where $\delta^*(0)$ is the initial displacement thickness. The 'mild' acceleration case in the large-eddy simulation by Piomelli et al.

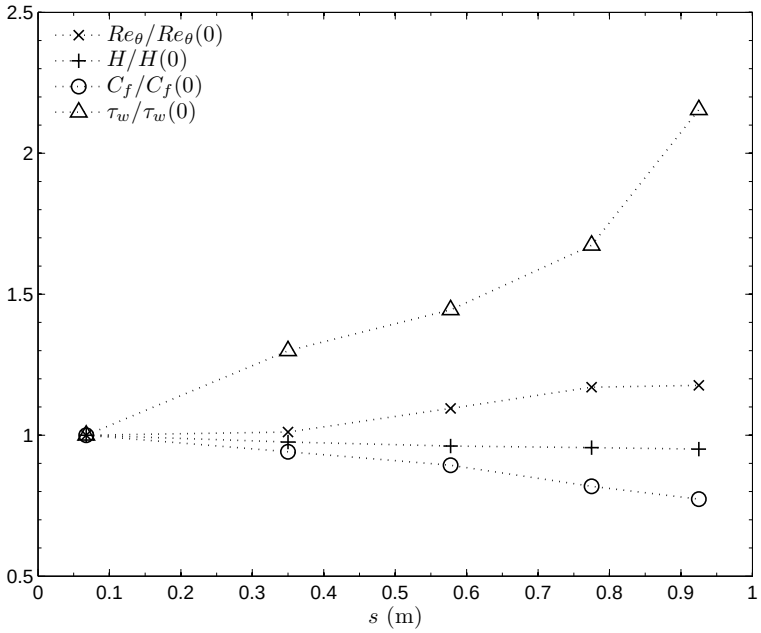

Figure 4.12: The streamwise evolution of the Case 1 mean-flow parameters. Measurements are normalised with the initial values.

Quantity	$\partial P/\partial s = 0$	$\partial P/\partial s < 0$
Q_e (m·s^{-1})	0.122	0.124
Re_θ	1080	923
Re_τ	530	484
H	1.4	1.37
δ_θ (m)	0.0089	0.0074
δ^* (m)	0.0125	0.0102
τ_w (kg·m^{-1}s^{-2})	3.2×10^{-2}	3.37×10^{-2}
C_f	0.0043	0.0049

Table 4.1: The initial flow parameters of the turbulent boundary layer in the favourable pressure gradient compared with the zero-pressure-gradient values.

(2000) appears to be most comparable to the results here in terms of the streamwise behaviour and magnitude of the parameters. Their acceleration parameter took a greater streamwise distance to reach its peak magnitude of $K \approx 2.9 \times 10^{-6}$ however, and their inlet Reynolds number is slightly lower than that used here (see Table A.1 in Appendix A).

Further noteworthy behaviour is the continued rise in the Reynolds number accompanied by a reduction in the coefficient of skin friction. The common response of a turbulent boundary layer to an accelerating perturbation is that, though the Re_θ continues to rise, C_f rises as well (see §2.3.2 also). Later downstream, as the stabilising effects of the acceleration start to dampen the turbulence, Re_θ starts to decline as does C_f. Here however, the Reynolds number continues to increase throughout the geometry even though the acceleration is large and the friction is falling. Some experiments such as the Case 1 test by Fernholz and Warnack (1998) show similar behaviour, but this only lasts while the acceleration is still relatively low, and it is usually followed later downstream by a more typical behaviour pattern.

Boundary-layer relaminarisation is also typified by large reductions in C_f. Relaminarisation is a gradual process whose onset is difficult to define (Bourassa and Thomas, 2009). Further, relaminarisation is distinct from a 'laminarescent' flow as the process during which the turbulent boundary layer is undergoing re-transition back to the two-dimensional state, rather than one whose ability to produce turbulence is being strongly attenuated but increasing nonetheless. Aside from the reduction in friction, the remaining parameters measured here do not strongly support the re-transition hypothesis as again, relaminarisation induced by acceleration is almost universally accompanied by a declining Reynolds number and by much smaller values of the shape factor H. During relaminarisation, H declines downstream and reaches a minimum around the same streamwise location that C_f reaches its peak. Downstream of this location, C_f starts to decline and H increases, as the boundary layer profile reverts back towards a laminar, Falkner-Skan shape. No min-

imum in H is seen here and the smallest value is H_{min}=1.3. Warnack and Fernholz (1998), Piomelli et al. (2000), Blackwelder and Kovasznay (1972), and Bourassa and Thomas (2009) all report values of H <1.3 before the onset of a decline in C_f. The thinning of the boundary layer here is shown in Appendix F, where the streamwise reduction in the boundary layer thickness measures is shown.

The favourable pressure gradient is generated by a lateral convergence of the duct walls, which in channel coordinates appears as $(dU/dx) = (dW/dz)$. This extra strain perturbation may explain some of the behaviour seen here. Though few in number, the results of investigations into the impact of lateral strain perturbations on a turbulent boundary layer show similar patterns to those measured here. McEligot and Eckelmann (2006) generate their favourable pressure gradient using a lateral convergence. Their experiment, however, is a better approximation of the idealised case of a converging duct, because a symmetric contraction should effectively be produced. The development length of their upstream boundary layer before contraction is also very short. A consideration of the lateral strain component here only follows from the idea that the boundary layer is perturbed by the convergence as clearly in the idealised case, the flow is entirely radial towards the sink and there is no spanwise straining.

Streamline convergence was investigated experimentally by Pompeo et al. (1993) and Panchapakesan et al. (1997). They isolated their experiments from streamwise strains by expanding the wall-normal flow area at the same time. Compared to a two-dimensional flow, the convergence was found to increase the rate by which C_f declines. H either increased slightly or 'flattened out'. These two observations correspond somewhat with the behaviour in Figure 4.12 where a C_f reduction was seen, in contradiction to the rising Reynolds number and declining H. The convergence was also found by Pompeo et al. and Panchapakesan et al. to trigger an increase in the growth rate of all three boundary-layer thicknesses. Though Figure F.1 showed that the boundary layer here is contracting, the reduction might

have been more severe otherwise. Neither Pompeo et al. nor Panchapakesan et al. see changes to the logarithmic behaviour of the inner layer, but convergence did appear to augment the wake component of the boundary.

The effects from the convergence appear to work in an opposite manner to a favourable pressure gradient. This is noted by Panchapakesan et al. (1997) who observed that, given their mean velocity results, it would be difficult to tell whether the flow was responding to a lateral convergence or to an adverse pressure gradient. This observation is also made by Coleman et al. (2009) in their numerical investigation of laterally-strained turbulent boundary layers.

4.3.3 Mean-Velocity Results

Profiles of the mean velocity in the mean-flow direction are shown in Figure 4.13 non-dimensionalised in outer units and included in the figure are the results from the zero-pressure-gradient experiment in the previous chapter. Also shown is the velocity profile of the self-similar solution for a laminar boundary layer in a sink-flow, which is described (Schlichting, 1979) by:

$$Q(\eta)/Q_e = 3\tanh^2\left(\frac{\eta}{\sqrt{2}} + 1.146\right) - 2 \tag{4.5}$$

where the similarity variable η is given as

$$\eta = y\sqrt{\frac{Q_e}{-\nu(L-s)}}$$

If the pressure gradient were continued for longer streamwise distances, or if the inlet turbulence in the boundary layer was less 'mature', then the measurement profiles would tend towards something resembling this shape.

The profiles show typical behaviour for a turbulent boundary layer undergoing streamwise acceleration in that the pressure gradient causes a 'thickening' of the viscous region as the profiles become more laminar-like (e.g. Blackwelder and

Kovasznay, 1972). The changes are less pronounced than those in similar rates of acceleration, in agreement with the mean-flow parameters. Figure 4.14 shows the

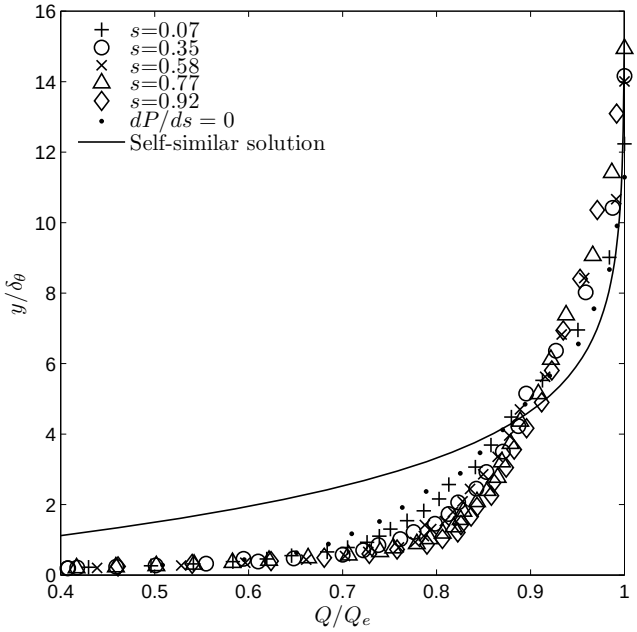

Figure 4.13: Profiles of the mean velocity in the Case 1 boundary layer flow versus streamwise distance. (–) the self-similar solution for a laminar sink-flow boundary layer, given by equation (4.5). A relaminarising boundary layer in a sink flow would tend towards the self-similar shape.

streamwise evolution of the boundary-layer mean velocity non-dimensionalised in inner units. As with Figure 4.13, the zero-pressure-gradient results are included as is the law of the wall. The friction Reynolds number, Re_τ, is also tabulated in the Figure and like Re_θ, continues to increase downstream despite the pressure gradient. Similar to above, the turbulent boundary layer responds in typical fashion to the favourable pressure gradient. As the viscous layer thickens, the profiles are displaced upwards and the onset of logarithmic behaviour occurs at greater wall-normal heights. The wake strength was not calculated, but it does appear that the wake decays in the streamwise direction and the logarithmic layer appears extended. The inner-unit scaled freestream velocity, Q_e^+=Q_e/Q_τ, rises downstream as shown in Figure 4.15, which corresponds with the fall in the coefficient of friction.

A further change in the velocity profiles, familiar to accelerated turbulent

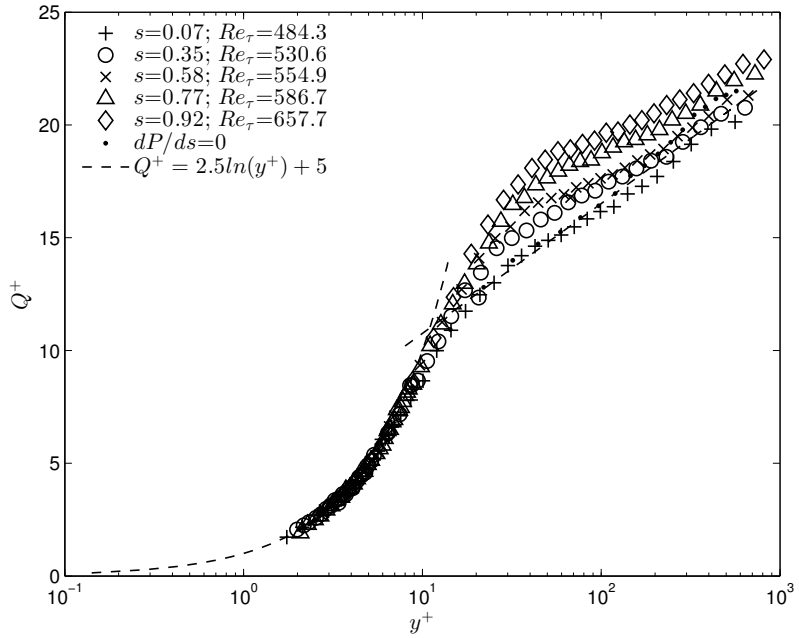

Figure 4.14: Profiles of the inner-unit scaled mean velocity in the boundary layer versus streamwise distance. The 'law-of-the-wall' (−−) and zero-pressure-gradient (···) are also shown.

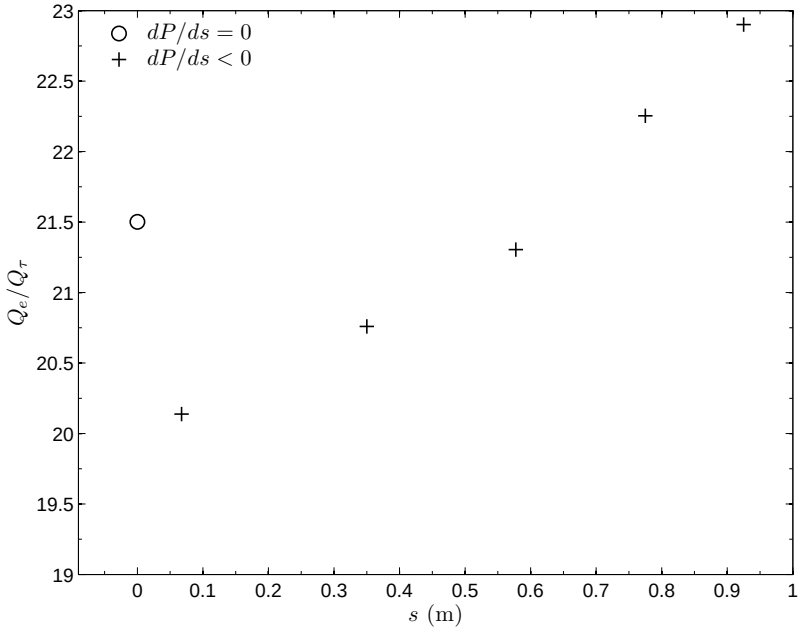

Figure 4.15: The streamwise evolution of the inner-unit scaled Case 1 freestream velocity in the favourable pressure gradient flow.

boundary layers, is the apparent reduction in the gradient of the logarithmic layer. Figure 4.16 shows this streamwise change, where the gradient for each profile was computed by applying the same procedure employed in the previous chapter. The zero-pressure-gradient result, also included in Figure 4.16, is larger than the favourable pressure gradient result at the station furthest upstream. This is likely due to the acceleration, which will begin to have an effect on the turbulence in the boundary layer upstream of the measurement region. A similar example of this can be seen in the results of Bourassa and Thomas (2009) who measured acceleration effects far upstream of their severe linear contraction. The log-law intercept (B) measured for the profiles here rises downstream from 7 to a maximum of 12. For the zero-pressure-gradient case, it is 4.8.

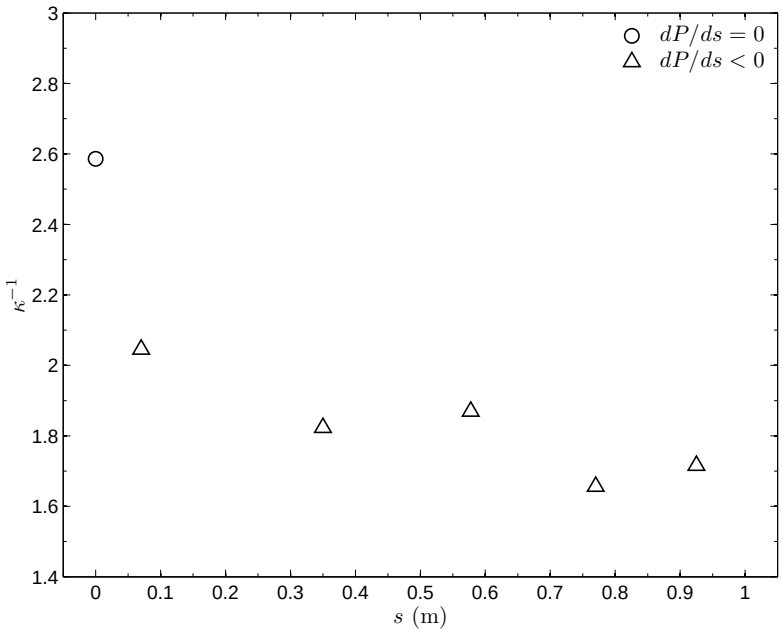

Figure 4.16: The streamwise change of the mean-velocity gradient in the Case 1 turbulent boundary layer (△). The zero-pressure-gradient result (○) is also shown.

These mean velocity results do not purport to significant levels of relaminarisation, which is typically characterised by a complete departure from logarithmic behaviour and large reductions in velocity gradient. Bourassa and Thomas (2009)

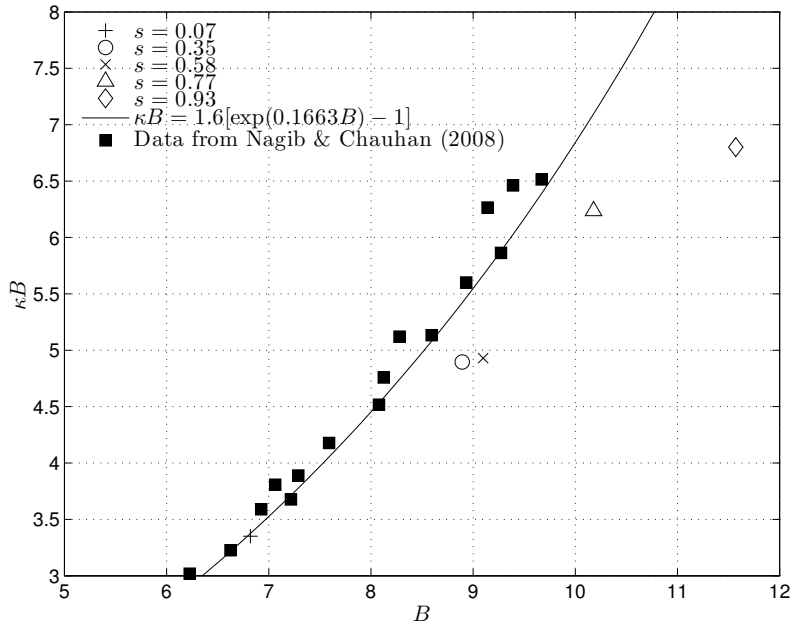

Figure 4.17: The streamwise change of κB in the Case 1 turbulent boundary layer; (–) the solution given by Nagib and Chauhan (2008) and some of their data (■).

investigated the behaviour of κ^{-1} in their contraction, which generated a favourable pressure gradient that was severe enough to induce relaminarisation. Values of κ^{-1} were seen to fall below 0.9 before relaminarisation onset. Both κ and B were both found to correlate with the acceleration and relaminarisation and are not simply arbitrary constants.

The gradual increase in κ suggests that the local eddy length scales, ℓ, increases under a favourable pressure gradient assuming $\ell \approx \kappa y$. This observation, made by Bourassa and Thomas (2009) among others, is based on similar arguments leading to the log-law. Johnstone et al. (2010) test the strengths of three arguments the, log-law among them, used in the treatment of turbulent boundary layers in flows with non-uniform stress. A constant stress layer ($\tau(y) \sim Q_\tau^2$) is a requirement in the derivation of the log-law yet the three arguments tested contradict each other when the stress is non uniform. Using a Couette-Poiseuille flow permits the use of both adverse and favourable pressure gradients as test cases in their DNS

experiments. Though the 'classic' log-law formulation is the 'victor' of the three Johnstone et al. (2010) note that even it is not wholly satisfied, suggesting instead that a pressure-gradient law of the wall be preferred.

The behaviour of κ and B for a variety of wall flow types are also investigated by Nagib and Chauhan (2008), who try to address the wide disagreement in their reported values. Despite showing the dependence of both parameters on the type of flow, pressure gradient and Reynolds number, Nagib and Chauhan (2008) demonstrate that both follow a unique trend regardless of the flow character. This trend, given by $\kappa B = 1.6[\exp(0.1663B) - 1]$, is plotted in Figure 4.17 along with the variation of κB with B for this experiment and some of the favourable pressure gradient data used by Nagib and Chauhan (2008). Though the scatter for all data is large, the exponential trend appears to be followed, except for the last station result.

4.3.4 RMS Velocity and Reynolds Stress

Profiles showing the absolute streamwise changes in the rms velocity in the local mean-flow direction, $\sqrt{\overline{q'^2}}$, are shown in Figure 4.18 along with the zero-pressure-gradient results. Inner units have been used for non-dimensionalisation and $Q_\tau(0)$ is the friction velocity at the first measurement station (s=0.07).

The changes in the rms velocity resulting from the imposition of a favourable pressure gradient vary between observations in the literature. This flow component appears to be particularly fundamental to the development of an accelerating boundary-layer, as it also corresponds strongly with the onset of relaminarisation (Fernholz and Warnack, 1998). Like relaminarisation, the behaviour of the fluctuating velocity seems to depend not only on the magnitude of the pressure gradient, but also the period in which the flow is exposed and the 'maturity' of the turbulence in the initial boundary layer.

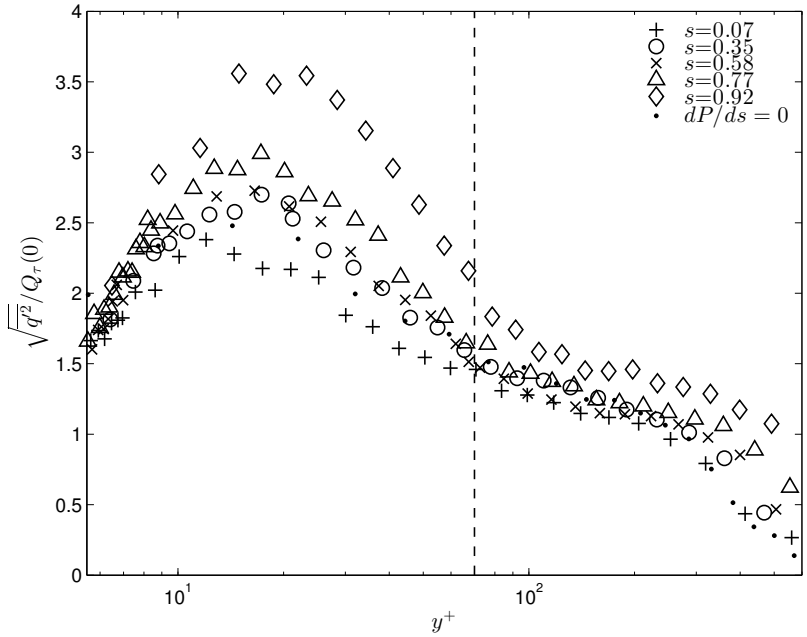

Figure 4.18: Boundary-layer profiles showing the absolute change in the rms of the streamwise velocity in the Case 1 generator. The measurements are scaled by the friction velocity at the initial measurement station ($Q_\tau(0)$). (−−) shows the y^+=70 height referred to in the text.

The absolute changes in the rms velocity generally show the greatest similarities between experiments in the literature. Much of the variation otherwise could be said to arise from the choice and behaviour of the scaling units. Choosing appropriate scales is not always clear for non-equilibrium turbulent boundary layers in general. Figure 4.18 clearly shows that $\sqrt{\overline{q'^2}}$ grows downstream around the peak in the profile that occurs in the near-wall region. Around $y^+\approx$70 (highlighted by the broken line in Figure 4.18) this growth stops and the profiles come close to collapsing downstream. The results for the last measurement station go against this trend, but as with the mean profiles and potential flow, the velocity at this station exceeded the reliable calibration range, so will likely be erroneous. This applies to all measurements presented for this station.

Absolute growth in the fluctuating velocity for the mean flow direction seems to be a universal response of a turbulent boundary layer to a favourable pressure

gradient perturbation (e.g. Bourassa and Thomas, 2009; Fernholz and Warnack, 1998; Piomelli et al., 2000; Warnack and Fernholz, 1998), as the turbulence responds to the rise in the local friction velocity. The behaviour of this velocity statistic in the outer layer differs more between studies, but changes are usually less pronounced than those in the inner layer and will be more dependent on the wall-normal non-dimensionalisation. Initially, Fernholz and Warnack (1998) measured similar behaviour in their Case 1 study to that seen here. At downstream stations however, absolute growth occurred. The relaminarisation Case 2 results in Warnack and Fernholz (1998) behaved in a similar manner in that after an initial absolute reduction, the streamwise rms velocity at downstream stations in the outer layer saw growth reaching ten times the initial value.

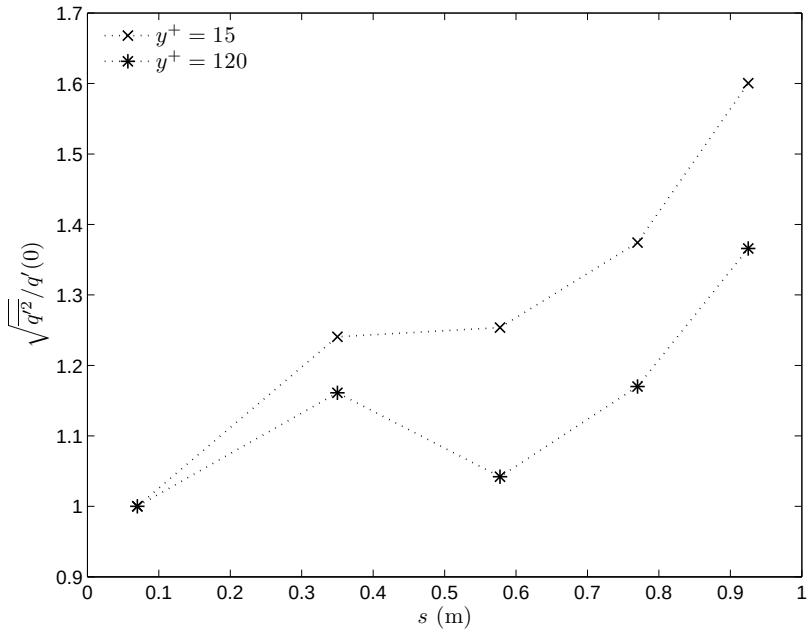

Figure 4.19: Streamwise development of the longitudinal velocity rms at two wall-normal heights in the accelerating boundary layer.

The apparent contradictory behaviour between the inner and outer layers is illustrated in Figure 4.19 where the streamwise development in $\sqrt{\overline{q'^2}}$ is shown at two boundary layer heights. Bourassa and Thomas (2009) suggest that the two

behaviours be separated about a wall normal height of y^+≈150, but this will depend on the Reynolds number and flow history. y^+≈70 seems more appropriate for this experiment. Independence between the inner and outer layers is not unexpected as the turbulence in the boundary layer typically responds this way to a perturbation (Coleman et al., 2009) and can also be seen for more general strains.

The behaviour looks quite different when non-dimensionalised using local inner units as shown in Figure 4.20. The absolute growth in the near-wall region appears to be scaling with the rise in the local friction velocity as shown in Figure 4.20a. The magnitude of the peak value does not change significantly from its zero-pressure-gradient value of $\sqrt{\overline{q'^2}}/Q_\tau$≈2.35. The location of the peak also stays around the equivalent wall-normal height at y^+≈15. In the logarithmic region above y^+≈70 to 80 a decrease is discernible, though this is only slight. At the very top of the boundary layer, above y^+≥250 to 300, the fluctuations decrease.

The values of the near-wall peak in Figure 4.20a are in approximate agreement that measured by Spalart (1986), who also found pressure gradient independence in the near-wall region. Jones et al. (2001) in their sink flow observe similar pressure gradient independence as do McEligot and Eckelmann (2006) in their lateral contraction. These studies approximated equilibrium flows. For the perturbed Case 1 flow in Fernholz and Warnack (1998), the Reynolds streamwise stress (their $\overline{u'^2}/U_\tau^2$) decreases slightly over the whole boundary layer with the near-wall peak value falling from 7 to 5. This is followed downstream by an increase, again over the entire layer and the peak magnitude rises from 5 to 8. For reference, profiles of the stress measured here are shown in Figure 4.20b. Upstream of their contraction, Bourassa and Thomas (2009) measure a similar decrease in $\overline{u'^2}/U_\tau^2$ over most of the layer. The wall-normal location of the peak rises from y^+=15 to y^+=23. Inside their contraction, where the relaminarisation occurs, the profiles show a reasonable collapse and the peak remains at y^+=23. The values are far lower than those measured here though, with their peak value staying around $\overline{u'^2}/U_\tau^2 \approx 3.5$.

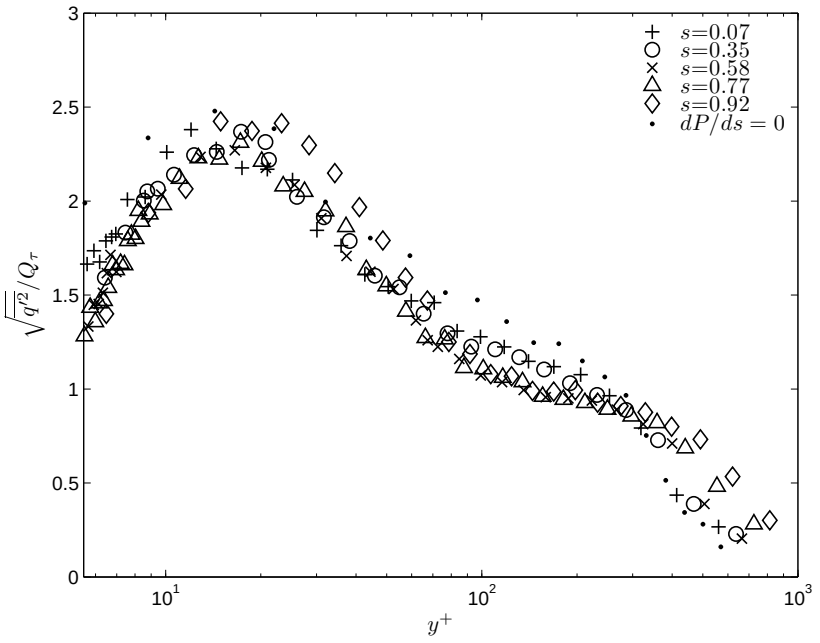

(a)

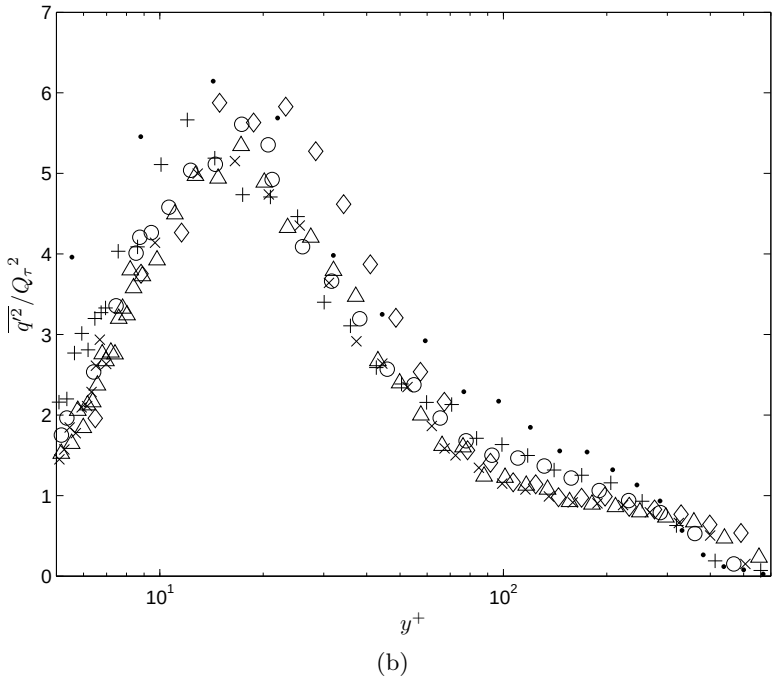

(b)

Figure 4.20: Boundary-layer profiles showing the streamwise evolution of the fluctuating velocity component, q', non-dimensionalised using local inner-units. (a) rms velocity $\sqrt{\overline{q'^2}}/Q_\tau$; (b) Reynolds stress in the local mean-flow direction $\overline{q'^2}/{Q_\tau}^2$. Symbols in (b) are the same as (a).

In summary then, the increase in the surface stress is roughly balanced by the growth in the turbulence in the near-wall region. At greater heights in the boundary layer, above $y^+ \approx 70$, this balance is lost as the turbulence adjusts to the rise in pressure force.

4.3.5 Spectra

The Case 1 velocity spectra are calculated using the same technique applied in §3.6.3. The validity of Taylor's hypothesis in a favourable pressure gradients, however, remains to be confirmed. The Taylor microscale Reynolds number (Re_λ) through the geometry is shown in Figure 4.21. For the first four stations, the Reynolds number behaves in a similar manner to the rms velocity; remaining approximately constant over a portion of the inner layer down to $y^+ \approx 70$, below which it increases as the boundary layer progresses downstream. The Reynolds numbers for the last station are greater with the peak near the wall (not shown) reaching a magnitude of around Re_λ=800.

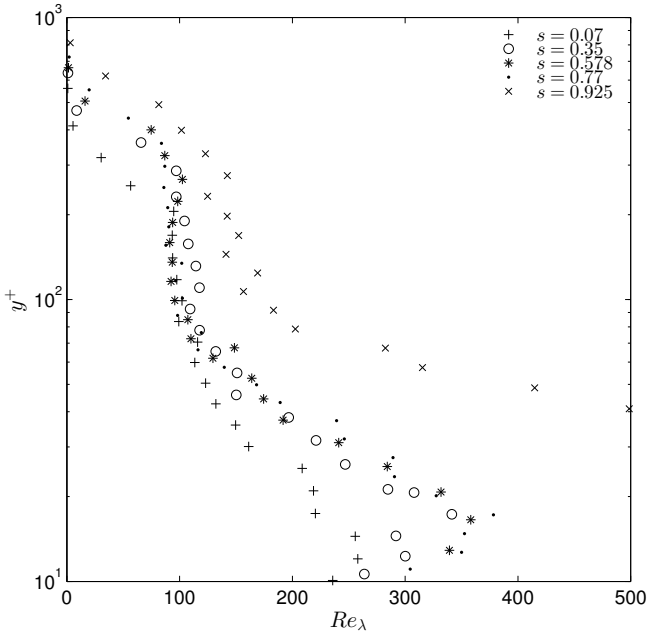

Figure 4.21: The Taylor microscale Reynolds number in the favourable pressure gradient boundary layer

The streamwise change in spectra are shown in Figure 4.22 for a location in the boundary layer where the Reynolds number remains approximately constant ($y^+ \approx 100$). The scatter in the measurements at lower wavenumbers makes possible $E \sim k_s^{5/3}$ scaling behaviour difficult to discern. The higher wavenumber range appears to collapse with streamwise distance. Warnack and Fernholz (1998) found that the spectra in their mild Case 1 experiment corresponded with that in a zero-pressure-gradient boundary layer. During periods of relaminarisation, their stronger Case 2 spectra did not collapse for any wavenumbers. This period also sees a large increase in the streamwise integral length scale Λ_x (local mean velocity U multiplied by the integral of the autocorrelation function $\rho(\tau)$) across the layer, which is not seen here.

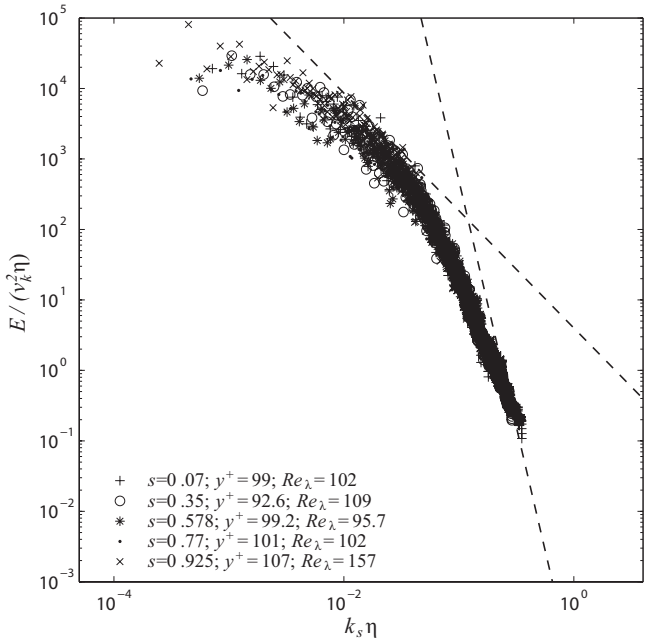

Figure 4.22: The Taylor microscale Reynolds number in the favourable pressure gradient boundary layer. Dashed lines indicate $k^{5/3}$ and k^{-7} scaling behaviour.

4.3.6 Velocity Moments and Probability Density Functions

The higher moments of skewness (S_q) and kurtosis (K_q), were described in the previous chapter. Profiles showing the streamwise evolution of the velocity moments through the generator are shown in Figure 4.23 and Figure 4.24. The results from the zero-pressure-gradient experiment are also plotted in each. The scatter in the data is high and the variations slight, but some observations can be made. In a similar manner to the rms velocity, the boundary layer is roughly divisible into two to three regions which respond differently to the favourable pressure gradient. Lines have been added to the profiles, dividing the boundary layer into these regions for illustration. The region nearest the wall, $y^+ \leq 30$, is described by McEligot and Eckelmann (2006) as the 'viscous layers'; that is, the part of the boundary layer where viscous effects are significant. That definition is used here also. A central region is also shown, which falls approximately between $30 \leq y^+ \leq 150$. An outer region extends for the remainder of the boundary layer height.

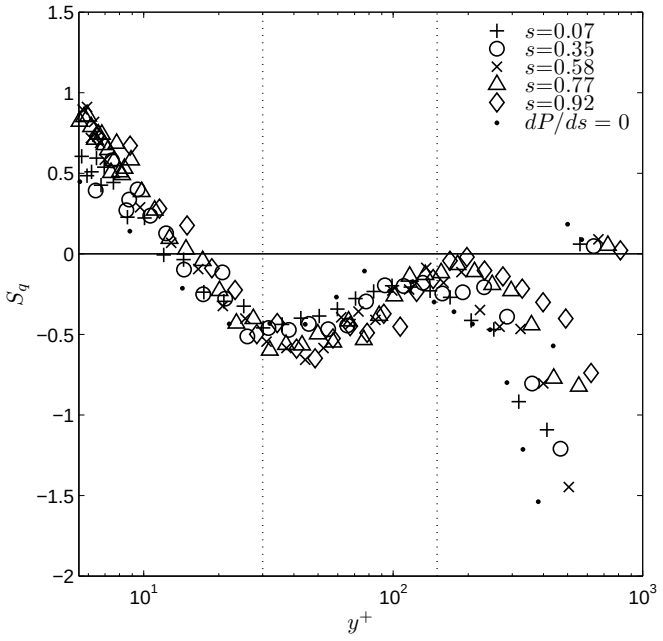

Figure 4.23: Case 1 boundary-layer profiles showing the streamwise evolution of the longitudinal velocity skewness. Gaussian skewness (—) and the zero-pressure-gradient result (·) are shown for comparison.

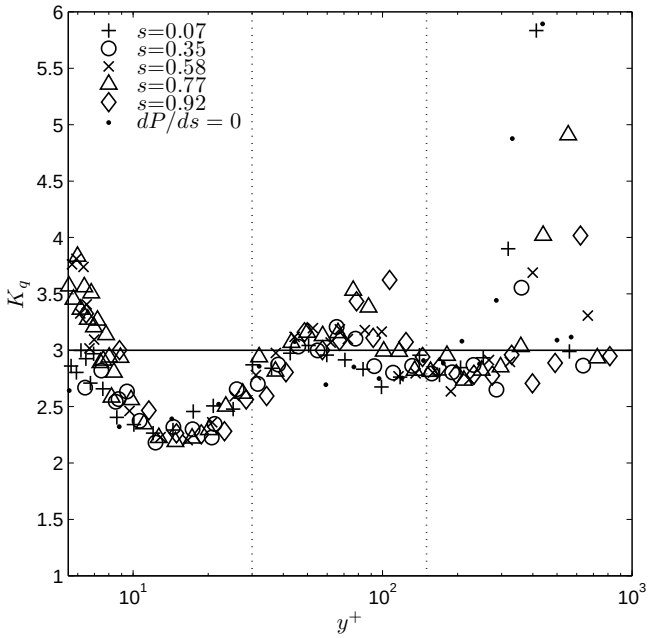

Figure 4.24: Case 1 boundary-layer profiles showing the streamwise evolution of the longitudinal velocity kurtosis. (—) Gaussian kurtosis and the zero-pressure-gradient result (·) are shown for comparison.

Below y^+<10 in the viscous layer, K_q rises downstream, increasing by almost 45% above the zero-pressure-gradient value. S_q appears to double around the same location. McEligot and Eckelmann (2006) found little change to the streamwise higher moments in the viscous layers. They did detect a slight increase near the wall, though not nearly as pronounced as the results here, and a slight decrease above y^+>20. Fernholz and Warnack (1998) measured higher moments of streamwise velocity in all four of their Cases, using both a traversing hot-wire probe and wall-mounted film probe. For the viscous layer, their traversing probe measurements in Cases 1 and 3 show an independence of these moments from pressure gradient effects. Their wall-mounted probe measurements however, suggest that in the lower Reynolds number Case 1 experiment, the region of acceleration induces an increase of 30% in both statistics. In their Case 2 experiment, the strong pressure gradient, combined with low Reynolds number, induce substantial changes in the moments in the viscous layers, with S_q more than doubling downstream and K_q increasing

fourfold. In the viscous region then, the turbulence continues to grow despite the strong favourable pressure gradient, however it is being increasingly dominated by large amplitude positive q' fluctuations.

To further elucidate the change in moments, Figure 4.25 shows the effects of the pressure gradient on the probability density distributions of q' located in the viscous region of the boundary layer at $y^+ \approx 9$. Figure 4.25a shows the q' distribution measured at an upstream station (s=0.07 m) of the generator geometry and Figure 4.25b shows the result at a downstream station (s=0.77 m). The zero-pressure-gradient results are included for comparison. For each, the equivalent Gaussian distribution is shown with the same mean and standard deviation as the data. As was noted in the previous chapter, the streamwise velocity distribution in this region shares the distinctive log-normal shape as the viscous layer low-speed streak spacing. The increase in skewness can be seen as a lengthening of the right tail of the distribution as the amplitude of these positive fluctuations increases. The rise in kurtosis appears as a rise in the markers, just to the left of the distribution peak, further above the Gaussian lines. These results along with those above suggest that the favourable pressure gradient causes an increase in the amplitude of positive q' for $y^+ < 10$.

Above the viscous layers in the central region, S_q decreases steadily through the generator and K_q rises. The scatter in the kurtosis measurements is high, but the values recorded for the stations furthest downstream clearly lie above the Gaussian K=3 dividing line. In a similar manner to Figure 4.25, Figure 4.26 shows the q' probability density distribution, for a location in this central region at $y^+ \approx 60$. The increase in the kurtosis is revealed by a rise around the peak of the distribution and a reduction elsewhere; the distribution becomes 'sharper'. The peak value of the Gaussian distribution increases from 0.27 to 0.31. It may also be observed that for $sgn(q')(q'/Q_\tau)^2 < -10$ on the far left, more of the markers sit above the Gaussian line.

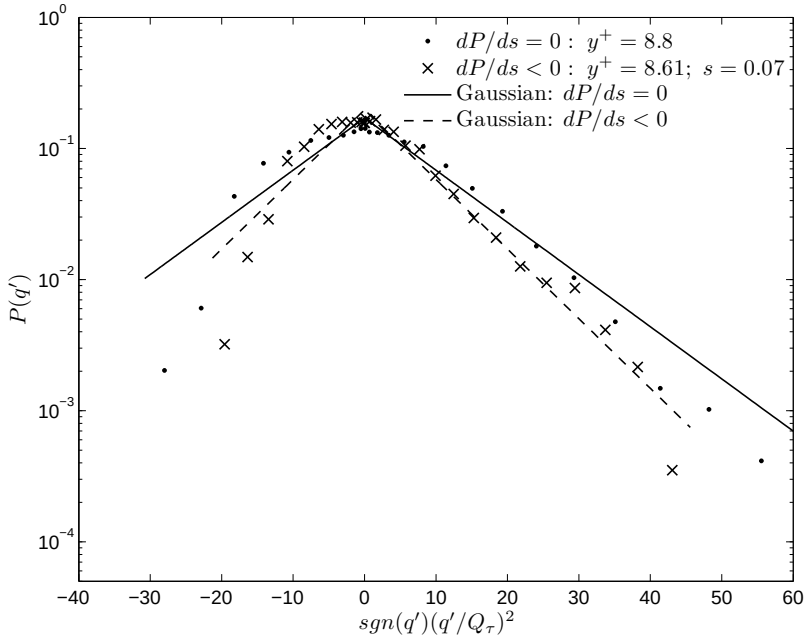

(a)

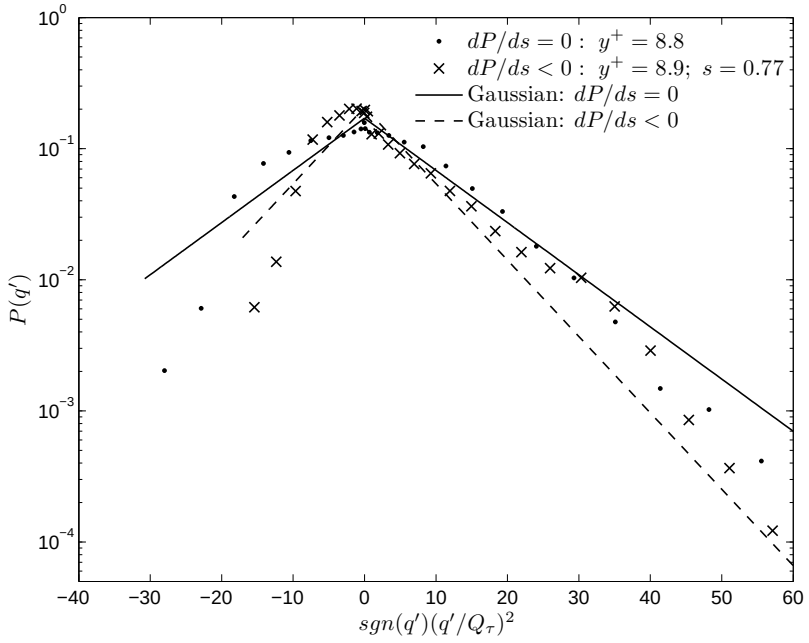

(b)

Figure 4.25: Probability density functions of Case 1 q' measurements at y^+≈9: (a) upstream station (s=0.07 m); (b) downstream station (s=0.77 m). The Gaussian distributions (—, −−) have the same mean and spread as the data.

A decrease in the skewness indicates that the flow is increasingly permeated by infrequent negative velocity fluctuations. A rise in the kurtosis indicates that these negative velocity fluctuations have a relatively large amplitude. Figure 4.20 showed a decrease in the mean magnitude of q' which, combined with the moments measurements, suggests that the pressure gradient induces a more quiescent region of flow overall, yet large scale negative velocity fluctuations remain. In the central region of all their test cases, Fernholz and Warnack (1998) also saw a rise in their K_q measurements and decreases in S_q caused by the pressure gradient.

Above the central region, an interpretation of the results becomes confused because choosing wall units to non-dimensionalise the wall-normal location in the outer region may be inappropriate; especially in light of the independence between the behaviour of the layers seen in the previously. The skewness, however, appears to increase downstream towards a more symmetric distribution suggesting a decrease in large, infrequent, negative q'. A sharp peak near the edge of the boundary layer dominates the kurtosis profiles. This peak, along with the negative skewness, is a product of intermittency at the edge of the boundary layer as large velocity fluctuations penetrate into the non-turbulent freestream. A reduction in intermittency suggests that the fluid in the outer reaches of the boundary layer is being disturbed less by the turbulence from lower (hence negative q') boundary layer heights.

4.4 Viscous Layer Low-Speed Streak Spacing

The spanwise spacing of the low-speed streaks was measured in the Case 1 geometry at s=0.77 m. The last measurement station was not used as the velocity results had a higher uncertainty and were also closest to the exit of the generator. The old visualisation arrangement was removed from inside the test region and discarded and another set up at the new location. The setup was rotated slightly so that it was orientated with the local freestream direction.

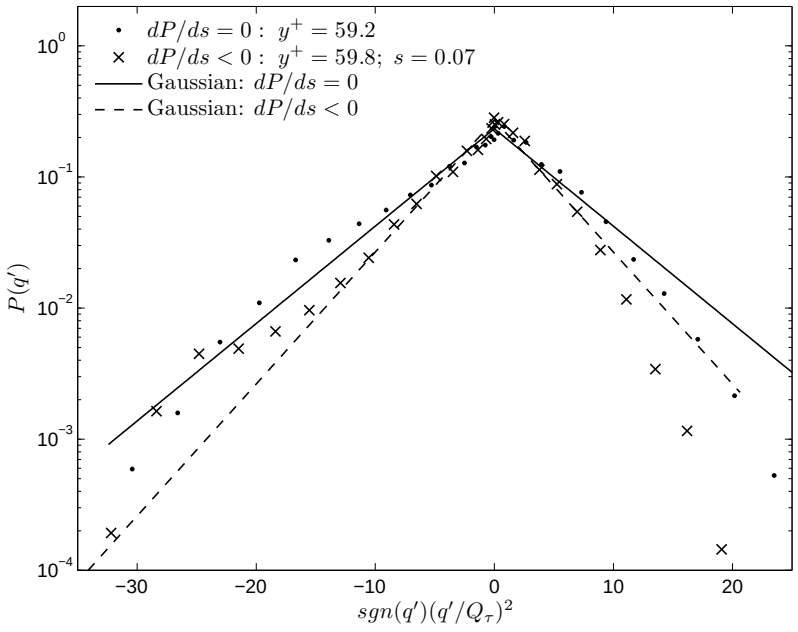

(a)

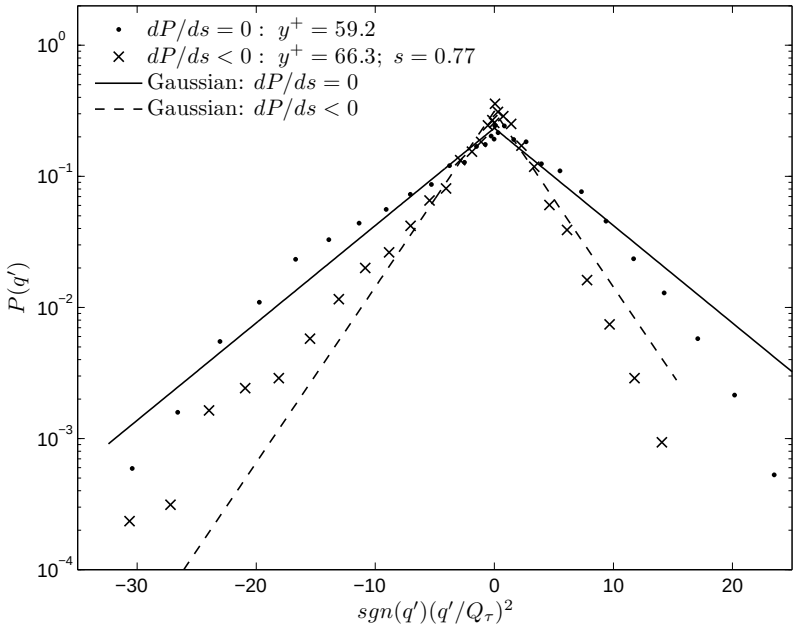

(b)

Figure 4.26: Probability density functions of Case 1 q' measurements at y^+≈60: (a) upstream station (s=0.07 m); (b) downstream station (s=0.77 m). The Gaussian distributions (—, – –) have the same mean and spread as the data.

4.4.1 Visualisation Method

The spacing measurement procedure developed in the previous chapter is reapplied here also with some modifications, most of which were a result of the effects from the pressure gradient. In order to position the wire and shims robustly, the measurement station and required wire positions were located using the traverse. The distance between the shims was increased slightly to 280 mm as it was felt the previous shim distance was slightly too restrictive, that is, their positions were very close to the interrogation window in the images.

An effect of the acceleration is that the inner length scale, $l^+ = \nu/Q_\tau$, at this downstream location is smaller than that in the zero-pressure-gradient case. For that case, the typical viscous length scale was of the order of $l^+ \approx 0.17$ mm and at this measurement station in the geometry, $l^+ \approx 0.11$ mm. The immediate consequences of this are to increase the non-dimensional diameter of the platinum wire and the height of the 45° mirror that reflects the laser sheet onto the bubbles. The wire remains well within the laminar regime and the mirror height becomes $y^+ \approx 45$. The change in scale also means, however, that the mirror is located further downstream of the wires.

Approximately the same physical dimensions of the image interrogation window were used for the streak spacing calculation as the zero-pressure-gradient case and the reduction in the inner-units means the effective interrogation window size is longer and larger ($\Delta x^+ \approx 462$; $\Delta z^+ \approx 1200$). As was carried out previously, a reference grid, printed on transparent, overhead projector paper was photographed under the new setup, allowing a translation from pixels to meters. Two wire heights were used and in a similar manner to the zero-pressure-gradient case, their heights were measured and checked using the micrometer depth gauge. In the previous chapter, wire heights of $y^+ \approx 4$ and $y^+ \approx 8$ were used for visualisation. The resultant wire heights were $y^+ \approx 2$ and $y^+ \approx 5$.

Moving the camera and light sheet optics from the zero-pressure-gradient location was made easier thanks to the three-axis traverse that was fixed under the test region, and the rotating stage of the laser sheet optics allowed the sheet to be rotated onto the new mirror position. The same Nikon camera and settings were used and consequently, the non-dimensional time between each image capture increases. The independence between images may not be anticipated to get larger however, because, as was found by Bourassa and Thomas (2009) and Fernholz and Warnack (1998), the streamwise macroscale (streamwise integral time) near-the wall increases as a result of the streamwise straining. A consequence, according to their measurements, is that the flow structures in the boundary layer undergo 'dilation', or stretching, in the streamwise direction.

Figure 4.27 is an image obtained during the visualisation, showing the image interrogation window, streaks and wires. The window in each image was shifted slightly downstream compared with the zero-pressure-gradient method, as a consequence of the different appearance to the streaks under the favourable pressure gradient. No other changes to the image processing or analysis methods were made.

4.4.2 Visualisation Results

Comparing the image results obtained for each wire elevation, those using the lower wire appeared dimmer and fewer bubbles were evident, suggesting a problem with the light sheet or platinum wire setup. As a result, the analysis is only performed for the upper wire results, which appear brighter and the streaks more visible. The wire is also at a more comparable height to the results in the previous chapter.

A few samples of streak images obtained are shown in Figure 4.28 along with a sample from the zero-pressure-gradient visualisation. Streak 'bursting' is still evident though the streaks are far less active compared to the unaccelerated case (also shown). A scale is marked by a Δ indicates a distance of 100 wall units. Using

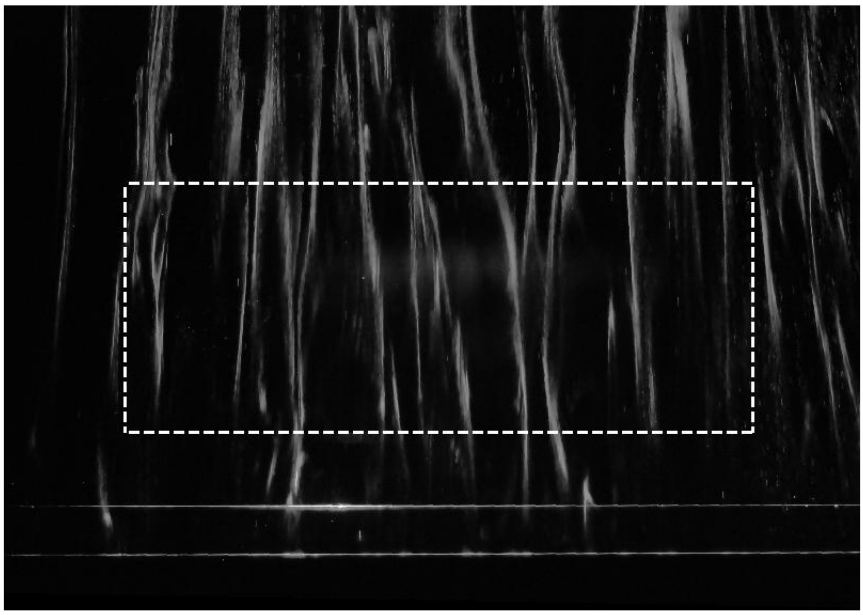

Figure 4.27: An example photograph of the streak visualisation plane showing the platinum wires, low-speed streaks and measurement window (−−). The width of the interrogation window is $\Delta z^+ \approx 1200$. The flow direction is up the page.

this scale, the lengths of the accelerated streaks can be inferred to extend for greater non-dimensional lengths upstream. The acceleration results are shown in Figure 4.29 as a histogram with a log-normal probability function fit to the data. The log-normal function again passed the Kolmogorov-Smirnov goodness of fit test showing that it still provides an appropriate description of the low-speed streak spanwise spacing. The first four statistical moments are given in the figure showing that the mean streak spacing increases by 41% from the typical zero-pressure-gradient value of $\bar{\lambda}^+$=100. The other three moments also show marginal differences.

That a streamwise acceleration triggers an increase in streak spacing has been known since Schraub and Kline (1965), who conducted a similar experiment to that here. They found streak spacing to be largely independent of the pressure gradient within the range $-2\times10^{-6}<K<1\times10^{-6}$. The mean streak spacing rose to $\bar{\lambda}^+$=180 for $K=3\times10^{-6}$ and up to $\bar{\lambda}^+$=240 for $K\approx4\times10^{-6}$. Spalart (1986) saw streak-free spots appearing in a DNS of a sink flow at $K=3\times10^{-6}$ and these had a higher local spanwise streak spacing. Talamelli (2002), in their relaminarisation study, measured $\bar{\lambda}^+$=270 at $K=3.1\times10^{-6}$.

For their highest acceleration range, Kline and Scraub (1967) showed that 'quiescent' or laminar-like regions of bubbles begin to appear and streaks become more fixed in space, i.e. 'wiggling' less. The images in Figure 4.28 clearly show streak bursting is still present in this turbulent boundary layer. In agreement with the observations of Bourassa and Thomas (2009), Piomelli et al. (2000) and others, the streaks appear longer and straighter, extending out of the actual images themselves. This also confirms that the streamwise strain causes a dilation of the near-wall structures downstream.

4.5 Chapter Summary

The experimental results of this chapter were obtained from tests conducted on a turbulent boundary layer perturbed by a strong streamwise favourable pressure

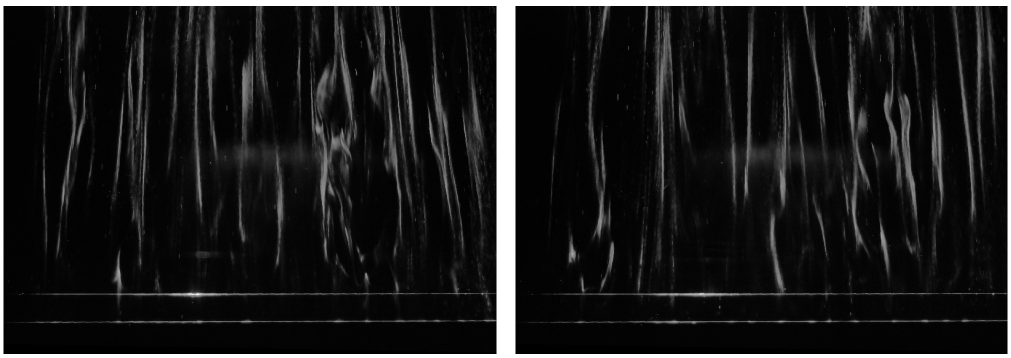

(a) (b)

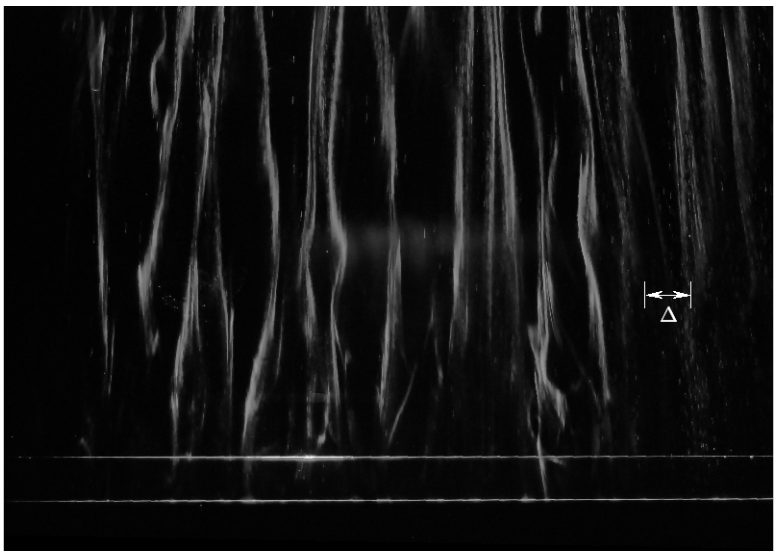

(c)

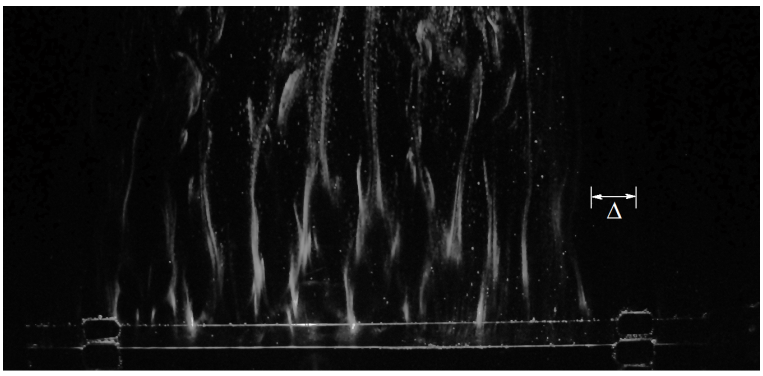

(d)

Figure 4.28: Some example images of the low-speed streaks in a favourable pressure gradient: the accelerated streaks (a)-(c); the streaks in a zero-pressure-gradient flow (d). A scale is marked in (c) and (d) by (Δ symbol) indicating a length of 100 wall units. The flow direction is up the page. The streaks in (a)-(c) can be seen to be longer than those in (d). Streak bursting is still evident in the accelerating boundary layer.

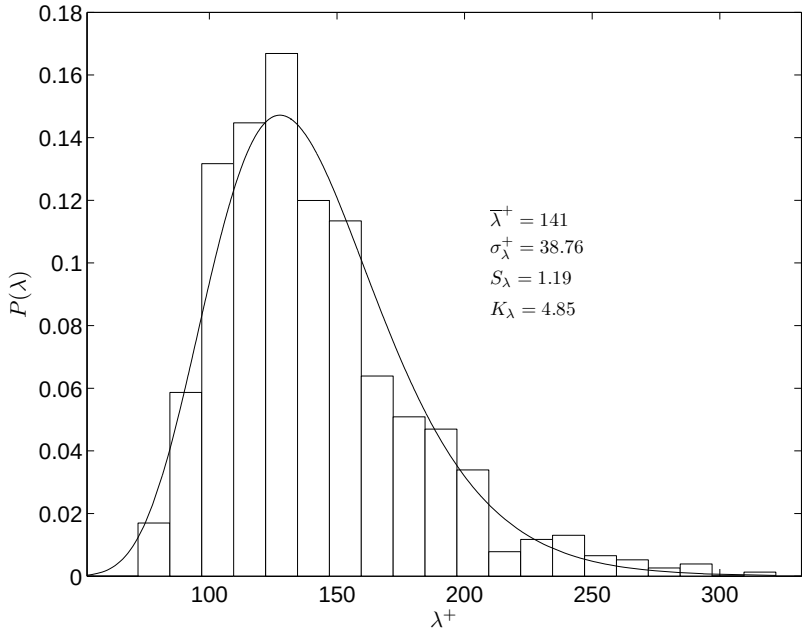

Figure 4.29: Streak visualisation results for the favourable pressure gradient generator (histogram) and a log-normal probability density function fitted to the data (— curve).

gradient, generated using the non-canonical method of a lateral convergence of the channel walls. The results therefore furnish the existing empirical record for similar flows, which is relatively sparse compared to other types of turbulent boundary layer perturbations.

The specific design and implementation of the pressure gradient generator was described in §4.1. The acceleration of the flow was made large K=3.2×10^{-6} and in the idealised case, the geometry generates a sink-flow behaviour of the freestream velocity. The resulting potential flow (§4.2) was obtained from hot-film probe measurements of the velocity (§4.2.1) and the flow angle (§4.2.2). After a brief period near the inlet, the freestream flow over the test region approximated the idealised case surprisingly well.

The streamwise evolution of the boundary-layer velocity was measured using the hot-film probe and the results are shown in §4.3. The development of the mean-flow parameters, given in §4.3.2, bears a striking resemblance to that seen

for turbulent boundary layers perturbed by general lateral strains. The profiles of the mean velocity presented in §4.3.3 show a gradual decline of the mean-velocity gradient and a rise of the velocity intercept. The variation of the corresponding log-law parameters κ and B agrees with the empirical relationship given by Nagib and Chauhan (2008), providing evidence of its applicability in boundary layers accelerated by a lateral convergence.

The turbulence in the boundary layer develops a dual-layered structure, as shown in §4.3.4, with growth seen near the wall and decay elsewhere. The higher velocity moments, provided in §4.3.6, reveal that the flow near the wall is increasingly dominated by large amplitude, positive velocity fluctuations. This is consistent with the measured increase of the spanwise space between near-wall low-speed streaks in §4.4.2, because the fluid between the streaks would be mainly at or above the local mean velocity. §4.4.1 details the measurement of streak spacing using the hydrogen bubble visualisation method.

The acceleration causes the streamwise lengths of the low-speed streaks to extend and their behaviour becomes 'calmer', with less evidence of streak 'wiggling' or bursting. This again corresponds with the velocity moments, which show that at greater heights in the boundary layer the flow becomes more quiescent overall, but with strong negative velocity fluctuations remaining. As ejections too have negative streamwise velocity, it may be concluded with Bourassa and Thomas (2009) that reduced streak activity results in fewer 'lifted' or ejected streaks.

Chapter 5

Case 2: Spanwise Pressure Gradient Experiments

The previous chapter investigated a turbulent boundary layer perturbed by a strong streamwise pressure gradient (Case 1). In this chapter, the investigation is repeated with an additional spanwise pressure gradient superimposed with the original favouable streamwise component. This experiment is referred to here and throughout as Case 2.

In this chapter, §5.1 and §5.2 follow an identical outline and scope to §4.1 and §4.2, with §5.1 describing the design and construction of the Case 2 pressure gradient generator, and §5.2 presenting the potential flow produced by it over the testing area. For the remainder of the chapter the presentation of information in each section changes to enable a comparison between the two cases. The structure remains the same however, with §5.3 presenting the hot-film measurement data obtained in the turbulent boundary layer and §5.4 discussing the behaviour of the viscous sublayer streaks.

5.1 Case 2 Generator Design and Implementation

The addition of a spanwise pressure gradient complicates the Case 2 generator design compared to the single component case and the practical implementation becomes far more demanding. Noted previously, the design of the Case 1 geometry originated and was derived from the generator developed in this chapter, and can be viewed as a simplified or particular form of its design. This is the main reason for the non-canonical way in which the streamwise acceleration was created and the peculiar orientation of the experimental geometry in the flow channel. Many of the Case 1 design parameters given in the previous chapter were also decided by the Case 2 values presented here.

5.1.1 Design

Previous experimental investigations of three-dimensional turbulent boundary layers in which pressure is the driving force behind the streamwise vorticity, have been hampered by uneven pressure gradients spanning across and along the particular flow region investigated. The constant area ducts of Flack and Johnston (1998) and Schwarz and Bradshaw (1994) for example, have different streamwise accelerations on either side of the channel which, despite being small, Coleman et al. (2000) found to be significant. In blockage experiments such as Compton and Eaton (1997), the spanwise pressure gradient (and streamwise) differs across the width of the flow. Overcoming these problems is difficult if not impossible, especially when the aim is to investigate large area statistics such as the spanwise spacing of the viscous sublayer low-speed streaks. The approach here aims to overcome some of the drawbacks in such a way that large-area statistics can be measured.

Principally, by controlling the curvature of the flow channel walls, the curvature of the streamlines and hence the spanwise pressure gradient can be controlled within the test region. To keep the pressure gradients the same over a large area, the

same curvature has to be used on both sides of the channel. This results in a streamwise pressure gradient. By using a laterally converging sink-flow for this streamwise component, the same curvature can be applied on both sides of the channel without affecting the streamwise component behaviour, thereby allowing the strength of the spanwise pressure gradient to be controlled in a relatively independent way. This approach is a variation of swept-wing designs, but now the streamlines of the oncoming flow are radial around a downstream sink point rather than parallel.

Further, by increasing the curvature of the channel walls in the streamwise direction, the ratio of the two pressure gradients can be kept constant in both streamwise and spanwise directions over the whole area. The result, in the idealised case where the inlet is an infinite distance upstream of the sink, is that with respect to the same streamwise distance along all streamlines, the flow histories and Reynolds numbers are the same, and the ratio of streamwise to spanwise pressure gradient strengths is constant. Large spatial lengths are thus obtained over which statistics such as the streak spacing can be measured.

In Chapter 4 the streamwise pressure gradient component in the laterally converging duct was established to increase in proportion to the radial distance $(L-s)$ from the sink point. This follows from a simple consideration of the geometry and continuity. The flow area is curved, and the curvature is defined by:

$$c_1(s) = \frac{1}{L-s}$$

From the discussion above, the spanwise pressure gradient can be kept proportional to the streamwise by controlling the curvature of the streamlines (c_2) so that:

$$c_2(s) = \beta c_1$$

where β is a constant. The external flow that results is a free-spiral-vortex; that is, the superposition of a free vortex and a sink flow. β determines the ratio between

the sink and vortex strengths. Further, a sweep angle Λ may be defined as:

$$\Lambda = \tan^{-1} \beta$$

and describes how the flow has been turned out of the radial direction towards the sink point. This parameter relates the Case 2 flow to swept wing designs, such as those from Baskaran et al. (1990) and Bradshaw and Pontikos (1985), where Λ defines the angle made by the 'wing' to the direction of the oncoming flow. A main difference between the design here and a swept wing is that the lines of constant pressure over a wing (known as 'generators' in wing nomenclature) are straight and parallel with the leading edge whereas here they are curved. One of the advantages in the design developed here is that the three-dimensionality is being constantly driven into the boundary layer by the pressure gradient. Over a swept wing, Λ tends to zero with streamwise distance.

The flow used here is also related to rotating disk turbulent boundary layers, such as that investigated by Littell and Eaton (1994). Rotating disk flows have no streamwise pressure gradient component, but generate a simple effective spanwise pressure gradient: $-\rho\Omega_{disk}^2 r$, where r is the radial distance from the centre of the disk, and Ω_{disk} is the disk angular velocity. Littell and Eaton (1994) find mean-flow self-similarity on their rotating disk, indicated by a constant Clauser parameter, G (§3.6.1). Degani et al. (1993), discuss self-similar solutions for three-dimensional turbulent boundary layers. The free-spiral-vortex type appears to satisfy their conditions for the external flow patterns that result in boundary layer self-similarity at high Reynolds number. The free-spiral-vortex type of flow may therefore result in self-similar behaviour which seems appropriate, given that it is the superposition of a sink flow and rotating disk, both of which result in self-similar behaviour.

From a consideration of the geometry, it follows that the freestream velocity as a function of the radial (i.e. straight line) distance from the sink point R, behaves

according to:

$$Q_e(R) = \cos(\Lambda) Q_e(0) L R^{-1} \tag{5.1}$$

where $Q_e(0)$ and L were defined in §4.1.1. The flow is no longer purely radial, but instead makes an angle of Λ with the radial direction. The total streamwise distance that the flow traverses between inlet and sink point is therefore greater and the local radial distance to the sink is defined by:

$$R(s) = \frac{(L - s)}{\sqrt{1 + \tan^2 \Lambda}}$$

When this is substituted into equation 5.1 the streamwise velocity, $Q_e(s)$, can be written as:

$$Q_e(s) = Q_e(0) L (L - s)^{-1}$$

which is identical to Case 1 (equation 4.1). The streamwise pressure gradient is also identical to Case 1 (equation 4.4) and the pressure gradient in the orthogonal direction n to s behaves according to:

$$\frac{1}{\rho} \frac{\partial P}{\partial n} = -c_2 Q_e^2 = -\beta c_1 Q_e^2$$

To illustrate the types of flows being considered, Figure 5.1 displays an example coordinate 'mesh' showing a section of flow in a free-spiral-vortex. Shown in the figure are the streamlines (s-axis) and spanlines (n-axis) and lines equidistant from the sink point. These lines are equivalent to the wing generator lines defined above and along each, the pressure and velocity magnitude are the same. The sweep angle is revealed by the difference between the n-axis and the generators. In the Case 1 design there is no difference and the two are aligned. The pressure indicated by each generator line decreases towards the sink point. The spanwise axis spans multiple generator lines illustrating the spanwise pressure gradient.

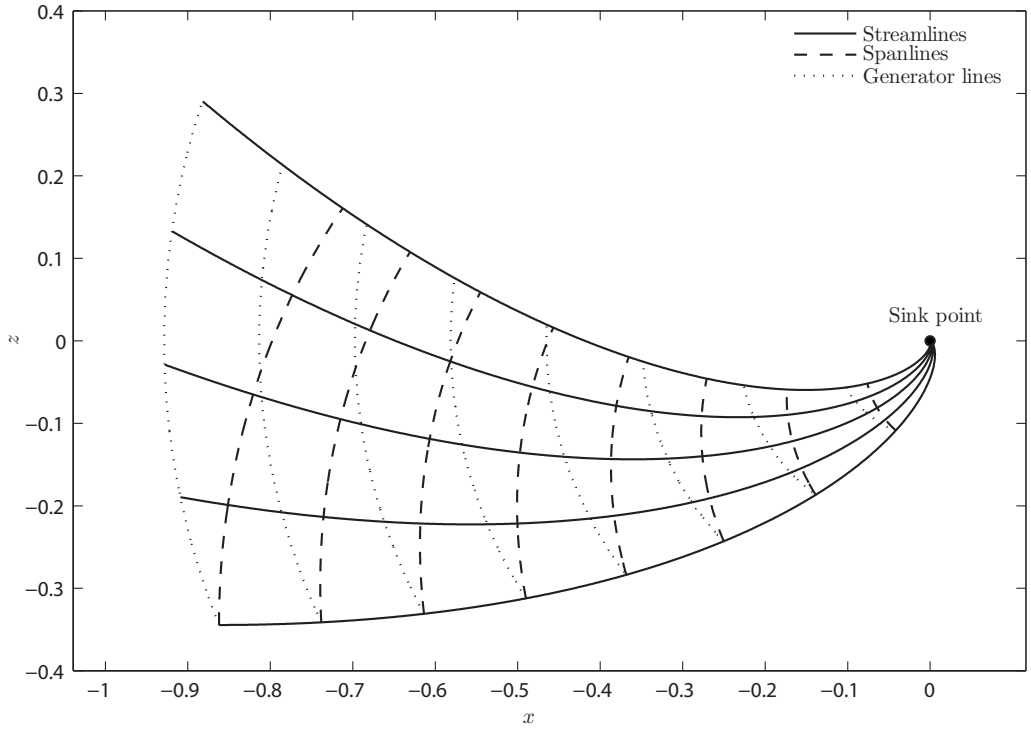

Figure 5.1: An example section of flow in a free-spiral-vortex with the sink (or source) point located at: x=0, z=0. The sink point 'consumes' the flow, hence flow direction is towards the sink and as the point is approached, the velocity magnitude tends to infinity. A streamline, curvilinear coordinate system also shown. (For illustration purposes: $ds \neq dn$)

5.1.2 Parameter Selection and Final Shape

The desired freestream flow in this experiment was outlined in §2.4, where a freestream deflection of $\gamma_e \approx 10^\circ$ and streamwise acceleration of $K \approx 3\times10^{-6}$ were specified. The final shape and size of the geometry is defined by the two parameters: β and L. Maximising β will yield the greatest freestream deflection and three-dimensionality in the boundary layer; which is clearly an advantage to the comparison study here as the differences to Case 1 will be easier to distinguish. The perturbed nature of the investigation however, means that the oncoming flow from the channel must be turned into the generator geometry. This was also seen for Case 1 and results in an initial spanwise pressure gradient at the inlet. In the designs here, this initial pressure gradient is in the opposite direction to that produced by the test gradient generator. In a similar way, a larger β makes the angle at the interface between the generator and the channel wall greater (seen at z=1 in Case 1); resulting in larger disturbances to the flow around this point.

The parameter L which defines the total streamwise distance from the inlet to the 'sink' point has the opposite effect of the parameter β. A large L reduces the angle between the channel and streamlines at the generator inlet, but increases the overall length of the generator shape. It will therefore reduce the freestream deflection and growth rate of the boundary layer three-dimensionality, as the streamline curvature takes a longer distance to reach a particular magnitude. In addition to these factors, there are physical limits placed on the maximum allowable size resulting from the manufacture and fitting of the test generator in the channel rig itself.

Combinations of L and β were tested using numerical simulations of a simplified two dimensional inviscid flow field, both to aid in the design process and to obtain an initial idea of the resulting flow performance. The simulations are discussed further in the following sections. Other designs such as aligning the central streamline of the test generator flow with the channel x-axis were also simulated.

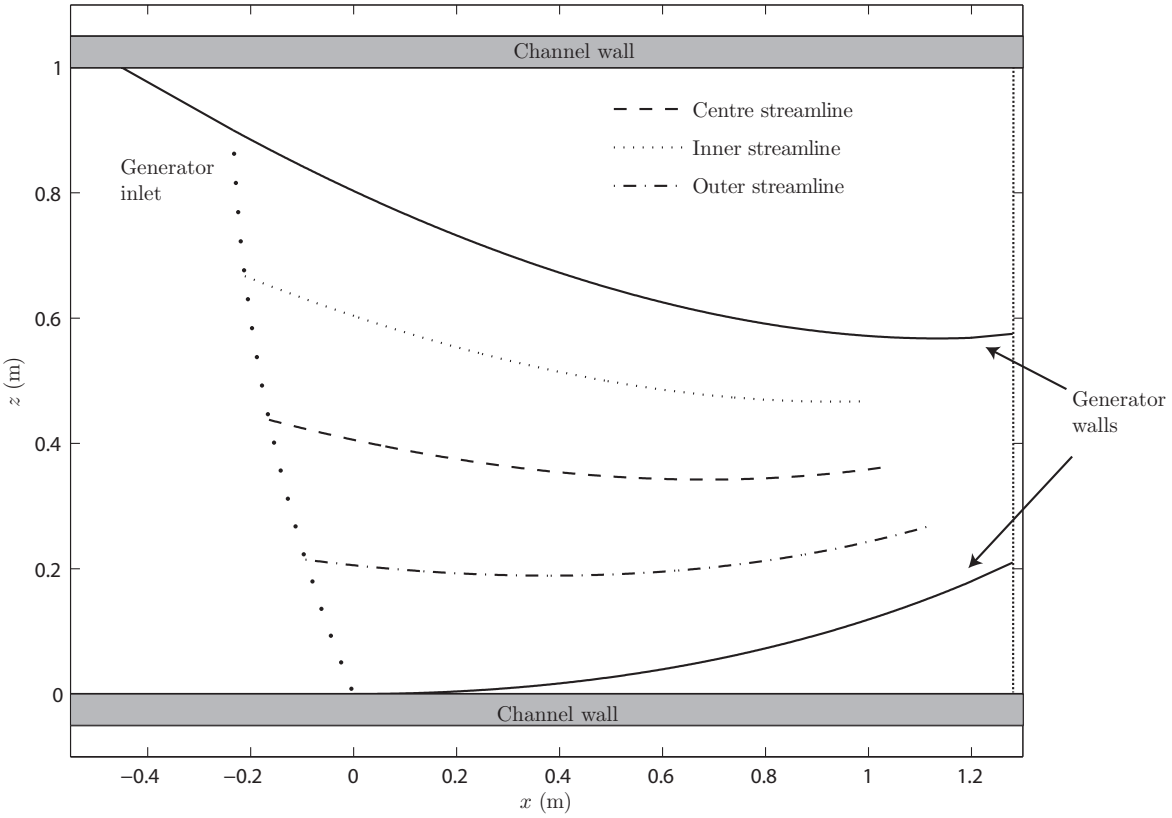

Figure 5.2: A schematic of the Case 2 pressure gradient generator in the channel flow rig. The three streamlines indicated by (−−), (·) and (−·) are the three-dimensional equivalents of the Case 1 streamlines. The wide dotted (· · ·) 'generator inlet' is used as a reference line throughout this thesis and should not be confused with the inner streamline. The generator inlet was positioned primarily to maximise the region of the geometry measurable with the traverse.

The resulting shapes of these were, however, considered too physically demanding to manufacture and fit in the flow channel, and the simulations yielded poor results. The best compromise was found when one wall of the test generator is aligned with the channel and the shape allowed to 'fan outwards' across the channel width. This explains the unusual orientation of the Case 1 geometry in the channel.

An L of 2.5 m and β of 0.5 were eventually chosen as this combination satisfies the requirements specified in §2.4, whilst minimising the flow disturbances around the generator-channel interface point. The streamwise acceleration created by the generator becomes $K{\approx}3.2{\times}10^{-6}$ and by $x{\approx}0.5$ m, the freestream is predicted

to have turned by γ_e=10° (the predicted flow is given in §5.2.3). The results of the simulation with this choice of parameters are discussed and shown later in this chapter. The resulting sweep angle is Λ=26.5°. An L of 2.5 was therefore also used in the design of Case 1, but with β set to 0. The difference between the centre streamline and the oncoming flow direction is 12° in Case 2 (Case 1 is 10.6°). The angle between the generator and channel interface is 24°. This is slightly larger than the Case 1 geometry which makes an angle of 21° with the channel wall. A schematic of the Case 2 pressure gradient generator in the water channel is shown in Figure 5.2.

5.1.3 Test Generator Construction

The final geometries of both cases are drawn numerically using a curvilinear co-ordinate system. Unlike Case 1, Case 2 requires that both walls must be shaped over the testing region to generate the pressure gradient. The curved walls are each constructed by attaching flexible, 3 mm thick Perspex sheets to large templates of the desired shapes to form the curved walls. Two templates are required for each wall profile and they are laser cut from 10 mm thick Perspex. The templates define the shapes and serve as the base and lid to each wall profile forming a box-like structure. The templates are separated and strengthened by ribs to create a depth. Additional locating geometry is included to ensure each wall slots into the rig at the correct position. Figure 5.3 shows a photograph of the finished generator in the channel.

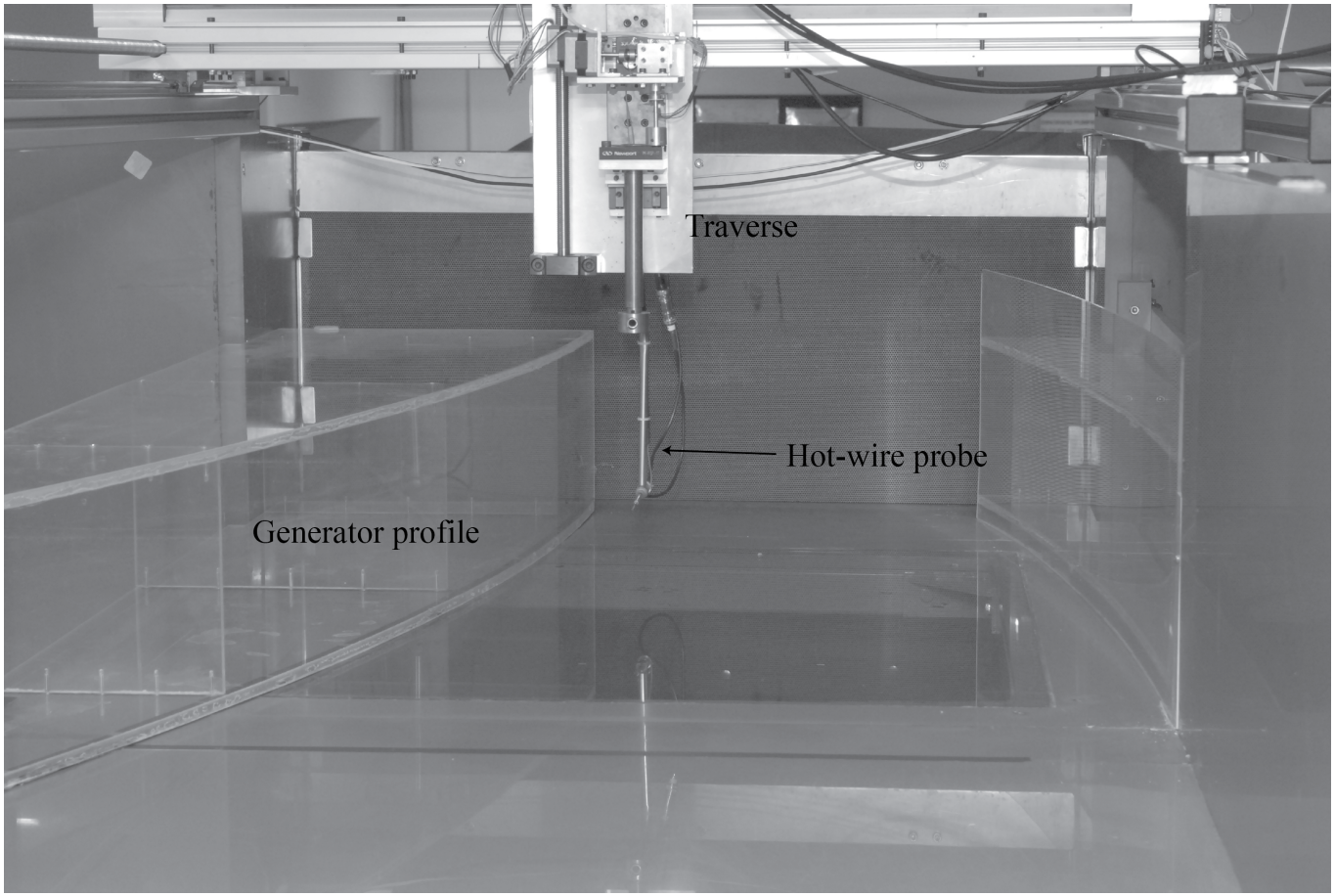

Figure 5.3: A photograph showing the Case 2 generator in the experimental rig. The left and right hand sides of the photograph correspond to the 'inner' and 'outer' regions of flow referenced in the text respectively.

In a similar manner to Case 1, the defined inlet curve to the pressure gradient generator only spans 90% of the width of the flow channel. A straight length of wall spans the remaining gap, which was added due to the same concerns raised in Case 1 over the flow disturbances created at this point. The large streamwise acceleration in Case 1 limits the downstream growth of flow disturbances at this point. Disturbances to the Case 2 flow were investigated using dye markers around the interface point and were found, as was seen in Case 1, to remain small with downstream distance. This is expected as the streamwise acceleration is identical for both tests. The angles made by the generators at the interface point were also seen above to be similar in both cases.

5.2 Potential flow

Measurements of the potential flow generated by Case 2 were carried out using the hot-film anemometer in an identical way to Case 1. Measurements of the freestream velocity in the streamwise direction and the flow angle in the generator are again presented using Cartesian channel coordinates. Clearly, however, the x and z axes are related to the generator geometries in distinct ways. An idealised case will be compared with the resulting potential flow as was done in the previous chapter. This case corresponds to an unperturbed free-spiral vortex flow of similar dimensions and shape to the generator, and with the same initial inlet velocity. Again, it is not critical that the resulting flow obey any specific pattern. The main requirements for the Case 2 generator are that the streamwise pressure gradient component be comparable with Case 1 and that the freestream behaviour approach that outlined in §2.4.

The streamlines in Figure 5.2 indicate the curved channel equivalents of those in Case 1 and are referred to repeatedly throughout this chapter when referencing measurement locations, and indicate the idealised flow behaviour given in §5.1.1

through the generator. Their initial directions compared to the channel x-axis at the inlet are -18° for the inner streamline, -12° for the centre and -6° for the outer streamline. The negative value indicates turning in the $-z$ direction.

5.2.1 Numerical Simulation

In §5.1.2, the parameters L and β were discussed along with the factors influencing the values selected. Numerical simulations were conducted using commercial CFD software (Star CCM+) to test various combinations of L and β as well as other experimental arrangements.

The entire experimental flow rig including the outlet are included in the simulated model. The outlet to the weir gate had to be extended a distance upstream, however, in order to prevent reversed flow occurring as this causes numerical problems. A pressure outlet and velocity inlet boundaries are used with the velocity magnitude set to approximately the same magnitude as that used later for the experiments. For obvious reasons, the boundary layer is not simulated and consideration only given to the external flow.

Since the channel is open, large changes in velocity will result in a change of water depth (h) and consequently the flow rate. This would require a consideration of the free-surface in the simulation. As mentioned previously though, the low water velocities used in the experiment result in the small depth changes through the generators ($\Delta h_{max} = \Delta P/\rho g \approx 1-2$ mm) and will therefore have a small impact on flow rate. Consequently, the simulation can be greatly simplified by making the flow field two-dimensional allowing more simulations to be performed and more combinations of L and β to be considered.

The results corresponding for L=2.5 m and β=0.5 are employed in this section to compare with the experimental measurements of the potential flow. Some differences between the results is expected due to slight dissimilarities between the simulation model and the final generator shape and small differences in the inlet velocities.

5.2.2 Freestream Velocity

The Case 2 experimental results for the freestream velocity magnitude are shown in Figure 5.4 at five channel locations along each reference streamline. Markers indicate measurements normalised by the initial velocity on the centre streamline and the lines indicate the velocity for the idealised, unperturbed case discussed in §5.1.1. The measurements at the inlet appear close to the results for the Case 1 generator which is expected. The turning of the flow at the inlet is seen again to cause the initial flow of the inner streamline to slow down. By x=0.2 m the velocity magnitudes are approximately equal. The flow on the outer streamline slows down, as the difference in streamline curvature across the channel begins to have an effect and the pressure increases on the outside. By 0.4 m the flow on the inner streamline leads the remainder of the flow as the pressure falls. Analogous with Case 1, the last measurement velocity was just beyond the calibration range and hence the error in the measurements will be larger.

The results from the CFD simulation are compared with the experimental measurements in Figure 5.5 and both flows show similar behaviour inside the generator geometries with the velocity magnitudes equalising at similar channel locations. The CFD results show an almost linear increase for the inner streamline velocity and it therefore does not appear to follow the sink flow idealised case behaviour.

5.2.3 Mean-Flow Direction

The freestream flow angle (γ_e) measurements are presented in Figure 5.6. The flow into the Case 2 generator has turned to a greater extent upstream compared with Case 1. This is expected as the angle made by the geometry to the channel is slightly larger in Case 2. The inner-streamline measurements fall short of the flow angle for the idealised case behaviour but then turns more sharply after x=0.4 m.

In summary, though, the flow behaves surprisingly close to the idealised behaviour for both the freestream direction and velocity magnitude. This suggests

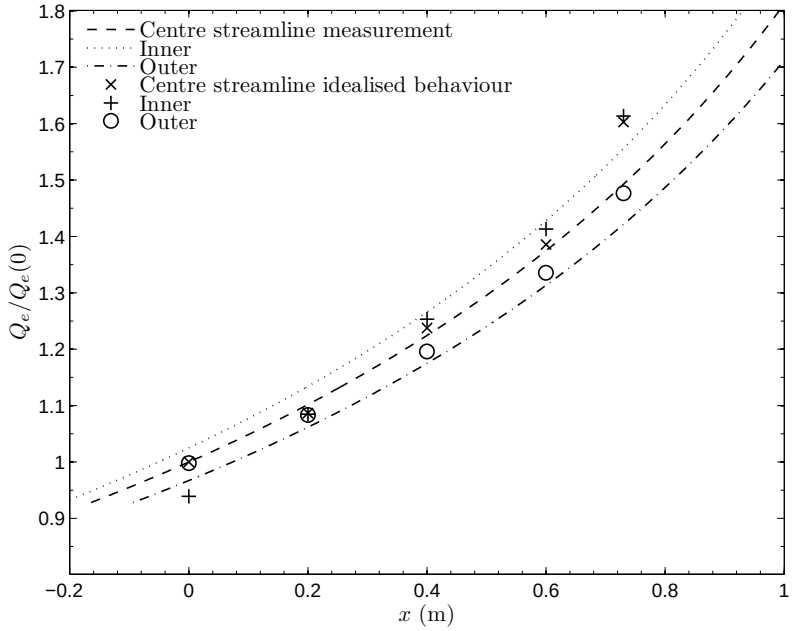

Figure 5.4: The evolution of the freestream velocity magnitude over the testing region compared with the idealised flow behaviour. The initial measurement value of the centre streamline is used for normalisation and channel coordinates are shown.

that satisfactory flow conditions are being created by the generator shape over a large area of the testing region. This is particularly apparent after x=0.4 m where significant magnitudes of freestream turning are reached ($\gamma_e \approx 10°$). The measurements are used to compute streamlines (Figure 5.7) to illustrate the external flow through the generator. The measurement locations are shown and the results for each are indicated by the vectors.

5.2.4 Pressure and Acceleration

The streamwise acceleration parameter, K, is plotted in Figure 5.8 and, though comparable in magnitude to Case 1, shows a greater streamwise fluctuation. Error bars are also shown, calculated in an identical manner to §4.2.3. The measurement at the last station shows a larger difference compared with the remainder of the results, though the error present in the velocity calibration is greater at this station.

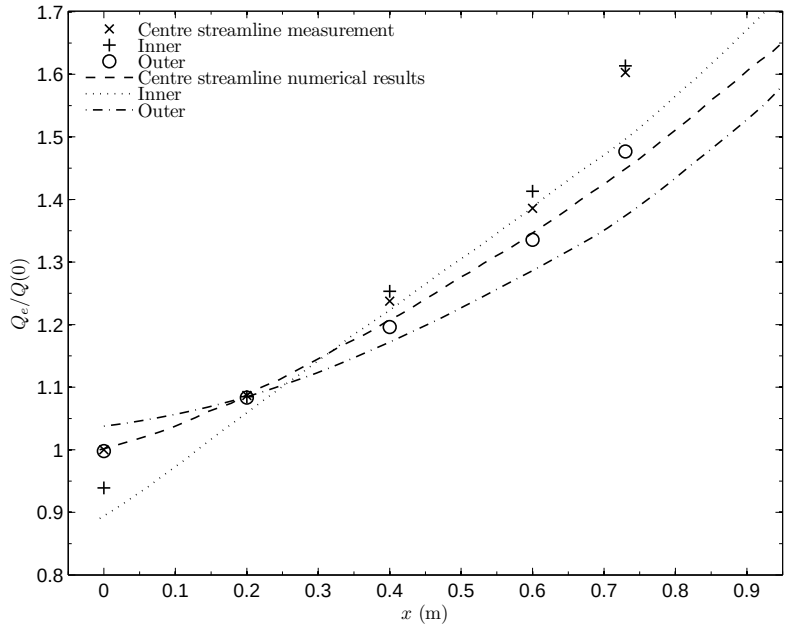

Figure 5.5: The change of the freestream velocity magnitude over the Case 2 testing region compared with the numerical simulation results. The lines indicate numerical results and the markers indicate measurements. The initial value on the centre streamline is used for normalisation.

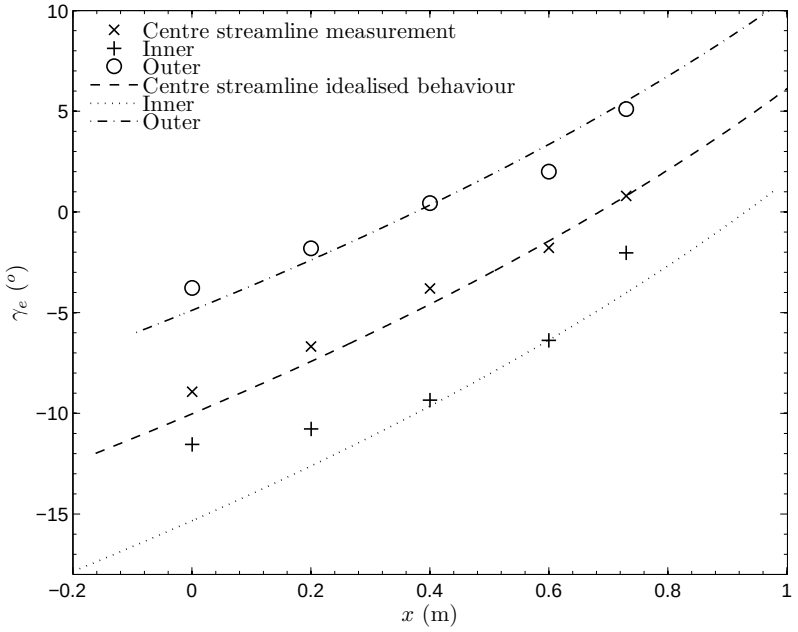

Figure 5.6: The change in the direction of freestream flow through the Case 2 generator versus channel coordinates. The lines indicate the idealised behaviour and markers indicate measurements.

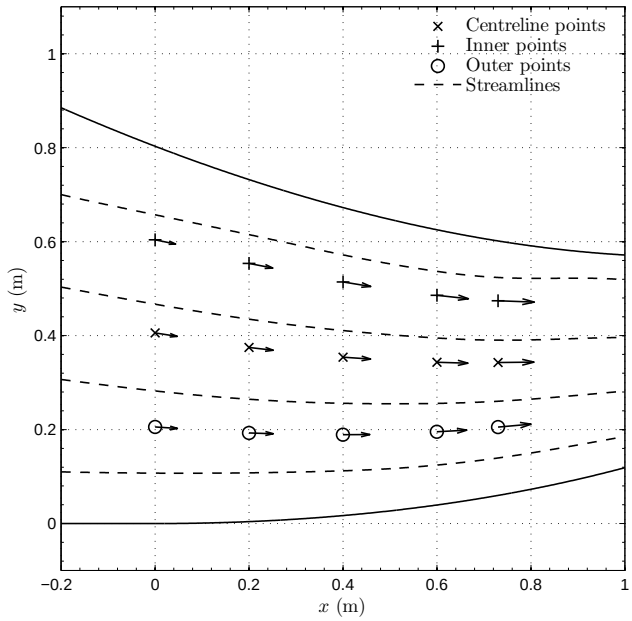

Figure 5.7: The freestream flow through the pressure gradient generator. Velocity vectors are shown at the measurement locations (markers) and streamlines (−−) are included to demonstrate the broader behaviour. The streamlines are computed by interpolating the measurements onto a larger mesh.

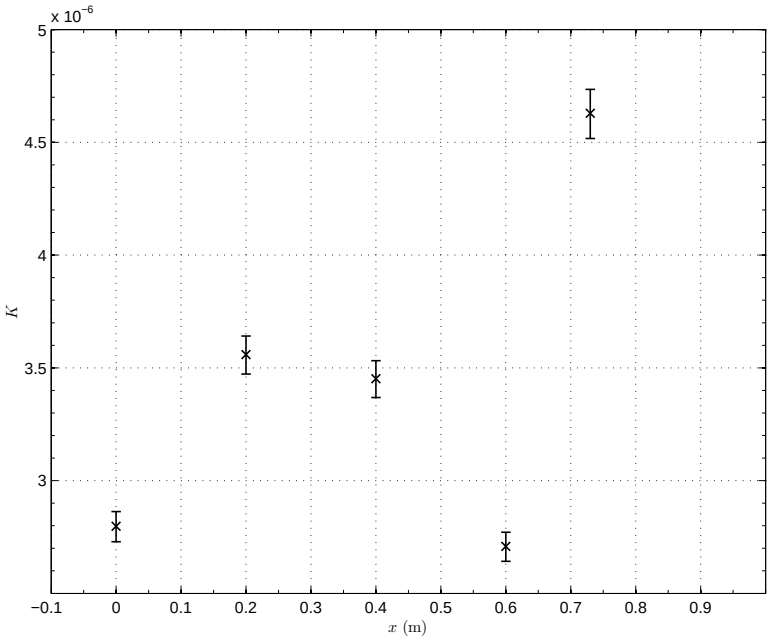

Figure 5.8: The behaviour of the centre streamline pressure gradient parameter in Case 2 versus channel coordinates. The error bars are calculated assuming negligible uncertainty in s and 2.3% error in Q_e.

The coefficient of pressure is calculated using the flow-field data, as was carried out in §4.2.3, with the reference pressure ($P(0)$) and velocity ($Q_e(0)$) given by the centreline measurement at the furthest upstream station. The behaviour of the pressure through the geometry is shown in Figure 5.9. Initially, C_p is highest on the 'inner' side of the generator as the Case 2 geometry turns the oncoming flow in the same direction to Case 1. By x=0.2 m the pressure has equalised across the channel and further downstream a difference develops between the outer streamline and inner streamline. The effect of the change in pressure is illustrated more clearly by the pressure gradient which is shown in Figure 5.10 for the streamline (s-n) coordinate system. The pressure gradient from Case 1 is also shown to allow a comparison between the two experiments. As was seen above, the spanwise pressure gradient ($\delta^*(0)\partial P/\partial n$) of Case 2 is initially positive as it is in Case 1, due to the initial turning of the flow into the generator at the inlet. By s=0.4 m it has changed sign becoming negative, and increases in magnitude downstream. A large negative spanwise pressure gradient value is clearly desired here and indicates a favourable pressure gradient in the direction of the radius of curvature. The streamwise pressure gradient, $\delta^*(0)\partial P/\partial s$, is similar in magnitude and streamwise development to Case 1, which is a necessary condition for a comparison between the two cases to be made.

5.3 Boundary Layer Measurements

The Case 2 measurement stations used for the boundary layer experiments are located at five streamwise locations along the centre streamline referenced in Figure 5.2 and Figure 5.11 shows the stations in the rig. Their locations can be seen to correspond with the same streamwise distances as Case 1 from the generator 'inlet' line. The data are also presented using the streamline coordinate system.

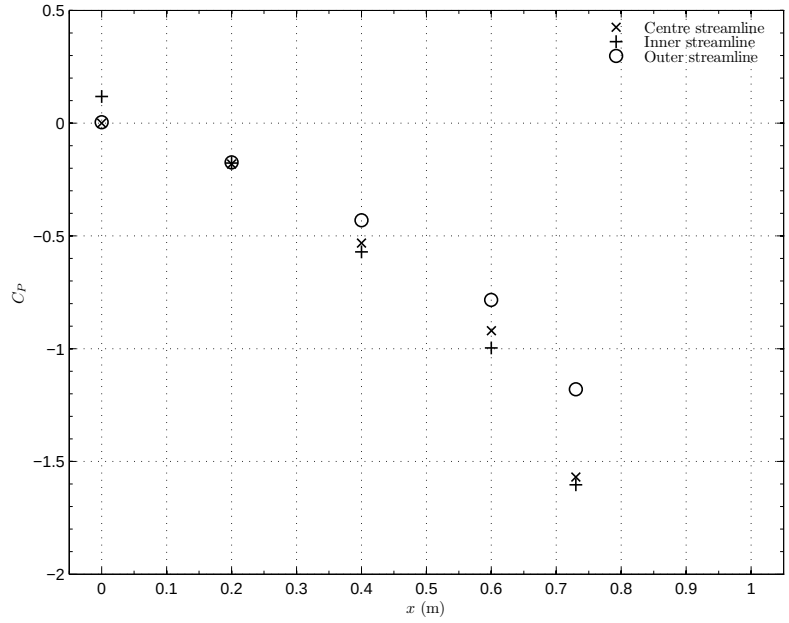

Figure 5.9: The change in C_p produced by the Case 2 pressure gradient generator versus channel coordinates.

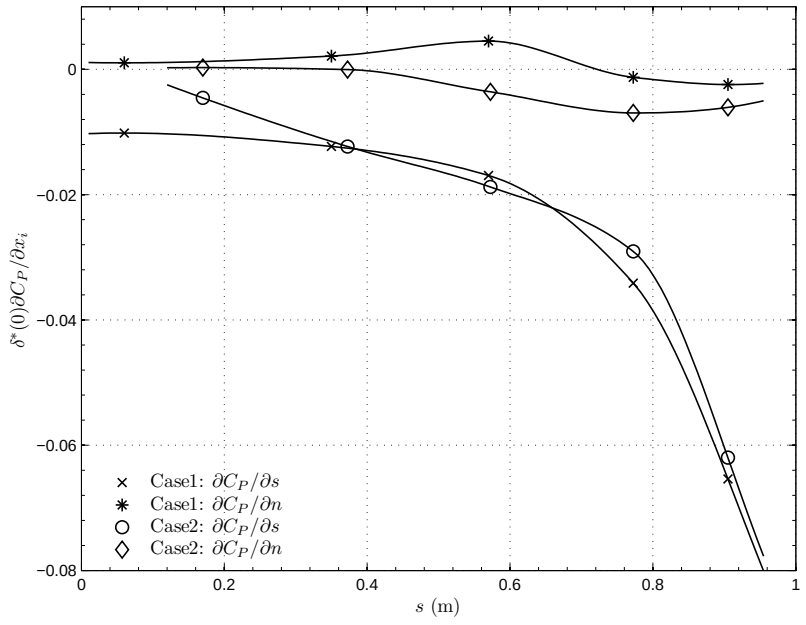

Figure 5.10: The streamwise and spanwise pressure gradients of both cases versus streamwise coordinates, non-dimensionalised with the initial displacement thickness of the boundary layer from each case.

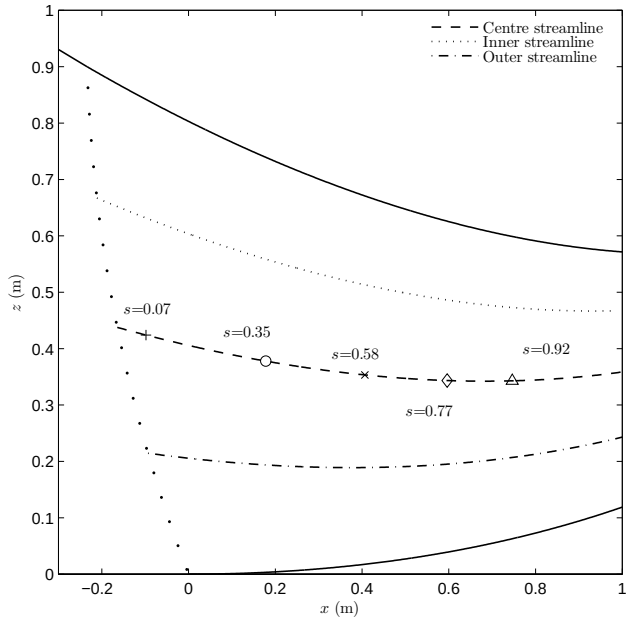

Figure 5.11: The measurement station locations in the Case 2 geometry used to sample the turbulent boundary layer. The streamwise distance from the inlet line is given at each station.

5.3.1 Mean-Flow Direction in the Boundary Layer

The mean-flow direction ($\gamma - \gamma_e$) in the Case 2 boundary layer is measured using the same procedure described in §4.3.1 and the results are shown in Figure 5.12. For the measurements at the third station, splines were fitted to the measurements in place of a polynomial for the curves used for mean-velocity measurement due to a poor fit.

The three-dimensionality in the boundary layer behaves in a more complex manner compared to Case 1, as the spanwise pressure gradient in this experiment changes sign in the generator (Figure 5.10). Turning the channel flow into the generator geometry causes the initially positive pressure gradient values and is behind all the three-dimensionality in the Case 1 boundary layer, which subsequently decayed downstream. The change in the pressure gradient sign in this experiment, means that the mean-flow in the boundary layer changes direction, which is clearly evident in Figure 5.12.

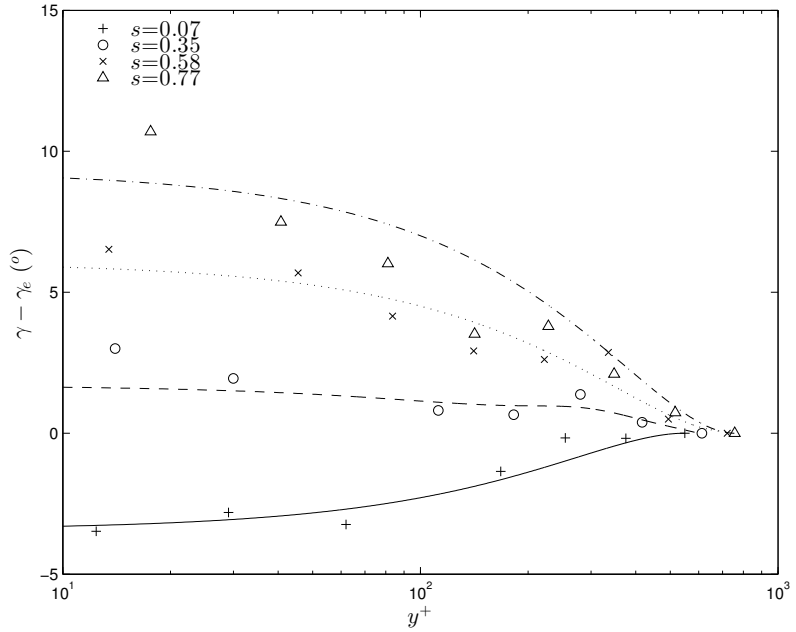

Figure 5.12: Profiles showing the mean-velocity skewing in the Case 2 boundary layer. The curves illustrate the probe direction used during mean velocity measurement

The extent of mean-flow skewing at the first measurement station is comparable in magnitude to Case 1. The boundary layer changes direction between the first and third stations and follows the change in sign of the pressure gradient. The results for the second station appear erroneous and the uncertainty is large so the results are not shown in Figure 5.12. This should not present further problems however, as the measurements for this station are small. Downstream of this station the wall layer turns reaching relatively high skewing magnitudes of around 9° to 11° by the last station. The maximum boundary layer deflection is similar to that obtained by Littell and Eaton (1994), but is not as great as expected given the extent of turning in the freestream. The development of the crossflow is discussed further in the following section.

All the measurements show a similar slight positive bias at around $y^+ \approx 100$. This is reminiscent of the cross-over profiles discussed by Bradshaw (1987). Crossover profiles result from when there is a change in the sign of the pressure gradient for

a boundary layer with a pre-existing streamwise vorticity, which is clearly the case here. This has been noted in more complex flows such as S-shaped ducts (Bruns et al., 1999; Lofdahl et al., 1995) and wing-body junctions (Olcmen et al., 2001; Olcmen and Simpson, 1995). The slower wall-flow has a lower inertia and is consequently more sensitive to spanwise pressure gradients than the remainder of the boundary layer. Similar behaviour may be present in the boundary layer in this experiment between the first and second stations, but definitive conclusions cannot be drawn from the measurements.

5.3.2 Boundary Layer Mean-Velocity Results

The non-dimensional boundary-layer parameters and quantities of interest chosen in Chapters 3 and 4 are tabulated for the initial measurement station in Table 5.1. The values are reasonably close to the Case 1 flow, but compared to the zero-pressure-gradient case the lower momentum-thickness Reynolds number (Re_θ) of Case 2 may complicate any comparisons between these two. A comparison between Case 1 and 2 is the focus of this study and their respective Reynolds numbers are more agreeable. Re_τ is slightly higher than Case 1 at the inlet and behaves similarly to Re_θ, rising more slowly through the test section reaching only $Re_\tau \approx 580$ downstream.

The streamwise development of the parameters is shown in Figure 5.13. Case 2 shows the same unusual rise in Reynolds number and reduction in C_f as Case 1, which was unexpected given the large streamwise pressure gradient component. The lateral contraction was thought to be the cause of this behaviour and the Case 2 generator design also uses a lateral contraction for the streamwise pressure gradient. The idealised case with an unperturbed potential flow has no spanwise contraction, so in a similar way to Case 1 it would only be the perturbed nature of the experiment which might explain this result; if the lateral convergence is the underlying cause. The change is less pronounced than in Case 1 and the last station measurements are more characteristic of turbulent boundary layers in large stream-

Quantity	$\partial P/\partial n < 0$
Q_e ($\mathrm{m{\cdot}s^{-1}}$)	0.125
Re_θ	879
Re_τ	538
H	1.34
δ_θ (m)	0.007
δ^* (m)	0.0094
τ_w ($\mathrm{kg{\cdot}m^{-1}s^{-2}}$)	4.01×10^{-2}
C_f	0.0051

Table 5.1: Initial mean-flow quantities and parameters of the Case 2 turbulent boundary layer.

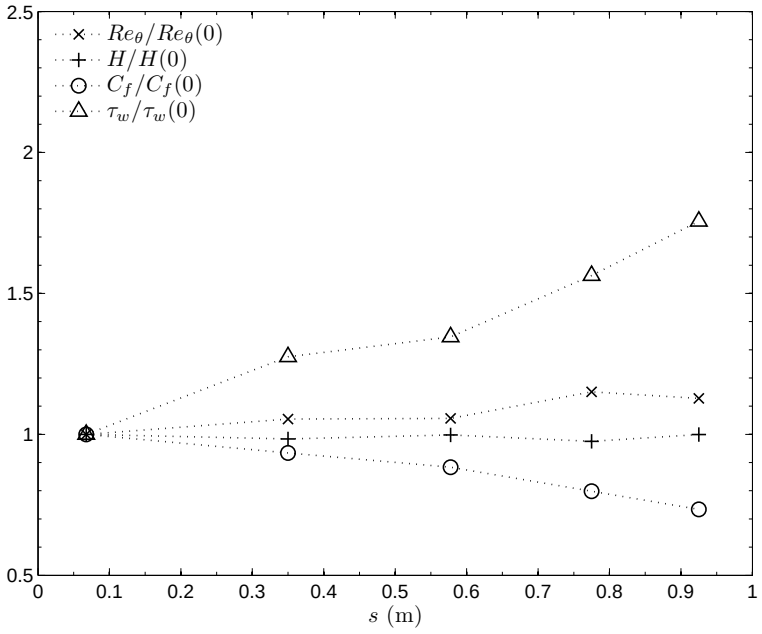

Figure 5.13: The streamwise development of the mean-flow parameters versus streamline coordinates. Measurements are normalised with their initial values.

wise accelerations, with a reduction in Reynolds number and shape factor (H) by the last station.

These results suggest that the level of streamwise vorticity generated by the spanwise pressure gradient does not affect the overall streamwise development of the turbulent boundary layer. The similarity between the two cases is highlighted in Figure 5.14, which compares the mean-velocity profiles from the two cases at the first and fourth measurement stations. There is a slight difference at the first measurement station but by the second station the results from the two cases appear almost identical. This is repeated in Figure 5.15 where the velocity profiles at the second and fourth stations are shown, non-dimensionalised in inner units. The behaviour of the mean-velocity gradient (κ^{-1}) and the velocity intercept (B) are correspondingly similar and therefore not shown. The effects of the favourable pressure gradient, which were seen in Chapter 4, are evident in both profiles and appear to be unaffected by the mean-flow skewing.

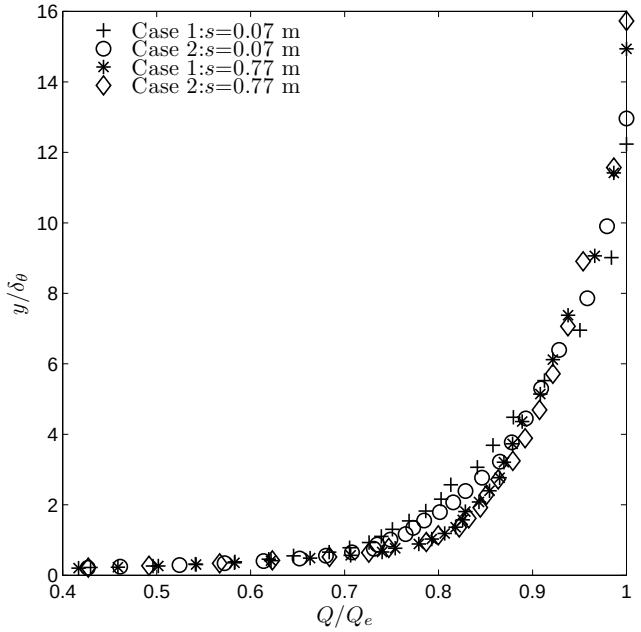

Figure 5.14: Mean-velocity profiles sampled at the first and fourth measurement stations in the Case 1 and Case 2 turbulent boundary layers, non-dimensionalised in outer scales.

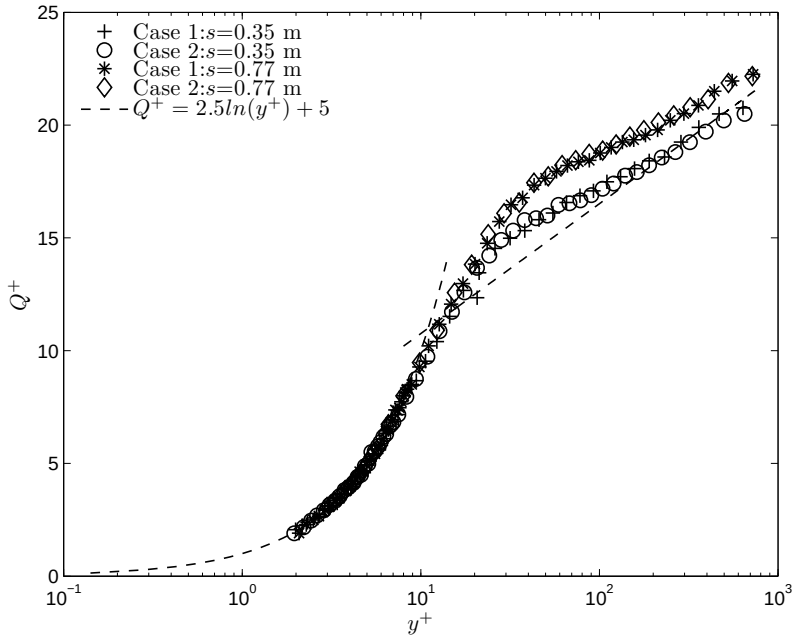

Figure 5.15: Mean-velocity profiles sampled at the second and fourth measurement stations, non-dimensionalised in inner units.

To examine the extent of the three-dimensionality in the Case 2 boundary layer, the mean velocity is separated into streamwise (U) and spanwise (W) components for the coordinate system aligned with the local freestream direction:

$$U = Q\cos(\gamma - \gamma_e) \qquad W = Q\sin(\gamma - \gamma_e)$$

and where $U(\delta) = Q_e$. Profiles of these mean-velocity components for the last three stations of Case 2 are shown in Figure 5.16 non-dimensionalised in inner units. The friction velocity components are:

$$U_\tau = Q_\tau\cos(\gamma_w - \gamma_e) \qquad W_\tau = Q_\tau\cos(\gamma_w - \gamma_e)$$

where γ_w is the skew-angle at the wall. Similar to Case 1, γ_w was obtained from the curves fitted to the flow angle data.

The possible Reynolds number and pressure gradient dependence of the cross-

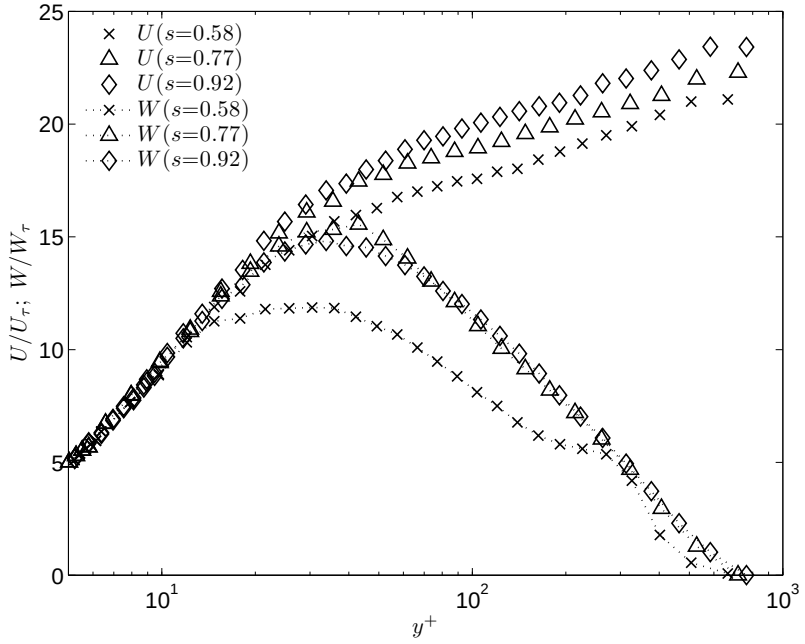

Figure 5.16: Mean-velocity profiles in Case 2, scaled in inner units, for a coordinate system aligned with the freestream direction.

flow was noted in §2.2.2. Degani et al. (1993) suggests that as the Reynolds number increases, the crossflow develops a logarithmic behaviour similar to the streamwise component. The wall-normal height of the peak in crossflow also increases, as does the magnitude. The peak in Figure 5.16 occurs around the top of, or just above, the buffer layer which agrees with the results of Flack and Johnston (1998), who measure a peak in the crossflow in the buffer layer of their curved channel experiment. For their investigation, Re_θ=1400. The scatter in both experiments is high, though. Itoh and Kobayashi (2000) find peak crossflow occurs around the start of the logarithmic behaviour in the streamwise velocity, between $25 \leq y^+ \leq 60$. Their Reynolds number range was Re_θ=1200 to 5830 in a swept wing flow with an adverse streamwise pressure gradient.

As is conventional in three-dimensional turbulent boundary layer studies, a hodograph or triangular plot of the mean-velocity components is shown in Figure 5.17 and compared with plots from other three-dimensional studies at a similar

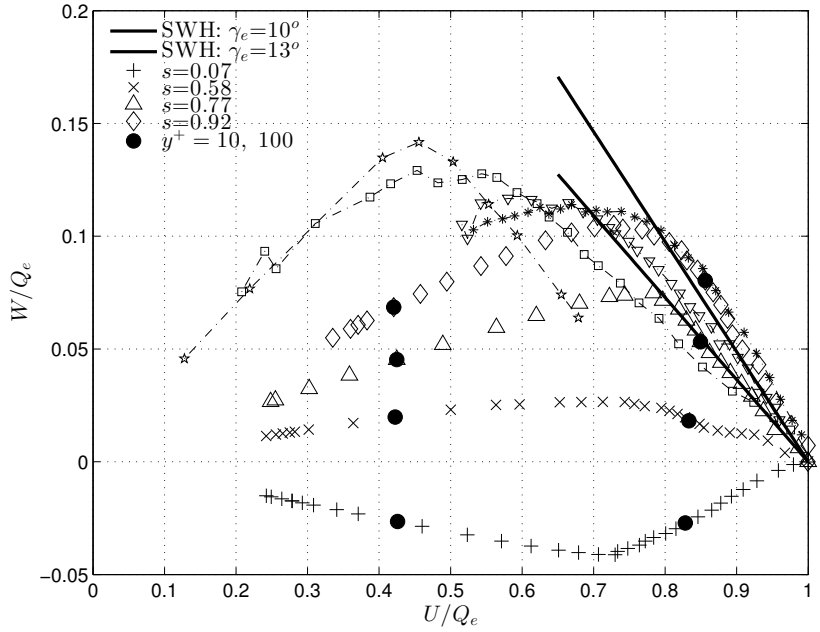

Figure 5.17: Triangular plot showing the streamwise evolution of the mean velocity in Case 2, for a coordinate system aligned with the freestream direction: (–) The Squire-Winter-Hawthorn prediction for γ_e=10° and 13°; (· –) indicates literature; ▿, Schwarz and Bradshaw (1994) (γ_e=6°); ▫, Flack and Johnston (1998) (γ_e=7.5°); ⋆, Compton and Eaton (1997) (γ_e=5.6°); ⋆, Littell and Eaton (1994).

level of crossflow. This form of plot is used to show the development of the peak crossflow magnitude in the boundary layer. Following Flack and Johnston (1998) two black circles in each Case 2 profile indicate the wall-normal positions y^+=10 and y^+=100, which can be used for reference. The two solid black lines in the plot are described below. The degree of Case 2 three-dimensionality is characteristic of many three-dimensional experiments including Bradshaw and Pontikos (1985), Coleman et al. (2000) and Littell and Eaton (1994), with the crossflow velocity reaching a peak of 11% of the local freestream magnitude by the last measurement station. The shape of the profile at s = 0.92 is also similar to that of Littell and Eaton (1994) who comment that this three-dimensionality must be considered a 'major' feature of the flow. From the measurements in these investigations then, significant changes to the boundary layer would be expected unless otherwise affected by influences such as the acceleration.

The Squire-Winter-Hawthorn (SWH) relationship was described in §2.2.2. The flow predicted using the SWH relationship (equation (2.1)) is shown by the solid black lines in Figure 5.17 for two values of γ_e. Despite the streamwise acceleration, the SWH relationship appears to characterise the outer part of the measurements here reasonably well. For the last two stations the freestream has also turned by $\gamma_e \approx 10^\circ$ and 13° as evident in Figure 5.6. The presence of an adverse pressure gradient shifts the hodograph to the left (Coleman et al., 2000), as the difference between the wall and freestream velocities tends to zero. It is conceivable then, that the favourable pressure gradient present here is responsible for a rightward shift of Figure 5.17 though again, Reynolds number may also have an effect (Degani et al., 1993). The acceleration may also be partly responsible for the lower magnitudes of near-wall turning seen here as suggested by (Hanjalic et al., 1994).

5.3.3 Fluctuating Velocity Results

Both case studies use a favourable streamwise pressure gradient and the large variation in the behaviour of the fluctuating velocity in accelerated turbulent boundary layers is noted in §2.3.2 and §4.3.4. The magnitudes of the streamwise pressure gradient and Reynolds numbers of the two case flows here are comparable and the resulting behaviour of the mean velocity was indistinguishable between the cases despite the skewing. This similarity at least provides a more favourable environment to compare the fluctuating velocity.

Profiles of the absolute change in the rms velocity in the local mean-flow direction from the two cases are compared in Figure 5.18. Inner units have been used for the non-dimensionalisation of the wall-normal height. Application of a single-normal probe in a three-dimensional flow was discussed in §3.4.4. The turbulence shows little sensitivity to the introduction of the spanwise pressure gradient as it did for the mean-flow. A difference between the boundary layers is apparent in the outer region, however this difference exists at the upstream stations as well, so cannot be said to result from skewing effects. Figure 5.19 shows differences in the local rms velocity from both cases and Figure 5.20 compares profiles of the stress. Again, both boundary layer profiles behave in a similar way. Differences between the cases are present at the inlets but no effects from the curvature are evident.

Unlike the mean velocity measurements the fluctuating velocity cannot be transformed into a local freestream coordinate system, so for comparisons with the literature the turbulence intensity in some cases will be used. Schwarz and Bradshaw (1994), in their 30° curved duct flow, measure large changes in turbulence intensity in the outer layer during the crossflow development. Growth of the intensity starts at a low heights in the boundary layer then progresses outwards. Their lowest measurement point is at $y/\delta \approx 0.1$ so this growth may start lower. Observations similar to these are made by Flack and Johnston (1998) who suggest that the growth is due to an increase in the spanwise component (w'). Despite the severe acceleration

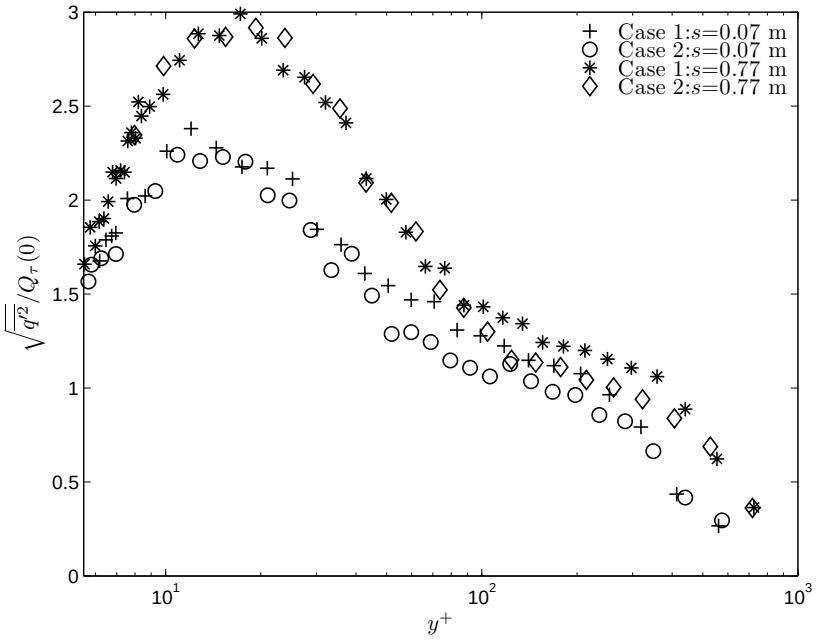

Figure 5.18: Boundary-layer profiles comparing the absolute change in the rms velocity through both case generators. The results are given for the first and fourth measurement stations of both cases and the values non-dimensionalised by the friction velocity at the initial measurement station ($Q_\tau(0)$).

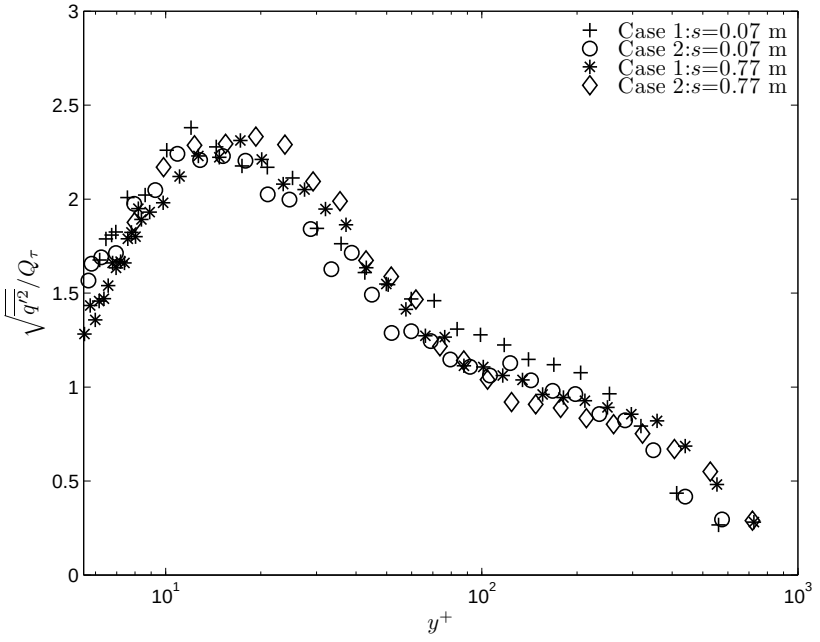

Figure 5.19: Profiles comparing the local change in the rms velocity in the boundary layer between cases. The results are given for the first and fourth measurement stations and the values and non-dimensionalised in inner units.

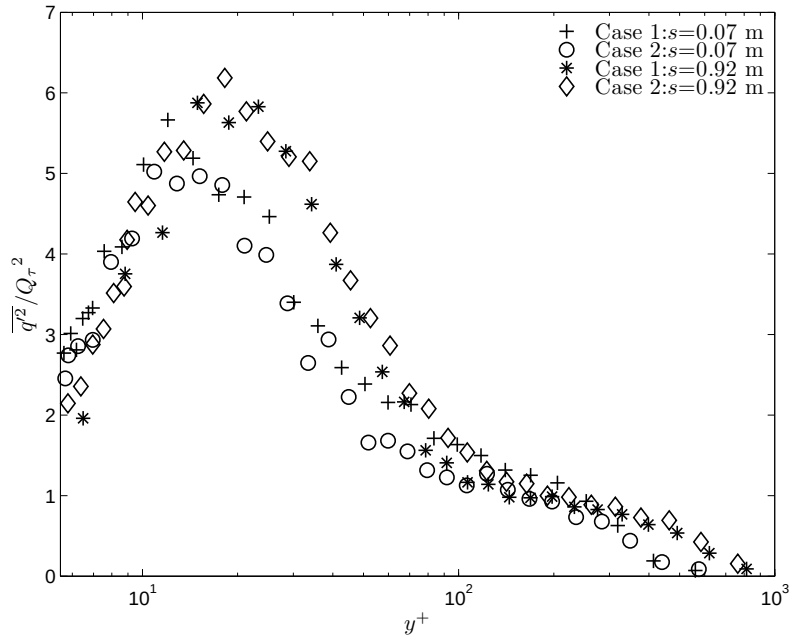

Figure 5.20: Profiles comparing the stress in the mean-flow direction between Cases.

with K approaching $20{\times}10^{-6}$, Hanjalic et al. (1994) found an almost constant value of the streamwise fluctuating velocity (u'), again sustained by the spanwise stress from their moving wall.

The measurements of turbulence intensity by Littell and Eaton (1994) are comparable in magnitude to those here. They found an independence of Reynolds number ($Re = \Omega r^2/\nu$) in their measurements but as they discuss, the three-dimensionality is being constantly driven into the disk boundary layer rather than induced by a perturbation. This is also the case in the idealised free-spiral-vortex flow, though it is unknown if the turbulence intensity should remain self-similar and certainly, conclusions cannot be drawn from the boundary layer flows investigated here. The changes in the mean and fluctuating velocity components in this investigation are more the result of the streamwise acceleration. The crossflow velocity introduced into the boundary layer appears to have little discernible effect; at least for the measurements made.

5.3.4 Velocity Moments

The strong similarity between the cases is also displayed by the higher moments of velocity. Figure 5.21a and Figure 5.21b compares profiles of the skewness (S_q) and kurtosis (K_q), which were introduced in §3.6, at two streamwise measurement stations from each case study. The changes in Case 2 again show no significant differences to Case 1, and therefore serve to further strengthen the observations made in the previous chapter regarding the effects of the favourable pressure gradient on these two statistics. Skewness and kurtosis of the individual velocity components are not often shown in the three-dimensional turbulent boundary layer literature so again comparisons with other experiments cannot be made.

5.3.5 Spectra

Velocity spectra are determined using the procedure described in §3.6.3. Figure 5.22 compares profiles of the Taylor-microscale Reynolds number (Re_λ) at each measurement station in Case 2. Re_λ increases slightly downstream, but not to the same extent as Case 1. Figure 5.23 compares the streamwise change in spectra in Case 2 with that from Case 1 in the inner layer at $y^+ \approx 100$. From §4.3.5 the acceleration is not expected to have a significant impact on the spectra unless relaminarisation is present. The figure shows that, though the Reynolds number is slightly lower than Case 1, the Case 2 spectra reveal no effect caused by the streamwise turning and the four results show reasonable collapse, particularly at high wavenumbers. From shear-driven experiments, Le et al. (2000) and Kiesow and Plesniak (2003) for example, a shift of energy to higher wave-numbers is seen in the inner-layer as the coherent structures are 'shredded' into smaller streamwise lengths by the shear at the wall. This shredding of structures has not been seen for pressure-driven flows; perhaps due to the lower rate at which the spanwise strain is applied. The spectra very near the wall here cannot be measured as the increased turbulence intensity limits the application of Taylor's hypothesis.

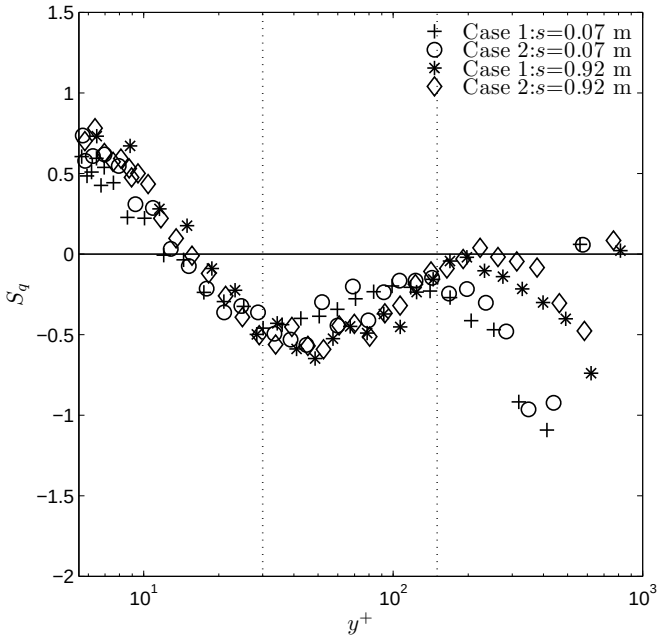

(a)

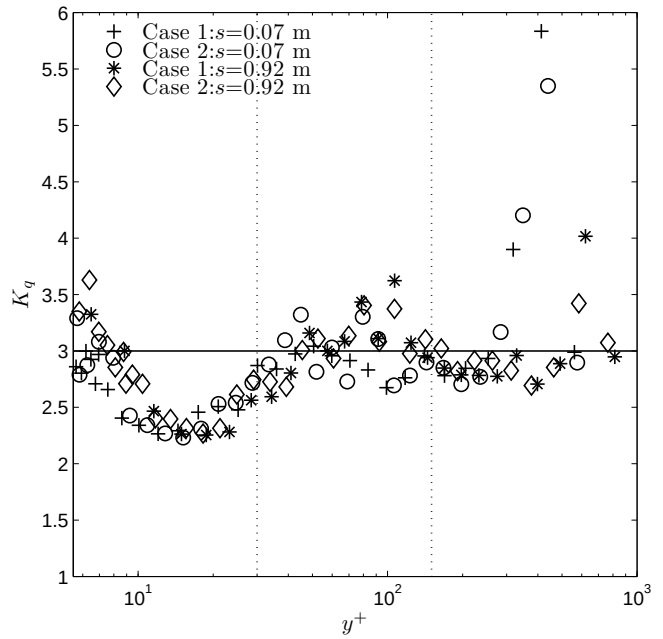

(b)

Figure 5.21: Boundary-layer profiles comparing the streamwise evolution of the velocity moments in the local mean-flow direction from the two cases: (a) skewness; (b) kurtosis. The results shown in each profile are the measurements made at first (s=0.07 m) and last measurement stations (s=0.92 m). Local inner scales are used for wall-normal non-dimensionalisation.

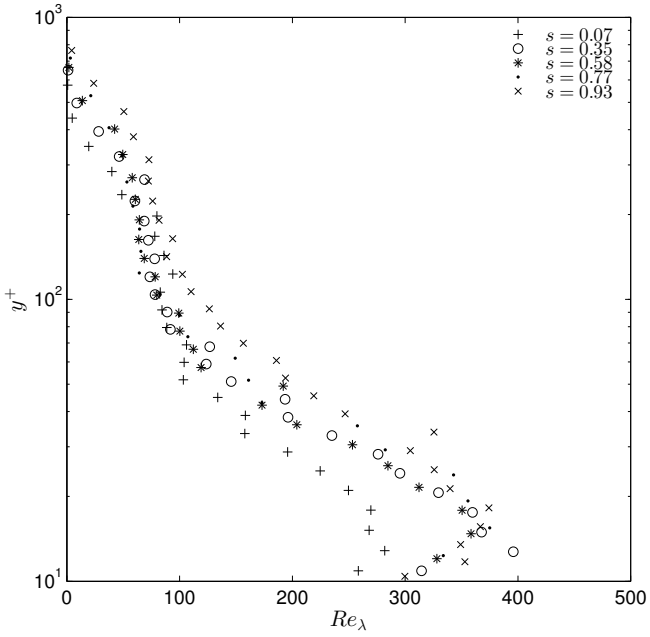

Figure 5.22: Profiles showing the streamwise development of the Taylor microscale Reynolds number in the Case 2 boundary layer.

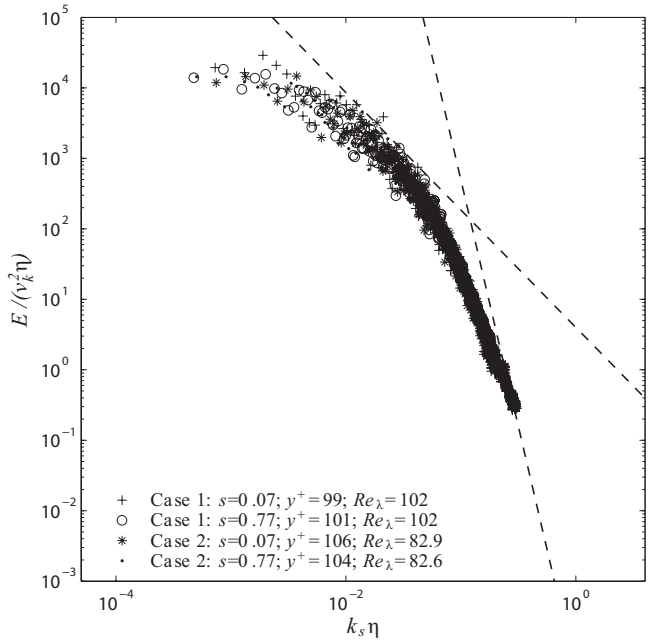

Figure 5.23: The streamwise change in spectra compared between both Cases.

5.4 Viscous Sublayer Low-Speed Streak Spacing

As is the case with favourable pressure gradients, investigations of the near-wall structures for three-dimensional boundary layers usually starts with an assumed topology of the near-wall boundary layer turbulence. In §2.2.4 it was remarked that the flow in the three-dimensional boundary layer is generally assumed to be a modified form of the popular streamwise vortices and low-speed streak model that describes equivalent two-dimensional turbulent boundary layers and was introduced previously in this thesis.

The measurement of the spanwise spacing of the low-speed streaks ($\bar{\lambda}^+$) in three-dimensional turbulent boundary layers is complicated by, amongst other factors, the non-alignment between the spanwise n-axis and the 'generator' lines introduced in §5.1.1. Figure 5.1 illustrates this non-alignment and shows how it relates to the spanwise pressure gradient. Consequently, the potential flow and pressure gradients will change along the n-axis. Any particular measurement of the spanwise spacing of the streaks will therefore be local to the particular measurement coordinates.

In this experiment, the streak behaviour can be observed independently of this non-alignment if the spacing is measured along the generator lines themselves instead of along the n-axis. Discussed previously in §5.1.1, the generators are lines of similar pressure, velocity and streamwise development. The effects of the spanwise pressure gradient on the low-speed streaks can therefore be seen by streamwise changes in the streaks along these lines. Streak spacing can only be measured in a similar way in swept wings, though in these flows, the sweep angle (Λ) changes with streamwise distance. In the Case 1 pressure gradient generator design, the generator lines are aligned with the spanwise direction (at least for the idealised flow).

5.4.1 Visualisation Method

Figure 5.24 shows the approximate location in the Case 2 channel where the visualisation is carried out. The line shown in the figure indicates the position and orientation of the platinum bubble wire and the s=0.77 m measurement station is also shown. The wire is orientated to lie along the generator line at this location and therefore s is approximately constant along the line. In the idealised case, the external flow is also the same. The position of the wire is slightly upstream of s=0.77 m so as the interrogation window can be position there. Though the generator line itself is curved, the platinum wire is kept straight, which was a similar situation in the previous chapter.

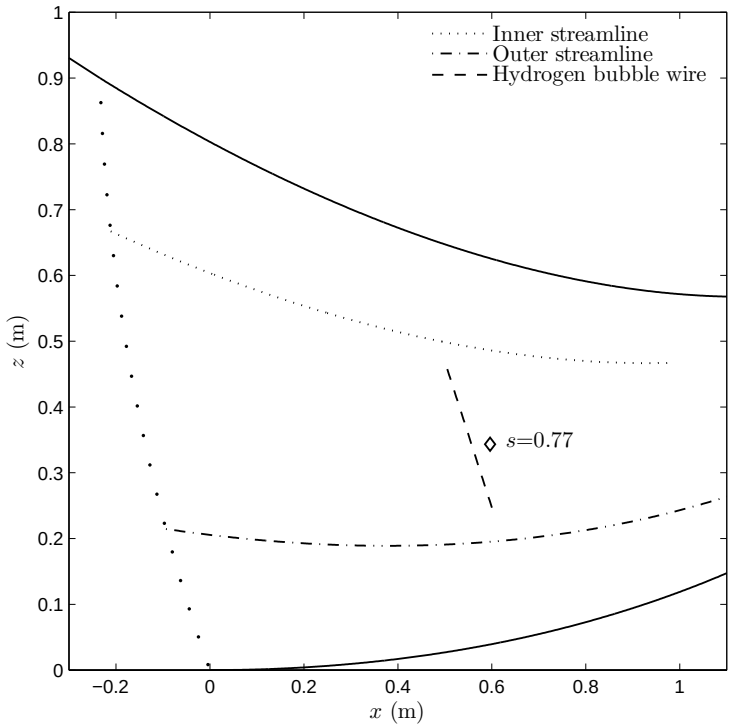

Figure 5.24: A schematic showing the approximate position (−−) of the hydrogen bubble wire. The s=0.77 m measurement station is also shown ($\diamond$).

The Case 1 arrangement was removed and a new one was set up at the required position. To locate this position in the rig, the traverse was employed in a

similar way to that described in §4.4.1. The distance between the shims is 220 mm and the non-dimensional shim heights used in the calculation were $y^+ \approx 6$, which approximately corresponds with Case 1. The heights were again measured with the micrometre depth gauge. Inner-length scales are also similar at $l^+ = \nu/Q_\tau \approx 0.11$ mm, so other non-dimensionalised measurements such as the 45° mirror height, are the same as Case 1. The movement of the camera and optics was carried out as described §4.4.1.

A further complication in this three-dimensional experiment is where to position the interrogation window in each image, as the streaks are not perpendicular to the generator line. Noted above, the spanwise (i.e. n-axis) spacing between the streaks must be measured along the generator line. Each interrogation window therefore had to be rotated to align it with the wire which is positioned along this line. If this was not carried out, the angle between the two would result in a streamwise distance developing between the wire and the window.

This complication is illustrated in Figure 5.25. These images show an example of the streaks in the Case 2 generator and compare the two possible arrangements of the interrogation window. In Figure 5.25a, where the window is aligned approximately with the streamwise direction, the streamwise distance between the window and the wire is longer on one side than the other. Figure 5.25b shows the preferred arrangement. The streak spacing obtained for each image using this arrangement is translated back into the streamwise direction afterwards. Figure 5.26 shows the final window orientation and position used. The image window is decreased in length to $\Delta x^+ \approx 312$ compared with Case 1 in order to keep the calculation as local to the wire as possible. Aside from this rotation and length adjustment, the remainder of the spacing calculation followed the procedure documented in the previous chapters.

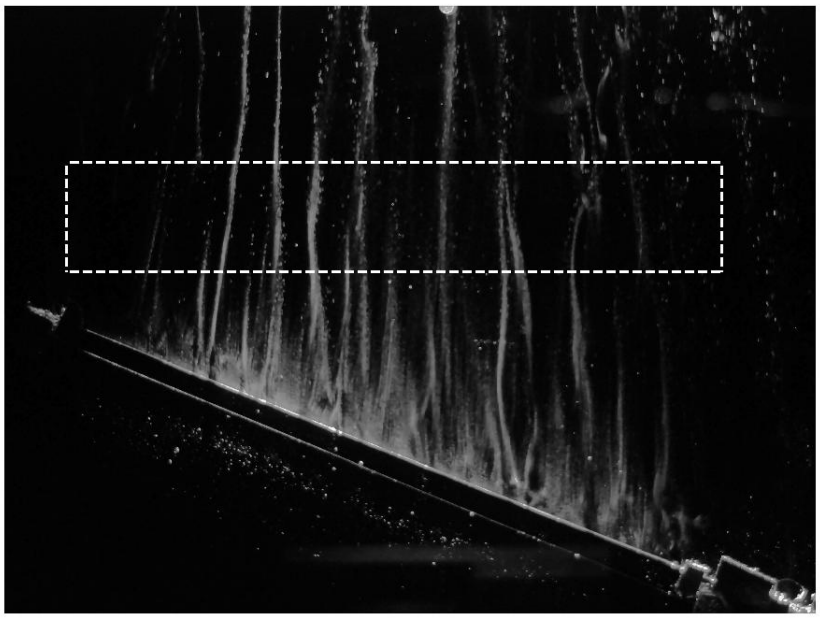

(a)

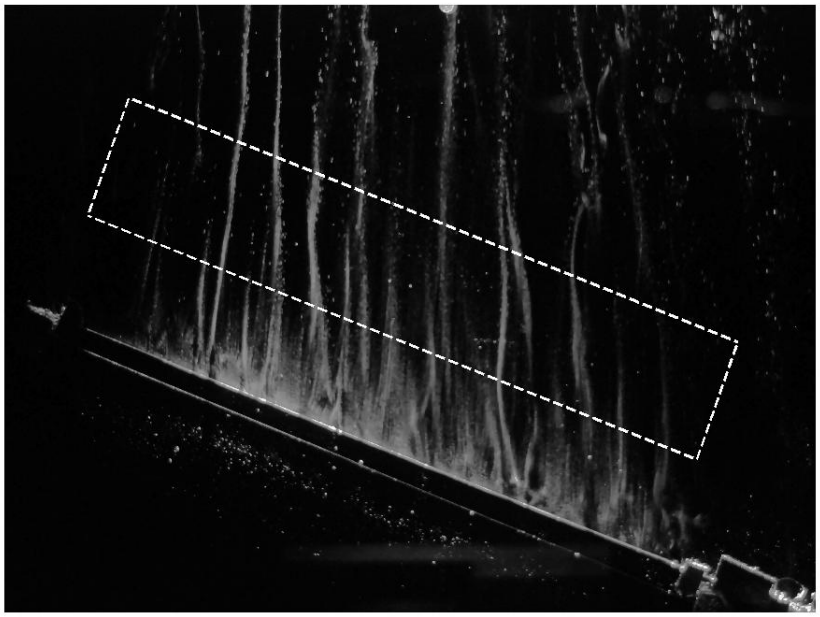

(b)

Figure 5.25: Two sample images showing the possible arrangements of the spacing calculation interrogation window (−−) in Case 2. (a) The window is approximately aligned with the freestream direction, (b) the window is aligned with the generator line and platinum wire.

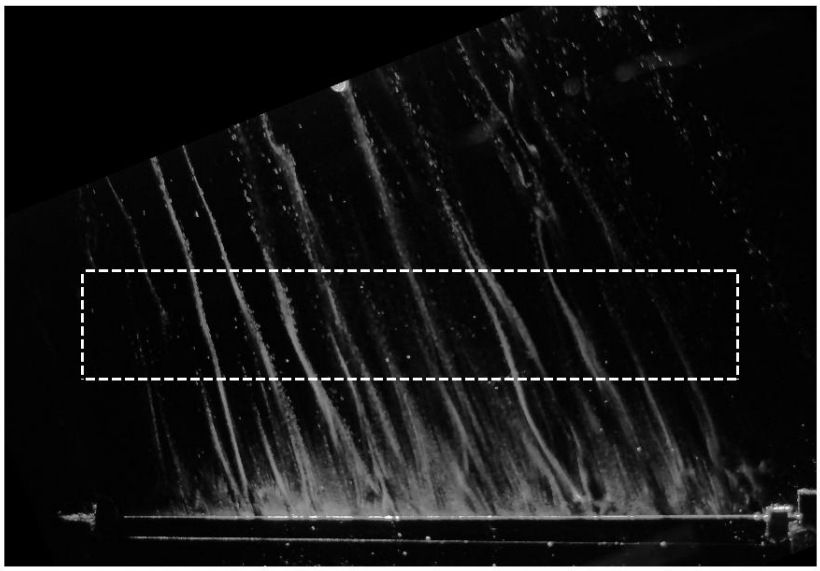

Figure 5.26: The final position of the interrogation window used in Case 2.

5.4.2 Visualisation Results

Some observations can already be made from the streak images shown in Figures 5.25 and 5.26. The favourable pressure gradient causes the same streamwise lengthening of the streaks that was seen in the Case 1 experiment. Near-wall streak 'bursting' activity is still present with streaks still wiggling as they go downstream. It may also be noted that the level of streak skewing is not large. This is highlighted in Figure 5.27 which shows the streaks and includes streamlines demonstrating the freestream direction. The mean-flow skewing between s=0.77 m to s=0.92 m was $(\gamma - \gamma_e) \approx 6^\circ$ to 11° so only a small amount of turning can be expected from the streaks.

The results of the streak spacing calculation are shown in in the Figure 5.28 and compared with the results from the Case 1. The data are presented in the same format used in §3.7.2 and §4.4.2; that is, histograms of the measurements and a log-normal PDF fitted to the data. $\bar{\lambda}^+$ increases by a similar order of magnitude to

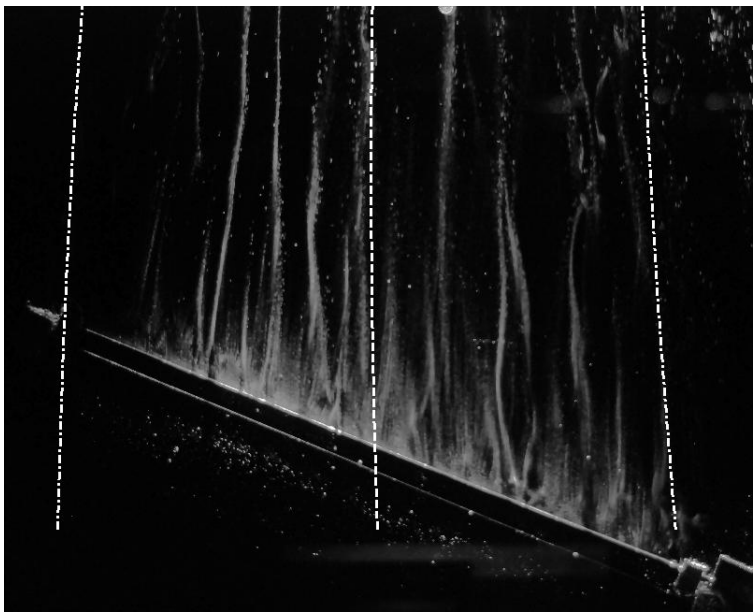

Figure 5.27: A sample streak image showing the centre (−−) and two other example (− · −) streamlines of the external flow. The streamwise direction is up the page and the crossflow direction is left to right.

Case 1 so must be must ascribed to the favourable pressure gradient. Changes in the other statistical moments, tabulated for this case in Figure 5.28, also show only marginal differences to Case 1. Evidently, the low-speed streaks are insensitive to the levels of mean-flow skewing generated in this experiment.

Observations in the literature about the effects of mean-flow skewing on the near-wall structures is limited and often appears contradictory. This was discussed in Chapter 2. Measurements of streak spacing were carried out in a curved duct flow by Flack (1997). The platinum wire in their duct was aligned with the radial axis of the duct curvature so streamwise and spanwise pressure gradients as well as the flow history of the near wall fluid will change along this line. Some evidence of a change in $\bar{\lambda}^+$ with increasing three-dimensionality was seen as it was Fleming and Simpson (1994 unpublished) in their complex wing body geometry.

The other three-dimensional studies discussed in Chapter 2, which consider the near-wall turbulent structures, are mostly shear-driven flows. These generally

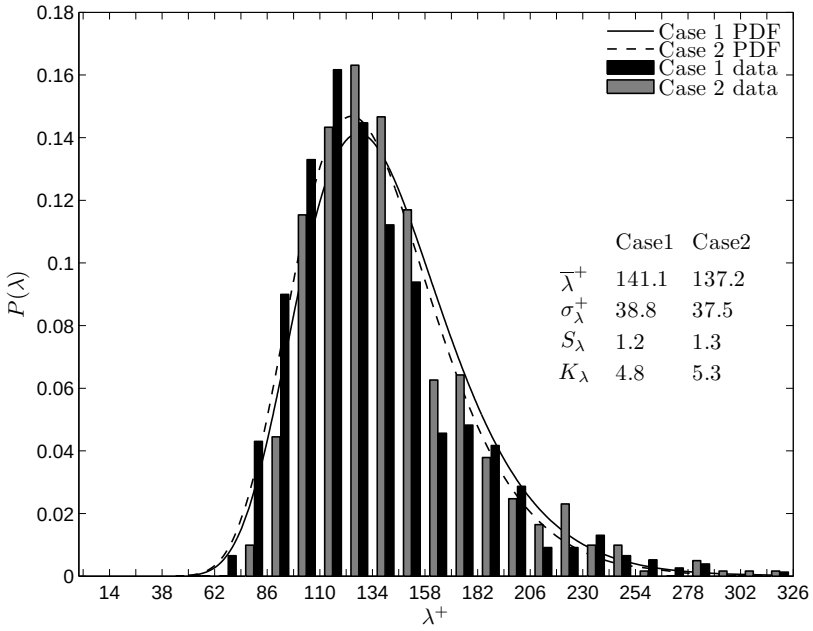

Figure 5.28: The Case 2 streak spacing results compared with Case 1.

showed a strong correspondence in the changes seen when the spanwise shear stress is applied. Most show the streaks to be 'broken up' into shorter, fewer structures. A 'layering' of the streaks and vortices is also hypothesised by some.

There are clear differences between the sheared and the pressure driven three-dimensional boundary layers. In the pressure-driven flows investigated here and by Flack (1997), the three-dimensionality in the boundary layer develops slowly and the streak structure appears to change little from its two-dimensional form. The reduction in streak spacing seen by Flack (1997) and Fleming and Simpson may be the result of the extraneous conditions in the experiments. Equally, conclusions cannot be furthered by the results here given the modest level of mean-flow skewing.

5.5 Chapter Summary

In this chapter the experimental approaches used previously for a turbulent boundary layer perturbed by a single favourable pressure gradient were applied to a pressure-driven three-dimensional turbulent boundary layer. As well as the spanwise

pressure gradient, the turbulent boundary layer was also subjected to a streamwise pressure gradient which had the same strength as the single component case, allowing the three-dimensional component to be examined relative to the streamwise strain effects.

The two pressure gradient components were generated using a novel approach which aims to overcome most of the complicating factors afflicting previous pressure-driven three-dimensional experiments. The design and implementation of the generator is described in §5.1 and is based on the properties of a free-spiral-vortex. The external flow pattern generated by this type of potential flow maintains streamwise and spanwise pressure gradient consistency over large areas, and therefore allows statistics such as streak spacing to be measured. The potential flow created in the experimental generator was measured in §5.2. The streamwise pressure gradient component was comparable to the single component case study, which was a necessary condition to compare the results from the two cases, and the magnitude of curvature in the external streamlines is of a similar order to many three-dimensional experiments.

Mean-flow measurements in the boundary layer are presented in §5.3.1 and §5.3.2. A significant level of three-dimensionality develops in the boundary layer, with the crossflow velocity reaching 11% that of the local freestream; a magnitude comparable to many three-dimensional experiments. The wall-normal location of the peak crossflow occurs just above the buffer layer. The Squire-Winter-Hawthorn relationship provided an agreeable description of the crossflow for the upper portion of the boundary layer. The behaviour of the fluid towards the wall proved less reliable, with more modest levels of skewing seen for a given level of freestream turning. At the furthest downstream measurement station, the near-wall flow had turned by $(\gamma - \gamma_e) \approx 9^\circ$ to 11°. A rightward shift of the mean-velocity hodograph is evident, conceivably caused by the acceleration. Hanjalic et al. (1994) also suggests that an acceleration may act to dampen the development of the crossflow.

Despite the magnitude of the crossflow velocity, the turbulent boundary layer proved relatively insensitive to the skewing, as seen in §5.3.3, §5.3.4 and §5.3.5, where the fluctuating velocity measurements and spectra are shown. At similar levels of crossflow, the turbulence in many three-dimensional flows undergoes much greater changes. No boundary layer stabilisation or destabilisation effect is caused by the additional strain, and the recognisable influence of the acceleration is evident to the same degree as Case 1. The similarity between the cases helps reinforce the observations made in the previous chapter regarding the effects of the streamwise pressure gradient.

A similar insensitivity to the skewing was observed in the near-wall low-speed streaks in §5.4. The visualisation procedure developed in previous chapters was reapplied with slight modification in the three-dimensional turbulent boundary layer at a comparable streamwise distance to the single pressure component case (§5.4.1). The results are given in §5.4.2 and the changes in mean streak spacing between the two cases was found to be marginal. The streaks showed all the characteristics from the favourable pressure gradient and bursting activity was still present. It may be concluded that any effects on the turbulent boundary layer that might be induced by the streamline curvature, are being dominated by the streamwise pressure gradient.

Chapter 6

Numerical Study

In this chapter a numerical modelling strategy is adopted to investigate the near-wall disturbances in the boundary layer and their behaviour in different mean-velocity distributions. The mathematical method is described in §6.1 and the pertinent assumptions about the boundary layer dynamics are given. The numerical techniques are described in §6.2 where the integrity and accuracy of the model are also tested. In §6.3, the established approaches of optimal perturbations are introduced, and used to simulate the near-wall streaks in a turbulent boundary layer. In §6.4 the two-dimensional experimental data is substituted into the model and finally in §6.5, the perturbation response to an additional crossflow velocity component is simulated.

6.1 Computational Model

The previous chapter showed that a highly accelerated turbulent boundary is surprisingly insensitive to the introduction of a spanwise pressure gradient. The near-wall low-speed streaks also demonstrated little change despite the crossflow velocity approaching 11% that of the freestream. The observations in the literature addressing boundary layer three-dimensionality and turbulent structures (§2.2.4) suggests that

a modification of the near-wall streaky structure takes place, but there seems to be much discrepancy as to the magnitude and nature of this structural alteration. The modification of the near-wall streaks by the acceleration is more familiar in the literature, but the reasons behind the changes in both types of flow are still unclear. The changes to the streaks in the previous chapter were also in the presence of a large acceleration. It remains possible then, that subtle effects from the spanwise force are being obscured by the streamwise pressure gradient.

A computational investigation has therefore been performed to further explore the near-wall turbulence. A simplified model of the boundary layer dynamics is developed which permits the use of a known, undisturbed flow represented by the mean velocity and vorticity fields. Disturbances are then introduced by superposing perturbations on to the undisturbed field. The total flow field is therefore represented by the sum of a mean or 'base' flow and the perturbations. This approach is popular in studies of boundary layer transition, where the use of perturbations in a laminar background flow field is easily justified and a physical interpretation of the results is clear. The method has also had some recent success at reproducing some of the features of turbulent flows, including the viscous sublayer streaks.

6.1.1 Variables and Coordinate system

In what follows, the coordinate system is aligned with the local freestream direction such that $Q_e = U(\delta) = U_e$ and the flow decomposed into the orthogonal velocity components in the x, y and z directions. The flow field comprises an undisturbed base flow velocity field $\mathbf{Q}$ and vorticity field $\mathbf{\Omega}$ on which the perturbation flow field velocity $\mathbf{q'}$ and vorticity ω' are superposed. The total flow field is therefore described by:

$$\mathbf{q} = \mathbf{Q} + \mathbf{q'} = \begin{bmatrix} U + u' \\ V + v' \\ W + w' \end{bmatrix} \qquad \omega = \mathbf{\Omega} + \omega' = \begin{bmatrix} \Omega_x + \omega'_x \\ \Omega_y + \omega'_y \\ \Omega_z + \omega'_z \end{bmatrix}$$

To keep the modelling simple, the parallel flow assumption is made, which may be justified by the small time scales being investigated. Streamwise and spanwise curvature effects will consequently be small compared to local length scales. Further, as the crossflow velocity generated in the Case 2 experiment was small, any spanwise velocity is assumed steady. The base flow is known from the mean-velocity field and is assumed to satisfy the following conditions: $V = 0$; $\Omega_y = 0$. The perturbations are also assumed independent of the streamwise (x) direction. The mean vorticity components are then described by:

$$\Omega_x = \frac{\partial W}{\partial y} \qquad \Omega_y = 0 \qquad \Omega_z = -\frac{\partial U}{\partial y}$$

The perturbation vorticity components are described by:

$$\omega'_x = \frac{\partial w'}{\partial y} - \frac{\partial v'}{\partial z} \qquad \omega'_y = \frac{\partial u'}{\partial z} \qquad \omega'_z = -\frac{\partial u'}{\partial y}$$

One boundary condition on the fluctuating flow field is imposed by no-slip at the wall ($y = 0$):

$$u'(0,t) = 0 \tag{6.1}$$

$$v'(0,t) = 0 \tag{6.2}$$

$$w'(0,t) = 0 \tag{6.3}$$

and far from the wall the perturbation velocities are assumed to become negligible:

$$u'(\infty,t) = 0 \tag{6.4}$$

$$v'(\infty,t) = 0 \tag{6.5}$$

$$w'(\infty,t) = 0 \tag{6.6}$$

To enforce the boundary conditions for the velocity gradients, dummy 'nodes' are

introduced above and below the domain. These have no effect other than to enforce the correct conditions at the boundaries.

For the form of the solution, the following ansatz is made:

$$\mathbf{q}'(y,z,t) = \hat{q}(y,t)e^{i\beta z} \tag{6.7}$$

$$\omega'(y,z,t) = \hat{\omega}(y,t)e^{i\beta z} \tag{6.8}$$

which is discussed further in §6.3. The vorticity perturbation components become:

$$\omega_x' = \frac{\partial}{\partial y}(\hat{w}e^{i\beta z}) - i\beta(\hat{v}e^{i\beta z}) \tag{6.9}$$

$$\omega_y' = i\beta(\hat{u}e^{i\beta z}) \tag{6.10}$$

$$\omega_z' = -\frac{\partial u'}{\partial y} \tag{6.11}$$

The continuity equation for the perturbed velocities becomes:

$$\frac{\partial}{\partial y}(\hat{v}e^{i\beta z}) + i\beta(\hat{w}e^{i\beta z}) = 0 \tag{6.12}$$

If equation (6.12) is differentiated with respect to the wall-normal height y:

$$\frac{1}{i\beta}\frac{\partial^2}{\partial y^2}(\hat{v}e^{i\beta z}) = -\frac{\partial}{\partial y}(\hat{w}e^{i\beta z}) \tag{6.13}$$

equation (6.9) can be used to write the streamwise vorticity as:

$$\omega_x' = -\frac{1}{i\beta}\frac{\partial^2}{\partial y^2}(\hat{v}e^{i\beta z}) - i\beta(\hat{v}e^{i\beta z}) \tag{6.14}$$

6.1.2 Governing Equations

A velocity-vorticity formulation of the Navier-Stokes equations is employed and the equations governing the flow are given by the transport equations for the streamwise perturbation velocity and vorticity. Only the initial development of the perturba-

tion field is being investigated in this thesis, a point further discussed below, which permits use of the linearised governing equations. Linearisation makes the modelling and simulation times more manageable. In the flow field assumed above, the (linearised) dimensionless equation for the streamwise vorticity of the perturbation becomes:

$$\frac{\partial \omega_x'}{\partial t} + v' \frac{\partial \Omega_x}{\partial y} + W \frac{\partial \omega_x'}{\partial z} = \Omega_z \frac{\partial u'}{\partial z} + \omega_y' \frac{\partial U}{\partial y} + \frac{1}{Re}\left[\frac{\partial^2 \omega_x'}{\partial y^2} + \frac{\partial^2 \omega_x'}{\partial z^2}\right] \tag{6.15}$$

If the vorticity components Ω_z and ω_y' are replaced with their velocity equivalents, the following simplification of equation (6.15) can be reached:

$$\frac{\partial \omega_x'}{\partial t} + v' \frac{\partial \Omega_x}{\partial y} + W \frac{\partial \omega_x'}{\partial y} = \frac{1}{Re}\left[\frac{\partial^2 \omega_x'}{\partial y^2} + \frac{\partial^2 \omega_x'}{\partial z^2}\right] \tag{6.16}$$

The ansatz forms of the perturbation ($\omega_x' = -\frac{1}{i\beta}\frac{\partial^2}{\partial y^2}(\hat{v}e^{i\beta z}) - i\beta(\hat{v}e^{i\beta z})$; $v' = \hat{v}e^{i\beta z}$) are now substituted into equation (6.16), which becomes:

$$\begin{aligned}\frac{\partial}{\partial t}\left\{-\frac{1}{i\beta}\frac{\partial^2}{\partial y^2}(\hat{v}e^{i\beta z}) - i\beta(\hat{v}e^{i\beta z})\right\} + (\hat{v}e^{i\beta z})\frac{\partial^2 W}{\partial y^2} + W\left\{\beta^2(\hat{v}e^{i\beta z}) - \frac{\partial^2}{\partial y^2}(\hat{v}e^{i\beta z})\right\} \\ = \frac{1}{Re}\left[\frac{\partial^2}{\partial y^2}\left\{-\frac{1}{i\beta}\frac{\partial^2}{\partial y^2}(\hat{v}e^{i\beta z}) - i\beta(\hat{v}e^{i\beta z})\right\} - i\beta\frac{\partial^2}{\partial y^2}(\hat{v}e^{i\beta z}) + i\beta^3(\hat{v}e^{i\beta z})\right]\end{aligned} \tag{6.17}$$

To simplify the notation and equation (6.17), $\hat{v}e^{i\beta z}$ is replaced with $\tilde{v}$ and the equation is made dimensionless with the friction velocity and and viscosity (equivalent to Re=1). After rearranging and simplifying, equation (6.17) becomes:

$$i\beta\frac{\partial \tilde{v}}{\partial t} - \frac{i}{\beta}\frac{\partial}{\partial t}\left[\frac{\partial^2 \tilde{v}}{\partial y^2}\right] + \tilde{v}\left[i\beta^3 - \frac{\partial^2 W}{\partial y^2} - \beta^2 W\right] + \frac{\partial^2 \tilde{v}}{\partial y^2}[W - 2i\beta] - \frac{1}{i\beta}\frac{\partial^4 \tilde{v}}{\partial y^4} = 0 \tag{6.18}$$

This is simplified to:

$$i\beta\frac{\partial \tilde{v}}{\partial t} - \frac{i}{\beta}\frac{\partial}{\partial t}\left[\frac{\partial^2 \tilde{v}}{\partial y^2}\right] + \hat{v}A + \frac{\partial^2 \tilde{v}}{\partial y^2}B - \frac{1}{i\beta}\frac{\partial^4 \tilde{v}}{\partial y^4} = 0 \tag{6.19}$$

by collecting and defining the terms:

$$A = \left[i\beta^3 - \frac{\partial^2 W}{\partial y^2} - \beta^2 W \right] \tag{6.20}$$

$$B = [W - 2i\beta] \tag{6.21}$$

The (dimensionless) transport equation for streamwise velocity perturbations in the flow field reads:

$$\frac{\partial u'}{\partial t} + W\frac{\partial u'}{\partial z} + v'\frac{\partial U}{\partial y} = \frac{\partial^2 u'}{\partial y^2} + \frac{\partial^2 u'}{\partial z^2} \tag{6.22}$$

After substituting in the simplified forms of the perturbation ansatz ($v' = \hat{v}e^{i\beta z} = \tilde{v}$ and $\tilde{u} = \hat{u}e^{i\beta z} = u'$), equation (6.22) becomes:

$$\frac{\partial \tilde{u}}{\partial t} + \tilde{u}(i\beta W + \beta^2) - \frac{\partial^2 \tilde{u}}{\partial y^2} + \tilde{v}\frac{\partial U}{\partial y} = 0 \tag{6.23}$$

6.2 Numerical Scheme

The governing equations are solved using a Crank-Nicholson numerical scheme. For the wall-normal perturbation velocities, the following temporal discretisation results:

$$\frac{\partial \tilde{v}}{\partial t} = \frac{\tilde{v}^{n+1} - \tilde{v}^n}{\Delta t} \tag{6.24}$$

$$\tilde{v} = \frac{\tilde{v}^{n+1} + \tilde{v}^n}{2} \tag{6.25}$$

$$\frac{\partial^2 \tilde{v}}{\partial y^2} = \frac{1}{2}\left(\frac{\partial^2 \tilde{v}^{n+1}}{\partial y^2} + \frac{\partial^2 \tilde{v}^n}{\partial y^2} \right) \tag{6.26}$$

$$\frac{\partial^4 \tilde{v}}{\partial y^4} = \frac{1}{2}\left(\frac{\partial^4 \tilde{v}^{n+1}}{\partial y^4} + \frac{\partial^4 \tilde{v}^n}{\partial y^4} \right) \tag{6.27}$$

The discretised forms are substituted into equation (6.19) which, after rearranging, becomes:

$$\frac{i\beta}{\Delta t}\tilde{v}^{n+1} + \frac{A}{2}\tilde{v}^{n+1} - \frac{i}{\beta\Delta t}\frac{\partial^2\tilde{v}^{n+1}}{\partial y^2} + \frac{B}{2}\frac{\partial^2\tilde{v}^{n+1}}{\partial y^2} + \frac{i}{2\beta}\frac{\partial^4\tilde{v}^{n+1}}{\partial y^4} = \frac{i\beta}{\Delta t}\tilde{v}^{n} - \frac{A}{2}\tilde{v}^{n} - \frac{i}{\beta\Delta t}\frac{\partial^2\tilde{v}^{n}}{\partial y^2} - \frac{B}{2}\frac{\partial^2\tilde{v}^{n}}{\partial y^2} - \frac{i}{2\beta}\frac{\partial^4\tilde{v}^{n}}{\partial y^4} \quad (6.28)$$

where A and B were defined above. The following terms are now defined:

$$C = \left[\frac{i\beta}{\Delta t} + \frac{A}{2}\right]$$
$$D = \left[\frac{B}{2} - \frac{i}{\beta\Delta t}\right]$$
$$E = \left[\frac{i}{2\beta}\right]$$
$$F = \left[\frac{i\beta}{\Delta t} - \frac{A}{2}\right]$$
$$G = \left[-\frac{B}{2} - \frac{i}{\beta\Delta t}\right]$$
$$H = \left[-\frac{i}{2\beta}\right]$$

and, substituted into equation (6.28), the final form of the streamwise vorticity equation is reached:

$$C\tilde{v}^{n+1} + D\frac{\partial^2\tilde{v}^{n+1}}{\partial y^2} + E\frac{\partial^4\tilde{v}^{n+1}}{\partial y^4} = F\tilde{v}^{n} + G\frac{\partial^2\tilde{v}^{n}}{\partial y^2} + H\frac{\partial^4\tilde{v}^{n}}{\partial y^4} \quad (6.29)$$

A similar temporal discretisation is performed for the streamwise perturbation velocity equation. For the wall-normal perturbation velocity, the following approximation is used:

$$\bar{v} = \frac{\tilde{v}^{n-1} + \tilde{v}^{n}}{2} \quad (6.30)$$

The final form of the streamwise perturbation velocity equation is:

$$AX\tilde{u}^{n+1} + BX\frac{\partial^2\tilde{u}^{n+1}}{\partial y^2} = CX\tilde{u}^{n} + DX\frac{\partial^2\tilde{u}^{n}}{\partial y^2} - \bar{v}\frac{\partial U}{\partial y} \tag{6.31}$$

where the following simplifying terms have been employed:

$$\begin{aligned} AX &= \left[\frac{1}{\Delta t} + \frac{i\beta W}{2} + \frac{\beta^2}{2}\right] \\ BX &= \left[-\frac{1}{2}\right] \\ CX &= \left[\frac{1}{\Delta t} - \frac{i\beta W}{2} - \frac{\beta^2}{2}\right] \\ DX &= \left[\frac{1}{2}\right] \end{aligned}$$

The Crank-Nicholson scheme requires central differences be used for spatial discretisation. For the wall-normal perturbation velocity, second order terms are estimated using:

$$\frac{\partial^2\tilde{v}}{\partial y^2} = \frac{\tilde{v}(y_{j+1}) - 2\tilde{v}(y_j) + \tilde{v}(y_{j-1})}{\Delta y^2} \tag{6.32}$$

where the discrete spatial locations are indexed j=$[1, ..., N]$ and N is the total number of coordinates used. N=1000 for all simulations carried out in this Chapter. Fourth order terms are calculated as:

$$\frac{\partial^4\tilde{v}}{\partial y^4} = \frac{\tilde{v}(y_{j+2}) - 4\tilde{v}(y_{j+1}) + 6\tilde{v}(y_j) - 4\tilde{v}(y_{j-1}) + \tilde{v}(y_{j-2})}{\Delta y^4} \tag{6.33}$$

Similar expressions are defined for the $\tilde{u}$ velocity components. Using these definitions, the spatial discretisation may be summarised in matrix form by defining the pentadiagonal matrices M_L and M_R in the vorticity equation, and N_L and N_R in the boundary layer equation (the subscripts L and R denote left and right respectively). For example, each row of the matrix M_L is populated with the following components:

$$
\begin{aligned}
M_L(j-2) &= E/\Delta y^4 \\
M_L(j-1) &= -4E/\Delta y^4 + D/\Delta y^2 \\
M_L(j) &= 6E/\Delta y^4 - 2D/\Delta y^2 + C \\
M_L(j+1) &= -4E/\Delta y^4 + D/\Delta y^2 \\
M_L(j+2) &= E/\Delta y^4
\end{aligned}
$$

where again, j indexes the discretised wall-normal height y_j. For the coordinates: $j = 1, 2, ..., N-1, N$, a one-sided sixth-order finite difference approximation is employed to approximate first derivatives. The values of the coefficients at each coordinate can be found in tables (Abramowitz and Stegun, 1973).

The spatial discretisation step for $\tilde{v}^{n+1}$ may be performed by multiplication with M_L. Using these definitions, the streamwise perturbation vorticity equation can be written as

$$M_L\tilde{v}^{n+1} = M_R\tilde{v}^n \tag{6.34}$$

and the streamwise perturbation velocity expressed as:

$$N_L\tilde{u}^{n+1} = N_R\tilde{u}^n - \bar{v}\frac{\partial U}{\partial y} \tag{6.35}$$

A simple description of the solution process follows from these equations. At each time step, the spatial discretisation of $\tilde{v}^n$ is performed by simple multiplication:

$$M_R\tilde{v}^n \tag{6.36}$$

$\tilde{v}^{n+1}$ is then calculated by multiplication with the inverse of the left hand matrix:

$$\tilde{v}^{n+1} = M_L^{-1} M_R \tilde{v}^n \tag{6.37}$$

The average between the two approximations, $\bar{v}$, is then used in the spatial discretisation step of the streamwise velocity:

$$N_R \tilde{u}^n - \bar{v} \frac{\partial U}{\partial y} \tag{6.38}$$

$\tilde{u}^{n+1}$ is then calculated by multiplication by the inverse of the left hand side matrix:

$$\tilde{u}^{n+1} = N_L^{-1} \left(N_R \tilde{u}^n - \bar{v} \frac{\partial U}{\partial y} \right) \tag{6.39}$$

The spanwise perturbation velocity $\tilde{w}^{n+1}$ follows from continuity. One advantage of this numerical scheme is that the inverse matrices M^{-1} and N^{-1} need only be calculated once at the beginning of each simulation, dramatically reducing the computational time.

6.2.1 Numerical Integrity

To test the numerical performance, simulations have been performed to investigate the effects of Reynolds number and resolution. The base-flow velocity field used during the testing procedure is the two-dimensional turbulent boundary layer formed in a channel, under zero-pressure-gradient conditions. This is described by a Spalding-Coles velocity profile given in §3.6.1. Initial conditions are required for the perturbation velocities and the following forms are chosen:

$$\tilde{u}(y, 0) = 0 \tag{6.40}$$

$$\tilde{v}(y, 0) = \hat{v} e^{-b(y-y_f)^2} e^{-i\beta z} \tag{6.41}$$

The spanwise component $\tilde{w}$ can be calculated again from continuity. This form generates a Gaussian function for $\tilde{v}$ whose wall-normal thickness is governed by the parameter b. The constant y_f determines the wall-normal height of the perturbation profile and β is the spanwise wavenumber. These quantities are fixed for all tests.

Resolution

The effects of varying the time-step length Δt and grid spacing Δy are investigated as well as the overall height of the computational domain h. The base-flow velocity profile in the resolution tests has a Reynolds number and non-dimensional freestream velocity of Re_{δ^*}=10,000 and U_e^+=26. First, however, a suitable run time for the simulation is required. This is governed by the parameter τ. If the run time is too short then the perturbation may still be developing; too long and computational effort will be being wasted. Figure 6.1 shows what effect changing the non-dimensional simulation length τ^+ has on the perturbation velocity components. Figure 6.1a shows the profile of the streamwise perturbation velocity (u'^+) at the end of the simulation time, $t^+ = \tau^+$ and in Figure 6.1b, the wall-normal velocity component (v'^+) is shown. Clearly, τ^+=2 is too short as the perturbation streamwise velocity component is still developing. By τ^+=20, the perturbation has reached a peak magnitude and is now slowing down. τ^+=20 is therefore used for the remainder of the validation tests.

In Figure 6.2, the effect of varying the grid spacing and domain height are shown. Again, streamwise velocity profiles are shown in Figure 6.2a and wall-normal profiles in Figure 6.2b. The profiles show the results corresponding to t^+=τ^+=20. Neither parameter appears to affect the results significantly; at least for values of grid spacing required. The greatest changes occur around the peak of the perturbation when the grid spacing is widest. A spatial resolution of Δy^+=0.4 is more than sufficient and altering the domain height has a negligible effect.

Finally, the effect of changing the time on the perturbation velocity profile

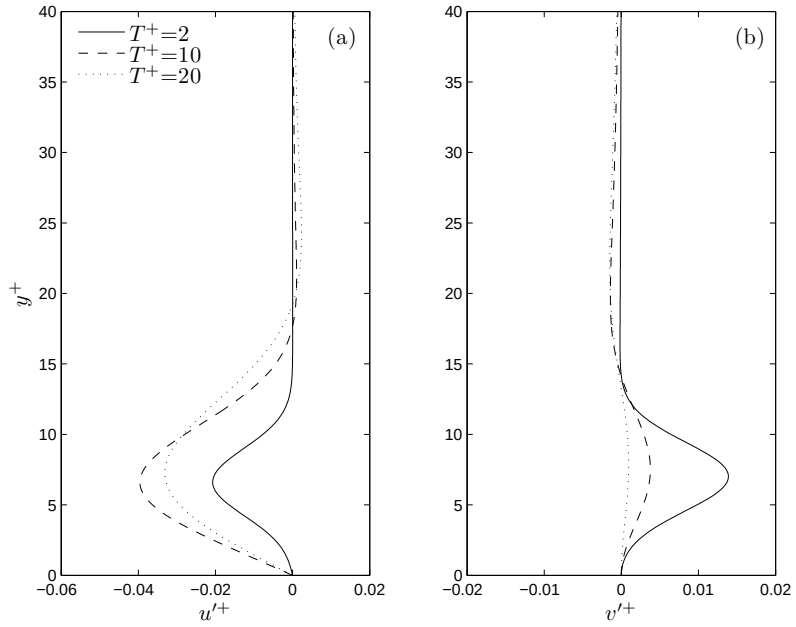

Figure 6.1: Profiles of the perturbation velocity components showing the disturbance at the end of the simulation period $t = \tau^+$ for different values of τ^+: (a) the streamwise velocity u'^+; (b) the wall-normal velocity v'^+.

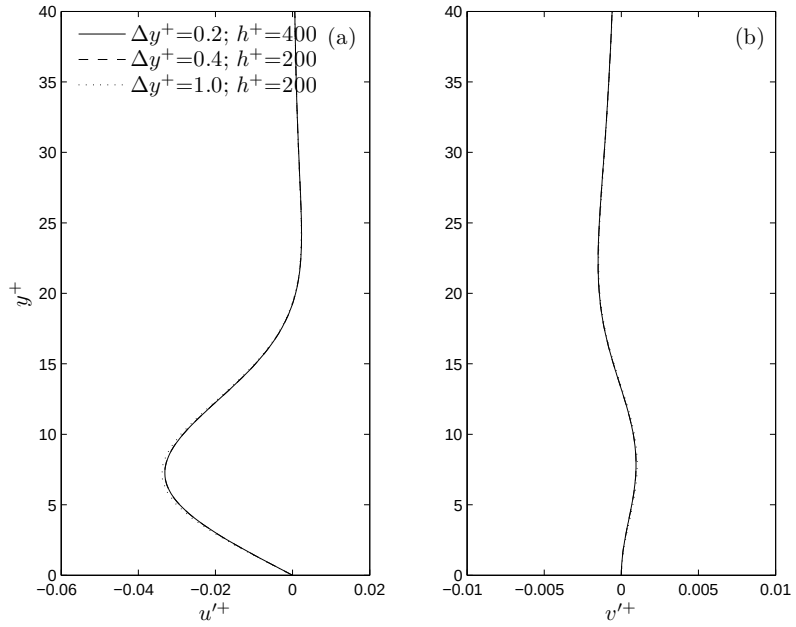

Figure 6.2: Velocity profiles of the perturbation at $t = \tau^+$ showing the effect of changing the domain height and grid resolution: (a) the streamwise velocity u'^+; (b) the wall-normal velocity v'^+. For the values tested, the perturbation is not affected strongly by the grid resolution or the domain height.

is shown in Figure 6.3. Even at the coarsest temporal resolutions, the impact of increasing Δt^+ is practically negligible. Though not evident in the figure, the peak is slightly larger for Δt^+=2; Δt^+=1 is consequently used in the remainder of the tests.

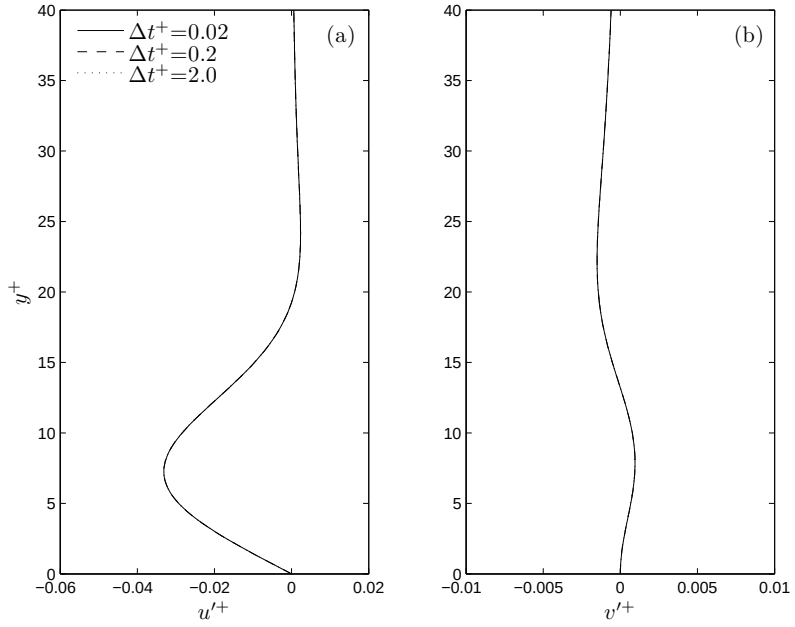

Figure 6.3: The effect of changing time step length between $0.02 \leq \Delta t^+ \geq 2.0$ on the perturbation velocity components at $t = \tau^+$: (a) the streamwise perturbation velocity u'^+; (b) the wall-normal perturbation velocity v'^+. The correspondence between the curves shows the negligible effect changing Δt^+ has on the perturbation, for the values used.

Reynolds Number

Changes to the base-flow profile are now investigated. The experimental flows generated in the flow rig have a low Reynolds number which gives the mean-velocity profiles certain characteristic features such as a smaller log region and slight changes around the buffer regions. It is important then that the model is suitable for these low Reynolds number profiles. Figure 6.4 shows the effect on u'^+ and v'^+ of reducing the Reynolds number of the Spalding-Coles velocity profile from Re_{δ^*}=5,000 to Re_{δ^*}=600, which corresponds with the experimental study. Clearly, the Reynolds

number has little effect on the growth of the perturbation at these values, which is anticipated given the similarity in the near-wall regions. Significant changes to the near-wall mean-velocity profile occur only at very low Reynolds numbers ($Re_\tau \approx 180$). Low Reynolds number effects were discussed further in §4.4.

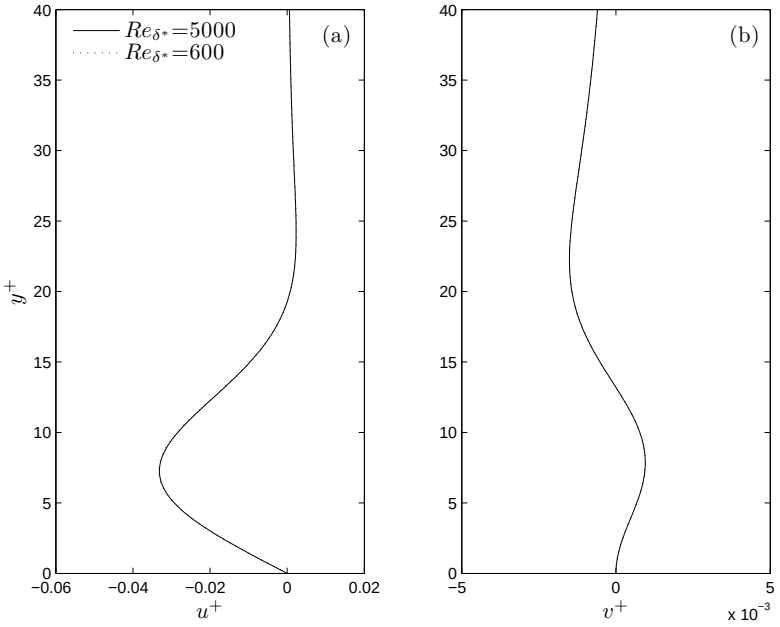

Figure 6.4: The effect of reducing the Reynolds number on the perturbation velocity components: (a) the streamwise velocity u'^+; (b) the wall-normal velocity v'^+.

6.3 Optimum Perturbations and Streak Modelling

In order to study the effects of a mean streamwise vorticity on the streaks, it is necessary to simulate the streaks themselves. The method here involves the use of 'optimal' perturbations. Landahl (1980) showed that an arbitrary three-dimensional disturbance in an inviscid shear flow can experience growth via the 'lift-up' mechanism which behaves linearly for short time scales. To distinguish it from the exponential growth of Tollmien-Schlichting waves it is termed *algebraic* growth. The optimal perturbations, as described by Corbett and Bottaro (2001), are the initial conditions of the arbitrary disturbances that produce the strongest or most 'ener-

getic' perturbations to the mean flow. The algebraic growth decays after a time due to viscous damping (Henningson et al., 1987; Hultgren and Gustavsson, 1981) and the combination of these mechanisms is called *transient* growth. Despite the damping, Henningson et al. (1993) showed that transient growth can be a mechanism for transition. Using DNS, they found that some disturbances can achieve sufficient growth to cause the appearance of turbulent spots in the boundary layer. This boundary-layer transition mechanism occurs independently of Tollmien-Schlichting (T-S) instability and therefore 'bypasses' the conventional instability mechanisms.

The lift-up mechanism has since been thought to play a role in the formation of the sub-layer streaks in turbulent boundary layers. This connection has been made by Landahl (1990), Butler and Farrell (1992, 1993) and Kim and Lim (2000) and is drawn upon again here for the modeling of the viscous layer low-speed streaks. Butler and Farrell (1992) find the optimal perturbations for a variety of viscous shear flows. They further extended the technique by substituting the mean-velocity profile of a turbulent boundary layer for the base flow to their model (Butler and Farrell, 1993). It is assumed during their analysis that the initial disturbances are localised to the viscous layers and the model is linearised, hence, only valid for short time periods after the initiation of growth. Nevertheless, the optimal perturbations found have a strong resemblance to the viscous sublayer streaks; sharing the same non-dimensional mean spanwise spacing and Reynolds number independence.

6.3.1 Initial Conditions and Optimum Definition

Following optimal perturbation procedure, the low-speed streaks are introduced into the model by assuming a suitable form of the initial perturbation velocities and then simulating the growth or otherwise of these disturbances. The optimal perturbation will be sought to model the low-speed streaks and their dependence on the mean-velocity field investigated with the use of different base-flow profiles. The results of similar analyses such as of Butler and Farrell (1993) suggests that an optimal

perturbation should have characteristics similar to the following:

$$u'(0,t) = \hat{u}(y)e^{i\beta z} = 0 \tag{6.42}$$

$$v'(0,t) = \hat{v}(y)e^{i\beta z} \tag{6.43}$$

$$w'(0,t) = \hat{w}(y)e^{i\beta z} \tag{6.44}$$

This was applied above in equation (6.8). The requirement that the perturbation velocity satisfy the boundary conditions at the wall and for large y, leads to the following as a reasonable simplified initial perturbation form:

$$\hat{u} = 0 \tag{6.45}$$

$$\hat{v} = y^2 e^{-by^2} \tag{6.46}$$

and from continuity:

$$\hat{w} = -\frac{i\beta y^3 - 2y}{\beta} e^{-by^2} \tag{6.47}$$

where the parameters b and β are fixed. β is the spanwise wavenumber of the perturbation, and the constant b sets the height of the peak in perturbation amplitude to $y = 1/\sqrt{b}$ from the wall. Only the real part of the disturbance velocity is used for the physical interpretation of the results. An investigation can then made to find the combination of b and β that achieve the maximum growth of the disturbance. Duque-Daza et al. (2012) employ an identical form for their initial condition as that used here successfully, to simulate the effect from waves of spanwise velocity, traveling in the streamwise direction, on the growth of the low-speed streaks.

A definition of 'growth' has yet to be made and this will clearly depend on the underlying assumptions about the physical nature of the disturbance and their relationship to the base flow. It has been assumed that the lift-up mechanism behind the growth of the perturbations in shear flows is representative of that responsible for near-wall streaks in a turbulent boundary layer. It is therefore tempting to base

the optimum conditions on the streamwise velocity component. This strategy was used by Lockerby et al. (2005) and Carpenter et al. (2007). Their model differs slightly to the typical optimal perturbation approach and makes use of a submerged vortex sheet to force the growth of streaks. Generally, a search is made for those disturbances that gain the largest growth in kinetic energy within some time period, τ (Corbett and Bottaro, 2001). Butler and Farrell (1993) also use this definition to search for linear disturbances in a turbulent velocity profile and achieve some success. Consequently, the kinetic energy is also used here and defined as:

$$E(t) = \frac{1}{2}\int_0^\infty (|\tilde{u}^2| + |\tilde{v}^2| + |\tilde{w}^2|)dy \tag{6.48}$$

The optimum perturbation is that which achieves the greatest growth, G, in kinetic energy within the time period τ:

$$G(t) = \frac{E(t)}{E(0)} \tag{6.49}$$

where $E(0)$ is the initial unit energy of the perturbation. The value of a suitable growth period τ must be determined and again depends on the flows being considered.

6.3.2 Model Validation

To validate the model, a number of tests are performed and the results are compared with the literature. Particular attention is paid to the results of Butler and Farrell (1992, 1993) as their methods differ only slightly to those here. For the validation procedure, the base flow velocity profile corresponds again to a turbulent boundary layer with a Reynolds number Re_{δ^*}=10,000, U_e^+=26.6.

First, the non-dimensional simulation time τ^+ is tested. τ^+ is varied from 40 to 120 and the parameter space (b^+,β^+) is searched for each τ^+ to find the combination which maximises the perturbation amplitude G. The results of the test

are shown in Figure 6.5. Figure 6.5a shows the non-dimensional spanwise spacing $\lambda^+ = 2\pi/\beta^+$ of the optimum perturbations obtained at the end of the simulation $t^+ = \tau^+$, as for most of the simulations the maximum amplitude G occurs at this time. The results of of Butler and Farrell (1993) are also shown. Figure 6.5b shows similar results, but the energy corresponds to the maximum disturbance amplitude G during the simulation. The slight differences between the figures for the lower wavenumbers means that these disturbances achieve a maximum growth before the end of the simulation at $t^+=\tau^+$. The remainder continue to grow until $t^+=\tau^+$ when the the simulation ends.

Figure 6.5a is in good agreement with the results of Butler and Farrell (1993), though the energy gained by in their model is 25-30% above the levels reached here. It is interesting that the results share the distinctive log-normal PDF shape as the spanwise distribution of the sublayer low-speed streaks (see §3.7.2). It should be noted that Butler and Farrell (1993) optimised for the maximum amplitude within the time τ^+. Their results however, correspond to $G(\tau^+)$ not maximum G and the difference is highlighted in Figure 6.5

Butler and Farrell (1993) consider that the duration allowed for the growth must be shorter than the eddy turnover time (τ_e), as non-linear effects and turbulence will disrupt the growing structures after this time is reached. As eddy turnover time increases with boundary layer height, the 'optimisation' time τ^+ must be a function of y^+. Setting τ^+=80, they find the 'global' optimum to correspond with a spanwise wavelength of λ^+=110 and the peak in the streamwise velocity occurs at $y^+\approx$19. τ^+=80 was selected as above this value, the peak disturbance velocity occurs in a region where the eddy turnover time is shorter than τ^+. A similar procedure is carried out here by setting λ^+=110 and the optimisation process carried out only for the parameter b^+. Figure 6.6 shows a profile of the streamwise velocity for three values of the simulation time τ^+. The peak in streamwise velocity occurs at a wall-normal height of y^+=19.2; in agreement with Butler and Farrell (1993). A

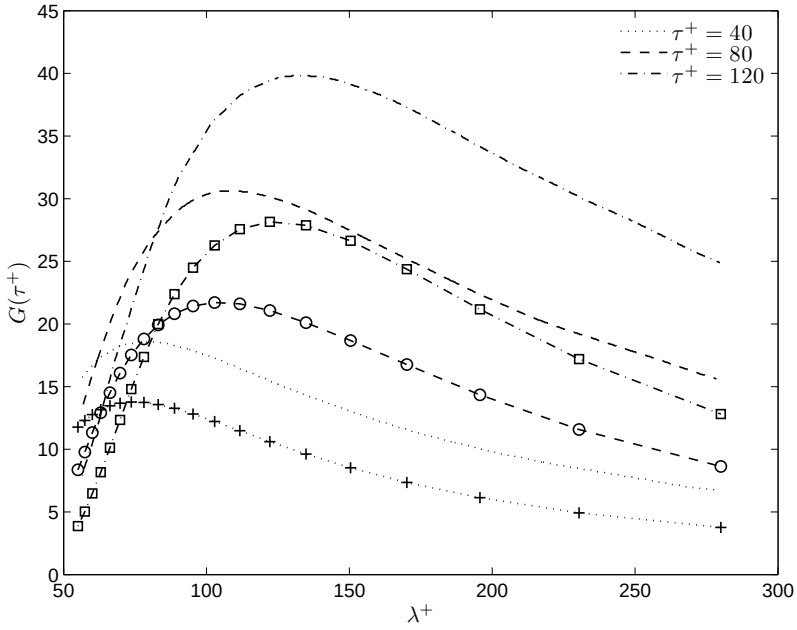

(a)

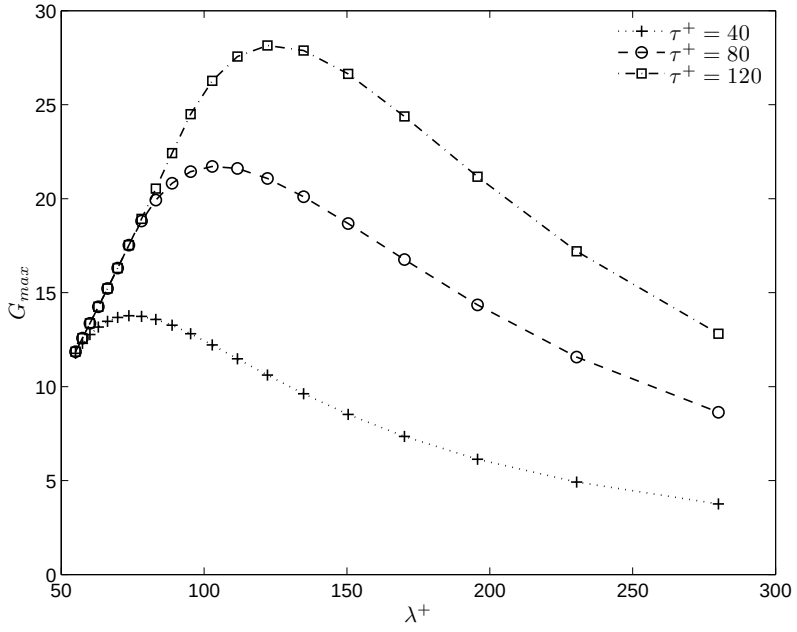

(b)

Figure 6.5: The spanwise wavelength of the perturbation (λ^+) versus the perturbation amplitude for various simulation times: (a) the disturbance corresponding to τ^+ (markers) compared with the results of Butler and Farrell (1993) (no markers); (b) disturbance at peak amplitude G.

similar 'global' optimum test was performed here to obtain the τ^+=80 results shown in Figure 6.5, but only for the two-parameters b^+ and β^+. The spanwise wavelength of the optimal disturbances corresponds to λ^+=104, which is similar to the results of Butler and Farrell (1993) and corresponds with the established spanwise spacing of the low-speed streaks.

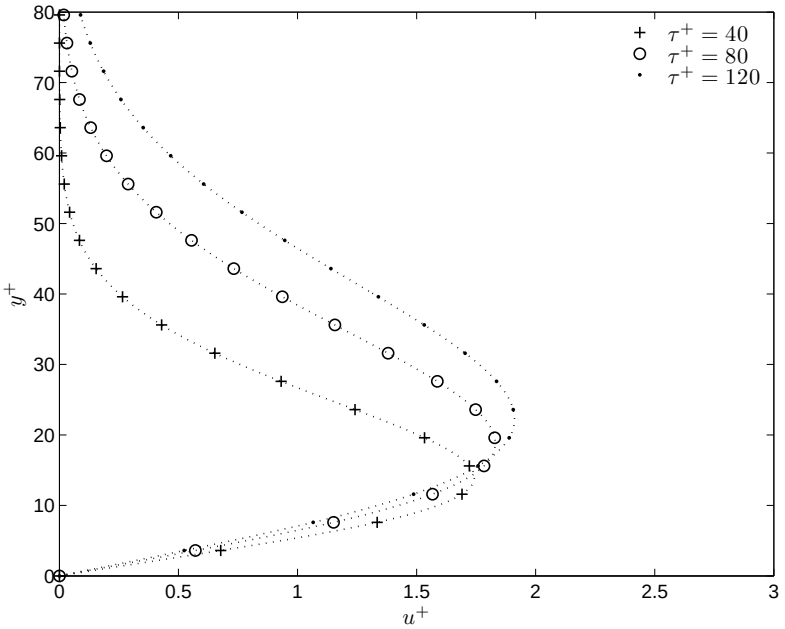

Figure 6.6: Profiles of the perturbation streamwise velocity component (u'^+) at t^+=τ^+=80 using λ^+=110.

6.4 Two-Dimensional Base Flow Tests

In this section, the base flow of the model is changed from a Spalding-Coles mean-velocity profile to the mean-flow measurements obtained experimentally. Only the two-dimensional flows are tested in this section, including the zero-pressure-gradient and Case 1 experiments. As no crossflow component is included (W=0), the slight mean-flow skewing measured in Case 1 (see §4.3.1) is omitted and the velocity component Q^+ is used for U^+ and assumed straight.

The raw experimental data cannot be substituted immediately into the nu-

merical model because the experimental wall-normal resolution of the measurements is far coarser than is needed (see §6.2.1). A curve is therefore fitted to the data and this sampled at discrete wall-normal heights. The samples can then be substituted for the base flow. The curve fitting procedure is documented in Appendix G.

6.4.1 Zero-Pressure-Gradient Profile Tests

The sampled velocity profiles of the zero-pressure-gradient results are sampled using a spatial resolution of Δy^+=0.4. The sampled data is then substituted into the base flow of the numerical model. The optimisation process is performed using a simulation or 'optimisation' time of τ^+=80 and the perturbation is optimised for the two parameters b^+ and β^+. The results of the optimisation procedure are displayed in Figure 6.7, which demonstrates how the disturbance amplitude varies with spanwise wavelength. The non-dimensional spanwise wavelength of the optimum perturbation is $\lambda^+ \approx 102$. Figure 6.7a shows the resulting energy gain at the optimisation time ($G(\tau^+)$) and Figure 6.7b shows the maximum amplitude (G_{max}) gained during the simulation. The peak in energy occurs at τ^+ for most results and only the lower wavelengths show any differences. This was also seen when the Spalding-Coles profiles were used. Figure 6.8a displays the velocity profile of the perturbation at $t^+ = \tau^+$ and Figure 6.8b shows the velocity profile corresponding to G_{max}. The results for the zero-pressure-gradient case are similar to those obtained using the Spalding-Coles profile confirming the suitability of the curve-fitting method and the modelling approach used.

6.4.2 Case 1 Profile Results

The measurements obtained in the favourable pressure gradient experiments of Case 1 are now used for the base flows of the simulation model. The small crossflow velocity seen in Case 1 is not included in these tests and Q^+ is substituted for U^+. The period of linear growth of the perturbations is assumed small compared to the

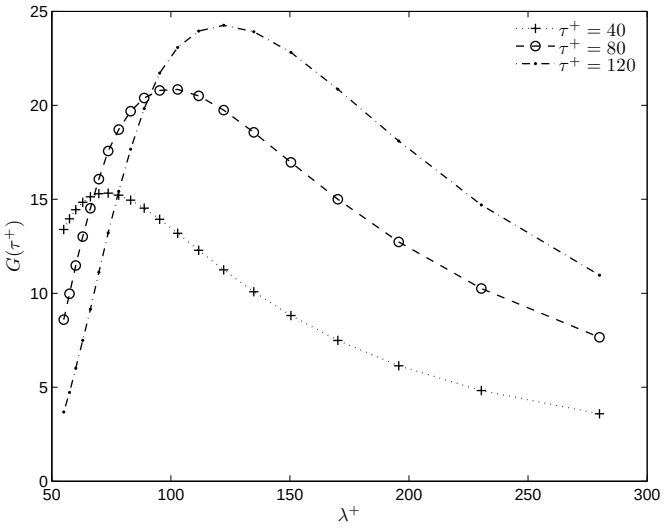

(a)

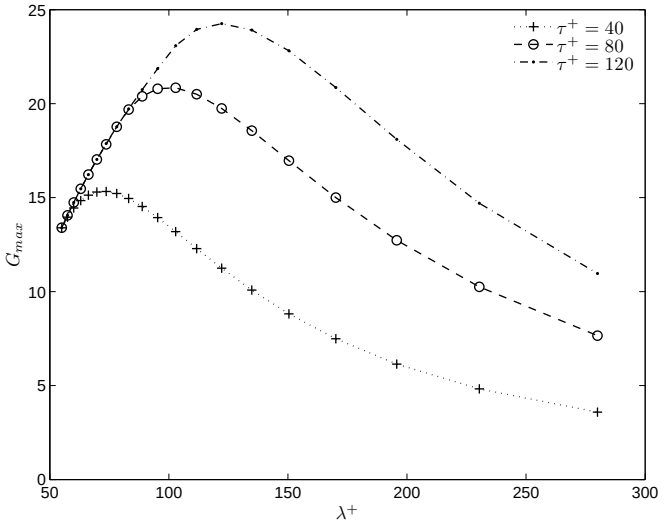

(b)

Figure 6.7: The spanwise wavelength of the optimum perturbation (λ^+) versus the energy amplitude using the zero-pressure-gradient base flow profile: (a) the energy amplitude at the optimisation time $G(\tau^+)$; (b) the maximum energy amplitude (G_{max}) during the simulation.

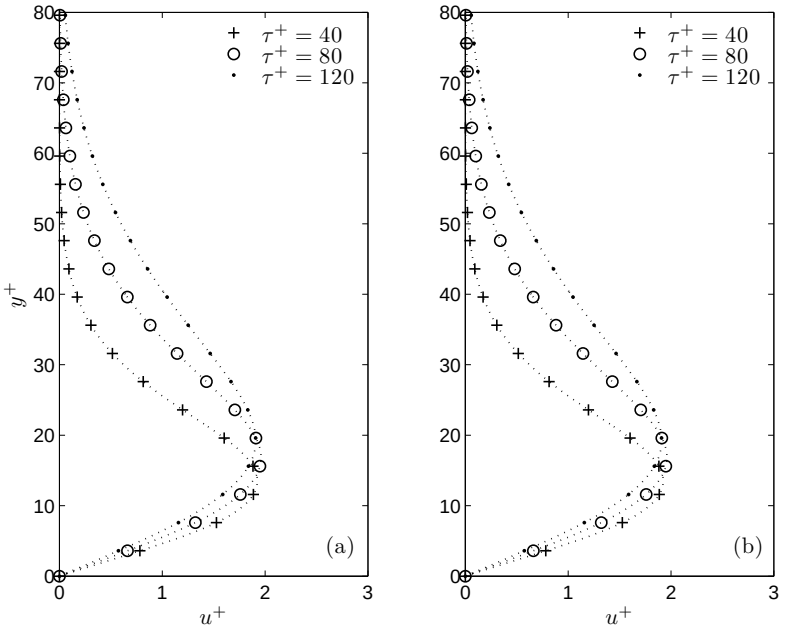

Figure 6.8: The streamwise velocity (u'^+) profile of the disturbance using the zero-pressure-gradient base flow profile: (a) at the optimisation time $G(\tau^+)$; (b) at the peak in energy growth (G_{max}).

time scales of the mean strain and, hence, the disturbances are independent of the streamwise direction (i.e. $\partial/\partial x$ = 0). The freestream velocity and shear stress at the wall increases between the profiles and only these differences can be simulated. Curves are again fitted to the experimental data and sampled every Δy^+=0.4 to construct the base flows for the simulation.

In the first test, the zero-pressure-gradient optimisation time (τ^+=80) is used and optimisation carried out for b^+ and β^+. Figure 6.9 shows how the spanwise wavelength λ^+ affects the growth in energy for the five acceleration profiles in Case 1, with Figure 6.9a showing the results at the optimisation time and Figure 6.9b at peak energy gain. The spanwise wavelength of the optimum perturbation is not affected significantly as it was in the experiments. The experimental increase however, was largely due to a change in the non-dimensional units.

The results show that the energy gained increases 'downstream' (i.e. with s). The increased perturbation energy may be the result of the lift-up mechanism

which, according to Landahl (1980), increases in proportion to the mean shear:

$$\frac{du'}{dt} = -v' \frac{dU}{dy}(y)$$

Piomelli et al. (2000) interpreted the absolute rise in the magnitude of the near-wall streamwise velocity fluctuations, produced by a strong favourable streamwise pressure gradient as being indicative of 'stronger' sublayer streaks (see §2.3.3). The conclusion that the streaks grow stronger parallels with the result here, that the distortion of the mean shear by the acceleration causes the perturbation energy to increase.

Figures 6.10a and 6.10b show the streamwise velocity profile of the perturbation at t^+=80 and at peak energy growth. In both plots, the streamwise velocity gained by the perturbations increases with s and the wall-normal location of peak velocity rises from y^+≈15.5 to y^+≈18. The increase in streamwise velocity is consistent with the streamwise extension of the streaks seen in the experiments, as the faster perturbations will travel further downstream within their growth period.

The optimisation time is kept constant at τ^+=80, which corresponds with the local eddy turnover time of a non-accelerating turbulent boundary layer. The effects of pressure gradients on the time scales of the turbulence, however, may make it necessary to change τ^+. To investigate a τ^+ dependence then, the parameter space is fixed at the two-dimensional optimum values (b^+_{2D} and β^+_{2D}). The effects of acceleration on the perturbation energy growth rates is shown in Figure 6.11. Though the magnitude of the growth is increased, the peak in perturbation amplitude occurs at similar simulation times and the overall temporal behaviour is not significantly different between the results. This does not necessarily mean that the optimal time of τ^+=80 is correct, merely that no τ^+ dependent behaviour can be expected and the particular selection should not affect the conclusions drawn in the results in this section. Were a different τ^+ applied for each base flow profile, any changes which

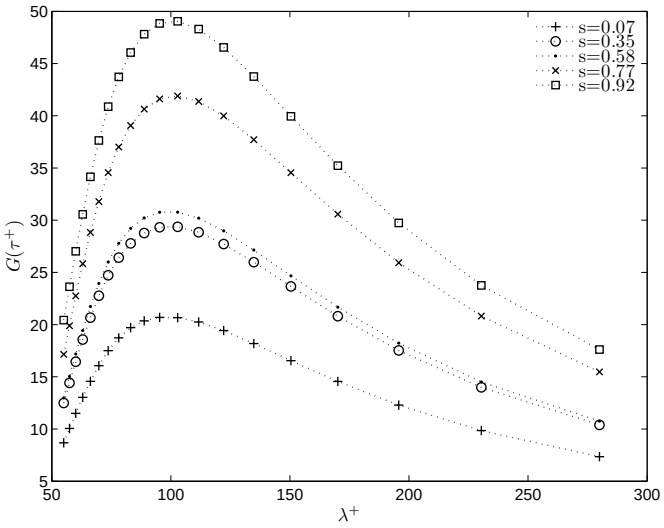

(a)

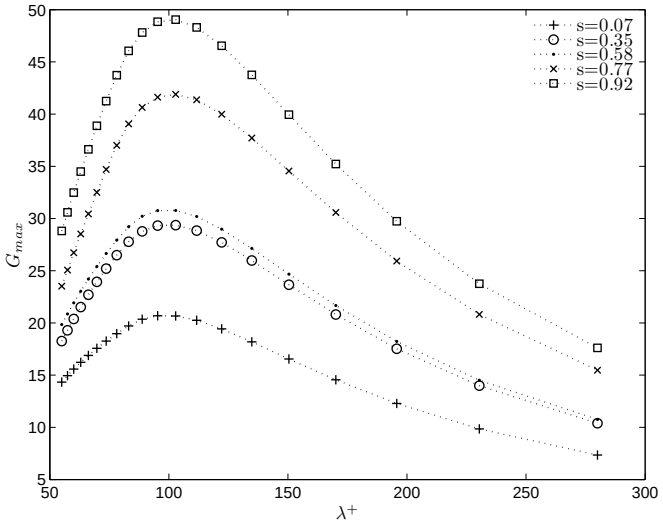

(b)

Figure 6.9: The spanwise wavelength (λ^+) of the optimum perturbation versus the energy amplitude (G) using the five Case 1 velocity profiles: (a) the perturbation amplitude at t^+=τ^+; (b) the maximum amplitude gained by the perturbation during the simulation.

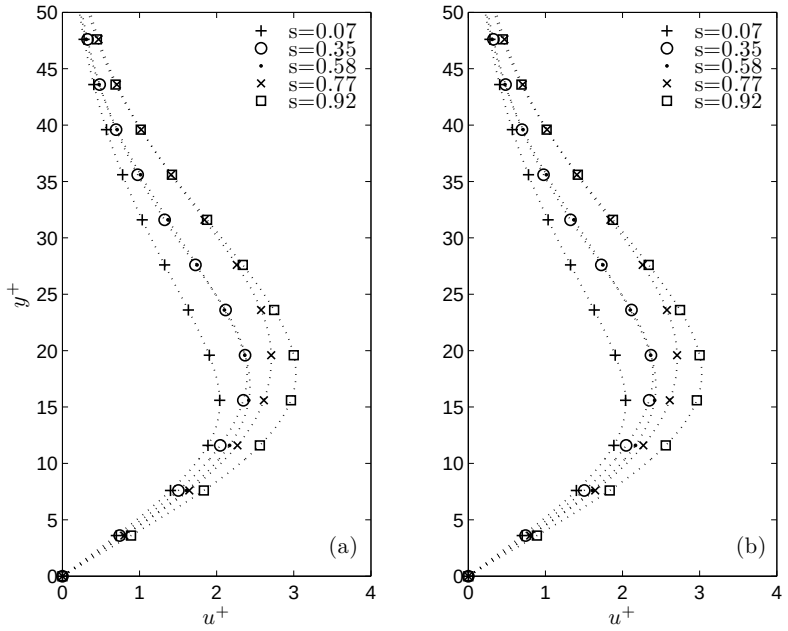

Figure 6.10: Profiles of the perturbation streamwise velocity (u'^+): (a) the perturbation velocity at τ^+=80; (b) the perturbation velocity at maximum G.

occur will result from this adjustment. The effects of changing the eddy turnover time can also seen above in §6.3.

6.5 Three-Dimensional Base Flow Tests

In the previous section the base flows were two-dimensional and the spanwise mean velocity was zero. In this section the spanwise velocity component is introduced into the model. As was the case with the favourable pressure gradient results however, there is no spanwise acceleration as such and the local flow in this direction is assumed steady for the duration of the perturbation growth.

6.5.1 Shear-Driven Crossflow Test Profile

Before the Case 2 simulations are performed, a simple test crossflow profile is used, both to determine the generic response of the model to a steady crossflow velocity component, but also to simulate the effects of a shear-driven three-dimensional

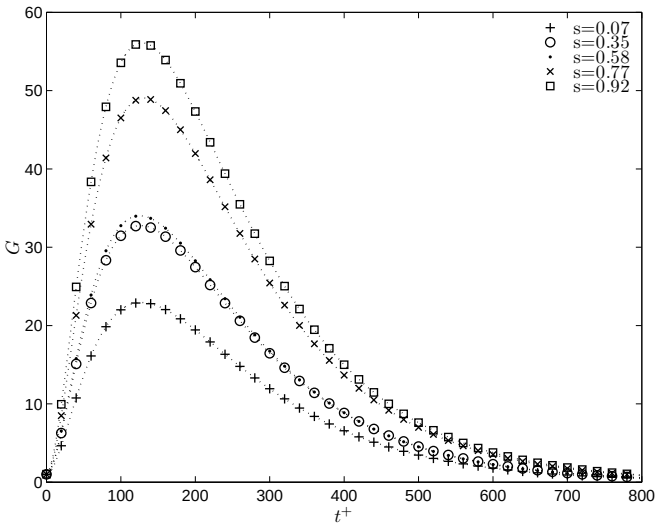

Figure 6.11: The growth rate of the perturbation for the five Case 1 base flow velocity profiles. The parameters b^+_{2D} and β^+_{2D} corresponding to the two-dimensional optimal values are applied for the simulations and held constant. t^+ is the non-dimensional simulation time.

boundary layer. This allows a comparison to made between the effects of shear and pressure-driven three-dimensionality on the behaviour of the perturbations. The profile used has the form:

$$W(y) = W(0)e^{-0.1y} \tag{6.50}$$

and creates a mean-velocity profile similar to that generated by shearing a wall in the spanwise direction with a velocity $W(0)$.

Figure 6.12 shows the results of an optimisation test performed for the (b^+, β^+) parameter space using an optimisation time of τ^+=80. Figure 6.12a shows the results at t^+=τ^+ and Figure 6.12b at peak energy. Increasing the crossflow velocity limits the maximum energy gained by the perturbations and at the same time, increases their spanwise spacing.

Aside from the first and second spanwise crossflow results shown in Figure 6.12b, the peak in energy occurs around a similar spanwise wavelength. The reason for this difference lies in the temporal behaviour of the perturbations. Applying the fixed parameter values (b^+_{2D}, β^+_{2D}), the perturbation growth is simulated

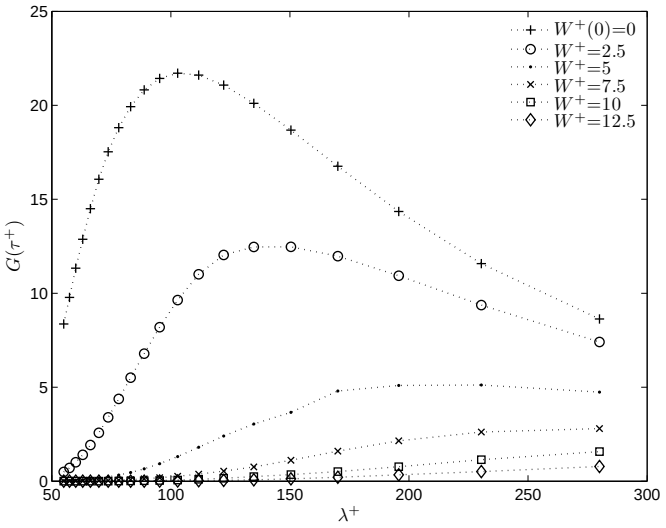

(a)

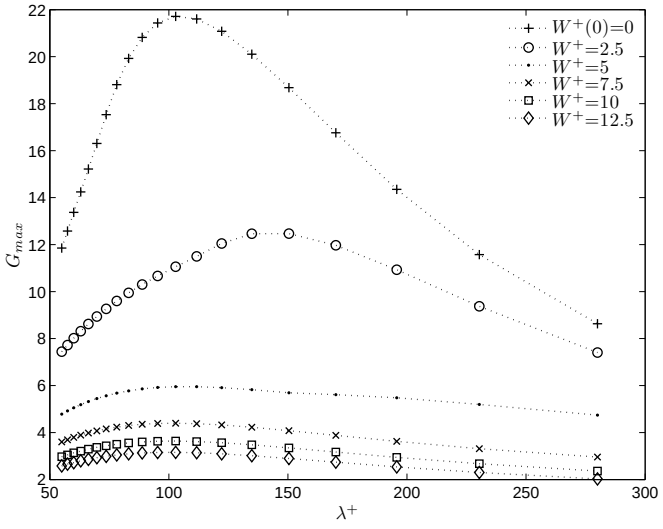

(b)

Figure 6.12: The effect of increasing the level of the artificial crossflow velocity (W^+) on the spanwise wavelength of the optimum perturbation (λ^+): (a) the amplitude of the perturbations corresponding to the optimisation time τ^+=80 ($G(\tau^+)$); (b) the maximum amplitude during the simulation (G_{max}).

for different spanwise velocities. The resulting temporal behaviour is shown in Figure 6.13. The growth limiting effect of the crossflow causes the peak in energy to be reached earlier. By applying τ^+=80, the three perturbations growing under the largest crossflow have already peaked in energy. The remaining two are still growing, resulting in the different behaviour in Figure 6.12b.

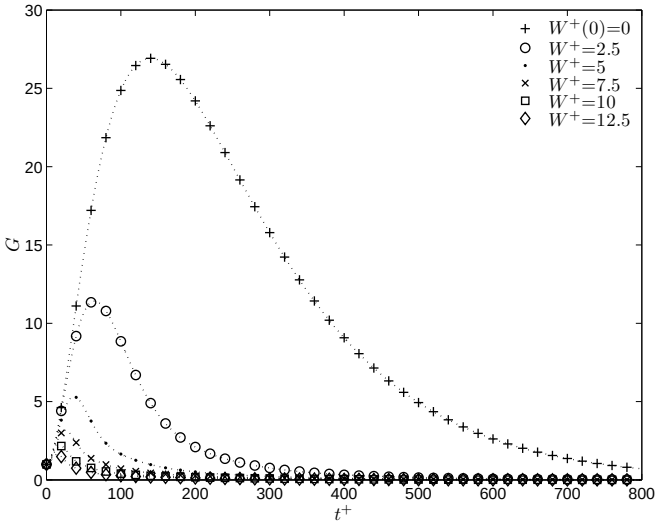

Figure 6.13: The effect of increasing the crossflow velocity component (W^+) in the test profile on the perturbation growth rate. The two-dimensional zero-pressure-gradient parameters b^+_{2D} and β^+_{2D} are applied for the simulations and held constant and (t^+) is the simulation time.

The consequence of this temporal dependency for the perturbation velocity profiles is shown in Figure 6.14. Here, the perturbation velocity magnitude in the resultant direction, $q'^+ = \sqrt{(u'^{+2} + w'^{+2})}$ is substituted in place of u'^+; though it was found that w'^+ remained small anyway. These results are from the (b^+, β^+) optimisation with τ^+=80. The velocity profiles at τ^+=80 and peak energy G_{max} are shown in Figure 6.14a and 6.14b respectively. The temporal dependency introduced by the crossflow is clearly evident in the two profiles at W^+=0 and W^+=2.5.

Case 1 Crossflow Test

In the Case 1 experiment in Chapter 4, a slight crossflow velocity component was

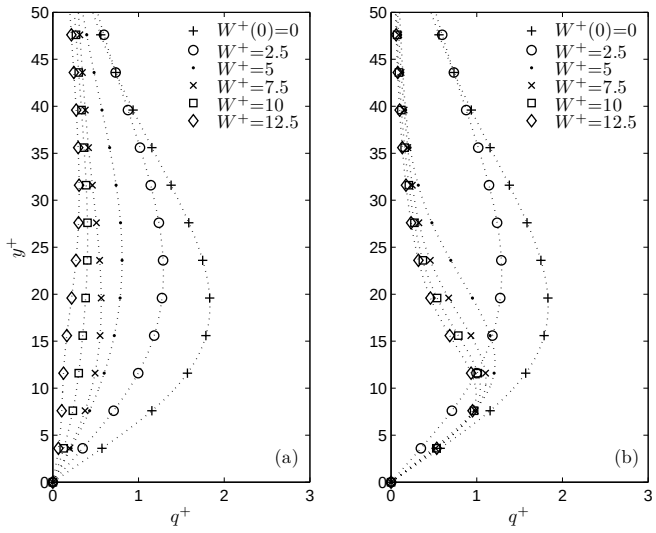

Figure 6.14: The perturbation longitudinal velocity (q'^+) profiles in the artificial base flow simulations at different magnitudes of mean crossflow velocity (W^+): (a) at τ^+=80; (b) the velocity profile at the maximum amplitude during the simulation.

created when the boundary layer was turned into the geometry. For completeness therefore, the Case 1 simulations are performed again, but with this small spanwise velocity component included in the base-flow profiles. The local streamwise velocity Q^+ is first separated into its constituent components in the x and y directions (U^+ and W^+). The results of these simulations are presented and discussed in Appendix H, where they can be seen to differ only marginally from the two-dimensional Case 1 results.

6.5.2 Case 2 Profile Results

For the Case 2 base-flow tests, only the three profiles at the furthest downstream stations were examined in order to avoid the second station results, which had a large flow angle uncertainty. A larger s therefore corresponds to a larger crossflow velocity and acceleration component in the base-flow profile. An optimisation for the (b^+, β^+) parameter space using τ^+=80 is carried out and the effects of the crossflow on the optimum λ^+ is shown in Figure 6.15, with 6.15a showing results for

t^+=τ^+ and 6.15b for the maximum gain in amplitude. The difference between the amplitude at τ^+=80 and G_{max}, is not as great as that seen in §6.5.1. By s=0.92, the spanwise wavelength of the optimum perturbation rises by over 20%. Similar to Case 1, the energy gained by the perturbations increases in response to the streamwise acceleration and is indicative of the 'stronger' streaks found by Piomelli et al. (2000).

The perturbation velocity profiles at τ^+=80 (Figure 6.16a) are similar to those at maximum amplitude (Figure 6.16b). The wall-normal height of the peak in streamwise velocity rises slightly more than the Case 1 results, from y^+≈17.5 to y^+≈21. A slight increase in magnitude between s=0.58 and s=0.92 is also evident, though much smaller than Case 1. In §6.4.2 the correspondence between this result and the streamwise extension of the streaks in a favourable pressure gradient was noted.

To examine the effects of τ^+, a simulation is performed with the parameter values kept fixed at (b^+_{2D}, β^+_{2D}). The results are shown in Figure 6.17. Like the shear-driven simulations, the energy peaks in magnitude earlier as the crossflow velocity is increased. The overall perturbation growth however, remains approximately the same for all profiles.

Discussion

The introduction of a crossflow into the model resulted in a reduction of the energy gained by the perturbations and an increase in their optimum spanwise wavelength. Though no corollary effect has been seen for the streak spacing in three-dimensional flows, the damping effect of three-dimensional turbulent boundary layers is one of their notable characteristics. That a crossflow reduces the energy, or 'strength', of the near-wall streaks may have significant consequences for the near-wall turbulence cycle.

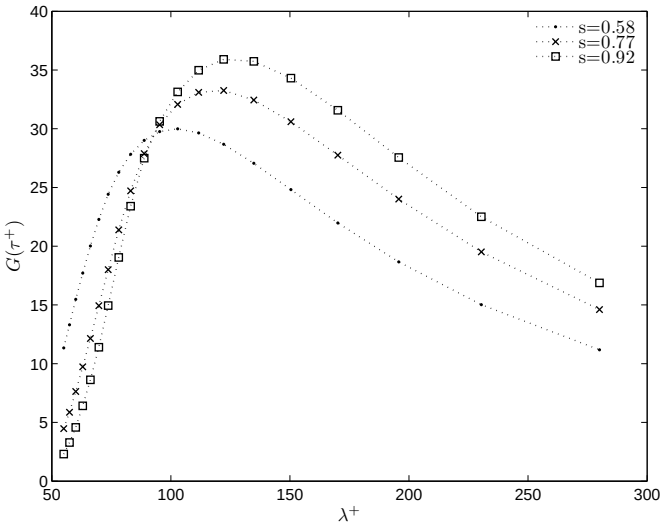

(a)

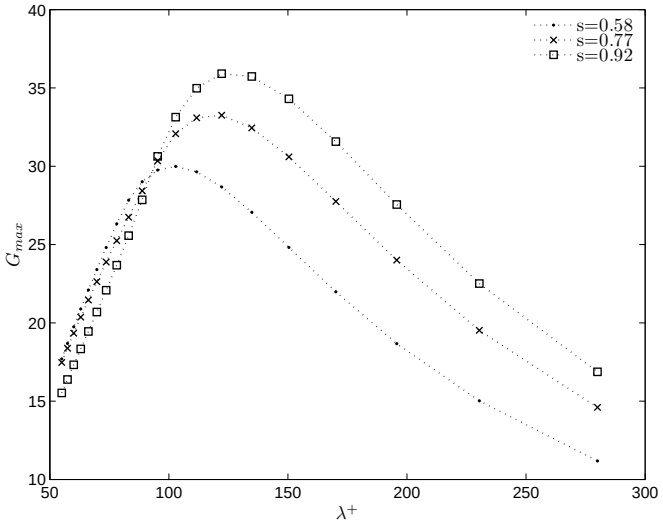

(b)

Figure 6.15: The effect of the crossflow component in the Case 2 velocity profiles on the spanwise wavelength of the optimum perturbation (λ^+): (a) the perturbation amplitude at τ^+=80 ($G(\tau^+)$); (b) the maximum amplitude gained during the simulation (G_{max})). s corresponds to the streamwise station of the particular Case 2 profile.

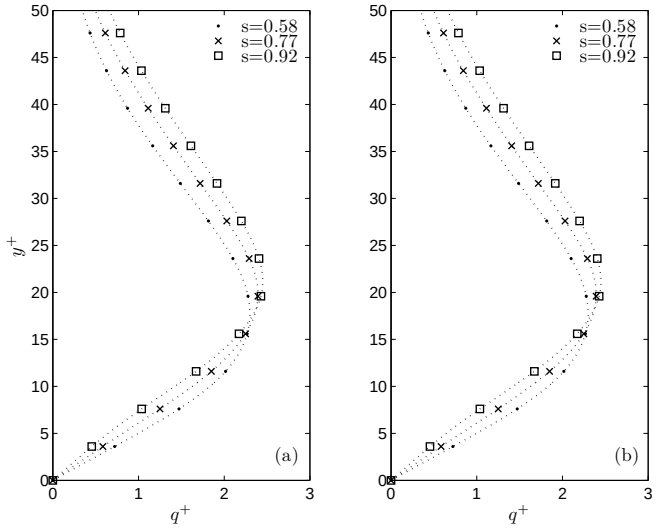

Figure 6.16: The longitudinal velocity of the perturbation (q'^+) in the Case 2 base-flow tests: (a) the velocity at τ^+=80; (b) the velocity at maximum G. s corresponds to the streamwise station of the particular Case 2 profile.

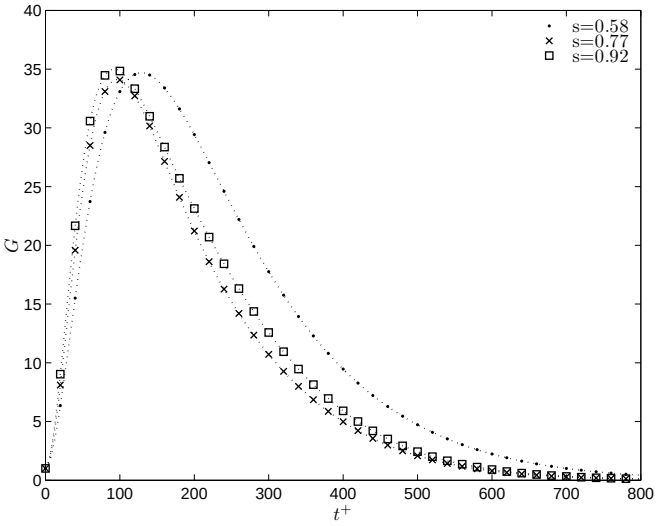

Figure 6.17: The effect of the crossflow component in the Case 2 experiment on the perturbation growth. The two-dimensional parameters (b^+_{2D} and β^+_{2D}) are applied for the simulations. t^+ is the simulation time and s corresponds to the streamwise station of the particular Case 2 profile used (see §5.3).

The introduction of a mean streamwise vorticity into an accelerating turbulent boundary layer in the Case 2 experiment (Chapter 5), would therefore combine the amplifying effect of acceleration, with the damping effect of the three-dimensionality. This may explain the relative insensitivity of the turbulence and the streaks to the mean-flow skewing seen in the Case 2 results and possibly reduce the development of the spanwise boundary layer. Figure 6.18 compares the spanwise velocity profiles of Case 2 with shear-driven test profiles. The streamwise vorticity (i.e. dW/dy) near the wall is comparable only between the weakest test profile ($W^+(0)$=2.5) and the last measurement station (s=0.92).

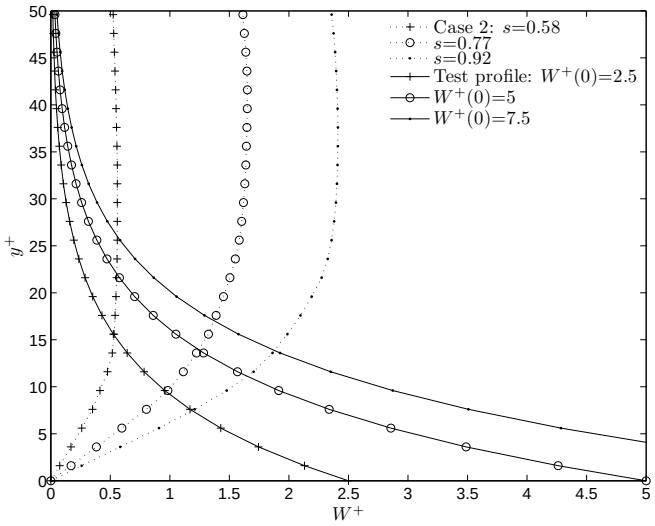

Figure 6.18: The Case 2 mean spanwise velocity profiles at the three furthest downstream stations (s=0.58 to 0.92) compared with three test profiles at different levels of crossflow velocity ($W^+(0)$=2.5 to 7.5). s corresponds to the streamwise station of the particular Case 2 profile.

6.6 Chapter Summary

The methods adopted in this chapter are a departure from the experimental techniques used so far in this thesis. A numerical approach was applied to investigate the near-wall behaviour of the turbulent boundary layer to changes in the mean-velocity profiles measured in the experiments. As only the near-wall region was of

interest, a simplified model of the boundary layer dynamics could be applied and the more complex behaviour governing the majority of the flow neglected in favour of model simplicity. Though this clearly limits the scope of the simulations, the results further elucidate the observations seen in previous chapters and a possible insight into the nature of three-dimensional turbulent boundary layers in general.

In the mathematical model, described in §6.1, the total flow field is given as the sum of a fluctuating or 'perturbation' flow field and a steady 'base' flow. The base flow is represented by mean-velocity profiles. The perturbation flow field represents small amplitude departures away from the base. This approach permits the substitution of the experimental data into the model. Certain assumptions about the mean flow are required however, and these are described in §6.1 as well.

The numerical scheme is described in §6.2. The integrity of the computational model is examined through variations in the temporal and spatial resolutions. This allows the values of the relevant numerical parameters to be set which permits computational simulations to be performed in a rapid and efficient manner. To introduce near-wall streaks into the computational model, a strategy based on optimal perturbations is adopted and described in §6.3. These approaches are pervasive in the literature and the perturbation behaviour simulated here is compared and validated with the relevant observations from other authors.

In §6.4 and §6.5 the experimental mean-velocity profiles are used as the base flows for the simulations. The behaviour of the perturbations in the two-dimensional boundary layers bear strong similarities to the experimental results, with the energy amplitude of the disturbances increasing when the acceleration profiles are introduced. Streamwise accelerations have been shown to produce 'stronger' streaks (Piomelli et al., 2000). The perturbation streamwise velocity also increases, analogous to the streamwise extension of the near-wall streaks seen in the Case 1 experiments. It is observed that the increased shear near the wall, induced by the acceleration, is likely to be responsible for this modified streak behaviour.

Three-dimensional profiles were introduced in §6.5. First, an artificial mean flow distribution was generated that approximated a shear-driven boundary layer. The crossflow attenuates perturbation growth and at the same time, causes a rise in the optimum spanwise wavelength. For the Case 2 experimental data, both the amplifying effect of the acceleration and the damping effect of the streamwise vorticity are resulting in more modest changes. It is suggested that the additional mean streamwise vorticity component of the Case 2 experiment is not great enough to overcome the strong acceleration, resulting in the insensitivity seen in the turbulence and the streaks.

Chapter 7

Conclusions and Recommendations

In this chapter, the main conclusions from this investigation are summarised in §7.1 and in §7.2, recommendations for future research are made.

7.1 Conclusions

The following list summarises the conclusions from this thesis:

1. In Chapter 4.3, an acceleration perturbation with a strength of $K \approx 3.2 \times 10^{-6}$ was applied to a turbulent boundary layer using a lateral contraction of the channel walls. The mean velocity maintained a logarithmic character downstream, but with a steady decline in the velocity gradient and a rise in the intercept. The variation of the log-law parameters κ and B is consistent with the empirical relationship given by Nagib and Chauhan (2008). The mean-flow parameters however, develop in a way resembling that seen for general lateral-strain perturbations; showing less signs of a susceptibility to the streamwise acceleration (§4.3.2).

2. The acceleration precipitates the development of a dual-layered structure to the turbulence. The fluctuating velocity measurements in §4.3.4 and §4.3.6 show that the turbulence near the wall continues to grow, but is permeated by a rising number of large amplitude, positive streamwise velocity fluctuations, which is consistent with an increased spanwise spacing between the low-speed streaks. At greater heights in the boundary layer the flow becomes more quiescent, but with a rising proportion of negative velocity fluctuations. With Bourassa and Thomas (2009) and Piomelli et al. (2000) it is reasoned that these fluctuations define streak ejections, the strength of which is augmented by the streamwise strain but whose number is reduced. The velocity spectra in the inner region are displayed in §4.3.5 and remain consistent with universal behaviour, despite the strong favourable pressure gradient; in agreement with Warnack and Fernholz (1998).

3. The Squire-Winter-Hawthorn relationship is shown in §5.3.2 to provide a satisfactory prediction for crossflow development in the outer layer of a pressure-driven, three-dimensional boundary layer in the presence of a strong streamwise acceleration. A rightward shift of the mean-velocity hodograph develops (Figure 5.17), resulting from the increasing ratio of inner-layer to outer layer mean-velocity caused by the acceleration. The mean-flow skewing near the wall was not as great as expected given the extent of turning in the freestream. In agreement with Hanjalic et al. (1994) the acceleration is likely to be dampening the development of the spanwise boundary layer component near the wall.

4. In §5.3.3 the turbulence in the accelerating boundary layer is shown to be unaffected by the introduction of a crossflow velocity with a peak magnitude of W/Q_e=11%. The recognisable pattern of mean-flow distortion caused by the strong acceleration remained evident to the same extent, with or without streamwise vorticity. The development of the turbulence was also undisturbed as evident in §5.3.3,

§5.3.4 and §5.3.5. It is concluded that the imposed spanwise pressure gradient has neither a stabilising nor destabilising influence on the flow.

5. The viscous sublayer low-speed streaks experience considerable distortion in response to the streamwise acceleration. The non-dimensional spanwise spacing between the streaks increases by around 30% and their streamwise length is extended (§4.4.2). 'Wiggling' or bursting behaviour remained throughout the acceleration but the streaks become calmer resulting in a 'quieter' near-wall region; consistent with the reduced number of streak ejections. The crossflow velocity near the wall is shown to leave the near-wall streaks intact and the spacing between the structures with and without streamline curvature are almost indistinguishable (§5.4.2).

6. A relatively simple numerical approach is developed in Chapter 6 to simulate the response of the low-speed streaks to different mean-flow distributions. It is concluded that the growth and extension of the near-wall streaks found in the Case 1 experiment is in part caused by the increased mean-shear near the wall (§6.4.2), which augments the growth in streamwise perturbation energy and velocity. Further, when a crossflow velocity is introduced on a steady turbulent boundary layer, the linear growth of the streaks will be attenuated (§6.5.1). It is believed then, that the additional mean streamwise vorticity component developed in the Case 2 experiment is not great enough to overcome the stronger, opposing influence of the acceleration; resulting in the insensitivity of the turbulence and the streaks seen in the Case 2 experiment, and possibly impeding the development of the spanwise turbulent boundary layer.

7.2 Recommendations for Further Work

Recognisable patterns are beginning to emerge in the behaviour exhibited by turbulent boundary layers responding to strong acceleration perturbations. The Interpretation of these changes will improve as the knowledge into turbulent boundary layers in general advances. The same cannot be said though for three-dimensional boundary layers, where even the basic understanding of their flow physics is not well-established. Further research to complement and improve the current work are recommended in this section.

7.2.1 Improved Experimental Strategy

The experimental strategy employed for this project, that is, to compare the results of experiments with and without a streamwise vorticity, is a variation of that employed Coleman et al. (2000), but applied to a pressure-driven three-dimensional flow. This is a slight improvement on previous approaches to pressure-driven experiments as it allows the features of the crossflow to be viewed in relative isolation to practical artefacts. Non-linear effects cannot be excluded of course and there will necessarily be greater expense.

7.2.2 External Flow Study

The success of the experimental strategy relies on the pressure gradients being superimposable without affecting each other and the free-spiral-vortex is a necessary external flow pattern to achieve this. Using this external flow, a simple study may be carried out exploring just a single parameter; the ratio of spanwise to streamwise pressure gradient strengths. Reynolds number and other properties could be explored in more detailed studies. An inexpensive way of carrying out such an investigation is unclear and in this thesis, it was found that the practical complexity increased when the ratio magnitude becomes large.

7.2.3 Measurement Techniques

One of greatest limitations of this investigation has been the use of single-element hot-film probes. This was necessary to measure the mean-flow direction and the friction velocity. The finer details of the turbulent structure may be explored in future investigations by using multi-dimensional probes. Other techniques such as LDA and PIV are also worth considering.

The spanwise spacing between the viscous layer low-speed streaks was measured here, partially as it requires less subjective assessment than other structural features, but also because of its importance to turbulent boundary layers. Hydrogen bubble visualisation was used for this, though an alternative technique is to measure spacial correlations with multiple probes. A simpler way to detect changes in streak spacing however, may be to look for changes in the streamwise velocity skewness and flatness statistics near the wall. A rise in the skewness and kurtosis means that high speed streamwise turbulence is increasing as a proportion of the flow, identifying a rise in the spanwise spacing. How effective this approach is must be confirmed with more experimentation first.

7.2.4 Improvements to Computational Model

The simple numerical model developed in this project to study the viscous layer low-speed streaks suffers the drawback that the eddy turnover time must be specified beforehand. The eddy turnover time is used to limit the period of streak growth to a linear regime, but turnover time may change for different mean strain fields and consequently, the correct time must be known first. Many numerical studies employing 'optimum perturbation' strategies in turbulent wall flows appear to suffer this disadvantage and consequently, different values and methods to limit streak-perturbation growth have been suggested in the literature. Clearly, a more rigorous way to define a growth period would be welcome.

Appendix A

Favourable Pressure Gradient Literature

Table A.1 gives some of the literature addressing turbulent boundary layers in favourable pressure gradients. The investigations shown are those referred to often in this project and a number of parameters are included to facilitate an easier comparison with the results. A brief description of the streamwise behaviour exhibited by the acceleration parameter (K) is also included. The column headed as 'Case' references the particular experiment in that work.

No.	Author(s)	Case	K_{max}	K streamwise development	Re(in)	Re(min)	H min/max
1	Fernholz &	1	2	Rapid increase	θ 2549	1587	1.24/1.41
	Warnack, 1998	3	1.5	before relax	5814	1665	1.19/1.68
2	Warnack &	2	4	Rapid increase	θ 862	357	1.34/1.68
	Fernholz, 1998	4	3.88	before relax	2564	649	1.26/1.60
3	Talamelli et al., 2002	1	3.1	Constant	θ 735		2.4
4	McEligot &	1	1.6	Assumed	2h 8300		
	Eckelmann, 2006	2	2.4	constant	5600		
5	Piomelli et al.,	1	3	Rapid increase	θ 720	825	1.31/1.36
	2000	2	6	before relax	720	380	1.23/1.6
6	Blackwelder &	1	4.8	V. rapid increase	θ 2500	650	1.24/1.78
	Kovasnay, 1972			before relax			
7	Bourassa &	1	4.4	Rapid increase	θ 4600		1.2/1.7
	Thomas, 2009			before relax			
8	Jones &	1	1.5		θ 711	640	1.42/1.47
	Launder, 1972	2	2.5	Constant	391	339	1.5/1.62
		3	2.75		474	276	1.46/1.76
9	Jones et al.,	1	2.7		θ 3000		1.2/1.7
	2001	2	3.6	Constant	2300		
		3	5.4		1550		
10		1	1.5		θ 690		1.35
	Spalart, 1986	2	2.5	Constant	415		1.55
		3	2.75		330		1.6

Table A.1: The flow parameters and statistics for a selection of the favourable pressure gradient experimental flows reviewed. The 'Case' column references the particular experiment in the work; Re(in) and Re(min) give the initial and minimum Reynolds numbers measured in that Case; h refers to the half-height of the channel.

Appendix B

Hot-wire Calibration Drift

Figure B.1 shows the result of a calibration-drift error calculation. The curves show the heat-transfer model fits to the data obtained from two calibrations, one performed before and one after a boundary layer experiment. To calculate the error between the two curves, a set of 'test' voltages is converted to velocities using their respective heat transfer models. For the 20 'test' voltage values shown, the total rms error in the velocity is 0.15%.

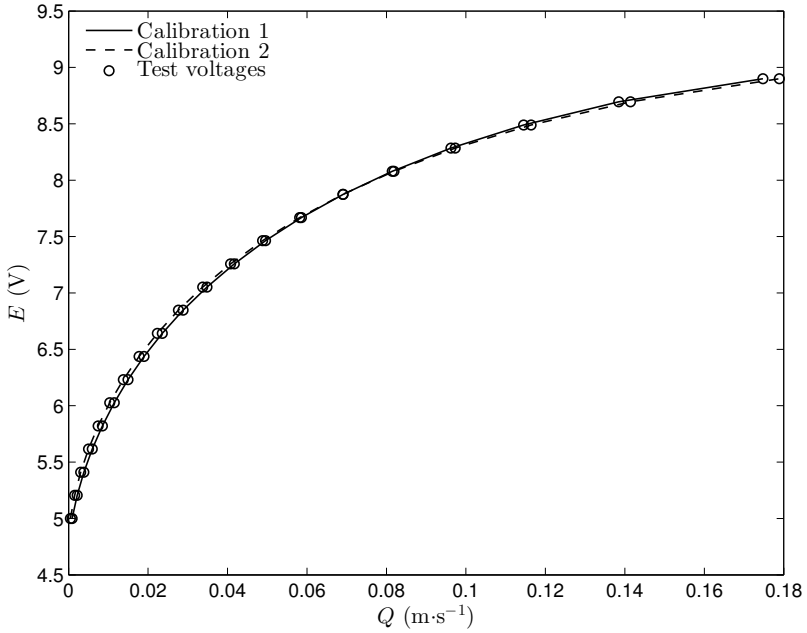

Figure B.1: The heat-transfer models fitted to two calibrations performed before and after a boundary layer profile scan. The circles indicate the 'test' voltages used for the subsequent calculation of the error between the two curve fits.

Appendix C

Laminar Boundary Layer

The laminar boundary layer, formed by a steady two-dimensional flow over a flat plate provides a good initial test case for examining the measurement accuracy, as it is fairly simple and has a well-established velocity profile described by a Blasius boundary layer. The profile of a Blasius flow can be obtained by solving the Blasius equation:

$$\psi''' + \frac{1}{2}\psi\psi' = 0 \tag{C.1}$$

for the non-dimensional stream function $\psi(\eta)$, where η is the Blasius similarity coordinate and the boundary conditions are $\psi(0) = 0$, $\psi(\infty) = 1$, and $\psi'(0) = 0$.

Velocity measurements on a laminar boundary layer were made in the test section using a free-stream velocity Q_e=0.12 m·s^{-1}. In order to compare the results against the Blasius profile, calculation of the boundary-layer thickness is required. Here, the definition δ_{99} is used, corresponding to the point in the mean-velocity profile where the Q reaches 99% of Q_{max}. At this point however, velocity gradients become very small whilst the spatial resolution stays the same, thereby increasing the error when estimating δ_{99}. To improve the comparison between profiles, δ_{99} is calculated by minimising the least squared error between the measured profile and the Blasius curve. The experiment was performed twice and Figure C.1 compares

the velocity data from one test to the theoretical curve. The agreement between the measurements and the Blasius velocity profile is within 2%, but the error in the derivative can be seen to be much larger.

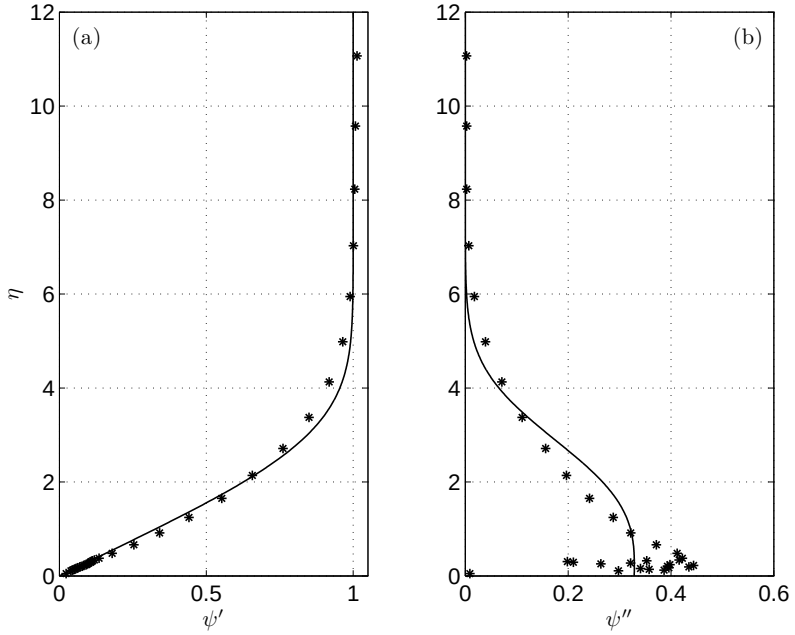

Figure C.1: The Blasius mean-flow profile (–) compared with experimental data (∗) obtained at a freestream velocity Q_e=0.12 m·s^{-1}. (a) The mean velocity and (b) the velocity gradient.

Appendix D

Mean flow

Profiles of the mean velocity in the centre of the channel for both boundary-layer experiments conducted in §3.6 are shown in Figure D.1 non-dimensionalised in outer units. Figure D.2 presents the mean-velocity data of the high Reynolds number flow as a 'defect' profile, where the function F' is the defect velocity defined as $F' = (Q_\infty - Q)/Q_\tau$, and Δ_c is a boundary-layer thickness parameter, calculated by $\Delta_c = \int_0^\infty F' dy$. The shape parameter G, given by $G = \int_0^\infty F'^2 d\frac{y}{\Delta_c}$, can be used as a test for flow equilibrium.

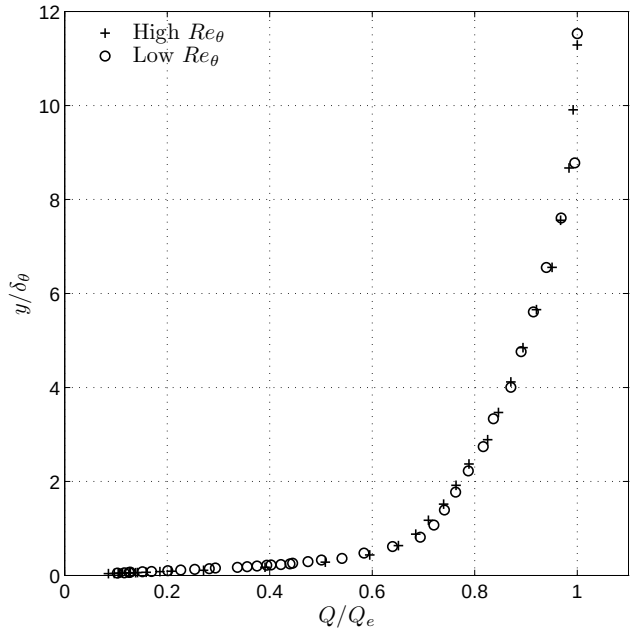

Figure D.1: Mean-velocity profiles of the two turbulent boundary layers non-dimensionalised in outer units. The parameters of each flow are given in Table 3.3. An erroneous measurement has been removed from the low Reynolds number flow.

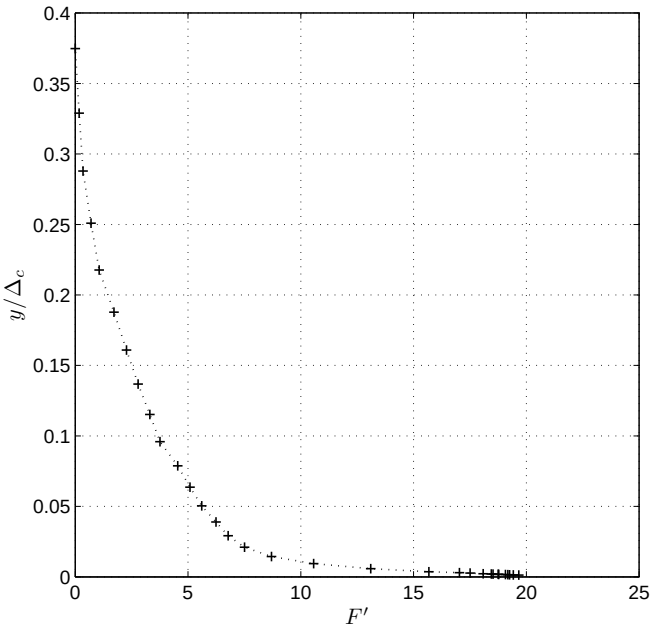

Figure D.2: Mean-velocity defect profile of the high Reynolds number boundary layer.

Appendix E

Skewness and Kurtosis

The skewness is the third normalised moment of a quantity, given here by:

$$S_q = \frac{\overline{q'^3}}{(\overline{q'^2})^{3/2}}$$

Skewness describes the symmetry of a quantity's probability density distribution, hence, the skewness is zero in a Gaussian distribution. A positive skewness indicates that large amplitude positive fluctuations are more frequent than large amplitude negative fluctuations. The right tail of the distribution is longer and the bulk of the measurements appear to shift to the left. Opposite attributes are indicated by negative skewness. Figure E.1 shows skewness profiles obtained in both zero-pressure-gradient turbulent boundary layer experiments conducted in §3.6 versus y^+. The agreement between the two flows is good in the viscous and log regions and less so at greater y^+.

The kurtosis (or flatness) is the fourth normalised moment of a quantity, given by:

$$K_q = \frac{\overline{q'^4}}{(\overline{q'^2})^2}$$

Kurtosis of a quantity describes the strength of the tails relative to height of the peak of the probability density distributions shape. For a Gaussian distribution, K_q=3.

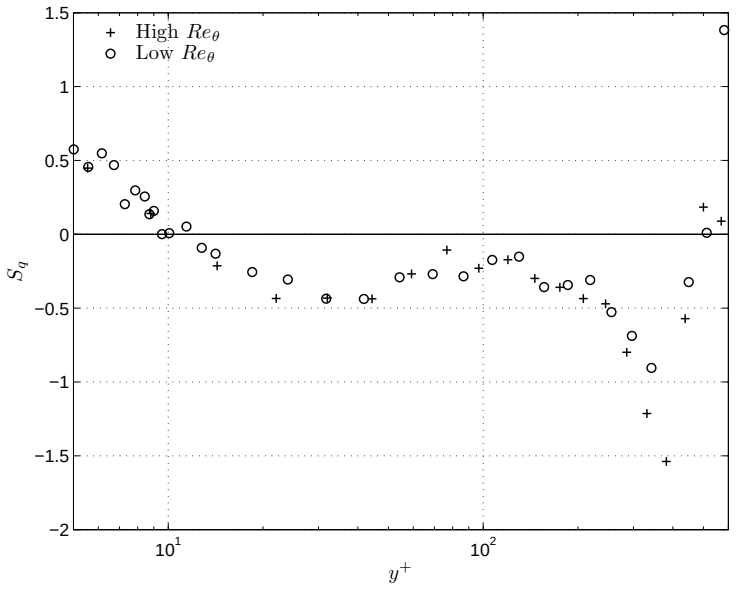

Figure E.1: Profiles of the streamwise velocity skewness versus y^+.

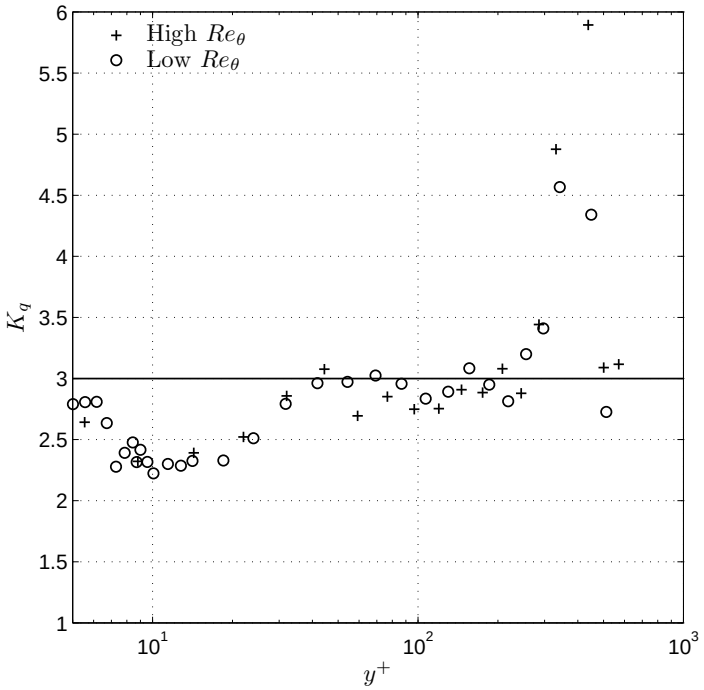

Figure E.2: Profiles of the streamwise velocity kurtosis (K_q) versus y^+.

A K_q>3 means the distribution has 'heavier' tails and a reduced peak: it is 'flatter'. Large amplitude fluctuations, either positive or negative are more frequent. A K_q<3 indicates a reduction in the frequency of large amplitude fluctuations. Figures E.2 shows kurtosis profiles for the two turbulent boundary layers in §3.6 versus y^+, and as was the case with the skewness, the agreement is good between the high and low Reynolds number flows.

Fernholz et al. (1996) review measurements of skewness and kurtosis for high Reynolds number turbulent boundary layers, showing that in the inner layer (viscous and logarithmic region), both statistics appear to be independent of Reynolds number. This may perhaps be a result of a reduction in the influence from outer layer behaviour (which is generally more dependent on the type of flow and Reynolds number), as the boundary layer turbulence develops. It would therefore be unsurprising that the inner layer results from low Reynolds number channel experiments, such as Kreplin and Eckelmann (1979) and the DNS results of Kim et al. (1987), differ from those of Fernholz et al. (1996).

Aside from variability in the outer layer, Figures E.1 and E.2 correspond favourably with profiles presented in Fernholz et al. (1996). Moving upwards from the wall, the point where skewness crosses zero and the location of minimum kurtosis both occur around the same y^+ region as the peak in the rms velocity (Figure 3.20). The near-wall peaks in skewness and kurtosis occur within $2<y^+<3$, and at a magnitude within the range given by Fernholz et al. (1996) ($0.9<S_q<1.65$; $4.1<K_q<7$). The only noticeable departure in favour of low Reynolds number behaviour is that the skewness in the log region ($50<y^+<300$) is not quite zero.

It is not known whether an association between the behaviour of the moments and a proper identification of the logarithmic region has been established yet in the literature. Spalart (1988) discusses the difficulty of identifying logarithmic behaviour, noting that the only rigorous way appears to be by locating the region of constant Ξ, which was employed in §3.6.1 above. From the high velocity results in

Fernholz et al. (1996), the logarithmic region appears to correspond with a long y^+ range of flat S_q and K_q (i.e. $dS_q/dy^+=0$ and $dK_q/dy^+=0$). In this region $S_q \approx 0$ and $K_q \approx 2.8$. As the Reynolds number increases, the turbulence in this overlap or 'core' region of the boundary layer becomes less influenced by the individual behaviours of the near-wall region and outer-layer wake as the Reynolds number increases.

Appendix F

Favourable Pressure Gradient Thickness

The streamwise change in the boundary layer momentum (θ) and displacement thickness (δ^*) measured in the Case 1 experiment (Chapter 4) are shown in Figure F.1. The thinning of the boundary layer induced by the favourable pressure gradient is clearly evident.

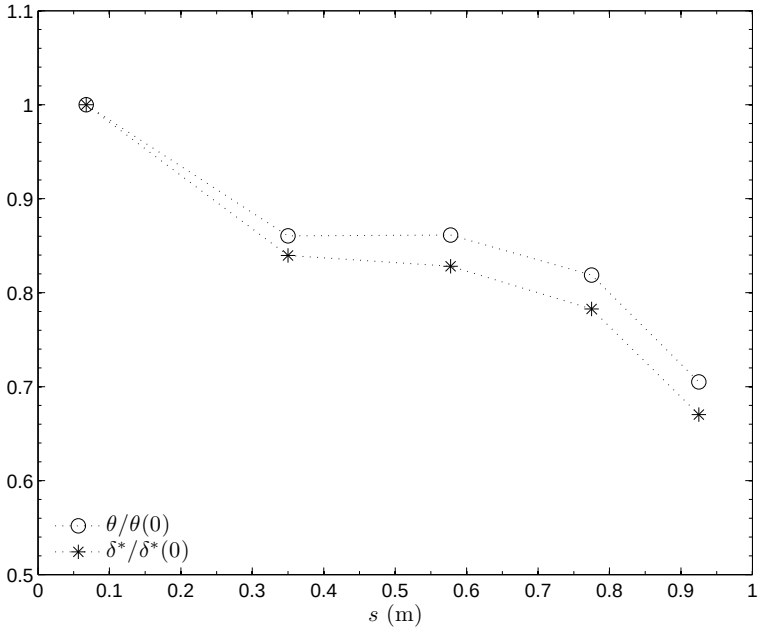

Figure F.1: The streamwise evolution of the momentum and displacement thickness in the Case 1 turbulent boundary layer showing the thinning of the boundary layer downstream. s is the streamwise distance from the defined generator geometry 'inlet'.

Appendix G

Spline fitting

This section documents the curve fitting procedure carried out on the experimental data in order to obtain base-flow profiles to use in the simulations. It was seen in §6.2.1 that altering the domain height does not affect the simulation results significantly. Consequently, any wake or outer layer effects in the experimental velocity measurements can be removed from the curves by shortening the domain height.

Due to variations in the experimental data, smoothing splines were used instead of standard interpolation or filtering processes. Were standard interpolation applied, spurious data and velocity variations would cause the velocity gradient of the profile to fluctuate wildly. The spline function (I), minimises the squared error between spline curve $S(y)$ and the data $U(y)$ and an additional 'smoothing' function:

$$I = \rho \sum_{i=1}^{n} [U(y_i) - S(y_i)]^2 + \int_{y_1}^{y_n} \left(\frac{d^M S(y)}{dy^M} \right)^2$$

Here, the order of the smoothness elements, M, is 3 as a smaller value does not guarantee a smooth first derivative for all profiles. The parameter ρ determines how closely the curve follows the data. Satisfactory results were found here when ρ is set such that the left hand side of the equation for I (the 'tolerance') has a value $1{\times}10^{-7}$.

Figure G.1a shows the curve fitted to the measurement data for the zero-pressure-gradient experimental result (see §3.6). The spline can be seen to smooth out some of the spurious data points giving a smoother first derivative (Figure G.1b).

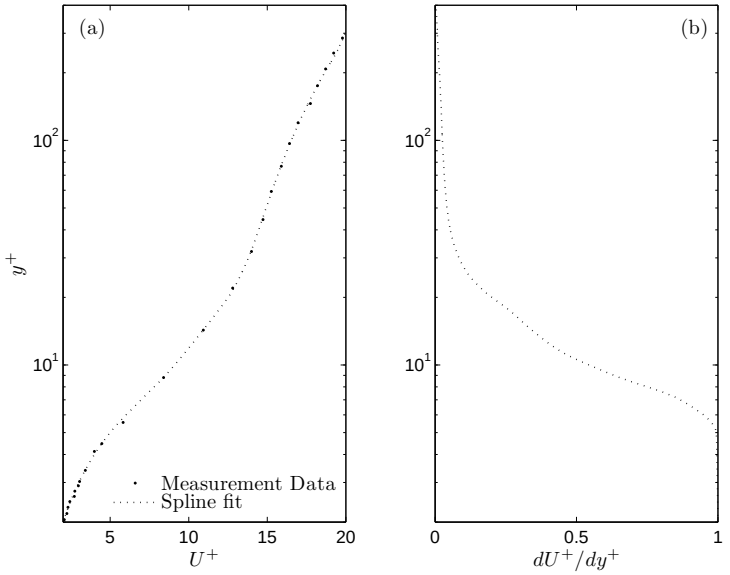

Figure G.1: Profiles of the streamwise mean velocity for a turbulent boundary layer measured in the flow channel, and a smoothing spline fitted through the data. The spline tolerance is $1{\times}10^{-7}$ and the order of the roughness elements measure is 3: (a) the mean-velocity profile (U^+); (b) the mean-velocity gradient of the spline (dU^+/dy^+).

Appendix H

Acceleration Profile Result

The Case 1 favourable-pressure-gradient experiment was seen to have a small spanwise velocity profile. For completeness, this section documents simulations using the Case 1 results where this small spanwise velocity component is included in the profiles. First, the local streamwise velocity in the mean flow direction Q^+ has to be separated into its constituent components in the x and y directions (U^+ and W^+).

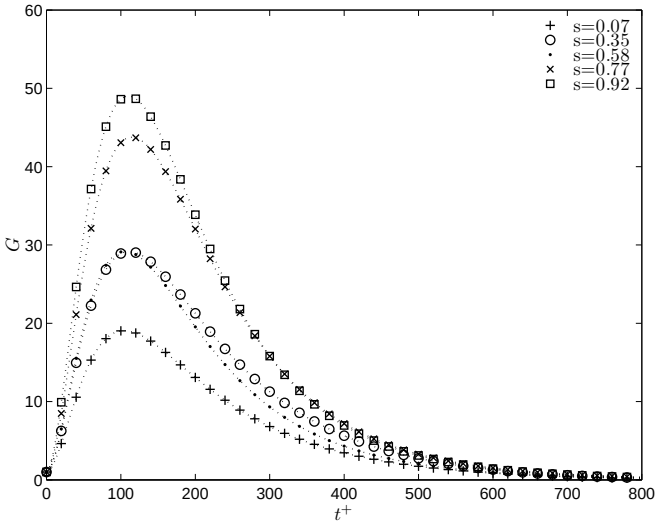

Figure H.1: The effect on the perturbation growth rate of including the slight spanwise component in the Case 1 base flow field. The two-dimensional parameters b^+_{2D} and β^+_{2D} are applied for the simulations. t^+ is the simulation time and s corresponds to the streamwise measurement station of the particular profile in the favourable pressure pressure gradient experiment (see §4.3).

The resulting growth is simulated using the two-dimensional perturbation parameters (b^+_{2D}, β^+_{2D}) and shown in Figure H.1. The overall behaviour is similar to the two-dimensional results for Case 1 (Figure 6.11) and only marginal differences are evident, with a smaller peak in amplitude and the spanwise wavelength corresponding to the peak becoming slightly shorter. Q^+ was used for the two-dimensional simulations, which is larger than U^+ so may cause some of the decline in amplitude on top of any spanwise effects.

Appendix I

References

Abramowitz, M. and Stegun, I A. *Handbook of mathematical functions with formulas, graphs, and mathematical tables*. Dover Publications, New York, 1973.

Adrian, R. J. Hairpin vortex organization in wall turbulence. *Physics of Fluids*, 19 (4), 2007.

Adrian, R. J., Meinhart, C. D., and Tomkins, C. D. Vortex organization in the outer region of the turbulent boundary layer. *Journal of Fluid Mechanics*, 422: 1–54, 2000.

Alfredsson, P. H. and Johansson, A. V. On the detection of turbulence-generating events. *Journal of Fluid Mechanics*, 139(Feb):325–345, 1984a.

Alfredsson, P. H. and Johansson, A. V. Time scales in turbulent channel flow. *Physics of Fluids*, 27(8):1974–1981, 1984b.

Anderson, S. D. and Eaton, J. K. Reynolds stress development in pressure-driven 3-dimensional turbulent boundary-layers. *Journal of Fluid Mechanics*, 202:263–294, 1989.

Baskaran, V., Pontikis, Y. G., and Bradshaw, P. Experimental investigation of 3-

dimensional turbulent boundary-layers on infinite swept wings. *Journal of Fluid Mechanics*, 211:95–122, 1990.

Bhatia, J. C., Durst, F., and Jovanovic, J. Corrections of hot-wire anemometer measurements near walls. *Journal of Fluid Mechanics*, 122(SEP):411–431, 1982.

Bissonnette, L. r. and Mellor, G. L. Experiments on behavior of an axisymmetric turbulent boundary-layer with a sudden circumferential strain. *Journal of Fluid Mechanics*, 63(APR3):369–413, 1974.

Blackwelder, R. F. and Kovasznay, L. S. Large-scale motion of a turbulent boundary-layer during relaminarization. *Journal of Fluid Mechanics*, 53(MAY):61–83, 1972.

Bourassa, C. and Thomas, F. O. An experimental investigation of a highly accelerated turbulent boundary layer. *Journal of Fluid Mechanics*, 634:359–404, 2009.

Bradshaw, P. Turbulent secondary flows. *Annual Review of Fluid Mechanics*, 19: 53–74, 1987.

Bradshaw, P. and Pontikos, N. S. Measurements in the turbulent boundary-layer on an infinite swept wing. *Journal of Fluid Mechanics*, 159(OCT):105–130, 1985.

Bruns, J. M., Fernholz, H. H., and Monkewitz, P. A. An experimental investigation of a three-dimensional turbulent boundary layer in an 's'-shaped duct. *Journal of Fluid Mechanics*, 393:175–213, 1999.

Bruun, H. H. *Hot-wire anemometry : principles and signal analysis*. Oxford University Press, Oxford; New York, 1995.

Bruun, H. H. Hot-film anemometry in liquid flows. *Measurement Science & Technology*, 7(10):1301–1312, 1996.

Bruun, H. H., Khan, M. A., Alkayiem, H. H., and Fardad, A. A. Velocity calibration relationships for hot-wire anemometry. *Journal of Physics E-Scientific Instruments*, 21(2):225–232, 1988.

Bruun, H. H., Nabhani, N., Alkayiem, H. H., Fardad, A. A., Khan, M. A., and Hogarth, E. Calibration and analysis of x hot-wire probe signals. *Measurement Science & Technology*, 1(8):782–785, 1990.

Butler, K. M. and Farrell, B. F. 3-dimensional optimal perturbations in viscous shear-flow. *Physics of Fluids a-Fluid Dynamics*, 4(8):1637–1650, 1992.

Butler, K. M. and Farrell, B. F. Optimal perturbations and streak spacing in wall-bounded turbulent shear-flow. *Physics of Fluids a-Fluid Dynamics*, 5(3):774–777, 1993.

Carpenter, P. W., Kudar, K. L., Ali, R., Sen, P. K., and Davies, C. A deterministic model for the sublayer streaks in turbulent boundary layers for application to flow control. *Philosophical Transactions of the Royal Society a- Mathematical Physical and Engineering Sciences*, 365(1859):2419–2441, 2007.

Chambers, F. W., Murphy, H. D., and McEligot, D. M. Laterally converging flow .2. temporal wall shear-stress. *Journal of Fluid Mechanics*, 127(FEB):403–428, 1983.

Chiang, C. and Eaton, J. K. An experimental study of the effects of three-dimensionality on the near wall turbulence structures using flow visualization. *Experiments in Fluids*, 20(4):266–272, 1996.

Coleman, G. N., Kim, J., and Le, A. T. A numerical study of three-dimensional wall-bounded flows. *International Journal of Heat and Fluid Flow*, 17(3):333–342, 1996.

Coleman, G. N., Kim, J., and Spalart, P. R. A numerical study of strained three-dimensional wall-bounded turbulence. *Journal of Fluid Mechanics*, 416:75–116, 2000.

Coleman, G. N., Fedorov, D., Spalart, P. R., and Kim, J. A numerical study of laterally strained wall-bounded turbulence. *Journal of Fluid Mechanics*, 639:443–478, 2009.

Coles, D. The law of the wake in the turbulent boundary layer. *Journal of Fluid Mechanics*, 1(2):191–226, 1956.

Compton, D. A. and Eaton, J. K. Near-wall measurements in a three-dimensional turbulent boundary layer. *Journal of Fluid Mechanics*, 350:189–208, 1997.

Corbett, P. and Bottaro, A. Optimal linear growth in swept boundary layers. *Journal of Fluid Mechanics*, 435:1–23, 2001.

Degani, A. T., Smith, F. T., and Walker, J. D. A. The structure of a 3-dimensional turbulent boundary-layer. *Journal of Fluid Mechanics*, 250:43–68, 1993.

DISA, . Instruction manual. disa 55m10 system, 1977.

Dixit, S. A. and Ramesh, O. N. Pressure-gradient-dependent logarithmic laws in sink flow turbulent boundary layers. *Journal of Fluid Mechanics*, 615:445–475, 2008.

Dixit, S. A. and Ramesh, O. N. Large-scale structures in turbulent and reverse-transitional sink flow boundary layers. *Journal of Fluid Mechanics*, 649:233–273, 2010.

Duque-Daza, C. A., Baig, M. F., Lockerby, D. A., Chernyshenko, S. I., and Davies, C. *Journal of Fluid Mechanics*, 2012.

Fernholz, H. H. and Vagt, J. D. Turbulence measurements in an adverse pressure-gradient 3- dimensional turbulent boundary-layer along a circular-cylinder. *Journal of Fluid Mechanics*, 111(OCT):233–269, 1981.

Fernholz, H. H. and Warnack, D. The effects of a favourable pressure gradient and of the reynolds number on an incompressible axisymmetric turbulent boundary layer. part 1. the turbulent boundary layer. *Journal of Fluid Mechanics*, 359: 329–356, 1998.

Fernholz, H. H., Janke, G., Schober, M., Wagner, P. M., and Warnack, D. New developments and applications of skin-friction measuring techniques. *Measurement Science & Technology*, 7(10):1396–1409, 1996.

Flack, K. A. Near-wall structure of three-dimensional turbulent boundary layers. *Experiments in Fluids*, 23(4):335–340, 1997.

Flack, K. A. and Johnston, J. P. Near-wall flow in a three-dimensional boundary layer on the endwall of a 30 degrees bend. *Experiments in Fluids*, 24(2):175–184, 1998.

Hammache, M. and Gharib, M. A novel method to promote parallel vortex shedding in the wake of circular-cylinders. *Physics of Fluids a-Fluid Dynamics*, 1(10):1611–1614, 1989.

Hanjalic, K., Jakirlic, S., and Durst, F. A computational study of joint effects of transverse-shear and streamwise acceleration on 3-dimensional boundary-layers. *International Journal of Heat and Fluid Flow*, 15(4):269–282, 1994.

Henningson, D., Spalart, P., and Kim, J. Numerical simulations of turbulent spots in plane poiseuille and boundary-layer flow. *Physics of Fluids*, 30(10):2914–2917, 1987.

Henningson, D. S., Lundbladh, A., and Johansson, A. V. A mechanism for bypass transition from localized disturbances in wall-bounded shear flows. *Journal of Fluid Mechanics*, 250:169–207, 1993.

Holstad, A., Andersson, H. I., and Pettersen, B. Turbulence in a three-dimensional wall-bounded shear flow. *International Journal for Numerical Methods in Fluids*, 62(8):875–905, 2010.

Hultgren, L. S. and Gustavsson, L. H. Algebraic growth of disturbances in a laminar boundary- layer. *Physics of Fluids*, 24(6):1000–1004, 1981.

Hutchins, N. and Choi, K. S. Accurate measurements of local skin friction coefficient using hot-wire anemometry. *Progress in Aerospace Sciences*, 38(4-5):421–446, 2002.

Itoh, M. and Kobayashi, M. Turbulent structure in the three-dimensional boundary layer on a swept wing. *International Journal of Heat and Fluid Flow*, 21(3): 271–277, 2000.

Itoh, M., Yamada, Y., Imao, S., and Gonda, M. Experiments on turbulent-flow due to an enclosed rotating disk. *Experimental Thermal and Fluid Science*, 5(3): 359–368, 1992.

Jeong, J., Hussain, F., Schoppa, W., and Kim, J. Coherent structures near the wall in a turbulent channel flow. *Journal of Fluid Mechanics*, 332:185–214, 1997.

Johnston, J. P. and Flack, K. A. Review - advances in three-dimensional turbulent boundary layers with emphasis on the wall-layer regions (data bank contribution). *Journal of Fluids Engineering-Transactions of the Asme*, 118(2):219–232, 1996.

Johnstone, R., Coleman, G. N., and Spalart, P. R. The resilience of the logarithmic law to pressure gradients: evidence from direct numerical simulation. *Journal of Fluid Mechanics*, 643:163–175, 2010.

Jones, M. B., Marusic, I., and Perry, A. E. Evolution and structure of sink-flow turbulent boundary layers. *Journal of Fluid Mechanics*, 428:1–27, 2001.

Jones, W. P. and Launder, B. E. Some properties of sink-flow turbulent boundary-layers. *Journal of Fluid Mechanics*, 56(NOV28):337–351, 1972.

Kannepalli, C. and Piomelli, U. Large-eddy simulation of a three-dimensional shear-driven turbulent boundary layer. *Journal of Fluid Mechanics*, 423:175–203, 2000.

Khoo, B. C., Chew, Y. T., and Teo, C. J. Near-wall hot-wire measurements part ii: Turbulence time scale, convective velocity and spectra in the viscous sublayer. *Experiments in Fluids*, 31(5):494–505, 2001.

Kiesow, R. O. and Plesniak, M. W. Near-wall physics of a shear-driven three-dimensional turbulent boundary layer with varying crossflow. *Journal of Fluid Mechanics*, 484:1–39, 2003.

Kim, H. T., Kline, S. J., and Reynolds, W. C. Production of turbulence near a smooth wall in a turbulent boundary layer. *Journal of Fluid Mechanics*, 50 (NOV15):133–166, 1971.

Kim, J. and Lim, J. A linear process in wall-bounded turbulent shear flows. *Physics of Fluids*, 12(8):1885–1888, 2000.

Kim, J., Moin, P., and Moser, R. Turbulence statistics in a fully-developed channel flow at low reynolds-number. *Journal of Fluid Mechanics*, 177:133–166, 1987.

King, L. V. On the convection of heat from small cylinders in a stream of fluid: Determination of the convection constants of small platinum wires, with applications to hot-wire anemometry. *Proceedings of the Royal Society of London. Series A*, 90(622):563–570, 1914.

Kline, S.J., Reynolds, W.C., Schraub, F.A., and Runstadler, P.W. The structure of turbulent boundary layers. *Journal of Fluid Mechanics*, 30(4):741–773, 1967.

Kreplin, H. P. and Eckelmann, H. Propagation of perturbations in the viscous sublayer and adjacent wall region. *Journal of Fluid Mechanics*, 95(NOV):305–322, 1979.

Landahl, M. T. A note on an algebraic instability of inviscid parallel shear flows. *Journal of Fluid Mechanics*, 98(MAY):243–251, 1980.

Landahl, M. T. On sublayer streaks. *Journal of Fluid Mechanics*, 212:593–614, 1990.

Launder, B. E. and Loizou, P. A. Laminarization of 3-dimensional accelerating boundary layers in a curved rectangular-sectioned duct. *International Journal of Heat and Fluid Flow*, 13(2):124–131, 1992.

Le, A. T., Coleman, G. N., and Kim, J. Near-wall turbulence structures in three-dimensional boundary layers. *International Journal of Heat and Fluid Flow*, 21 (5):480–488, 2000.

Lee, T. and Budwig, R. 2 improved methods for low-speed hot-wire calibration. *Measurement Science & Technology*, 2(7):643–646, 1991.

Ligrani, P. M. and Bradshaw, P. Spatial-resolution and measurement of turbulence in the viscous sublayer using subminature hot-wire probes. *Experiments in Fluids*, 5(6):407–417, 1987.

Littell, H. S. and Eaton, J. K. Turbulence characteristics of the boundary-layer on a rotating-disk. *Journal of Fluid Mechanics*, 266:175–207, 1994.

Lockerby, D. A., Carpenter, P. W., and Davies, C. Control of sublayer streaks using microjet actuators. *Aiaa Journal*, 43(9):1878–1886, 2005.

Lofdahl, L., Truong, T. V., and Bruns, J. M. Measurements of turbulent quantities in a complex 3-dimensional boundary-layer flow. *Experiments in Fluids*, 18(5): 335–342, 1995.

Lomas, C. G. *Fundamentals of hot-wire anemometry.* Cambridge University Press, Cambridge; New York, 1986.

McEligot, D. M. and Eckelmann, H. Laterally converging duct flows. part 3. mean turbulence structure in the viscous layer. *Journal of Fluid Mechanics*, 549:25–59, 2006.

McEligot, Donald M., Brodkey, Robert S., and Eckelmann, Helmut. Laterally converging duct flows. part 4. temporal behaviour in the viscous layer. *Journal of Fluid Mechanics*, 634:433–461, 2009.

Moin, P., Shih, T. H., Driver, D., and Mansour, N. N. Direct numerical simulation of a 3-dimensional turbulent boundary-layer. *Physics of Fluids a-Fluid Dynamics*, 2(10):1846–1853, 1990.

Moser, R. D., Kim, J., and Mansour, N. N. Direct numerical simulation of turbulent channel flow. *Physics of Fluids*, 11(4):943–945, 1999.

Murphy, H. D., Chambers, F. W., and McEligot, D. M. Laterally converging flow .1. mean flow. *Journal of Fluid Mechanics*, 127(FEB):379–401, 1983.

Nagib, H. M. and Chauhan, K. A. Variations of von karman coefficient in canonical flows. *Physics of Fluids*, 20(10), 2008.

Narasimha, R. and Sreenivasan, K. Relaminarization of a highly accelerated turbulent boundary- layers. *Journal of Fluid Mechanics*, 61(NOV20):417–447, 1973.

Olcmen, M. S., Simpson, R. L., and George, J. Some reynolds number effects on two- and three-dimensional turbulent boundary layers. *Experiments in Fluids*, 31 (2):219–228, 2001.

Olcmen, S. M. and Simpson, R. L. An experimental-study of a 3-dimensional pressure-driven turbulent boundary-layer. *Journal of Fluid Mechanics*, 290:225–262, 1995.

Pailhas, G., Barricau, P., Touvet, Y., and Perret, L. Friction measurement in zero and adverse pressure gradient boundary layer using oil droplet interferometric method. *Experiments in Fluids*, 47(2):195–207, 2009.

Panchapakesan, N. R., Nickels, T. B., Joubert, P. N., and Smits, A. J. Lateral straining of turbulent boundary layers .2. streamline convergence. *Journal of Fluid Mechanics*, 349:1–30, 1997.

Panton, R. L. Overview of the self-sustaining mechanisms of wall turbulence. *Progress in Aerospace Sciences*, 37(4):341–383, 2001.

Piomelli, U., Balaras, E., and Pascarelli, A. Turbulent structures in accelerating boundary layers. *Journal of Turbulence*, 1:16, 2000.

Pompeo, L., Bettelini, M. S. G., and Thomann, H. Laterally strained turbulent boundary-layers near a plane of symmetry. *Journal of Fluid Mechanics*, 257: 507–532, 1993.

Pope, S. B. *Turbulent flows*. Cambridge University Press, Cambridge; New York, 2000.

Ricco, P. and Wu, S. L. On the effects of lateral wall oscillations on a turbulent boundary layer. *Experimental Thermal and Fluid Science*, 29(1):41–52, 2004.

Robinson, S. K. Coherent motions in the turbulent boundary-layer. *Annual Review of Fluid Mechanics*, 23:601–639, 1991.

Runstadler, P. W., Kline, S. J., and Reynolds, W. C. An experimental investigation of the flow structure of the turbulent boundary layer. Technical report, Department of mechanical engineering, Stanford University, June 1963.

Saddoughi, S. G. and Veeravalli, S. V. Local isotropy in turbulent boundary-layers at high reynolds-number. *Journal of Fluid Mechanics*, 268:333–372, 1994.

Samways, A. L., Ali, J., Aldeen, M. F. N., and Bruun, H. H. The calibration of and measurements with cylindrical hot-film probes in water flows. *Measurement Science & Technology*, 5(12):1551–1559, 1994.

Schlichting, H. *Boundary-layer theory.* McGraw-Hill, New York, 1979.

Schoppa, W. and Hussain, F. Coherent structure generation in near-wall turbulence. *Journal of Fluid Mechanics*, 453:57–108, 2002.

Schraub, A. F. and Kline, S. J. A study of the structure of the turbulent boundary layer with and without longitudinal pressure gradients. Technical report, Thermo Sciences Division, Stanford University, 1965.

Schwarz, W. R. and Bradshaw, P. Turbulence structural-changes for a 3-dimensional turbulent boundary-layer in a 30-degree bend. *Journal of Fluid Mechanics*, 272: 183–209, 1994.

Smith, C. R. and Metzler, S. P. The characteristics of low-speed streaks in the near-wall region of a turbulent boundary layer. *Journal of Fluid Mechanics*, 129 (APR):27–54, 1983.

Spalart, P. R. Numerical study of sink-flow boundary-layers. *Journal of Fluid Mechanics*, 172:307–328, 1986.

Spalart, P. R. Direct simulation of a turbulent boundary-layer up to $\mathrm{re}_\theta = 1410$. *Journal of Fluid Mechanics*, 187:61–98, 1988.

Talamelli, A., Fornaciari, N., Westin, K. J. A., and Alfredsson, P. H. Experimental investigation of streaky structures in a relaminarizing boundary layer. *Journal of Turbulence*, 3:13, 2002.

Tennekes, H. and Lumley, John L. *A first course in turbulence.* MIT Press, Cambridge, Mass., 1972.

Tewari, S. S. and Jaluria, Y. Calibration of constant-temperature hot-wire anemometers for very low velocities in air. *Review of Scientific Instruments*, 61(12):3834–3845, 1990.

Theodorsen, T. Mechanism of turbulence. In *Proceedings of the Midwestern Conference on Fluid Mechanics, 2nd, Columbus, Ohio*, volume 21, page 783. Ohio State University, 1952.

Warnack, D. and Fernholz, H. H. The effects of a favourable pressure gradient and of the reynolds number on an incompressible axisymmetric turbulent boundary layer. part 2. the boundary layer with relaminarization. *Journal of Fluid Mechanics*, 359:357–381, 1998.

Williamson, C. H. K. Oblique and parallel modes of vortex shedding in the wake of a circular-cylinder at low reynolds-numbers. *Journal of Fluid Mechanics*, 206: 579–627, 1989.

Wu, S. and Bose, N. Calibration of a wedge-shaped vee hot-film probe in a towing tank. *Measurement Science & Technology*, 4(1):101–108, 1993.

Wu, S. and Bose, N. An extended power-law model for the calibration of hot-film constant-temperature probes. *International Journal of Heat and Mass Transfer*, 37(3):437–442, 1994.

Zhou, J., Adrian, R. J., Balachandar, S., and Kendall, T. M. Mechanisms for generating coherent packets of hairpin vortices in channel flow. *Journal of Fluid Mechanics*, 387:353–396, 1999.